DEVELOPMENT OF SURFACE PREPARATION PROCEDURE RECOMMENDATIONS FOR WIND TURBINE BLADE FIELD REPAIRS

by

Ariel Francis Lusty

A dissertation submitted in partial fulfillment
of the requirements for the degree

of

Doctor of Philosophy

in

Mechanical Engineering

MONTANA STATE UNIVERSITY
Bozeman, Montana

December 2022

DEDICATION

For Ava and Dane.

ACKNOWLEDGEMENTS

Through a pandemic and breaking both my legs, pursuing a PhD has not been a walk in the park. It has been a stumble through the park with my face masked and a cane in hand. Nevertheless, it has been in a park surrounded by the world's most beautiful mountains, trees, and wildflowers. It has been in Montana, the most magical place I have ever lived. It has been a in a place with colleagues', friends', and family's (and medical personnels') hands outstretched to lift me back up when I've fallen. Most importantly, pursuing a PhD has led to strides in developing my confidence to do research.

Thanks to the support of my advisor, Dr. Doug Cairns, even broken legs did not stop me from climbing towards my doctorate. His guidance and suggestions were irreplaceable to my learning and growth. I also owe gratitude to my committee, Dr. David Miller, Dr. Ladean McKittrick, and Dr. Sarah Codd for sharing their knowledge and feedback. I have insurmountable gratitude for Daniel Samborsky's help. Dan's understandings and advice in the composites lab was decisive in many steps of my research process. I would also like to thank Sandia National Laboratories and the Department of Energy for funding this research under the Wind Turbine Blade Durability and Damage Tolerance Project. Josh Paquette's insights were invaluable and his leadership commendable. It has been an honor to learn amongst the world's brightest professors, instructors, and graduate students here at Montana State University. I am tremendously beholden to my community in and outside of the university.

TABLE OF CONTENTS

TABLE OF CONTENTS CONTINUED

TABLE OF CONTENTS CONTINUED

TABLE OF CONTENTS CONTINUED

LIST OF TABLES

Table Page

LIST OF TABLES CONTINUED

Table Page

LIST OF TABLES CONTINUED

Table Page

LIST OF FIGURES

Figure Page

LIST OF FIGURES CONTINUED

Figure Page

LIST OF FIGURES CONTINUED

Figure Page

LIST OF FIGURES CONTINUED

Figure Page

LIST OF FIGURES CONTINUED

Figure Page

LIST OF FIGURES CONTINUED

Figure Page

LIST OF FIGURES CONTINUED

Figure Page

LIST OF FIGURES CONTINUED

Figure Page

LIST OF FIGURES CONTINUED

Figure Page

LIST OF FIGURES CONTINUED

Figure Page

ABSTRACT

Wind turbine blades necessitate reliable field repairs. However, the effects of current wind turbine field repair surface preparation techniques were not well-documented. Poorly informed surface preparation procedures lead to poor quality repairs, so surface preparation procedure recommendations for wind turbine blade field repairs were developed. The effectiveness of current surface preparation techniques, the effects of contaminants, and alternative techniques were evaluated. Current surface preparation techniques involve using solvent wiping to remove contamination. Results indicated that solvent wiping does not significantly affect bond strengths, but solvents can gel resin surfaces. Measuring the changes in bond strengths due to contamination from composite dust and hydraulic oil with time indicated that contamination diffusion effects along bond lines were negligible, but that composite dust and hydraulic oil diminished bond strengths. Contaminants should thus be removed from bond line surfaces prior to repairs. The goal of considering alternative techniques was to increase and equalize the surface energy of repair surfaces using plasma or sizing. There were significant drops in contact angles on composite surfaces treated with plasma, so plasma treatments should continue to be considered for composite surface preparation methods. To examine sizing effects, sizing was applied to scarfed surfaces and specimens were tested in tension. Applying sizing to tapered surfaces prior to scarf repairs did not affect scarf tension ultimate stress values, failure modes, or failure surface elemental composition. In addition, there was a stiffness reduction in the scarfed specimens compared to unscarfed specimens, indicating that the scarf tension repair did not fully restore the composite plate's original properties. Scarf tension experiments were simulated using finite element analysis and results had good agreement between the experiments and the model. The surface preparation recommendation is to test whichever surface preparation methods and adhesive-substrate combinations are used for a repair prior to implementation in the field. Implementing testing of surface preparation methods with adhesive-substrate combinations into surface preparation procedures will decrease lifetime costs and increase energy production for wind turbines, which will ultimately reduce reliance on fossil fuels for societal energy needs.

1. INTRODUCTION

In 2020, wind energy was the largest renewable energy type in the United States, accounting for 43% of all utility-scale renewable energy generation and 8% of all energy generation [1]. Wind energy generation also increased by 226% from 2010 to 2020 in the United States at the utility-scale [2]. Wind turbine blades make up approximately a fifth of the costs of wind turbine components, and are susceptible to damage causes including rain, dust, bugs, birds, lightning, and mechanical fatigue [3]. Damage inhibits performance, but the blades can be restored with repairs. Unfortunately, repair instructions are often vague, which causes variability in a repair's quality and durability. Vague repair instructions are also a problem when combined with blade accessibility challenges, which include considerations like safety, weather, and tooling. Accessing a damaged area involves rappelling from the top of a wind turbine down to the damaged area, so safety is critical for the technicians. Weather must include low winds, low humidity, and low risks for lightning. Tooling is limited by its portability.

The goal of wind turbine blade repairs is to return the structure to its original properties. Repairs begin with damage assessment, and are followed by repair design, surface preparation, and finally, patching. Surface preparation involves removing damaged material, sanding the surface, and removing contaminants. A clean, rough surface is the foundation of a durable repair. Vague repair instructions combined with accessibility challenges and the importance of surface preparation together motivated the development of surface preparation procedure recommendations for wind turbine blade field repairs.

Developing surface preparation procedure recommendations for wind turbine blade field repairs began with a review of relevant literature to understand current wind turbine blade repair methods and identify the techniques and testing methods that can be used to improve repair surface preparation. The literature review was also used to identify potential surface preparation improvements, pose research questions, formulate objectives, and set forth the tasks that were used to complete the objectives.

Test methods including profilometry, contact angle, lap shear, double cantilever beam (DCB), end-notch flexure (ENF), and optical microscopy were used to understand the effectiveness of current wind turbine blade repair methods. Contact angle, scarf tension, digital image correlation (DIC), field emission scanning electron microscopy (FE SEM), energy dispersive x-ray spectrometry (EDS), and finite element analysis (FEA) were used to measure the effectiveness of potential surface preparation technique improvements. Background information on each test method used to complete the objectives is included in the literature review. Results from the test methods were used to inform the recommendation developed, which is to test whichever surface preparation methods and adhesive-substrate combinations are used for a repair using lap shear, DCB, ENF, and scarf testing prior to implementation in the field. Results from lap shear, DCB, ENF, and scarf tension tests should be used to inform the surface preparation procedures used in the field. The methods described in this work may be used to guide testing methods.

Using surface preparation procedures that align with repair and wind turbine blade design criteria can lead to more detailed estimates of repair costs and predictions of

repair patch durability. More detailed estimates of repair costs can be incorporated into repair cost models, which can be used to identify inefficiencies. Identified inefficiencies can be used to motivate improvements so that the cost of wind energy can continue to drop with time. Moreover, more informed repair costs will allow both wind energy providers and consumers to make more informed financial decisions.

In addition to reducing costs, improved repairs will help the transition towards a circular economy. Stahel (2016) describes a circular economy as one that turns goods that at the end of their service life into resources for others, closing loops in industrial ecosystems and minimizing waste. A circular economy would replace production with sufficiency, where products are reused, recycled, repaired, or remanufactured. A study of seven European nations found that a shift to a circular economy would reduce each nation's greenhouse-gas emissions by up to 70% and grow its workforce by about 4% [4]. Wind turbine blades are not currently designed for recyclability, and most remaining material after incineration is either landfilled or used in building materials [5]. Improving the quality of repairs will lower the rate of blade burials. Overall, informed repair procedures will decrease lifetime costs, increase energy production, and lower blade burial rates, ultimately leading to wind becoming a more viable form of renewable energy.

2. LITERATURE REVIEW

2.1 Wind Turbines

Modern wind turbines were originally invented by Daniel Halladay in 1850 for American railroad companies. The companies used wind turbines to pump water to fill steam engine water tanks. In Denmark, high fuel prices drove Pour La Cour to pioneer the transition of wind turbines from pumping water to generating electricity during World War I. Wind turbine innovations into the present day have continued to be driven by energy needs, and, in the past 20 years, by the need to combat climate change [6].

The two main wind turbine components are the tower and the tower head. The tower includes the tower structure, the foundation, and cabling. The tower head includes the rotor, the mechanical drive train, the nacelle, and the electrical system [3]. The rotor is the rotating assembly of a wind turbine and includes the hub and the rotor blades. Wind turbines can have either horizontal or vertical axis rotors. The components of a typical horizontal axis rotor are in Figure 1. The hub connects the rotor blades to the rotor shaft and the rotor blades harness the wind energy used to rotate the rotor. Each rotor blade has an independent pitch, which allows the blade to rotate along its own axis to change the area facing the wind. Vertical axis rotors typically have lower power coefficients than horizontal axis rotors, where the power coefficient is the ratio of the extractable mechanical power to the power contained in the air stream. With horizontal axis rotors, rotor speed and power output can be controlled by pitching the rotor blades about their longitudinal axis, which protects the wind turbine from high wind speeds. Pitch control

benefits and advances in propellor design combine to make horizontal axis rotors the most common wind turbine blade rotor design [3].

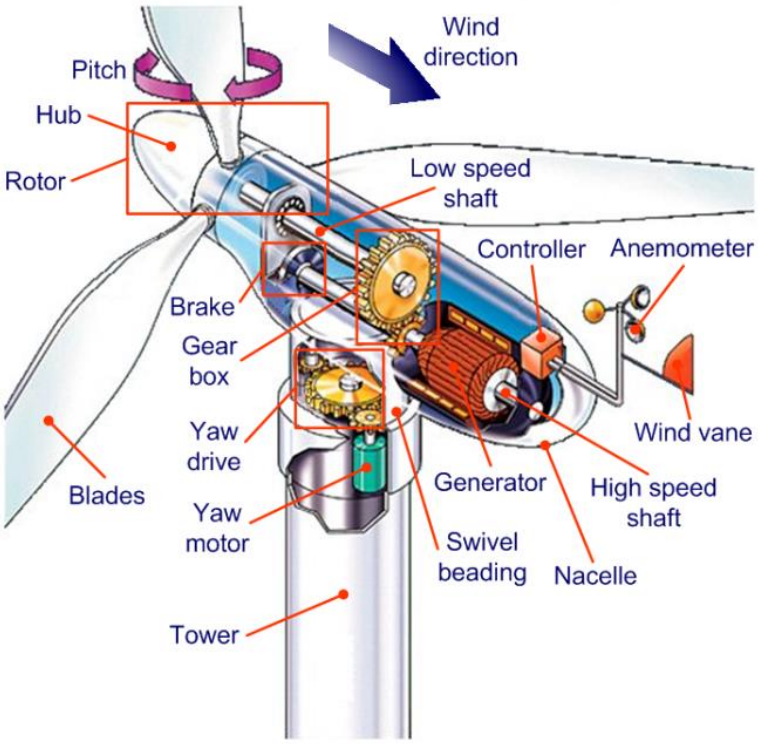

Figure 1. Major components of a typical horizontal axis wind turbine [7].

Wind turbines are either land-based or offshore. Land-based wind turbines are also termed onshore wind turbines. Land-based wind farms are typically placed in rural, remote areas while offshore wind farms are placed along coastlines. Coastal offshore wind farms are typically constructed on the continental shelf around 10 km from the coast with the base of the turbines' foundations around 10 m deep. Differences pertaining to electricity generation, transportation, and electricity transmission arise when a wind turbine is placed offshore. Because water has less surface roughness than land, the

average wind speed is usually considerably higher over open water [8]. The power that can be extracted from airflow by an energy converter increases with the third power of the wind velocity [3]. The higher wind speeds thus allow offshore wind turbines to typically generate more electricity than land-based turbines. With land-based wind turbines, difficulties in transporting large components can limit the number of acceptable locations for wind farms. Offshore locations can take advantage of transporting components using marine shipping and handling equipment, which far exceed the lifting requirement for multi-megawatt wind turbines. Land-based wind farms tend to be in more remote areas, so electricity must be transmitted over long power lines to cities. Offshore wind farms can be closer to coastal cities and require relatively shorter transmission lines [8].

Whether a wind turbine is land-based or offshore, rotor blades are critical for harnessing wind energy. A rotor blade's airfoil cross-section shape permits the utilization of aerodynamic lift [3]. The lift force rotates the rotor when the wind passes across the blade. The rotating rotor uses Faraday's law to induce a current in the generator and produce electricity. Electricity production is inhibited when a wind turbine blade is damaged. Repairs are performed to restore the damaged blades, and typically occur 2-5 years after installation [9]. Effective wind turbine blade repairs necessitate knowledge of wind turbine materials, cost considerations, design criteria, inspection procedures, and the scarf repair.

2.2 Wind Turbine Blade Materials

Most wind turbine blades are manufactured using sandwich composites, which are created by sandwiching a foam or balsa core between two glass fiber reinforced polymer (GFRP) face sheets. Composite materials are formed by combining two or more dissimilar materials to optimize their respective properties. GFRPs are composite materials made by impregnating a polymer resin such as epoxy or vinyl ester into stacks of woven mats of glass fiber fabric. The word polymer is derived from Greek terms *poly* meaning many and *mer* meaning parts. A polymer is defined as a chemical compound made up of small molecules (monomers) that are arranged in simple repeating structure to form a large molecule or a chain [10]. Each layer of glass fiber fabric is called a lamina, and are stacked with varied orientations to withstand repeated, multidirectional loading cycles. The foam or balsa core separates the two faces so that the moment of inertia of the faces is large, resulting in added stiffness and buckling resistance. In addition to high stiffness and buckling resistance, the use of composites enhances fatigue life and corrosion resistance. Barbero (2018) can be referenced for further information on composite materials design [11].

A wind turbine blade consists of two faces, one on the suction side and one on the pressure side. Suction and pressure side faces can also be termed blade shells. The suction and pressure sides are the convex and concave sides of the airfoil shape, respectively. Rotor blades are subjected to continuous aerodynamic forces that cause considerable bending moments, especially from lift forces [12]. Further details on aerodynamic forces are in Section 2.4: Wind Turbine Blade Design Criteria. To withstand

the shear loading on a blade, the two faces are joined together and stiffened by either shear webs or box beams (Figure 2) [13].

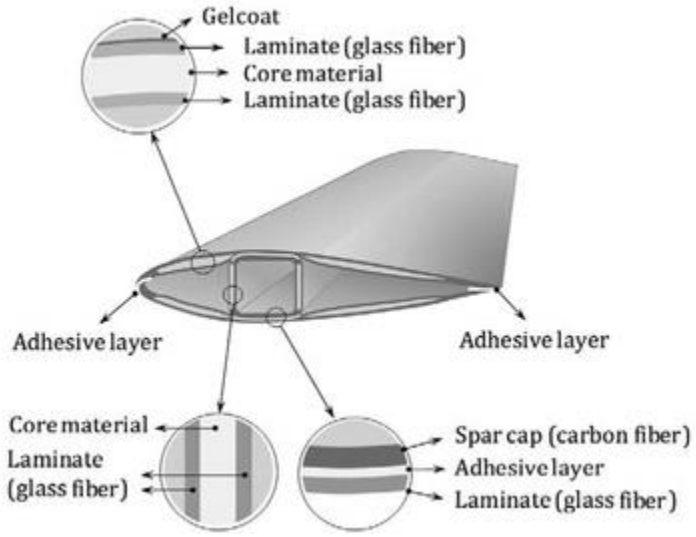

Figure 2. Typical cross-section of a wind turbine blade [14].

Wind turbine blades are manufactured using vacuum assisted resin transfer molding (VARTM) (Figure 3). As described by Lusty and Cairns (2021),

> "The VARTM process begins with stacking glass fiber fabric, peel ply, and flow media on a heated caul plate. Tacky tape is placed on the outside perimeter of the caul plate and a vacuum bag is pressed into the tacky tape. Vacuum pressure is applied via the vacuum port. Resin is introduced through the injection port and impregnates the fabric."

The heated caul plate accelerates resin cross-linking, resulting in a composite part that can be removed from the mold and post-cured if recommended [15]. Using VARTM to manufacture composites typically increases fiber volume fractions (Vfs), or fiber to resin ratios, as opposed to other methods such as hand lay-up [16].

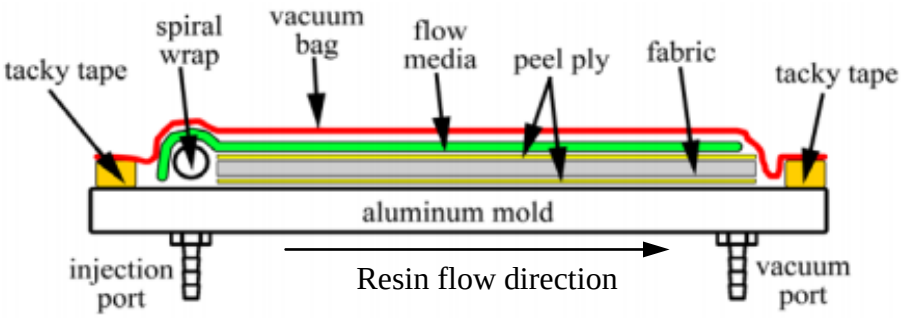

Figure 3. Cross-sectional view of VARTM setup [17].

Changes to a blade design at different length scales can affect the blade reliability. Poor interfacial adhesion in adhesive joints, for example, could cause an entire wind turbine blade to fail catastrophically. Conversely, an increase in the interfacial adhesion between fibers and matrices will increase the strength at the lamina scale and potentially the overall blade strength. The range of material length scales is shown in Figure 4.

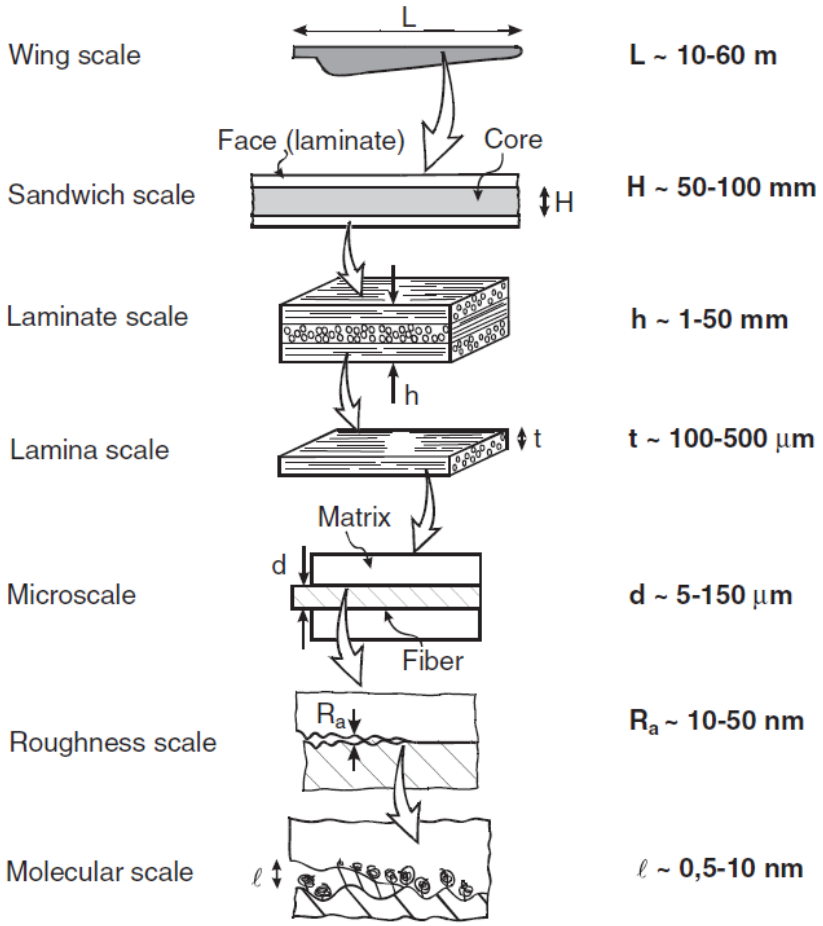

Figure 4. Material length scales in a wind turbine blade ranging from a few nanometers at the molecular scale to more than 60 meters at the blade scale [18].

2.3 Wind Turbine Blade Repair Costs: Equations and Estimates

The cost of wind turbine blade repairs is described in the context of the cost of wind energy. The cost equations may be used to make estimates for the cost of wind turbine blade repairs.

2.3.1 Wind Turbine Blade Repair Cost Equations

The cost of wind energy is typically described by the levelized cost of energy (LCOE) (1), which is an assessment of the cost-effectiveness, performance, and improvement of an energy supply technology. LCOE is defined as the price at which each unit of produced energy must be sold [19]. LCOE costs are reported in $/MWh, where a MWh is equivalent to 1,000 kWh [20]. LCOE has been used by the U.S. Department of Energy for several years to evaluate the total system impact of design changes [21].

$$LCOE = \frac{(CapEx * FCR) + OpEx}{(AEP_{net}/1000)} \quad (1)$$

where CapEx are capital expenditures ($/MWh), FCR is the fixed charge rate (%), OpEx are operational expenditures ($/kW), and AEP_{net} is the net average annual energy production (MWh/MW/yr). CapEx includes the turbine capital cost, the balance of system, and financial soft costs. The turbine capital costs include the costs of the rotor, the nacelle, and the tower. The balance of system costs includes electrical infrastructure, assembly and installation, site access and staging, the foundation, engineering management, and development. Financial soft costs are construction finance and contingency [22]. The FCR represents the amount of revenue required to pay the carrying charges as applied to the CapEx on that investment during the expected project economic life on an annual basis. Carrying charges include the return on debt, return on equity, taxes, and depreciation. FCR does not allow for detailed analysis of specific financing

structures; however, financing structures can be represented using a weighted-average cost of capital as the discount rate input.

The terms “OpEx” and “Operations and Maintenance (O&M) costs” are typically used interchangeably. OpEx (Equation 2) includes both fixed ($OpEx_{fixed}$) and variable ($OpEx_{variable}$).

$$OpEx = OpEx_{fixed} + OpEx_{variable} = OpEx_{fixed} + C_{PM} + C_{CM} \quad (2)$$

$OpEx_{fixed}$ are fixed cost elements such as rental, administration, and insurance. C_{PM} and C_{CM} are the costs of planned and unplanned plant maintenance, respectively [9]. C_{PM} is the most common maintenance practice and is usually carried out once or twice a year for a turbine and includes costs of activities such as inspection, monitoring, and control [23]. C_{CM} (Equation 3) includes the costs of unexpected failures.

$$C_{CM} = \sum_{N_F} (C_D T_D + C_{rep1}) \quad (3)$$

C_D are the costs of downtime per hour, T_D is the duration of the downtime, N_F are the number of failures per year, and C_{rep1} (Equation 4) are the costs of single repair. Downtime is when a damaged wind turbine is shut down.

$$C_{rep1} = C_{trans} + C_{equip} + C_{labor} \quad (4)$$

C_{trans} are transportation costs, C_{equip} are equipment and materials costs, and C_{labor} are costs of labor. $C_{labor} = M\ t_{rep}\ c$, where M is the number of personnel, c are the hourly costs, and t_{rep} is the repair time [9].

2.3.2 Wind Turbine Blade Repair Cost Estimates

In addition to cost equations, cost breakdowns are also used to estimate wind turbine blade repair costs. Stehly, Beiter, and Duffy (2020) reported the LCOE breakdown for the primary components of a representative wind power plant in Figure 5 and the LCOE values for each of the components in Figure 6 [22].

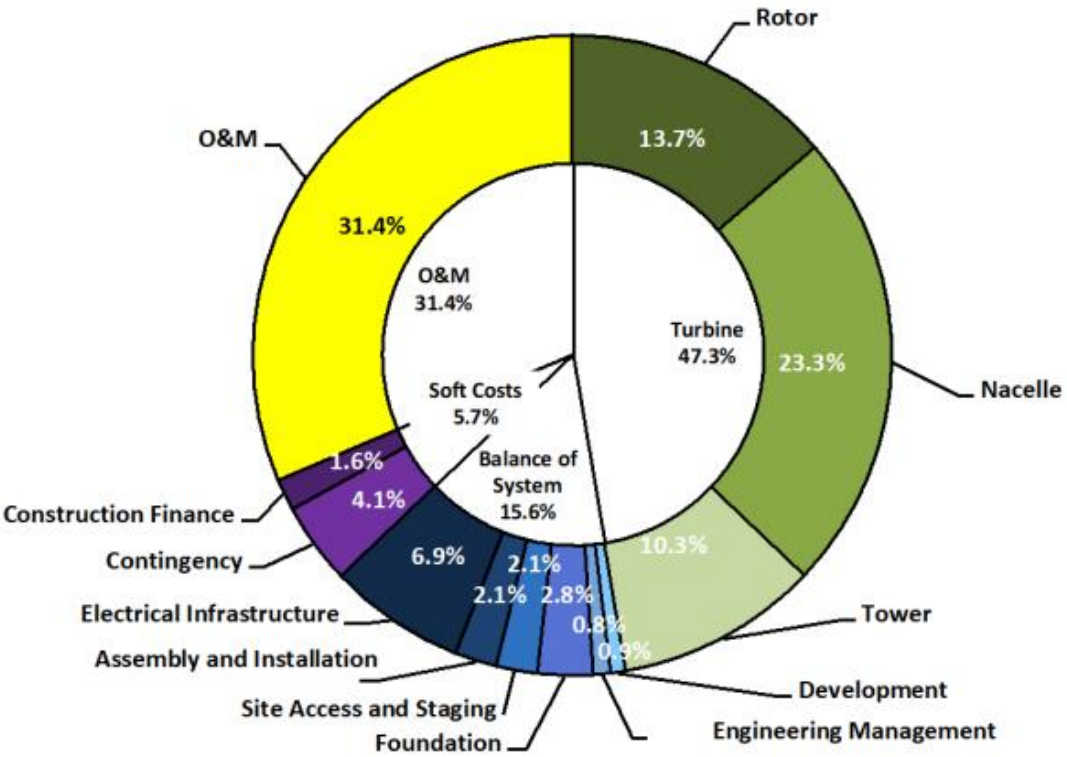

Figure 5. Component-level LCOE contributions for the 2019 land-based-wind reference project operating for 25 years with wind turbine initial component costs comprising 47.3% of the total component-level LCOE contribution [22].

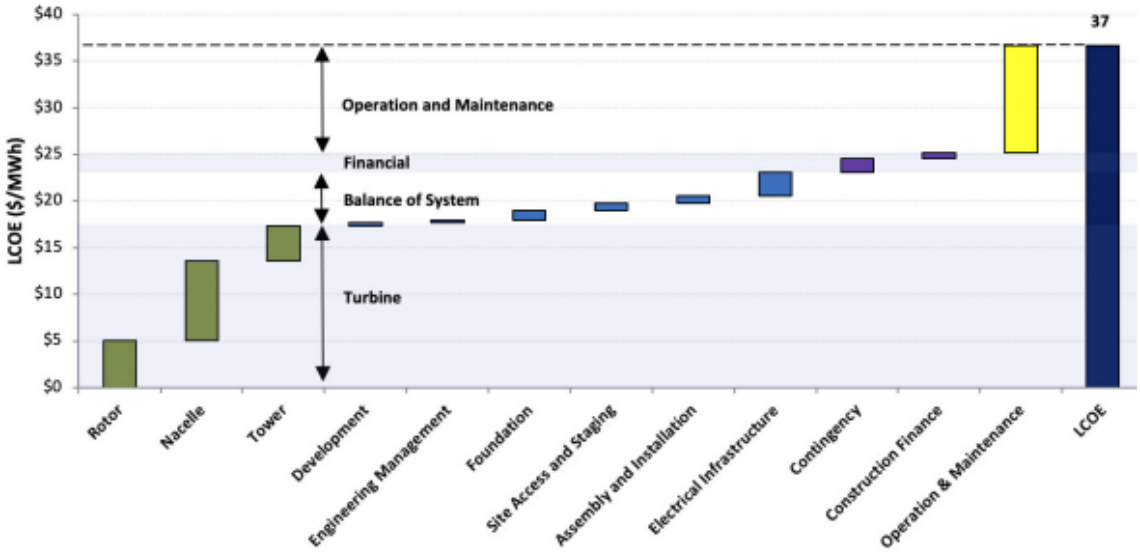

Figure 6. Component-level LCOE cost breakdown for the 2019 land-based-wind reference project [22].

The component costs provide a direct insight into the technology from a technical perspective. Two wind turbines may be of different technical concepts and sizes, but the component cost structures will not differ significantly [3]. Hau (2006) reported the blade costs of a 2 MW wind turbine with an 82 m rotor diameter as $306,000 for three blades. The three blades together made up 19% of all of the component costs [3]. Wind turbine blades have increased in size since 2006, which increases the rotor diameter (Figure 7). With increased blade sizes, costs per blade have increased. Johnson et al (2021) reported the costs for 65 m, 75m, 95m, and 115m blades at approximately $200k, $250k, $450k, and $650k, respectively [24].

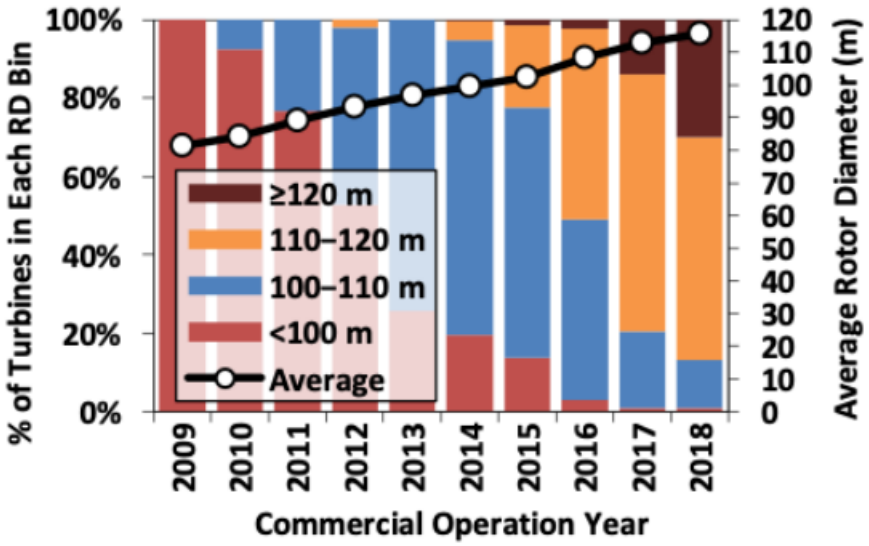

Figure 7. Trend in rotor diameter (RD) [24].

Wiser, Bolinger, and Lantz (2019) surveyed industry experts to assess wind power operating costs in the United States. Findings suggested that continued OpEx reductions may contribute 10% or more to the expected reductions in land-based wind's LCOE [25]. The costs of repairs fall under both fixed and variable OpEx. Martin-Tretton et al (2011) reported the structural and non-structural repair cost estimates for rotor blades for 2.1-3.0 MW and 1.5-2.0 MW wind turbines, which were the predominant turbines in the U.S. market in 2010 (Table 1) [25]. To the author's knowledge, updated cost estimates for repairs have not been published.

Table 1. Wind turbine blade repair cost estimates [25].

Turbine Power Output (MW)	Tower Height (m)	Cost of Wind Turbine Blade Structural Repair ($)	Cost of Wind Turbine Blade Non-Structural Repair ($)
2.1-3.0	90	318,000	16,000
1.5-2.0	80	154,000	23,000

The structural repair cost estimates assume that the wind energy facility rents a crane for any major replacement and that the replacements will occur on a per-unit basis. The terms “structural repair” and “replacement” were used synonymously, however, the term structural repair will not be used to describe replacing wind turbine blades for the remainder of this work. Structural repairs are used to restore a blade once there is structural damage, and non-structural repairs are used to restore a blade after non-structural damage. Moreover, the terms “non-structural repair” and “repair” were used synonymously, so the costs estimates reported in Table 1 will be interpreted as replacement and repair costs rather than structural and non-structural repair costs.

The differences between structural and non-structural damage merit further investigation, as there is no industry consensus in defining the two terms. Mishnaevsky (2019) and Nijssen and Manrique (2020) defined non-structural and structural damage differently. Mishnaevsky (2019) defines non-structural and structural damage in terms of repair requirements where non-structural damage requires filling, sealing, and resin injection and structural damage requires plug/patch and scarf repairs [26]. Scarf repairs will be described in Section 2.6: The Scarf Repair. Nijssen and Manrique (2020) defined structural and non-structural damage in terms of stiffness degradation, where each damage type has two thresholds: *affected* and *critical*:

> For non-structural damage, the *affected* threshold refers to the point where the damage in the non-structural section of the blade (such as the gelcoat) is intense enough to disturb the aerodynamic performance up to a point when the associated degradation of the Annual Energy Production (AEP) is large enough to outweigh the associated costs of repairing the blade. The *critical* threshold refers to the point where the damage is intense enough to not only affect the aerodynamic performance of the blade, but also compromise the structural integrity of it in

> various ways, i.e. by allowing the permeation of water inside the laminate structure.
>
> For structural damage, the *affected* threshold refers to the point where the damage in the structural section of the blade degrades the strength and/or stiffness of the same by 1% with respect to its original maximum. The *critical* threshold refers to the point where the damage in the blades structure is large enough that it will lead to a reduced operational life than originally designed [27].

If a unidirectional laminate is damaged such that 1% stiffness degradation occurs, without further investigation, considerable damage might be indicated. Damage negatively affects the performance of wind turbines, with direct economic impacts stemming from both downtime costs and the costs of the repairs themselves [28]. Damage effects on AEP was described in terms of leading edge erosion damage, but the effects of other forms of damage on AEP merit further investigation. More research is also required to identify the inspection techniques and measurements that would be used to determine whether damage is at either the affected or critical thresholds. Repair cost estimation can be facilitated by reaching a consensus across the industry on damage thresholds.

Despite the discrepancies in damage threshold definitions, the cost differences between replacement and repair in Table 1 are significant, where the cost of repair was 15% of the cost of replacement for the smaller wind turbines and the cost of repair was 5% of the cost of replacement for the larger wind turbines. The cost of repair is thus significantly cheaper than replacing a wind turbine blade for both wind turbine sizes.

2.4 Wind Turbine Blade Design Criteria

The design criteria for wind turbine blades is to attain the highest possible power output under specified atmospheric conditions [29]. Wind turbine blades have traditionally been designed using the safe-life approach, which involves investigating fatigue, manufacturing defects, and in-service damage [30]. Fatigue investigations demonstrate that a structure can withstand the repeated loads expected in service. Wind turbine blades are loaded by the wind, gravity, and blade rotations while in service. The wind load directions are flapwise, edgewise, and torsional (Figure 8). Gravity primarily generates edgewise bending. Blades rotate about the horizontal axis through the hub, which causes inertial forces [14]. A blade rotating about its own axis using a pitch system causes pitch loads [31]. Blades are typically designed for up to 10^9 load cycles, and the load cycles occur simultaneously in the flapwise and edgewise directions [32]. Fatigue strength investigations using coupon, sub-component, and full-scale testing (Figure 9) can be successfully used to demonstrate that wind turbine blades can withstand the expected loads in service. Design changes at varying length scales from Figure 4 can be reflected in coupon, sub-component, and full-scale strength testing results.

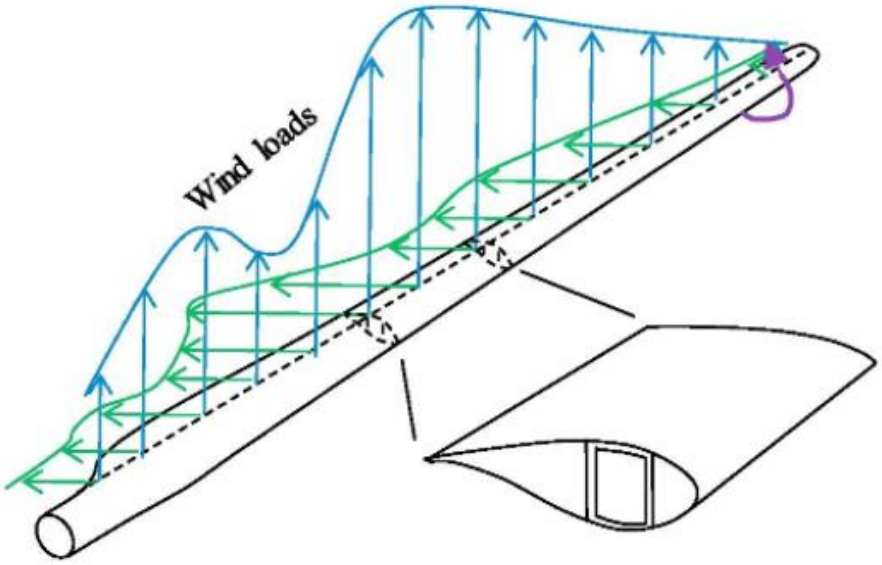

Figure 8. Flapwise (blue arrows), edgewise (green arrows), and torsional (purple arrow) loads [33].

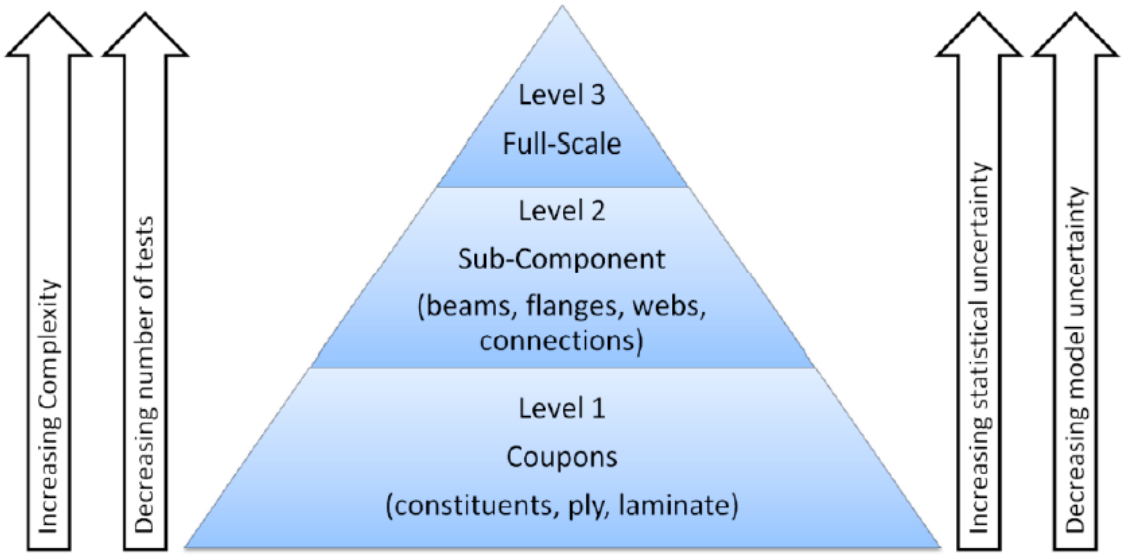

Figure 9. Types of tests used to assess materials used for wind turbine blades [13].

Manufacturing defects for composites can be categorized into fiber, matrix, and interface. Fiber defects include the following: misalignments, fiber waviness (Figure 10),

broken fibers, and irregularities of fiber distribution. Out-of-plane fiber waviness has been found to decrease compressive strength [34]. Matrix defects can be incomplete curing and voids. Interface defects can occur when composites are bonded together and include unbonded regions on fiber surfaces and delamination between layers [35]. Delamination is where a composite laminate exhibits poor or no bonding between adjacent plies (Figure 11) [36].

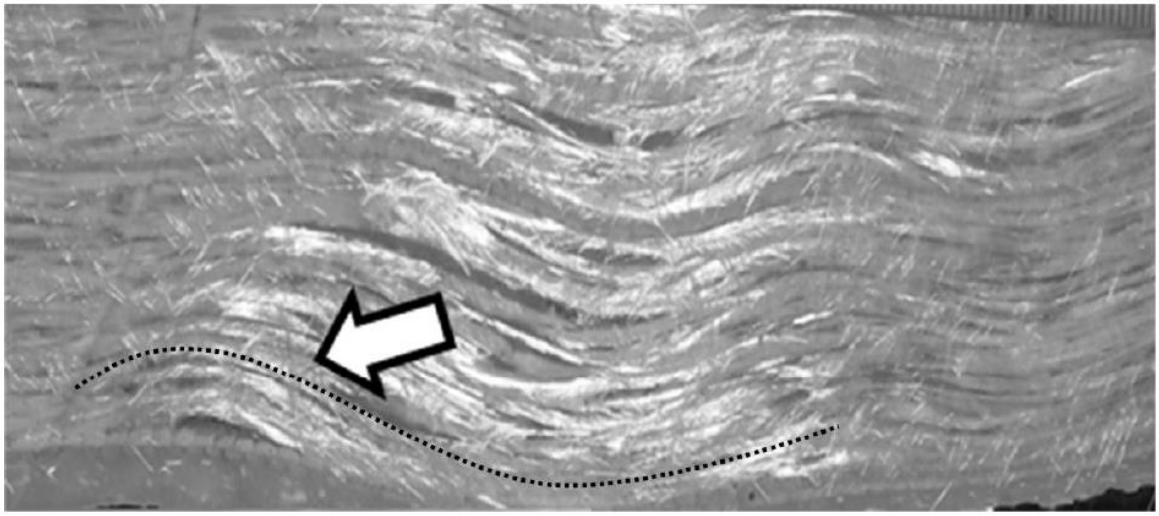

Figure 10. Example of out-of-plane fiber waviness found in a wind turbine blade laminate [34].

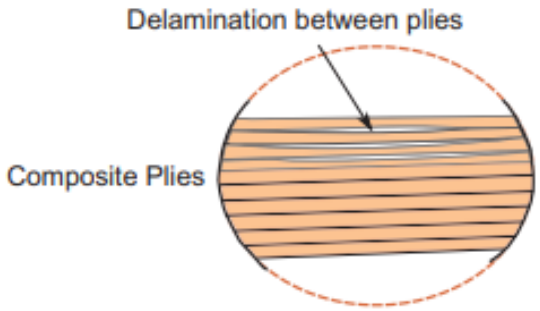

Figure 11. Schematic of delamination in a composite laminate [36].

In-service damage is caused by fatigue, foreign object impacts, lightning strikes, and leading edge erosion. The resulting damage modes are in Figure 12. Fatigue damage is exacerbated when initial, superficial cracks appear at stress concentrations. The initial cracks can progress through composite plies with repeated loading and induce delamination in the laminate [37]. An example of fatigue damage is included in Figure 13.

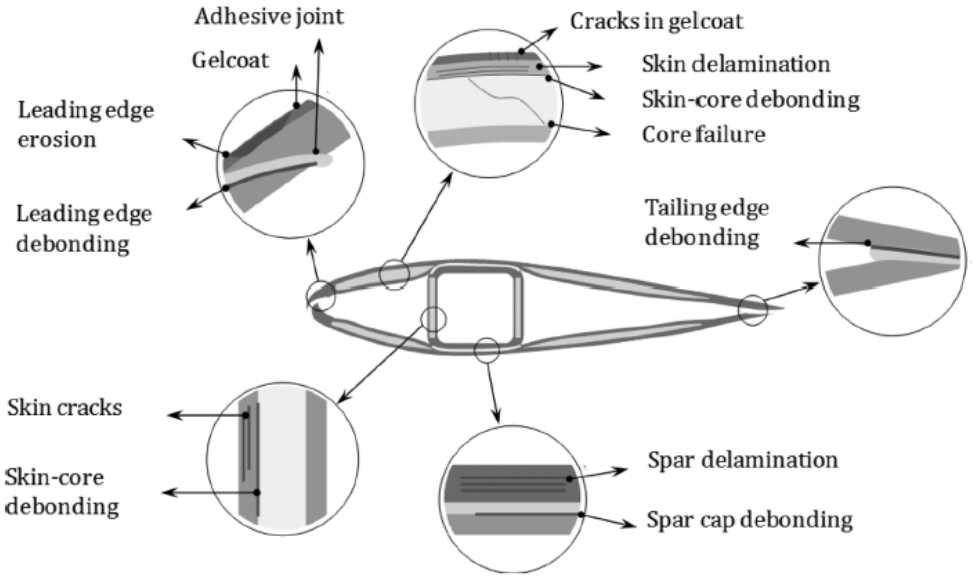

Figure 12. Common damage modes in composite wind turbine blades [14].

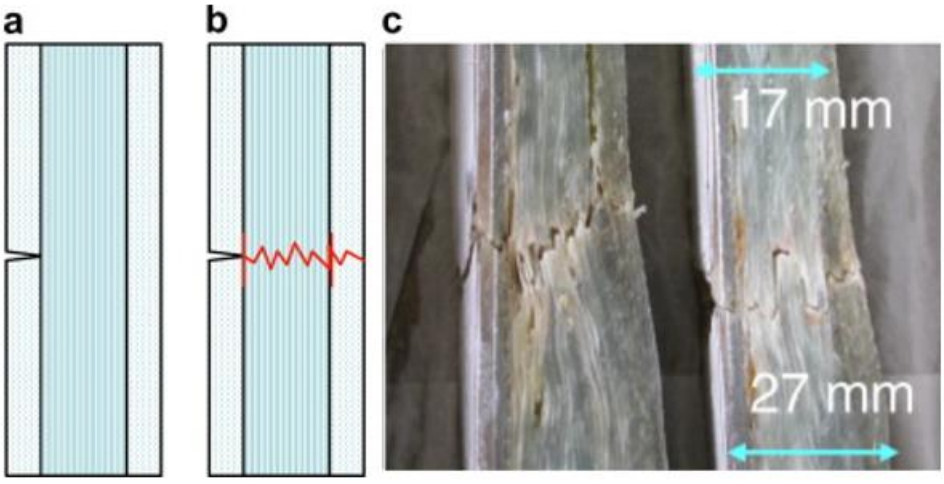

Figure 13. Schematics and photograph of a laminate that cracked an estimated 5 year fatigue life: a) crack in the superficial layer, b) crack in the resistant layer, c) crack through the laminate (left) and laminate dimensions (right) [37].

The poor properties of composite laminates and sandwich sections in the fiber off-axis and through-the-thickness directions make composites more susceptible to foreign

object impact damage. Birds and hail are commonly reported foreign objects, but blades can also impact surrounding structures during transportation and installation [36]. Impact damage modes to composites include delamination, surface buckling, matrix cracks due to shear and bending, and fiber breakage (Figure 14). Delamination reduces the flexural and compressive strength of a laminate because the laminate is subdivided into thinner sub laminates with lower buckling load [38]. The factors that affect the resulting impact damage modes include the face sheet layup configuration and thickness, core material and thickness, face-core interface properties, fabrication techniques, impact velocity and energy, temperature, boundary conditions, and environmental factors. Face-core debonding (Figure 15) can occur in regions surrounding the point of impact and the core may experience permanent deformation [39]. Debonding usually refers to large scales (blade shells) compared to delamination (plies) [28].

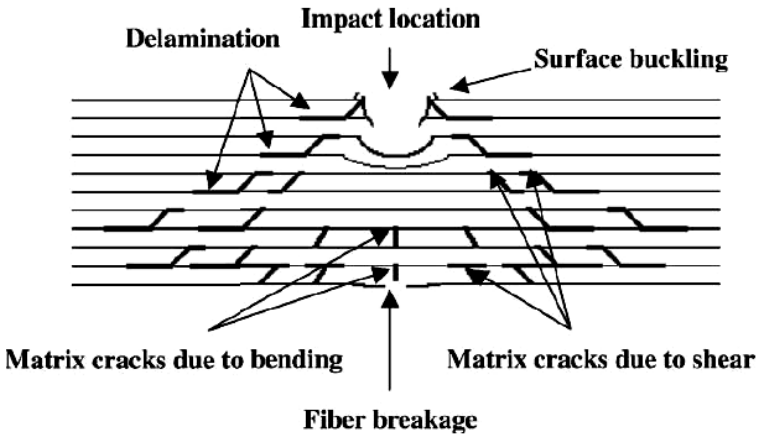

Figure 14. Typical impact damage modes for laminated composites [40].

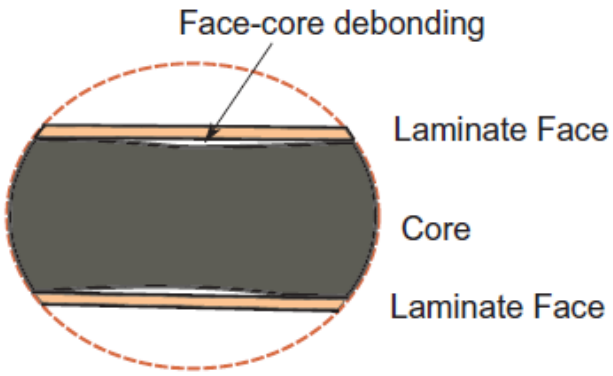

Figure 15. Face-core debonding schematic [36].

Lightning strike protection systems are commonly applied to wind turbine blades, yet the blades experience both cosmetic and structural damage when struck (Figure 16). When lightning strikes a composite structure, the high velocity electric charge particles within the lightning arc channel heats the material surface. The material absorbs energy from the lightning arc channel and experiences a rapid temperature rise. Under elevated temperatures, polymer matrices decompose and cause fluctuations in material properties [41]. Lightning strikes commonly cause debonding because the heat generated from the lightning expands the air inside the blade, which creates internal pressure. The vaporization of condensed moisture trapped inside the blade can intensify inner blade air pressurization [28].

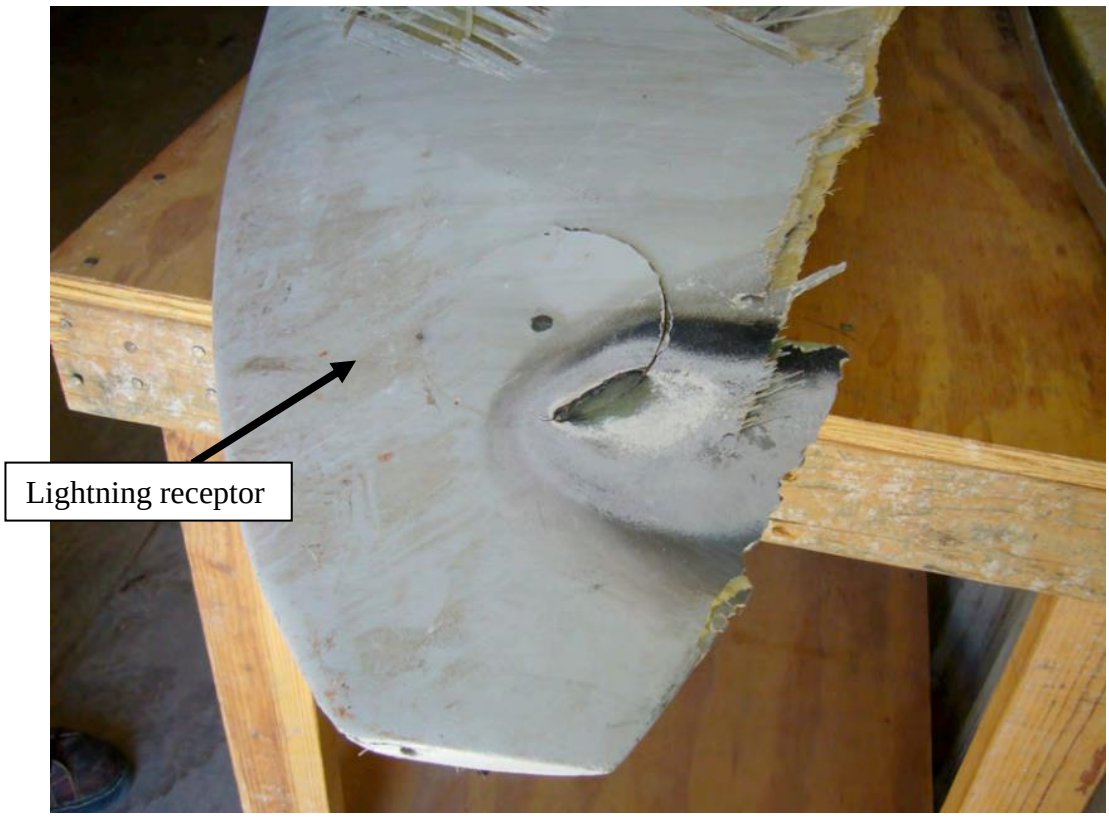

Figure 16. Typical lightning damage to a blade tip [42].

Leading edge erosion of a wind turbine blade is the result of its exposure to airborne particulates, UV radiation, humidity, and moisture [28]. Airborne particulates are usually in the form of rain, hailstone, sea spray, dust, and sand. Raindrops' kinetic energy, diameter, temperature, and sea salt content affect erosivity [43]. The effect of hailstones on a blade's coating is worse than rain, primarily due to the typically larger diameter particulates [28]. UV radiation deteriorates polymer material properties with time [44]. Composites swell when water is absorbed, which can lead to delamination [43]. Leading edge erosion gradually increases the blade's surface roughness, which negatively affects the blade's aerodynamic performance by increasing drag [28]. Nash,

Zekos, and Stack (2021) use two photographs (Figure 17) to describe the differences between minor and major leading edge erosion damage. According to Nijssen and Manrique (2020), the damage in Figure 17a would be classified as non-structural erosion damage at stages 1 and 2, while the damage in Figure 17b would be considered structural erosion damage at stage 5 [27]. The stages of erosion are in Figure 18.

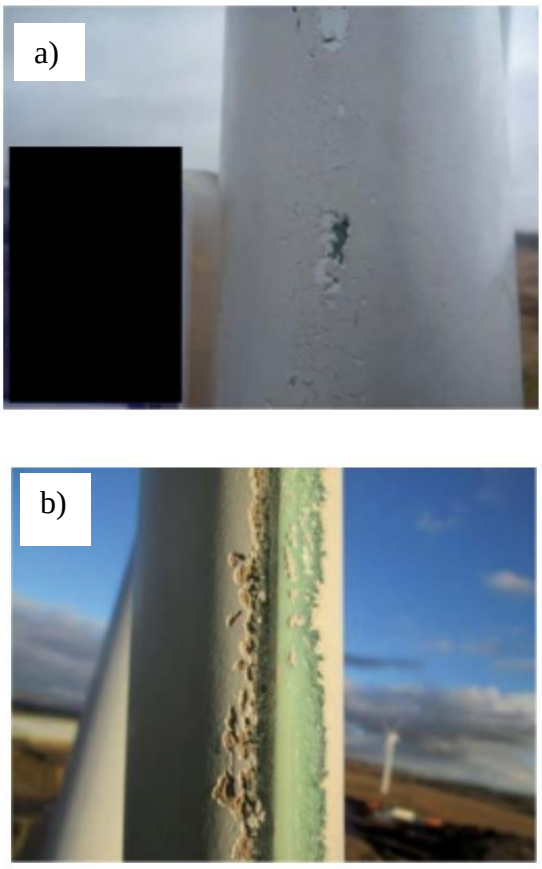

Figure 17. Minor (a) and major (b) erosion damage on the leading edge of wind turbine blades [43].

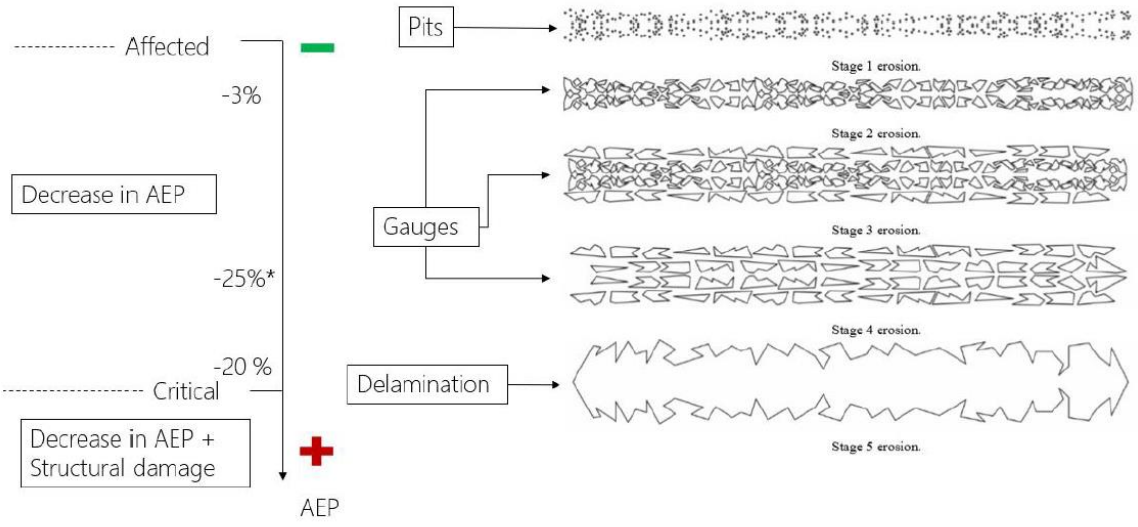

Figure 18. Stages of erosion vs. AEP loss [27].

Categorizing damage into stages can be used to prioritize which repairs are more critical. Damage categorization can also be used to inform future blade design considerations. However, quantifying manufacturing defects and in-service damage in the field proves to be difficult when competition between manufacturers limits the amount of information shared. Additionally, differences in production techniques make the production defects more manufacturer-dependent than in other industries [16]. Limited information sharing between manufacturers has resulted in minimal damage quantification across wind plants. A clear idea of damage causes, locations, and characteristics across wind plants could allow for patterns to be identified and improvements to wind turbine blade designs to be made. Collaboration between wind turbine blade inspectors, repair personnel, manufacturers, and engineers is imperative to the progress of wind turbine designs. Until there are vast improvements in wind turbine

blade designs, the safe-life approach will continue to be used and wind turbine blades will necessitate repairs.

Improvements in wind turbine blade designs will include implementing a damage tolerant approach. The basic philosophy of damage tolerant design is based upon three main criteria:

1. The acceptance that damage will occur.
2. The adequate system of inspection so the damage may be detected.
3. An adequate strength is maintained in the damaged structure [45].

Using a damage tolerant design approach results in an understanding of the structural performance in the presence of defects or damage, which is achieved through fracture mechanics, residual strength, and life prediction methodologies. Some objectives of fracture mechanics include determining:

1. The residual strength as a function of crack size.
2. The tolerable crack size at an expected service load (i.e. the critical crack size).
3. The time it takes for a crack to grow from a certain initial size to the critical crack size.
4. The size of pre-existing flaw that can be permitted when the structure starts its service life.
5. How often the structure should be inspected for cracks [46].

2.5 Wind Turbine Blade Inspection Procedures

Wind turbine blade inspections begin with damage detection and are followed by an initial damage extent assessment. Damage can be detected using two approaches: using condition monitoring systems or in-person inspections. Condition monitoring systems monitor blade health and detect damage using sensors such as strain gauges, vibrational sensors, fiber optics, and acoustic emission sensors. Sensors used for condition monitoring have been prototyped for wind turbine blade applications, but the

long-term reliability and durability of condition monitoring sensors have yet to be tested [47]. Since condition monitoring systems are still in the developmental stages, in-person inspections are primarily used to monitor blade health.

In-person inspections can be performed from the ground, by unmanned aerial vehicles (UAVs), or as close-up manned inspections. Ground inspections are conducted using binoculars, telephoto cameras, or computerized scan systems. Ground inspections are used to locate initial areas of interest, while inspections done by UAVs and by close-up technicians are used to identify the extent of damage. UAVs, commonly referred to as drones, can be equipped with both high definition and infrared thermography video equipment to detect internal damage [47]. Infrared thermography supplies information about the temperature map over a body surface. Infrared thermographic images contain temperature signals in each pixel that are transformed into the frequency domain using Fourier transformations [48]. Defects can be detected due to amplitude differences in reflected waves (Figures 19 and 20). Close-up manned inspections are conducted either using rope access (Figure 21), from a suspended platform (Figure 22), or by physically entering the blade. A combination of visual, thermographic, and other nondestructive testing techniques can be employed in close-up manned inspections. Visual inspection is often combined with photography to identify and characterize surface defects [49]. Procedures for how damage is photographed and recorded during close-up manned inspections have not been described in literature.

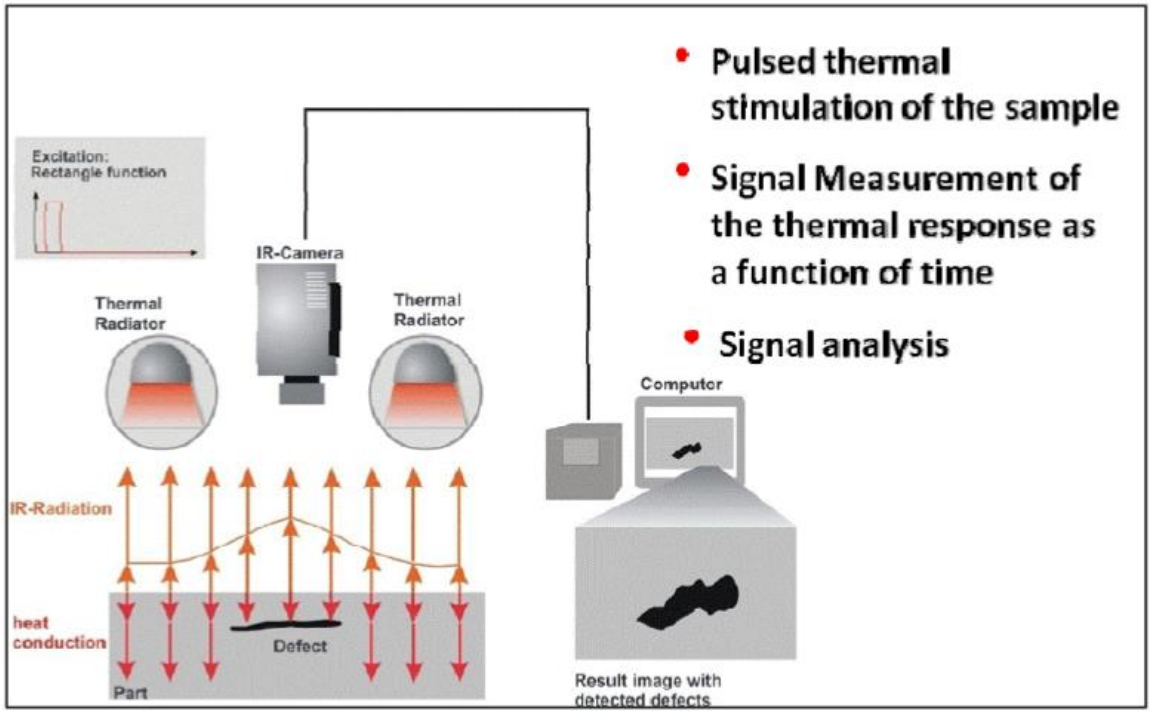

Figure 19. Thermography equipment setup [48].

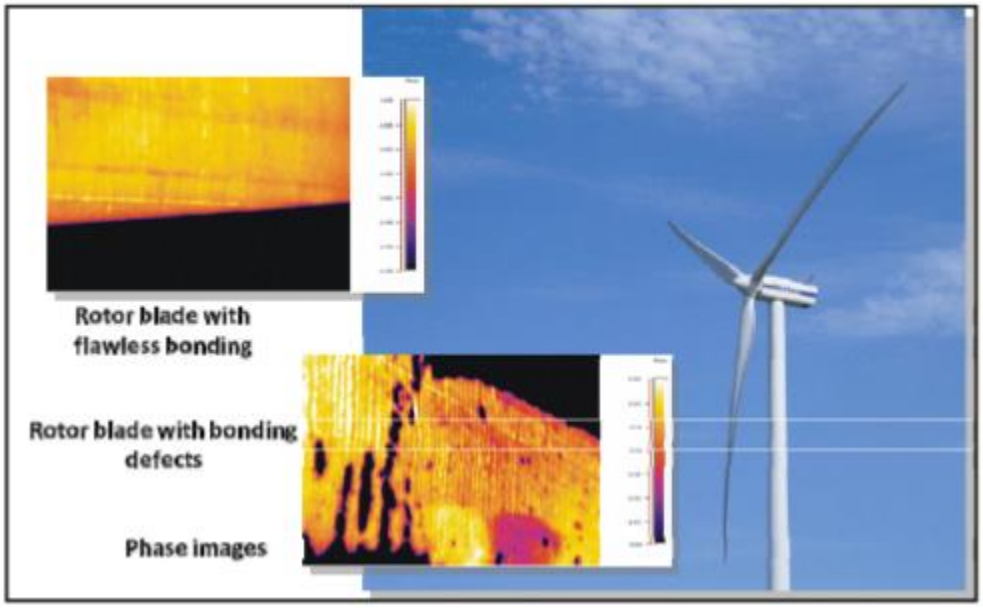

Figure 20. Thermographic images showing bond voids in a GFRP rotor blade [48].

Figure 21. Wind turbine blade technician [1].

Figure 22. A wind turbine blade technician using a suspended platform to conduct a large repair [1].

Nondestructive testing techniques that are commonly used include tap testing, local acoustic resonance spectroscopy (LARS), ultrasonic, and shearography [47]. Tap testing, or coin testing, involves knocking on the surface of a component with a small hammer or coin. If a component contains a defect such as a disbond or a delamination, a duller sound will be heard [50]. LARS extends the tap test by quantifying emitted and received frequencies. Instead of using a coin, LARS generates impulses using instrumented pulse hammers that contain load cells so that excitation forces can be measured. LARS then uses microphones to record the response of the structure to the impulse [51]. In ultrasonic testing, an emitter sends a signal into a material and a receiver detects the reflected signal amplitude. The signal attenuates over defective zones more

than pristine zones, so defects are identified as the regions with higher attenuation [52]. Ultrasonic testing enables inspectors to detect major defects such as delamination, foam-core disbonding, and porosity, which can all cause major structural disintegration in rotor blades. Ultrasonic testing inspection readings can be saved in the ultrasonic testing equipment [49]. Shearography, or digital speckle pattern shearing interferometry begins by using a laser to illuminate a test object. Then, a reference frame is taken using a charged coupled device (CCD) camera (Figure 23). The object is stressed, then a second frame is taken using the CCD-camera [53]. Digital subtraction between the two recorded images yields a fringe pattern, or a digital shearogram such as those in Figure 24 [54].

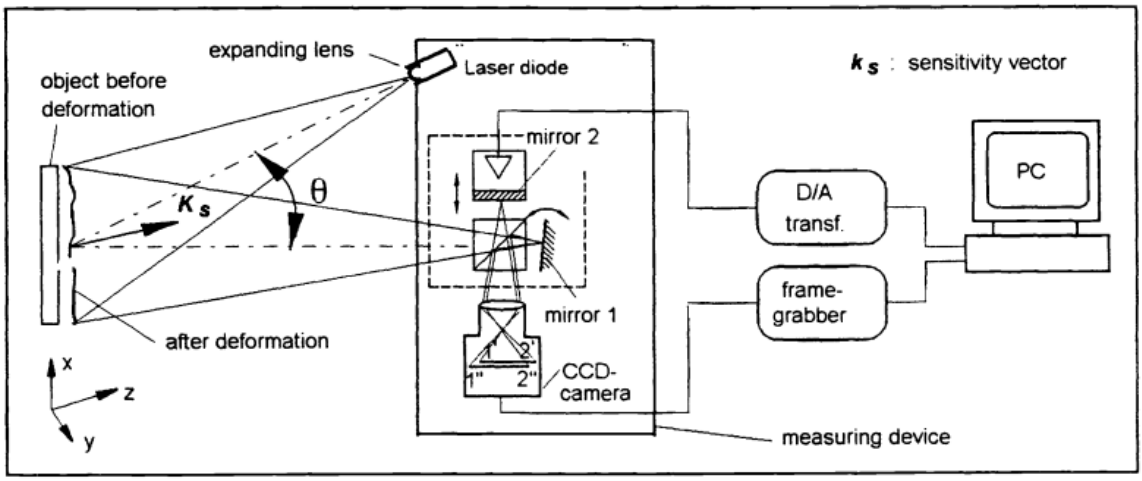

Figure 23. Shearography schematic [54].

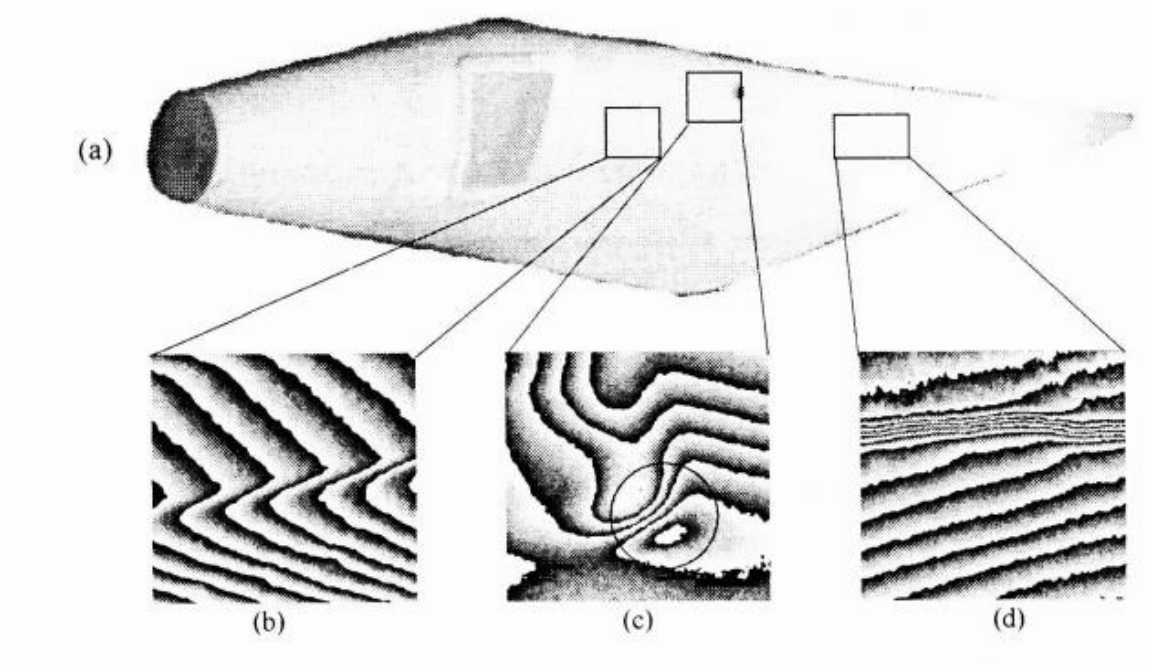

Figure 24. Shearography results of a GFRP rotor with a) a view of the rotor, b) the fringe pattern showing the undamaged laminate, c) the fringe pattern showing delamination, and c) the fringe pattern showing a microcrack [54].

2.6 The Scarf Repair

Until there is more clarity around what constitutes structural and nonstructural damage and for the scope of this work, unless otherwise specified, Mishnaevsky (2019)'s damage definitions will be used, where non-structural damage requires filling, sealing, and resin injection and structural damage requires plug/patch and scarf repairs [26]. If structural damage is found during wind turbine blade inspections, the next step in wind turbine blade maintenance is to repair the damage. A repair patch and the damaged area of a wind turbine blade forms a joint and the joint configuration used is critical to the resulting repair performance. Joint configurations including the single-lap joint, the double-strap joint, the tapered strap joint, and the scarf joint. Scarf joints are

advantageous compared to other joint configurations because bond strength increases even as substrate thickness and strength increase (Figure 25). Repair joint designs should minimize peel stresses and provide a shear dominant stress state. The scarf joint formulates the basis of a scarf repair (Figure 26.) because the scarf joint is the most effective configuration in restoring strength, avoiding load concentrations and eccentricities, and maintaining aerodynamic efficiency [55].

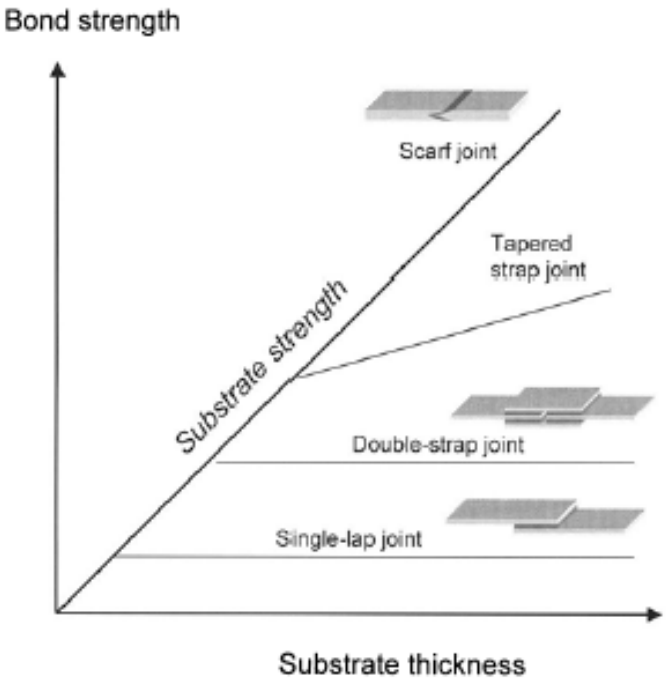

Figure 25. Effect of joint geometry on joint strength with respect to substrate thickness [56].

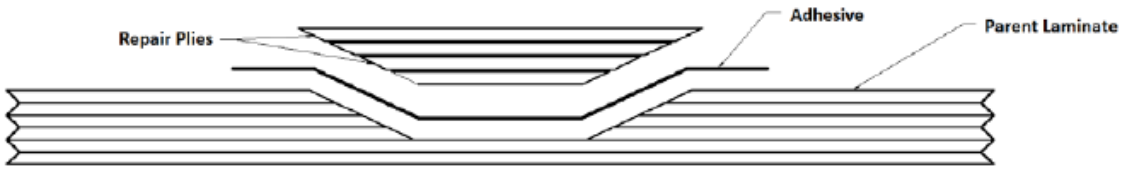

Figure 26. A typical scarf repair configuration [57].

2.7 General Structural Scarf Repair Steps

The general steps in performing a composite scarfed repair with a flush, bonded repair patch are as follows:

1. Get the best access possible, both sides if feasible.
2. Inspect for extent of damage.
3. Remove all damaged and contaminated material.
4. Determine the part's ply count, orientations, laminate thickness, and materials in preparation for repair design and scarfing.
5. Taper sand/scarf the repair area according to repair design instructions to create a smooth, flat surface with high surface energy.
6. Thoroughly dry the structure if moisture is present.
7. Develop a repair design based on the damage and original structure information.
8. Replace materials including the solid laminate and the through-damaged sandwich structure, if applicable.
9. Vacuum-bag and cure repair plies as required.
10. Inspect repair.
11. Sand and finish without sanding into the fibers of the repair plies [58].

Steps 5, 7 and 8 are discussed in further detail. Dorworth, Gardiner, and Mellema (2009) can be referenced for additional information on the remaining steps [58].

2.7.1 Step 5: Taper sand and scarf the repair area according to repair design instructions to create a smooth, flat surface with high surface energy.

Taper sanding and scarfing are synonymous terms. Scarfing is usually achieved using a compressed-air-powered high-speed grinder, which is a gentle process that

prepares the damaged area for application of a repair patch [58]. It is unknown whether repair design instructions are provided for wind turbine blade repairs. In the aerospace industry, structural repair manuals are provided to aircraft technicians that include repair design instructions [58]. Scarfing specifications can either be by distance per ply or by scarf angle. When using a distance per ply specification, a rough rule-of-thumb for material removal during scarfing is to taper sand approximately ½ -in of area per ply of composite laminate. For when a scarf angle specification is invoked, Dorworth, Gardiner, and Mellema (2009) note:

> The steeper the scarf, the less undamaged material is removed. Lightly loaded structures may be able to tolerate a smaller, steeper scarf. A typical angle for lightly loaded non-aerospace structures is 12:1 (~5°). The flatter the scarf (more area per ply), the larger the adhesive bond is and the lower the load per square inch on the bond. Heavily-loaded structures usually require a larger, gentler scarf [58].

Surface energy is defined in Section 2.8: Surface Energy. Considerations to make in creating a smooth, flat repair surface with high surface energy are discussed in Section 2.9: Surface Preparation of Composite Scarf Repairs.

2.7.2 Step 7: Develop a repair design based on the damage and original structure information.

It is generally recommended to repair a structure with identical original materials to the original part. It is unknown if the identical original material information is provided to wind turbine blade repair technicians. If identical material information is not provided, the information on typical wind turbine blade materials, general design, and manufacturing methods that was described in previous sections can be used to make an informed estimate on which materials to select for repair patch fabrication.

2.7.3 Step 8: Replace materials including the solid laminate and the through-damaged sandwich structure, if applicable.

Once identical original materials to the original part or a good estimate of the original materials are selected, the plies of the repair patch are cut with rounded corners to fit the prepared repair area. The repair patch is used to replace the damaged area in the composite laminate as exactly as possible. Thus, the number of plies and orientations of each repair ply must match, layer for layer, those of the original structure. Dorworth, Gardiner, and Mellema (2009) can be referenced for more information on replacing materials in through-damaged sandwich structures [58].

2.8 Surface Energy

Hiemenz (2016) defines a surface in the chemical sense of a phase boundary, rather than in a strictly geometric sense. Geometrically, a surface has area but not thickness. Chemically, however, a surface is a region in which the properties vary from those of one phase to those of the adjoining phase [59]. Sperling (2006) defines a surface (or *free* surface) as the part of a pure condensed substance in contact with a vacuum. In reality, however, surfaces may be in contact with air, oxidized, oily, or dirty [60]. For this work, a surface will be defined as the layer of atoms between a substance and air. Surface atoms are not bonded to the maximum number of nearest neighbors and are therefore in a higher-energy state than the atoms at interior positions. The bonds of the surface atoms that are not satisfied give rise to a surface energy, expressed in units of energy per unit area (J/m^2). Materials will minimize the total surface area to reduce surface energy. Liquids, for example, assume a spherical shape to have a minimum area [61].

Surface tension is different from surface energy and is a measure of the force acting at a boundary between two phases (mN/m). Temperature and molecular weight have a significant effect on surface tension. Solid surface tensions can be estimated using contact angle testing. The Young equation for contact angle is:

$$\gamma_l \cos\theta = \gamma_s - \gamma_{sl} \tag{5}$$

where γ_l is the free energy per unit area of a liquid surface and γ_s is the free energy per unit area of a solid surface. The free energy between solid and liquid surfaces is the work necessary to separate a liquid drop from a solid surface. Maximizing surface free energy results in improved interfacial contact [62]. Interfacial tension is similar to surface tension, but cohesive forces are involved [63] . Cohesive forces are also termed adhesive forces and can be measured using the work of adhesion [64].

The Dupré equation can be used to express the work of adhesion W between a liquid drop and a solid surface:

$$W = \gamma_s + \gamma_l - \gamma_{sl} \tag{6}$$

Combining Equations (5 and (6 brings forth the Young-Dupré-Pockels (YDP) equation:

$$W = \gamma_l(1 + \cos\theta) \tag{7}$$

which gives the work of adhesion of a liquid drop to a solid surface as a function of the liquid surface tension and contact angle. The observation of contact angles of liquids on solids may be used as a starting point for investigating solid surface tensions [65].

Contact angle testing involves the placement of a water droplet on a surface and measuring the resultant angle the droplet makes with the surface. Low contact angle values correspond with hydrophilicity, high wettability, and higher surface energy.

Alternatively, high contact angles indicate hydrophobicity, low wettability and lower surface energy [66]. Additionally, low surface energy typically results in more adhesive failure, and high surface energy will typically result in more cohesive failure [67]. A diagram of a typical contact angle test depicting the three interfacial tension forces is in Figure 27. While contact angle is a distinctly quantitative measurement, the results can be used qualitatively for determining the successful adhesive bond.

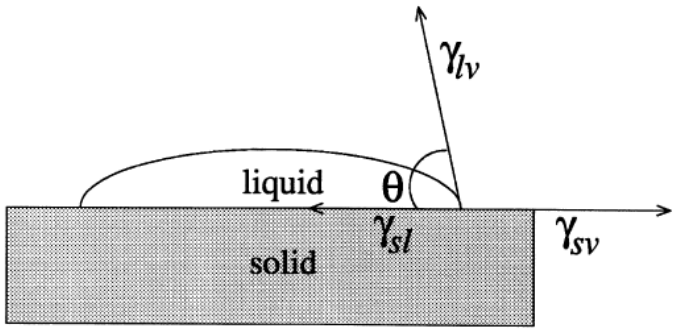

Figure 27. Schematic of a contact angle system at equilibrium [68]. The four variables θ, γ_{sl} , γ_{lv}, and γ_{sv} are defined as contact angle and interfacial tensions between solid and liquid, between liquid and vapor, and between solid and vapor, respectively [66].

2.9 Surface Preparation of Composite Scarf Repairs

The purpose of creating a smooth, flat surface with high surface energy is to have a strong resulting bond between the repair area and the repair patch. Ibitoye (2018) demonstrated with experimental and simulation testing that the repair strength of a laminate is dependent on the bond strength of the resin or adhesive interface layer [57]. The bond strength is contingent on several bonding factors (Table 2).

Table 2. Potential bonding factors [69].

Factor	Variables
Adherend Lay-up	$O^{\circ}_{[n]}$, quasi-isotropic, other lay-up; orientation of ply on bonding surface
Adherend Material	Fiber, matrix, metal, aviation materials
Adhesive Filler Material	Type of filler, percentage of filler
Adhesive Preparation	Hand-mixed, machine-mixed, apply vacuum to remove trapped air
Bondline Thickness Control	Glass microbeads/silane treatment, wires, tabs/tape, carrier cloth, applied pressure
Compressed "Shop Air" Blast	Pressure, exposure time
Grit Blast	Pressure, grit size, number of passes, speed of passes
Hand Sanding	Grit size, number of passes, pressure applied
Humidity Exposure	Humidity %, exposure time, prebond, postbond, under load
Peel Ply/Release Fabric	Nylon, polyester, none
Solvent Wiping	Acetone, isopropyl alcohol, number of wipes, applicator type
Temperature Exposure	Temperature, exposure time, prebond, postbond, under load
Water Bath	Temperature, exposure time, prebond, postbond, under load

A bonding factor not listed in Table 2 is the type of bonding process used. Bonding processes for composites include co-curing, co-bonding, and secondary bonding (Figure 28) [70]. Co-cured adhesive joints have no discernable interface in the cured structure due to interdiffusion of the adhesive and laminate during cure. Failures in co-cured structures are uncommon. Secondary bonded and co-bonded joints have at least one interface and exhibit interfacial failure modes [71]. Secondary bonded repairs use hard patches and co-bonded repairs use soft patches [57]. Co-curing techniques are not used in composite repairs.

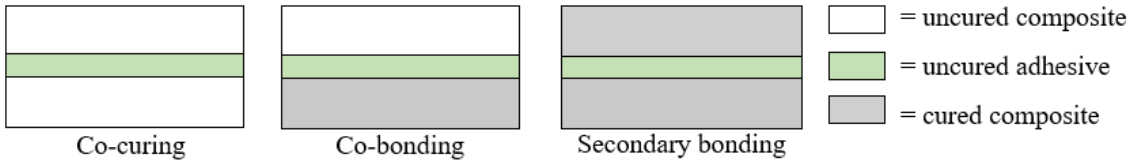

Figure 28. Diagram of the three types of bonding processes in composites.

Solvent wiping and sanding are factors that pertain to creating a smooth, flat surface with high surface energy in a scarf repair. Solvent wiping is used to remove contamination from a surface. Contaminants will be present before, during, and after damage removal, and can arise in a variety of forms that may inhibit resulting repair strength. A contaminant is any substance or surface condition that is detrimental to a structural adhesive bond [72]. Common contaminants in a field repair include hydraulic oil, dirt, dead insects, and composite dust. Internal and external fluid leakage can occur in fluid power pitch systems in wind turbines [73]. Furthermore, hydraulic oil can drip down from the brake and pitch controls in the nacelle into the blade and saturate blade materials such as the sandwich composite core during service. Hydraulic oil can also be present on the outside of the blade. Amaro et al (2014) used oil immersion tests to study the effects of engine oil and hydraulic oil on the flexural and impact strengths properties on GFRP laminates. Both oil types decreased the flexural strengths and flexural moduli of the laminates [74]. Furthermore, if hydraulic oil is not thoroughly removed from outside the damaged area or remains in surrounding core materials, the oil could enter and compromise the repair bond line. The bond line could also be compromised if solvent wiping brings hydraulic oil contamination from outside the repair area into the repair

area. After a repair is executed and if hydraulic oil remains in the core in the surrounding area, the hydraulic oil could diffuse from the core into the repair area.

The likelihood of each scenario has not been quantified but quantifying the effects of hydraulic oil contamination on a bond line can inform solvent wiping procedures and what measures should be taken if the scenarios do occur. Dirt and dead insects come from the environment, and composite dust arises during damage removal. Just as sawdust is a byproduct of cutting or sanding a piece of wood, there is a dust byproduct after cutting or sanding a composite. Composite dust consists of glass and polymer particles, as well as particles from whichever cutting or abrading method was used. Sandpaper particles, for example, would consist of sand, adhesive, and paper.

There are three options in addressing contamination:

1. Leave contamination on the surface.
2. Remove dust using dry techniques such as dry wiping, brushing, vacuum cleaning, or air blasting.
3. Use solvent-wipe techniques.

No recommendations were found that included leaving contamination on the surface prior to bonding. Shang (2013) and Musaramthota, Pribanic, and McDaniel (2014) have both demonstrated that contamination along a bond line will diminish bond strength [72, 73]. Shang (2013) examined the effects of three types of aviation hydraulic oil and two mold release agents on the bond line integrity of carbon fiber composites adhered with Loctite EA 9394 adhesive using DCB and nano-indentation testing, and

concluded that applied contaminants contributed to decreased interfacial fracture energy [75].

Musaramthota, Pribanic, and McDaniel (2014) also studied the effects of silicone spray and mold release on composite bond integrity by applying contamination using two different methods: the mesh approach and the stamp approach. The mesh approach involved spraying the contamination on a stainless-steel perforated plate, then placing the plate on top of a laminate to generate an imprint. The laminates were then bonded together using adhesives. The stamp approach involved using a sponge filled with a contaminant to wet a rubber stamp and placing the stamp on a composite surface, then the laminate was bonded with 3M AF 555M film adhesive. The failure surface of one of the stamped DCB specimens is in Figure 29. Surface characteristics and surface chemistry of laminates prior to bonding were analyzed using contact angle testing and FTIR spectroscopy. Gravimetric analysis was used to assess the weight changes of the laminate from the addition of contamination [76].

Figure 29. Failure surface of a DCB specimen contaminated with mold release [76].

DNV-GL is a standards and practices society of underwriters. DNV-GL (2015) recommends the following for solvent cleaning:

> The area to be repaired shall be prepared and cleaned in the following sequence:
> - Before cutting or grinding, the repair area shall be cleaned from any dirt, dust or grease present at the surface using dry or wet techniques (including solvent based liquids) as appropriate.
> - After cutting/chamfering, the surface of the repair area shall be ground thoroughly, e.g. by using sandpaper with a grain of 80 or 120.
> - Once all cutting, chamfering, and grinding is completed, the repair area should be thoroughly cleaned from any dust or contamination, using dry techniques (such as brushing, vacuum cleaning, or air blasting with compressed air free of oil contamination); no wet techniques shall be applied in this cleaning step, in order to avoid clogging of surface pores or cavities with wetted dust particles.
> - Only after thorough dry cleaning has been accomplished, a wet cloth may be used to clean the surface from residual dust particles; no solvent based liquid shall be used in this final cleaning step [77].

DNV-GL (2015) recommends using solvents prior to damage removal, and only recommends using water wiping on the composite repair surface. Generally, for sanding recommendations, grit size must be selected to promote adhesive adhesion to an adherend without causing further damage to an adherend. Additionally, appropriate grit size must be considered for the type of adhesive used.

Sanding grit size effects on a surface can be measured using profilometry. Gude et al (2011) used mechanical profilometry to measure the roughness average (R_a) of the surface of a composite laminate, where Ra is the arithmetical mean of the absolute values of the profile deviations from the mean line of the roughness profile (Figure 30) [78].

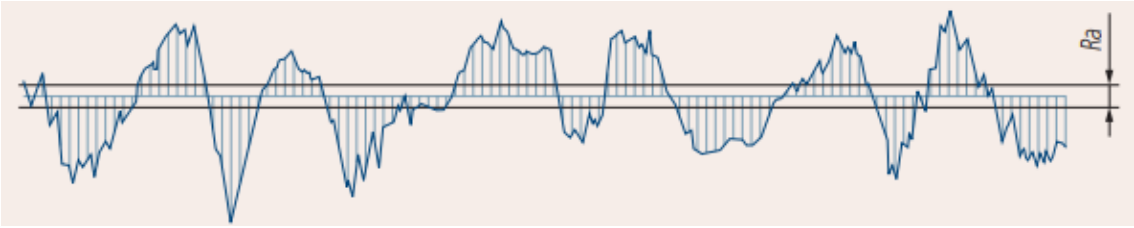

Figure 30. Mean roughness value R_a [79].

A material's surface topology consists of peaks and valleys that change with surface roughness. Consequently, a more viscous adhesive may not wet out a rougher surface because the adhesive will not be able to fully surround the peaks or fill in the valleys of a surface. If a surface is not wet out before bonding, air pockets will remain along a bond line. Air pockets along a bond line are stress concentrations that can propagate throughout a material and cause structural failure. Mishnaevsky and Thomsen (2020) used continuum damage mechanics to show that air pockets and voids in adhesives reduces the post-repair lifetime of wind turbine blades by 7%, where the post-repair lifetime is the time until the next repair [9].

DNV-GL (2015)'s recommendation of using FEPA 80-120 grit sandpaper might be beneficial for damage removal but using such large sand grains could damage intact fibers more than necessary for a repair. Dorworth, Gardiner, and Mellama (2009) recommend using 400-600 grit sandpaper, which are finer grit recommendations than DNV-GL (2015)'s [58]. The 320 grit sandpaper was experimentally found to be fine enough to mitigate fiber damage on a surface while removing mold release sufficiently to pass the water break test. In a water break test, water is applied to a level surface. If the surface energy produced is high enough, water will spread out in a slightly arched film on

the surface and should not “break” into beads. The water break test is like a contact angle test but uses visual observation rather than contact angle measurements.

Air blasting with compressed air free of oil contamination requires the use of an oil-less air compressor rather than an oil-injected air compressor. Depending on the accessibility method used for a repair, an air compressor might not be a feasible method of contamination removal. An air compressor could possibly be used when accessing a damaged area with a suspended platform (Figure 22), but not when a technician rappels to the damaged area from the nacelle (Figure 21).

There are some discrepancies between Horton (1990), Petrie (2007), Sperling (2006), and Dorworth, Gardiner, and Mellema (2009) around the use of solvent wiping [8, 63, 70, 77]. Horton (1990) says preparing composites for adhesive bonding using solvent wiping is usually a grossly inadequate treatment, and that solvents should be regarded with utmost caution. Allowing the solvent to evaporate off the surface results in the spreading of any contamination in a thin film over the entire area to be bonded. The correct technique is a two-handed operation, where one hand holds the solvent-soaked cloth, and the other holds a dry cloth that is used to wipe up the solvent before it has time to dry [72]. Contrary to Horton’s statement on solvent wipe treatment inadequacy, Petrie (2007) says thermosetting composites provide sufficient adhesion strength with only light abrasion and solvent cleaning, while recommending plasma treatment for thermoplastic-based composites [80]. However, Sperling (2006) says that the ability of polymers to bond to a surface must be altered significantly, either by plasma or corona treatments [60]. Plasma treatments are discussed in Section 2.12: Plasma.

Similarly to Horton's solvent wipe procedure recommendation, Dorworth, Gardiner, and Mellema (2009) recommend wiping a surface with reagent grade solvents such as acetone, methyl ethyl ketone (MEK), methyl isobutyl ketone (MIBK), or isopropyl alcohol (ISP) to remove contamination, and wiping again with a dry cloth to remove the solvent before evaporation. Dorworth, Gardiner, and Mellema (2009) note that, "it is important to know what the contaminant is made of, what the contaminant is, and to check any and all suggested procedures to ensure the solvent being used is capable of dissolving the foreign fluid without further damaging the composite structure [58]."

2.10 Polymer Adhesion

Adequate composite repair procedures are motivated by principles of polymer adhesion. Adhesion is the result of intermolecular forces between two different substances, and is generally caused by molecular interactions between the substrate and the adhesive and not necessarily by chemical bonds [80]. Usually, thin structures with well-defined load paths are good candidates for adhesive bonding, while thicker structures with complex load paths are better candidates for mechanical fastening [81]. The materials considered in the examination of adhesion in composite materials include glass fibers, the matrix used to impregnate the glass fibers, and the adhesive used to adhere two composite substrates together.

The adhesion of polymers can be caused by different mechanisms including mechanical coupling and molecular bonding. Mechanical coupling, or interlocking, occurs when an adhesive locks into the rough irregularities on a substrate's surface. In molecular bonding, intermolecular forces such as dipole-dipole interactions and

dispersion forces may occur between an adhesive and a substrate [82]. Dipole-dipole interactions arise from the electrostatic interactions of the positive and negative ends of molecules with permanent dipole moments. Dispersion forces occur across interfaces and are sometimes coupled by entanglements in polymer chains. The strengths of dispersion forces depend significantly on molecular shape because shape determines how much of one molecule can interact with its neighboring molecules at any given time. Chains across polymer interfaces chemically couple to the polymers on both sides of the interface (Figure 31). Mechanical interlocking contributes to improved adhesion if the surface free energy of a polymer substrate is not too low [62].

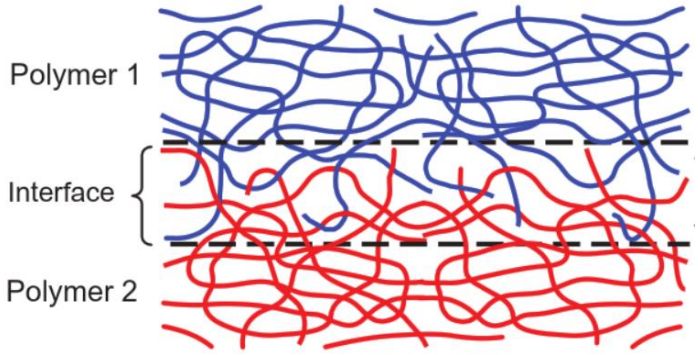

Figure 31. Illustration of the exchanges of polymer chains at a polymer-polymer interface [83].

2.11 Sizing

Besides contamination removal, other methods may be employed to promote adhesion. Fabbri and Messori (2017) examined trends in the surface modification of polymers and describe various methods to modify outermost layers of polymers to increase adhesion while maintaining bulk properties [84]. Surface treatment methods

such as chemical methods and plasma are candidates with higher feasibilities in meeting the accessibility challenges of field repairs. Chemical methods for surface modification usually involves wet chemistry, which is where a coating is applied to a surface to promote adhesion between a surface and an adhesive [85]. A coupling agent is a type of coating that promotes adhesion between polymers and minerals [86]. Sizing is a coupling agent that is applied to glass fibers during manufacturing to facilitate adhesion between fibers and an appropriate polymer matrix (Figure 32). Tanoglu et al (2000) demonstrated that composites made with sized glass fibers had improved structural integrity than those made with unsized glass fibers [87].

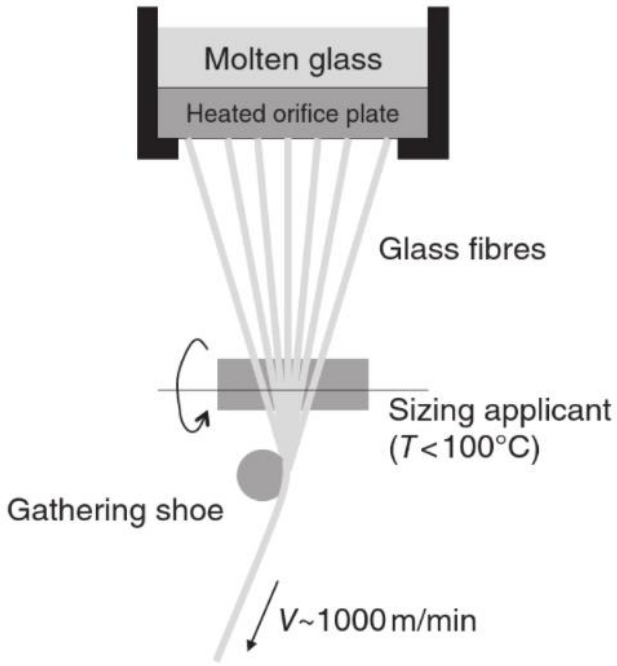

Figure 32. Glass fiber drawing process [88].

Sizings are typically alkoxysilane compounds [89]. Alkoxysilane compounds commonly have three alkoxy groups and are thus called trialkoxysilanes. An alkoxy group (R-O) is one where an alkyl (R) is singularly bonded to oxygen (O). An alkyl is a carbon and hydrogen chain. A silane is any series of covalently bonded compound containing only the elements silicon and hydrogen [90]. A group, or functional group, is a portion of an organic molecule which consists of atoms other than carbon and hydrogen, or which contain bonds other than C-C and C-H [91]. Zhu, Hu and Schaefer (2020) illustrate the process organofunctional trialkoxysilane bonding to an inorganic substrate in Figure 33 [92]. The prefix -*organo* indicates a compound containing an organic group. Organic compounds include hydrocarbon compounds and their derivatives. Hydrocarbons are organic compounds that contain only hydrogen and carbon [93]. Inorganic compounds include all chemical compounds without the chains or rings of carbon atoms that fall into the subcategory of organic compounds [94]. Molecules of organofunctional trialkoxysilanes undergo two key reactions during applications: hydrolysis and condensation. Hydrolysis converts hydrolysable groups (OR) to silanols (Si–OH) in the presence of water or moisture in the atmosphere. A group is hydrolysable if it can be decomposed by reacting with water. Condensation among silanols (Si–OH) forms a three-dimensional siloxane (Si–O–Si) structure. Condensation with hydroxyl groups on an inorganic substrate forms covalent bonds.

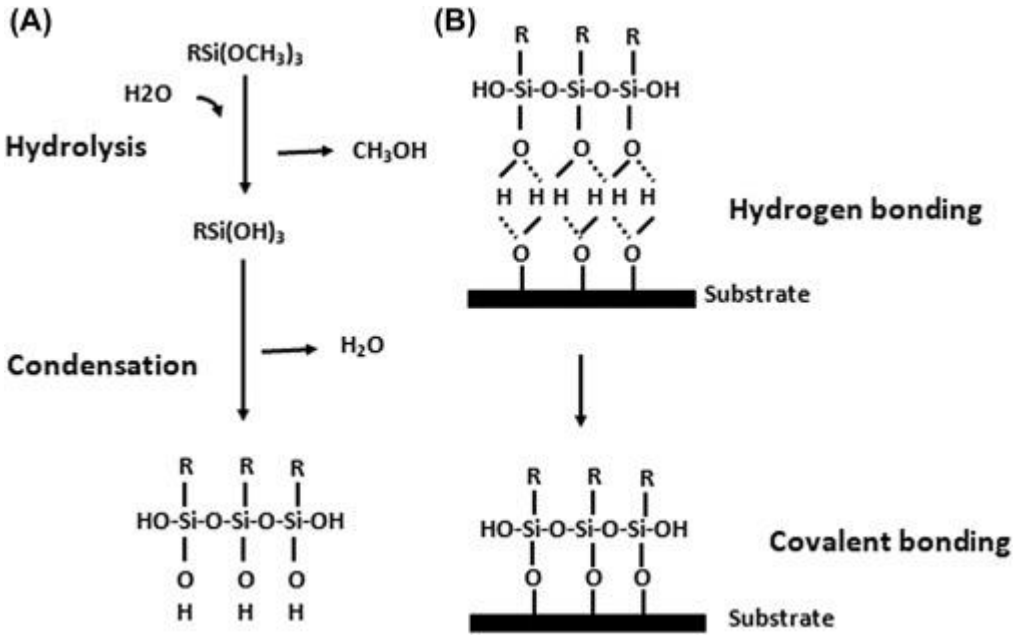

Figure 33. The process for organofunctional trialkoxysilane hydrolysis, condensation, and covalent bonding to an inorganic substrate; (A) hydrolysis and condensation to form oligomers in the silane solution and (B) adsorption to an inorganic substrate (such as ceramics or surface oxide layers on metals) by hydrogen bonding and then covalent bonding to the substrate by a condensation reaction with a hydroxyl group [92].

2.12 Plasma

Besides chemical methods, physical methods of surface treatment such as flame plasma and blown ion treatments can improve adhesion by introducing polar, oxygen-containing functional groups on originally nonpolar surfaces. Webster and Wightman (1990) demonstrated that covalent bonding occurs between plasma-induced surface species and epoxy [95]. In a flame plasma treatment, a fuel such as natural gas or propane is thoroughly premixed before combusting and creating a laminar flame [96]. Within a laminar flame are radical species that strongly oxidize the surface of polymeric materials to introduce polar reactive groups such as hydroxyl and carboxyl [97]. Radical species, or

free radicals, are atoms, molecules, or ions that have unpaired valence electrons that are highly reactive towards other substances or themselves [60]. Oxygen-containing functional and polar reactive groups increase adhesion because the oxygen in the structures bond well with polar substances such as water. Increased polar-polar bonding increases hydrophilicity, which corresponds with improved adhesion. Blown ion treatment increases surface energy due to surface reaction among the polymer matrix, energetic ions, and oxygen gas. The reaction begins by creating an unstable chain using ion irradiation and is followed by a chemical reaction between unstable radicals and oxygen gas [98]. Ion irradiation can create unstable chains when the ions' kinetic energies are sufficient to displace surface atoms from the atoms' lattice sites. Atom displacements cause an accumulation of defects which may eventually transform a surface from having a crystalline structure to an amorphous state [99]. Liston, Martinu, and Wertheimer (1993) provides typical examples of lap-shear bonding improvements after plasma treating several polymers (Figure 34) [100]. Background information on lap shear testing is in Section 2.14.1: The Lap Shear Test. In addition to lap shear testing, Liston, Martinu, and Wertheimer (1993) used water contact angle testing measure the effects of plasma treatments on polymer surfaces. Despite having increased maximum lap shear strengths for each of the polymers listed, each new application of plasma processing requires that the process conditions be clearly identified and optimized [100].

	Control		Plasma-treated	
	MN/m^2	psi	MN/m^2	psi
Polyimide (PMR®-15)/graphite	2.90	420	17.93	2600
Polyphenylene sulphide (Ryton® R-4)	2.00	290	9.38	1360
Polyether sulphone (Victrex® 4100G)	0.90	130	21.65	3140
Polyethylene/PTFE (Tefzel®)	—	Very low	22.06	3200
HDPE	2.17	315	21.55	3125
LDPE	2.55	370	10.00	1450
Polypropylene	2.55	370	21.24	3080
Polycarbonate (Lexan®)	2.83	410	6.40	928
Nylon®	5.86	850	27.58	4000
Polystyrene	3.93	570	27.58	4000
Mylar A®	3.65	530	11.45	1660
PVDF (Tedlar®)	1.93	280	8.96	1300
PTFE	0.52	75	5.17	750

Figure 34. Typical examples of lap shear bonding improvements after various plasma treatments [100].

2.13 Solvent-Polymer Interaction

The purpose of using solvents in composite repairs is to dissolve and remove contamination. During the dissolution and removal of contaminants, the solvents used will contact the composite surface, which consists of a polymer matrix and exposed glass fibers. The polymer matrices used in composites are usually thermosets, which are crosslinked polymers (Figure 35). Crosslinked polymers are branch structured macromolecules that have covalent bonds between polymer molecules [60]. Covalent bonds are formed when electrons are shared between atoms. Epoxy and vinyl ester are commonly used thermosets in composite materials. Examples of lightly crosslinked polymers are rubbers [101]. Thermoplastics are uncrosslinked, linear polymers (Figure 36), which consist of long continuous chains of covalent bonds. Linear polymer chains

are connected to one another by hydrogen bonds, which are weaker than covalent bonds [102].

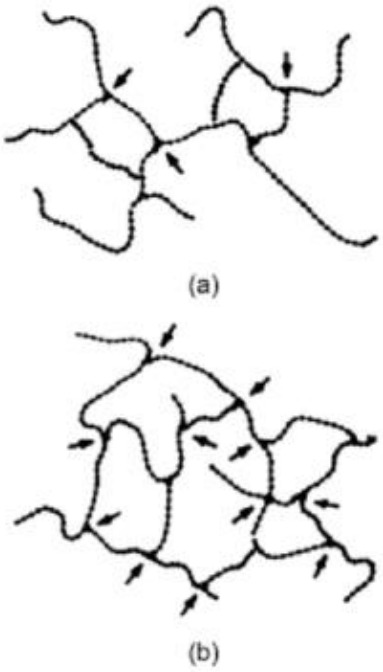

Figure 35. a) Lightly crosslinked polymer b) Highly crosslinked polymer [102].

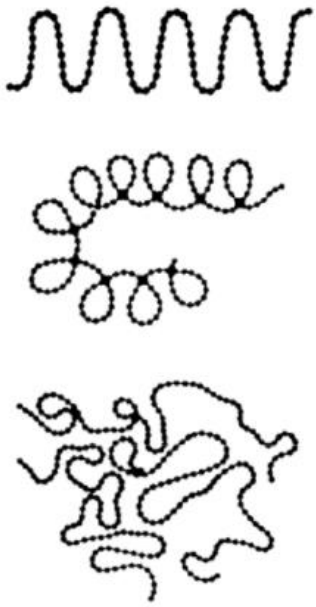

Figure 36. Simplified representation of various linear polymer configurations [102].

Miller-Chou and Koenig (2003) describe how an uncrosslinked polymer dissolves in a solvent:

> The dissolution of a polymer into a solvent involves two transport processes, namely solvent diffusion and chain disentanglement. When an uncrosslinked, amorphous, glassy polymer is in contact with a thermodynamically compatible solvent, the solvent will diffuse into the polymer (Figure 37). Due to plasticization of the polymer by the solvent, a gel-like swollen layer is formed along with two separate interfaces, one between the glassy polymer and gel layer and the other between the gel layer and the solvent (Figure 38) [103].

The thermodynamic compatibility between a polymer and a solvent can be estimated using the Flory-Huggins theory and the Gibbs free energy of mixing. The Flory-Huggins parameter χ characterizes a variety of polymer-solvent and polymer-polymer interactions and is given by:

$$\chi = \frac{(1 + n^{1/2})^2}{2\mathrm{n}} \cong \frac{1}{2} + \frac{1}{n^{1/2}} \quad (8)$$

where n is the degree of polymerization, which is defined by the number of monomer units in the polymer. The degree of polymerization is calculated as the ratio of the molecular weight of a polymer and the molecular weight of the repeat unit [10]. The molecular weight is the total weight of a polymer divided by the number of molecules. If χ is below 0.5, an amorphous and linear polymer will be soluble. When χ equals 0.5, then the Flory θ conditions exist. Flory θ conditions exist when a solvent goes from good to poor for a theoretical polymer of infinite molecular weight, and the molecular weight fraction would undergo phase separation. A good solvent is one that can dissolve a solute, and increasing temperature often increases solvent goodness [59]. A poor solvent is one that cannot dissolve a solute. For many nonpolar polymer-solvent systems, χ is in the range of 0.3 to 0.4 [60]. Generally, polymers will dissolve in solvents whose solubility parameters are not too different from their own. This principle is known as “like dissolves like,” which means that, as a general rule, structural similarity favors solubility [103].

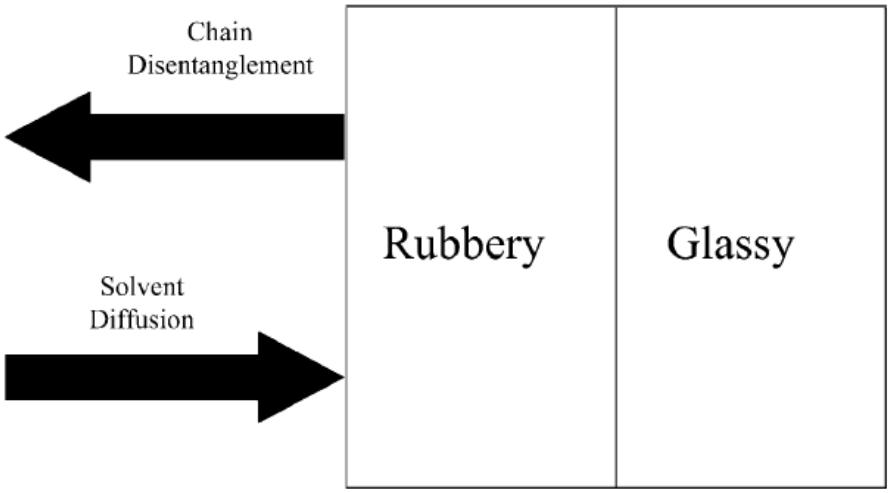

Figure 37. A schematic of solvent diffusion and polymer dissolution [103].

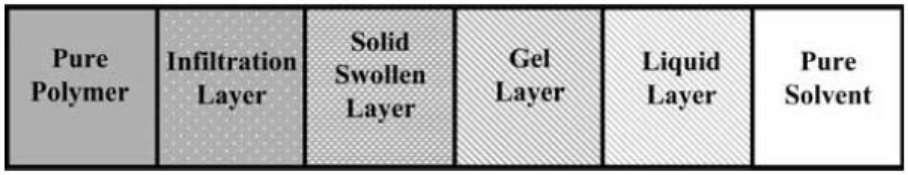

Figure 38. Schematic of the composition of a polymer surface layer interacting with a solvent [103].

Crosslinked polymers do not completely dissolve in thermodynamically compatible solvents in the way that uncrosslinked polymers do. Blinov and Tager (1987) says that crosslinked polymers can only reach the gel layer state when interacting with a solvent and do not reach the liquid layer state [104]. Sperling (2006) says thermosets are solvent resistant, but also notes:

> The orientation of a polymer at the surface is almost always different from the interior. The polymer chains may be lying flat, oriented in the surface plane, or if some special group (especially a group at the end of the chain) is attracted to the surface, the orientation of adjacent mers may be normal to the surface plane [60].

2.14 Mechanical Testing

Duncan and Crocker (2001) reviewed mechanical test methods that quantify the strengths of interfaces and to evaluate the effects of surface pre-treatments. In the review, mechanical test methods included the single lap joint test, the double cantilever beam (DCB) test, the end-notch flexure (ENF) test, and the scarf joint tension test [105]. DCB and ENF tests are used to calculate modes I and II critical energy release rates (CERRs), G_{IC} and G_{IIC}, which are derived from Griffith's energy approach to fracture. G_{IC} and G_{IIC} are also called the modes I and II fracture toughness values. In general, all the dissipative phenomena occurring during crack growth absorb a combined 2γ of energy per unit area of a crack A, where γ is the surface energy. The potential energy Π is the elastic strain energy U minus the work done by the external loads W, so $\Pi = U-W$. The energy release rate G is:

$$G = -\frac{d\Pi}{dA} \tag{9}$$

where A is one half of the surface area created [11]. The energy absorbed per unit crack area created is $G_c = 2\gamma$ and a crack will not grow if:

$$G \leq G_c \tag{10}$$

Broek (1975) can be referenced for a more detailed derivation of the critical energy release rate [46].

Mechanical tests of different joint configurations can either be conducted experimentally or simulated using finite element analysis (FEA). Digital image correlation (DIC), microscopy, and spectroscopy are used in this work's experimental mechanical testing methods. Subsections 2.14.1-2.14.4 discuss the uses, methods, and

outputs for single lap joint, DCB, ENF, and scarf tension testing. Sections 2.15 and 2.16 discuss the uses, methods, and outputs for DIC and FEA, respectively. Microscopy and spectroscopy are discussed in Section 2.17. Scarf tension experimental and simulation testing methods are reviewed in Section 2.18.

2.14.1 The Lap Shear Test

The single lap joint test is also termed the lap shear test and has several limitations and advantages. The first limitation is that the determination of joint parameters such as the true ultimate stress is limited because the stresses are concentrated at the ends of the overlap instead of through the adhesive [76, 98]. The second limitation is that the stiffness of the adherends influences peel stress concentrations at the end of the joint in lap shear testing. Peel stresses are associated with opening mode (mode I) crack extension and shear stresses are associated with sliding mode (mode II) crack extension (Figure 39) [106]. Although the test is termed “lap *shear*,” the test is mixed-mode with peel stress concentrations at the ends with shear stress in the center region makes. The third limitation is that increasing the modulus or thickness of adherends leads to an increase in apparent strength of the bond [105].

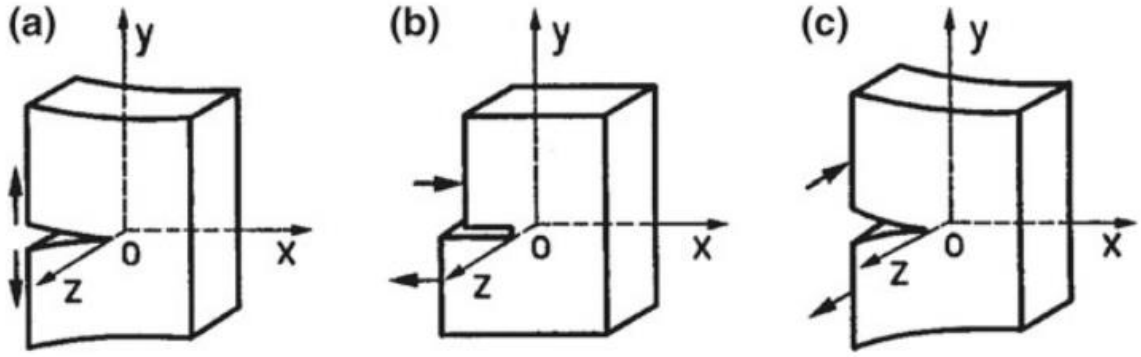

Figure 39. The three basic modes of crack extension: a) opening mode (mode I), b) sliding mode (mode II), and c) tearing mode (mode III) [106].

Despite its limitations, the lap shear test has advantages regarding the data obtained and in its test methods. Despite not being able to produce true ultimate stress, the lap shear test has value from a comparative standpoint. The lap shear test can be used to determine if a certain adhesive has a superior strength compared to another even though the actual design strength is not obtained [81]. The lap shear test can also be used to check the effectiveness of different surface preparations [105]. Lap shear specimens are straightforward to prepare and test. Typical lap shear specimen dimensions are in Figure 40. Although not included in Figure 40, end tabs are often adhesively bonded to the specimen to reduce the eccentricity of the load path. End tabs are cut from the material as the adherend [81].

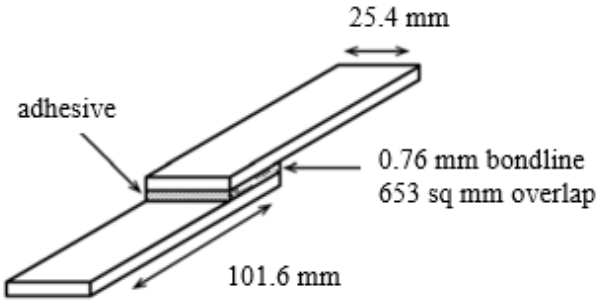

Figure 40. Schematic of two composite substrates adhered together to produce a single lap joint test specimen.

Data commonly obtained from lap shear tests include the maximum lap shear stress and adhesive failure modes (Figure 41). The maximum lap shear stress is calculated by dividing the failure load by the bond area. Adhesive failure modes provide a visual and sometimes microscopic description of how a material failed. In addition, adhesive failure modes can indicate manufacturing problems in adhesively bonded joints. Although the failure modes in Figure 41 are depicted on lap shear surfaces, the same types of failure modes can be used to characterize DCB, ENF, and scarf tension failure surfaces. The four adhesive failure modes are interfacial, cohesive, stock-break, and fiber-tear. Interfacial failure occurs along the adhesive-substrate interface and is usually due to a lack of chemical bonding. Interfacial failure is sometimes termed adhesive failure. Cohesive failure occurs within the adhesive and is typically the preferred type of failure in a bonded joint. Dillingham (2006) demonstrated using DCB testing that cohesive failure corresponded with higher mode I fracture toughness (G_{IC}) values and interfacial failure corresponded with lower mode I fracture toughness values [67]. Similar correlations between maximum lap shear stress values and failure modes have been

observed in lap shear testing [107]. Stock-break failure occurs when the substrate is either damaged or weaker than the adhesive bond [108]. Fiber-tear failure occurs when the top layer of the substrate is damaged, resulting in fiber re-exposure. ASTM D5868 (2014) recommends that lap shear specimens are tested in tension at loading rate of 13 mm/min [109].

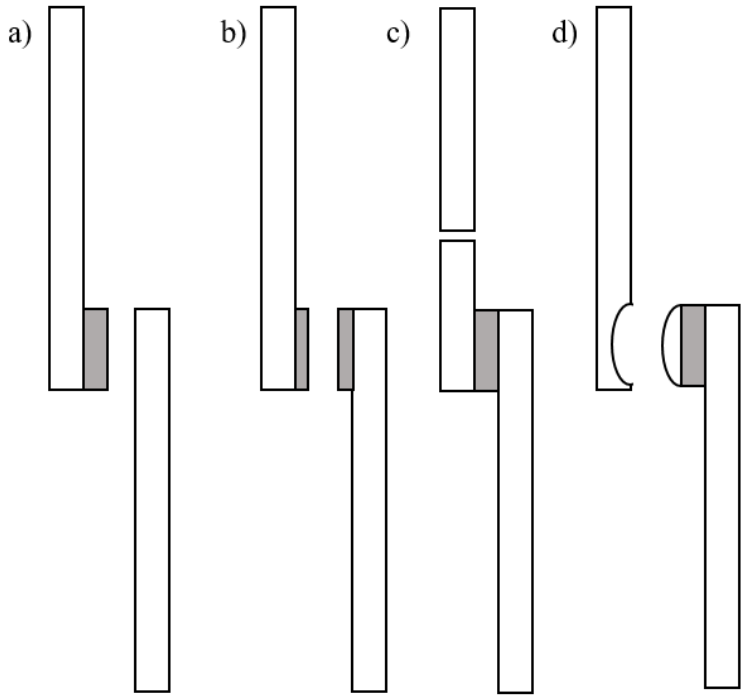

Figure 41. The four types of bonded joint failure modes: a) interfacial or adhesive failure, b) cohesive failure, c) stock-break or adherend failure, and d) fiber-tear or intralaminate failure.

2.14.2 The DCB Test

The DCB test is used to measure the initiation and propagation energy of a mode I crack. To manufacture DCB specimens, adherends are bonded together using an adhesive. End tabs need to be attached to allow the beams to be gripped (Figure 42) [105].

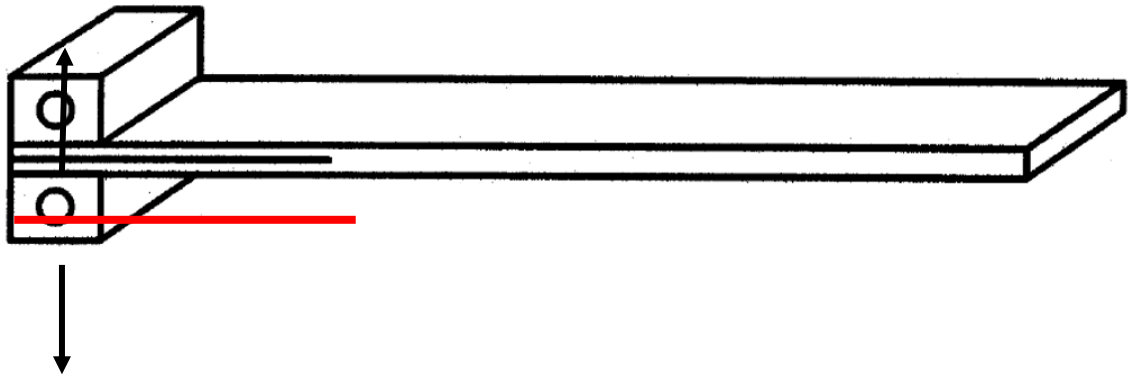

Figure 42. DCB specimen with tabs and pre-crack (red) [105].

G_{IC} is calculated using Equation 11:

$$G_{IC} = \frac{12P^2}{b^2h^3E_{11}}[a^2 + \frac{2a}{\lambda} + \frac{1}{\lambda^2}] \quad (11)$$

where

$$\lambda = (3k/bh^3E_{11})^{1/4}$$

and

$$k = 2bE_{22}/h$$

where P is the maximum load, b is the width, h is the average thickness of the plate used, a is the initial crack length, E_{11} is the longitudinal tensile modulus, and E_{22} is the transverse tensile modulus [110]. E_{11} and E_{22} can be calculated using [111]. P is

commonly approximated using the 5% rule, which involves finding the slope of the force-displacement curve generated in DCB tests, then taking 95% of the slope and using the load where the 95%-of-the-slope line intersects plotted data points. The 5% rule is used to account for the nonlinearity in DCB test data [112].

2.14.3 The ENF Test

The ENF test essentially involves loading the DCB specimen in three-point bend (Figure 43) [105]. The ENF test is used to measure G_{IIC}, where:

$$G_{IIC} = \frac{9P^2L^2}{16b^2h^3E_{11}}\left[a^2 + \frac{0.2h^2E_{11}}{G_{13}}\right] \tag{12}$$

where P is the maximum load at which crack propagation is observed and L is the distance between the center of the downward loading nose to the center of one of the supporting rollers [110]. Shear modulus G_{13} can be found using Iosipescu notched-shear tests and digital image correlation (DIC) [113]. DIC is described in Section 2.15, “DIC.” The remaining variables are defined the same way as in (11.

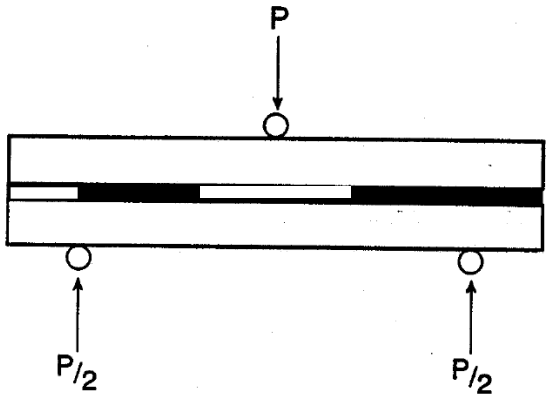

Figure 43. ENF specimen loaded in three-point bending [105].

2.14.4 The Scarf Tension Test

The scarf joint tension test, also termed the scarf tension test, can be used to examine the effects of the potential bonding factors from Table 2 on scarf joints. Some of the factors that have been examined in the literature using scarf tension testing include adhesive types, bondline thicknesses, adherend types, and scarf angles. In addition, scarf tension testing can test scarf angle effects on scarf joints. Outputs for scarf tension testing can include force-displacement curves, maximum scarf tension stress, strain contour maps, stress-strain curves, and failure modes. Lap shear, DCB, and ENF tests are commonly used and have well-defined manufacturing and testing methods. The scarf tension test is less common, however, so additional work is necessary to define manufacturing and testing methods. Since scarf tension testing does not have well-defined manufacturing methods, manufacturing methods are reviewed in this section. In addition, experimental and simulation methods that can be used in scarf tension testing

are reviewed in Section 2.18: Experimental and Simulation Testing Methods for Scarf Tension Testing.

To manufacture scarf tension specimens using composite materials Kumar et al (2006) used secondary bonding processes and Wales et al (2014) compared co-bonding and secondary bonding processes [110, 111]. No literature was found that used co-curing to manufacture scarf tension specimens. Kumar et al (2006) secondarily bonded carbon fiber reinforced polymer (CFRP) composite specimens with resulting coupon dimensions shown in Figure 44. Wales et al (2014) examined the roles of interface toughening mechanisms and moisture uptake on co-bonded CFRP repairs. For the co-bonded specimens, a tapered edge was CNC-machined out of a CFRP laminate (Figure 45). Then, the tapered laminate was repaired by stacking plies along the tapered edge. The layup was impregnated with resin using VARTM (Figure 46). Photos of resulting cross-sections for secondary and co-bonded laminates are in Figure 47 [115]. Outputs in Wales et al (2014) included failure loads and stress-strain curves [115].

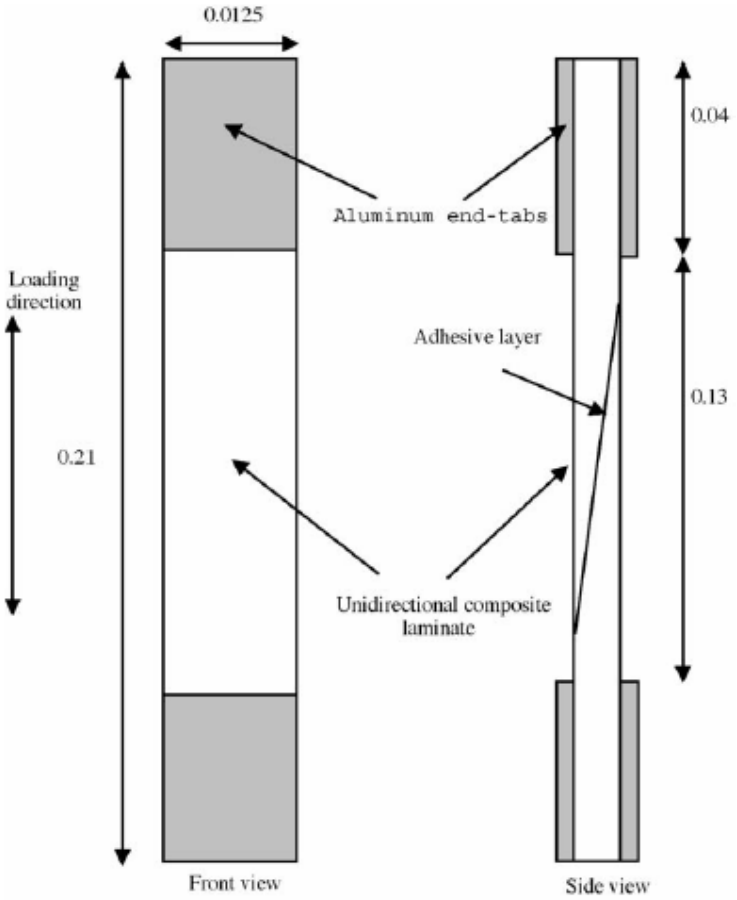

Figure 44. Dimensions (meters) of scarf tension specimens used in [114].

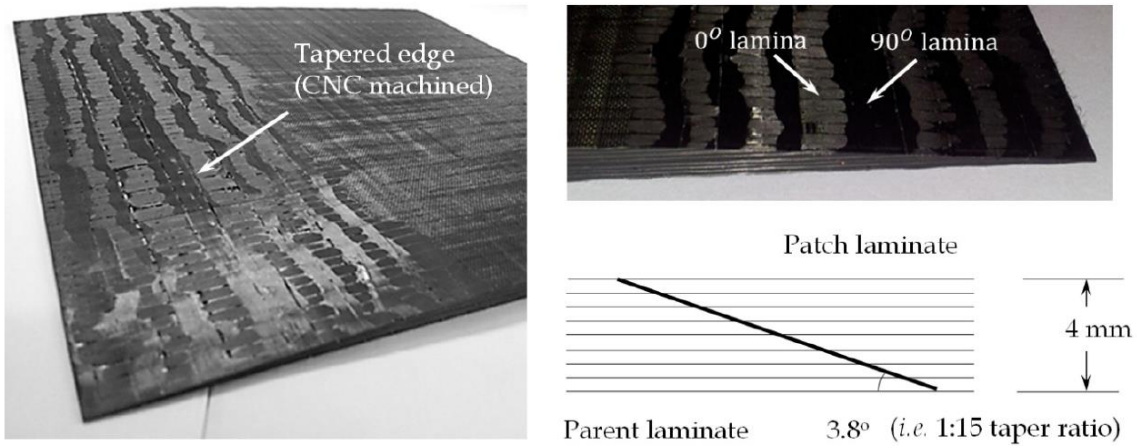

Figure 45. Photograph and schematic of CNC machined scarf used in [115].

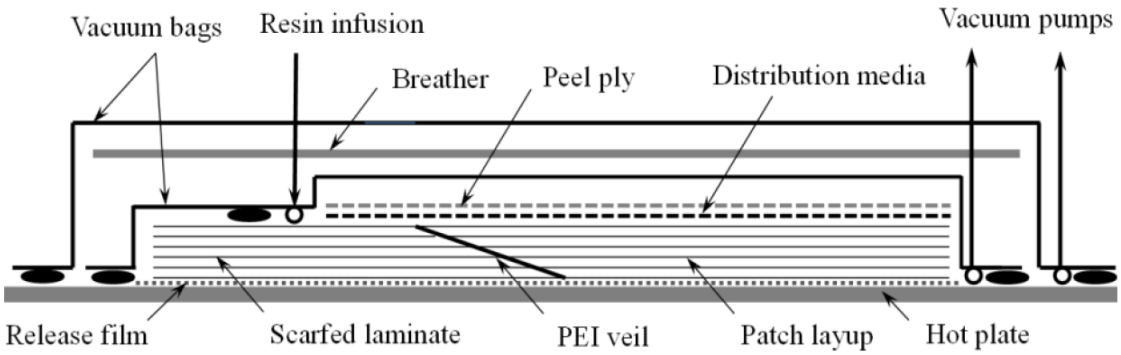

Figure 46. Schematic of VARTM setup used to repair tapered plate [115].

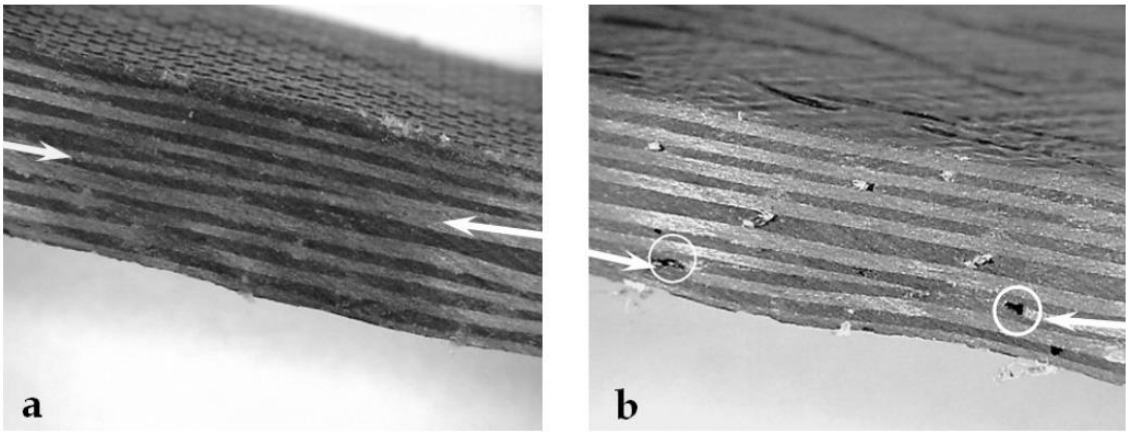

Figure 47. Cross-sectional views of: a) the secondary bonded joint with no visible bond line voids and b) the co-bonded joint with some bond line voids [115].

2.15 DIC

DIC uses stereo imaging to track an area of a sample at different stages of deformation. In DIC, a stochastic pattern is applied to the sample area of interest and pixels are tracked to measure surface strain (Figure 48). Aramis is a commonly used DIC software that is used for both data acquisition and processing [61, 112, 113]. Instructions for using Aramis are included in appendices A, B, and C. One measurement of surface strain that is commonly used to compare experimental DIC results with simulated FEA

results is logarithmic strain, which can be used to produce contour maps and stress-strain curves. Logarithmic strain accounts for strain history and is useful in calculating strain in small increments [117]. Logarithmic strain is defined as:

$$\epsilon^L = \sum_{i=1}^{3} \ln \lambda_i \boldsymbol{n_i} \boldsymbol{n_i}^T \tag{13}$$

where $\boldsymbol{\lambda_i}$ are the principal stretches and $\boldsymbol{n_i}$ are the principal stretch directions [118].

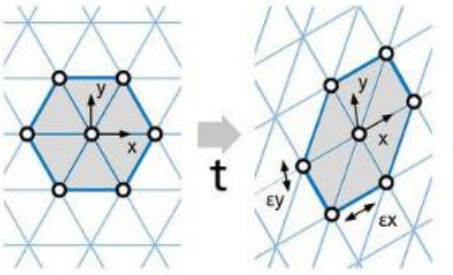

Figure 48. Strain calculation based on changes in point location.

2.16 FEA

Finite element analysis (FEA) is a numerical method used to determine the distribution of one or more dependent variables. FEA is versatile, with applications ranging from heat transfer to magnetic fields. FEA's versatility is amplified by having no geometric, boundary condition, or material property restrictions. FEA is used to solve constitutive models, which are mathematical frameworks that describe material behavior [119]. The distribution of stresses and strains in a material can thus be determined using FEA. Beyond analyzing a single material, FEA can be used to analyze the results of joint tests and, by providing detailed information on stress and strain states within substrates

and the bond, can be used to improve the interpretation of results [120]. Abaqus is a commercial FEA software used to find finite element solutions [121]. FEA modeling in Abaqus involves preprocessing, analysis, and postprocessing. The preprocessing steps include drawing part geometries, creating materials, assigning sections, assembling the sections, creating a step, assigning boundary conditions, meshing the assembly, and requesting outputs. The analysis consists of creating a job and running the model. Postprocessing includes visualizing and plotting the requested outputs from preprocessing. Cook et al (2002) can be referenced for more information on concepts and applications of FEA [122].

2.16.1 Composite Material Definition Options

In a finite element model, materials can either be created using the material module in Abaqus alone using the built-in options for constitutive responses or by using a UMAT subroutine that manually defines the constitutive response of the material. UMAT subroutines function in conjunction with the material module in Abaqus. More details on running UMAT subroutines in Abaqus are included in Appendix E. The built-in option for the constitutive response of a composite in Abaqus requires the engineering constants E_1, E_2, E_3, υ_{12}, υ_{12}, υ_{13}, υ_{23}, G_{12}, G_{13}, G_{23} and the constitutive matrix in Equation 14 from [57] is computed:

$$\begin{pmatrix}\sigma_{11}\\ \sigma_{22}\\ \sigma_{33}\\ \sigma_{23}\\ \sigma_{31}\\ \sigma_{12}\end{pmatrix} = \begin{bmatrix} \frac{1-\nu_{23}\nu_{32}}{E_2E_3\Delta} & \frac{\nu_{21}+\nu_{31}\nu_{23}}{E_2E_3\Delta} & \frac{\nu_{31}+\nu_{21}\nu_{32}}{E_2E_3\Delta} & 0 & 0 & 0 \\ \frac{\nu_{12}+\nu_{13}\nu_{32}}{E_3E_1\Delta} & \frac{1-\nu_{31}\nu_{13}}{E_3E_1\Delta} & \frac{\nu_{32}+\nu_{31}\nu_{12}}{E_3E_1\Delta} & 0 & 0 & 0 \\ \frac{\nu_{13}+\nu_{12}\nu_{23}}{E_1E_2\Delta} & \frac{\nu_{23}+\nu_{13}\nu_{21}}{E_1E_2\Delta} & \frac{1-\nu_{12}\nu_{21}}{E_1E_2\Delta} & 0 & 0 & 0 \\ 0 & 0 & 0 & 2G_{21} & 0 & 0 \\ 0 & 0 & 0 & 0 & 2G_{13} & 0 \\ 0 & 0 & 0 & 0 & 0 & 2G_{23} \end{bmatrix} \begin{pmatrix}\varepsilon_{11}\\ \varepsilon_{22}\\ \varepsilon_{33}\\ \varepsilon_{23}\\ \varepsilon_{31}\\ \varepsilon_{12}\end{pmatrix} \quad (14)$$

where

$$\Delta = \frac{1 - \nu_{12}\nu_{21} - \nu_{23}\nu_{32} - \nu_{31}\nu_{13} - 2\nu_{12}\nu_{23}\nu_{31}}{E_1 E_2 E_3}$$

The built-in option computes the stress in the material throughout the simulation but does not indicate when and where fiber and matrix damage occur. Composite structures can accumulate damage before structural collapse, which motivates using progressive damage modeling [123]. Progressive damage modeling can be used to predict the initiation and evolution of damage within a structure [124]. Typical progressive damage analyses include nonlinear analysis of establishing equilibrium, a stress calculation procedure, failure criteria, material degradation and damage evolution law, and re-establishing equilibrium with degraded composite material properties [123]. Failure criteria are curve fits of experimental data that are used to predict failure under multiaxial stress based on experimental data obtained under uniaxial stress [121].

2.16.2 The Cohesive Zone Method (CZM)

One finite element method that is commonly used to analyze joint tests is CZM. CZM in Abaqus begins during preprocessing when an adhesive is drawn as a thin rectangular part. A material with CZM properties and a section are created. The CZM material is assigned to the section, and the section is assigned to the thin rectangular part. During section assembly, the part is aligned with the adherends. During meshing, CZM geometry is discretized into elements [125]. The tops and bottom surfaces of a cohesive element are initially collapsed upon themselves (Figure 49). As a result, the nodes from

the top and bottom surfaces are superimposed, but retain independent degrees of freedom [126].

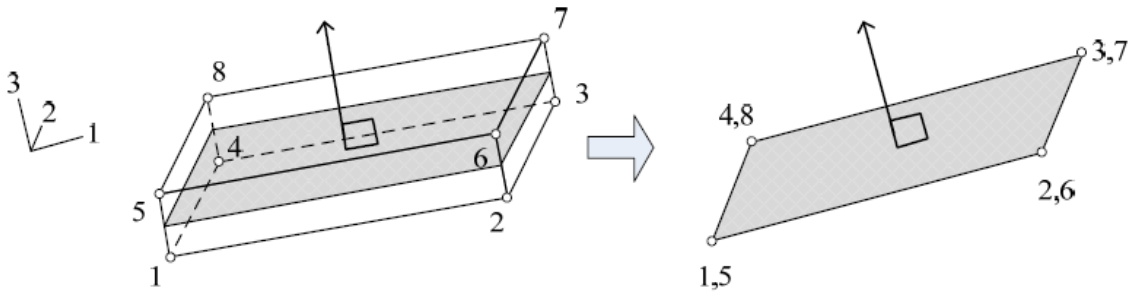

Figure 49. Collapsed cohesive element geometry at a bonded interface [126].

As the model executes, the separation of the paired nodes is described by a traction-separation relation. Traction-separation relations are commonly triangular, linear-exponential, or trapezoidal, but the triangular, or bilinear, separation relation will be described [127]. The four parts of a CZM bilinear traction-separation relation are illustrated in Figure 50 and described by Peterson (2013) as follows:

1. An initial, undamaged (linear elastic) constitutive behavior (path a-b-c');
2. Damage initiation (point b), representing the interfacial strength;
3. Damage evolution (path b-c), representing the process of material degradation;
4. Choice of element deletion upon complete material degradation (point c) [126].

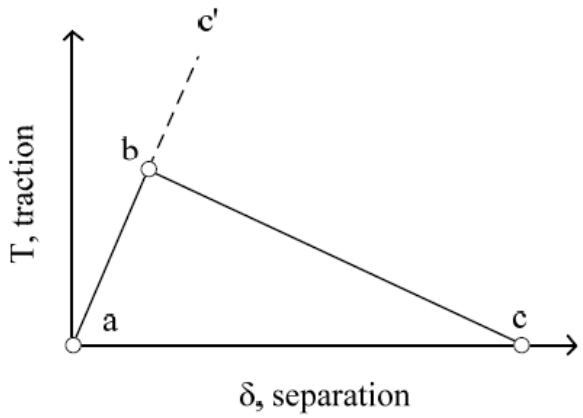

Figure 50. The CZM bilinear traction-separation relation [126].

The tractions σ_i from Figure 50 are described by:

$$\sigma_i = K_i \delta_i \tag{15}$$

where i = I, II, and III denote the three modes of crack propagation, δ_i are the separations between the opposite faces of the CZM element, and

$$K_i = (1 - D_i) K_i' \tag{16}$$

where D_i are the damage variables and K_i' are the stiffness values of the undamaged material at the interface. The damage variables satisfy the following conditions:

- D = 0 up to damage onset, which is during path a-b in Figure 50.
- 0 < D < 1 during degradation of the interface material, which is during path b-c in Figure 50.
- D = 1 at fracture, which is at point c in Figure 50. At fracture, there is neither remaining stiffness for the interface material nor cohesive connection between the two faces of the CZM element. Stress transfer capacity is no longer provided by the interface.

Damage initiation for single mode will be considered followed by damage initiation for mixed mode. The single mode case is used when one of modes I, II or II are active, while the mixed mode case is used when two or more of the modes are active. In the case of a single mode deformation at an interface, damage initiates when

$$\sigma_i = \sigma_i^0 \tag{17}$$

and the separation at damage is

$$\delta_i = \frac{\sigma_i^0}{\widetilde{K}_\iota} \tag{18}$$

where $\widetilde{K}_\iota$ are the stiffness values of the undamaged material at the interface. Since the total loss of stiffness does not take place until point c, the CZM is correlated with G_c (Equation 9) such that the separation at fracture δ_i^c can be calculated as:

$$\delta_i^c = \frac{2\,G_{ic}}{\sigma_i^0} \tag{19}$$

Barbero (2013) can be referenced for further derivation of the damage variables [121]. The damage variables can be described as:

$$D_i = \frac{\delta_i^c(\delta_i - \delta_i^0)}{\delta_i(\delta_i^c - \delta_c^i)} \tag{20}$$

D_i are eigenvalues of the damage tensor $\vec{D}$, which represents the damage history of orthotropic fiber-reinforced composite materials.

$$\vec{D} = D_i\delta_{ij} \tag{21}$$

where δ_{ij} is the Kronecker delta [121].

In the case of a mixed mode deformation at an interface, interface separation, damage initiation, the crack propagation criterion, and the damage variables are amended. The interface separation δ_m is:

$$\delta_m = \sqrt{\sum_{i=1}^{M} \delta_i^2} \tag{22}$$

where M is the number of modes involved. The single mode damage initiation criterion (Equation 17) is replaced by a quadratic stress criterion (Equation 27) to calculate the mixed mode separation δ_m^0 at damage onset under mixed mode loading.

$$\sum_{i=1}^{M} \left(\frac{\sigma_{\mathrm{i}}}{\sigma_i^0} \right)^2 = 1 \tag{23}$$

Two mixed mode crack propagation criteria that can be used to replace the single mode criterion in Equation 10 are the power criterion (Equation 24) and the Benzeggagh-Kenane (B-K) criterion. The power criterion is:

$$\sum_{i=1}^{M} \left(\frac{G_{\mathrm{i}}}{G_{\mathrm{ic}}} \right)^{\alpha_{\mathrm{i}}} = 1 \tag{24}$$

where the power law exponent α_{i} is typically assumed to be the same for all modes and set as $\alpha = 2$ [121]. The B-K criterion is:

$$G_c = G_{Ic} + (G_{IIc} - G_{Ic}) \left(\frac{G_{II}}{G_T} \right)^{\eta} \tag{25}$$

where $G_T = G_I + G_{II}$ and η is the exponent that considers the ductility of the resin used. The exponent $\eta = 1.81$ for brittle resins while $\eta = 2.28$ for ductile resins [128]. The damage variable for mixed mode conditions D_m is:

$$D_m = \frac{\delta_m^c(\delta_m - \delta_m^0)}{\delta_m(\delta_m^c - \delta_m^0)} \tag{26}$$

Moreover, CZM can be employed to study the fracture characteristics of composite joints. For mixed mode CZM modeling in Abaqus, the Quads damage criterion in Equation 23 is described using the following notation:

$$\left\{\frac{\langle t_n \rangle}{t_n^0}\right\}^2 + \left\{\frac{t_s}{t_s^0}\right\}^2 + \left\{\frac{t_t}{t_t^0}\right\}^2 = 1 \tag{27}$$

where t_n, t_s, and t_t are stresses in the normal, first, and second directions, respectively, and t_n^0, t_s^0, and t_t^0 are the nominal stress values in the normal, first, and second directions, respectively. Nominal stress is the applied load divided by the original cross-section of a material. True stress is the applied load divided by the actual cross-sectional area of the specimen at that load, where the cross-sectional area changes with respect to time. Traction-separation cohesive elements use nominal stress and strain measures, while conventional cohesive zone materials use true stress and strain measures. The Macaulay angle brackets ⟨ ⟩ signify that a pure compressive deformation or stress state does not initiate damage [118]. G_{ic} values for the power law in (24 are termed fracture energies in the normal, shear first direction, and shear second directions. When defining a cohesive material, elastic material behavior with Traction type is used. The data entered for the material are E/Enn, G1/Ess, and G2/Ett. The values E, G1, and G2 are the modulus of the adhesive, the mode I fracture toughness value, and the mode II fracture toughness value. Enn, Ess, and Ett are all equal to the thickness of the cohesive element.

2.17 Microscopy and Spectroscopy

Microscopy visualizes object features not detectable by eye, and microscope resolution is dependent on light source wavelength. The human eye on its own can see down to 100 µm. Optical microscope resolutions range from 100 nm – 1 mm and electron microscope resolutions range from 0.1 nm to 10 µm. A field emission scanning electron microscope (FE SEM) uses field emission to observe specimens down to the nanometer scale. Field emission happens when an extremely strong electric field is applied to the surface of a solid. The electric field results in a transformation of the potential threshold into a potential low barrier that is narrow enough to allow for electron tunneling. Electron tunneling occurs when electrons can phase through a potential barrier and leave the solid without a loss of energy [129]. The FE SEM uses the focused beam of the electrons produced by quantum mechanical tunneling to scan a specimen in a zig zag pattern. During testing, a specimen is placed in a vacuum and requires a coating if non-conductive [130].

Spectroscopy is used to study the interaction between matter and electromagnetic radiation. Light or radiant energy interacts with matter differently based on light frequency and matter properties. EDS is a chemical microanalysis technique that is typically performed in conjunction with an SEM. In an SEM, a highly focused, high-energy electron beam is used to penetrate a sample. X-rays are generated from the atoms in the electron beam's path. An EDS system detects and measures the energies of the X-rays are to characterize the chemical elements from where the X-rays were emitted. The emitted X-rays from the sample are used to characterize the elemental composition of the

area of interest on the sample. The rate of detection of the characteristic X-rays can be used to measure the amounts of elements present. An EDS system only provides information about the chemical elements present in the sample and does not specify the molecular structure [131].

2.18 Experimental and Simulation Testing Methods for Scarf Tension Testing

Experimental and simulation testing methods that can be used in scarf tension testing were reviewed. Experimental methods include SEM and DIC, while simulation methods include using FEA. Kumar et al (2006), Wales et al (2014), Sun et al (2018), and Swadener, Liechti, and Liang (2002) all used SEM to characterize failure modes [110–112, 125]. Those that compared DIC with FEA results include Sun et al (2018) and Ibitoye (2018) [61, 112]. Sun et al (2018) investigated the effects of adherend thickness and adherend material types on the fracture behavior of single lap adhesive joints. To visually characterize the fracture processes, an Aramis DIC system was used to capture real time full-field surface strain of the adherends and the strain distributions and evolutions along bond lines. In addition, SEM analysis was used to characterize failure modes. Besides failure modes, experimental outputs included force-displacement curves and strain contours of the adherends at peak load [116]. Ibitoye (2018) compared experimental and simulated results of different repair method types used on composite laminates and sandwich beams. Virtual extensometers were used in DIC and Abaqus to calculate strain. To use a virtual extensometer in DIC, two points are selected on a frame. The points are tracked, and strains are calculated in Aramis. In Abaqus, nodes on the

model are selected and outputs are created using the nodes to calculate strains. Similar locations are selected on the experimental and simulated test specimens [57].

In addition to the papers that compared DIC results with FEA results, supplementary papers were reviewed that used CZM to examine the failure of adhesive joints. The papers that were reviewed include Swadener, Liechti, and Liang (2002), Liao, Huang, and Sawa (2013), Ridha, Tan, and Tay (2011), and Campilho et al (2008) [123–126]. Swadener, Liechti, and Liang (2002) did numerical and experimental mixed-mode studies on composites bonded with two different adhesives. A cohesive zone model with a traction-separation relation to simulate the debonding process of the mixed-mode fracture experiments. Outputs included experimental and finite element load-displacement curves [132]. Liao, Huang, and Sawa (2013) examined the effects of adhesive thickness, adhesive type, and scarf angle on the mechanical properties of scarf adhesive joints subjected to uniaxial tensile loading using a mixed-mode CZM with a bilinear shape to govern the interface separation [133]. Ridha, Tan, and Tay (2011) presented an example of how CZM is influenced by crack evolution in a parametric study that concluded that the failure stress of a repaired composite panel is more sensitive to the strength of the cohesive elements than to its toughness when a linear or trapezoidal softening traction-separation law is used. However, the influence of adhesive strength was significant when exponential softening traction-separation law is used [134]. Lastly, Campilho et al (2008) presented numerical study concerning the tensile behavior of CFRP scarf repairs with varied scarf angles. To account for the ductile behavior of the adhesive used, a cohesive mixed-mode damage model including the adhesive plastic

region was used to simulate the adhesive layer. Validation of the model with the experiments was accomplished in terms of repair initial stiffness, maximum load and the corresponding displacement, and failure modes [135].

2.19 Literature Review Discussion

The benefits of developing more informed and straightforward wind turbine field repair surface preparation procedures are primarily cost-driven but can also improve safety for wind turbine blade repair technicians. To fully understand the impacts of developing more informed and straightforward repair procedures, damage classification criteria require further development and repair cost data merits collection. Repair cost data along with more informed and straightforward repair procedures can be used to identify inefficiencies, which will allow both wind energy providers and consumers to make more informed financial decisions.

Cost benefits include lowering OpEx, where the main factors affected are the costs of downtime, equipment, and labor. Downtime costs can be reduced with clear repair procedures because extra time from procedure uncertainty would be eliminated. In addition, downtime costs can be reduced if repairs are more durable and the need to repair the same area repeatedly is diminished. The durability of field repairs is currently unknown and requires further investigation. Equipment costs would be reduced because clear repair procedures would also include the equipment necessary to perform the repair, which would ensure that all materials necessary are prepared and used appropriately. Labor costs would be lowered as more straightforward repairs will increase automation.

Klise (2021) lead the development of the Assessment Robot or Resilient Optimized Wind Energy (ARROW$^{(e)}$) Non Destructive Inspection (NDI) robotic crawler system. The ARROW$^{(e)}$ crawler employs advanced inspection technology to find damage on blades to evaluate optimal repair strategies [136]. Further innovations could eventually lead to the development of a robotic crawler that performs both wind turbine blade inspections and repairs. Understanding the effects of surface preparation methods on repair adhesion will streamline the development of a blade repair robot. The surface preparation methods developed in this work could be used to inform the hardware and programming necessary to create a repair robot. The shift to more automated repairs can increase technician safety, as a robotic crawler would eliminate the need for technicians to rappel from the nacelle down to the damaged area to repair a blade.

Developing a repair robot could eventually eliminate the need for technicians to rappel from nacelles to perform repairs. In the meantime, clear repair procedures can lower human error. Mentes and Turan (2019) used risk-based maintenance decisions to increase the reliability and safety of offshore wind turbines and minimize total expected life cycle costs. Methods of eliminating human errors in offshore wind turbine maintenance operations were described, where one method is to “get little things right,” which can make safer and resilient maintenance operations. Getting little things right includes making sure all of the appropriate tools, equipment, technical information, and maintenance guide are prepared [137]. Getting little things right could also increase the reliability and safety of land-based wind turbine blade maintenance operations. Wind turbine blade surface preparation testing can be used to inform which tools, equipment,

technical information, and maintenance guides, which could, in turn, increase safety and lower life cycle costs.

Dorworth, Gardiner, and Mellema (2009)'s steps for structural scarf repairs create a foundation for additional research into developing more informed surface preparation procedures [58]. Developing more informed surface preparation procedures begins with evaluating the effectiveness of currently used methods and is followed by identifying potential improvements. One currently used surface preparation method that merits further research is solvent wiping, particularly due to the discrepancies between Horton (1990), Petrie (2007), Sperling (2006), and Dorworth, Gardiner, and Mellema (2009) around its use [8, 63, 70, 77]. The review of solvent-polymer interaction had two key findings concerning how a solvent might interact with a thermoset's surface. First, a crosslinked polymer will gel when a thermodynamically compatible solvent is applied. Second, there are differences in polymer orientations at the surface than the interior. The combined effects of the solvent-polymer interactions and differences in polymer orientations on the polymer surfaces on composite surface properties and resulting bond strengths are unclear. The discrepancies in recommendations combined with the potential for surface gelation effects on bond strengths motivated the first research question: Does solvent wiping negatively affect the surface energy and resulting bond strength of a repair surface?

The purpose of using solvents is to remove contamination, but the effects of common contaminants on bond strengths have not been fully considered. Shang (2013) and Musaramthota, Pribanic, and McDaniel (2014) have demonstrated that hydraulic oil,

mold release, and silicone spray along a bond line will diminish bond strength [72, 73]. In addition, Amaro et al (2014)'s oil immersion tests demonstrated that hydraulic oil can diffuse into and affect the strengths of GFRP laminates [74]. Yet, the time-dependence of hydraulic oil contamination diffusion into a bond line has not been studied. While likely to be the most common contaminant type, no studies have examined the effects of composite dust on bond strength. The lack of time-dependence on hydraulic oil diffusion into a bondline combined with the absence of studies on composite dust effects motivated the following research questions: Can the bond line of a repair tolerate certain types of contaminants over others? Is contamination diffusion into a bond line time-dependent?

Examining solvent wipe and contamination effects on bond lines evaluates the effectiveness of currently used repair methods, but potential improvements could include using chemical or plasma treatments to increase the surface energy of a repair surface prior to patching. Chemical methods are common surface treatment methods and sizing are chemicals used to treat glass fibers to facilitate adhesion between fibers and an appropriate polymer matrix [9, 27]. There are two types of composite surface in composite repair experimentation methods: as-manufactured and repair surfaces. As-manufactured surfaces are those that were on either side of a laminate during VARTM manufacturing and have a thin layer of resin protecting the fibers. Repair surfaces are those that result from scarfing methods and have exposed fibers along surfaces. Repair surfaces do not have a thin layer of resin protecting the fibers. When damage is removed in a wind turbine blade repair, fibers are re-exposed and may no longer have sizing on them since the sizing has already prompted a chemical reaction between the glass fiber

and the matrix in the blade's original manufacturing. Fiber re-exposure when damage is removed in a composite repair is like how fiber re-exposure is shown in Figure 51. Exposed glass fibers have different surface energies and topologies than the surrounding matrix material. Although sizing is typically only applied to glass fibers to improve adhesion to polymer matrices, applying sizing to a repair surface with exposed fibers had not been considered prior to this work. Sizing was thus considered as a chemical treatment to improve adhesion properties. Although previous findings by Webster and Wightman (1990) and Liston, Martinu, and Wertheimer (1993) indicated that plasma treatment would improve epoxy surface adhesion properties, each new application of plasma processing requires that the process conditions be clearly identified and optimized [93, 98]. Optimal plasma treatment processes have yet to be identified for wind turbine field repairs. The potential for either sizing or plasma to improve repair surface adhesion properties such as surface energy motivated the last research question: Can using sizing or plasma treatments improve repairs?

Figure 51. Glass fiber reinforced epoxy composite surface after sanding with FEPA 1000 grit sandpaper and etched with hydrofluoric acid (HF). The HF was applied to highlight the fibers for visual observation.

The scarf tension test was identified by Duncan and Crocker (2001) as a mechanical test method that can be used to quantify the strengths of interfaces and to evaluate the effects of surface pre-treatments. However, few studies have used the scarf tension test to evaluate repair methods. The studies that have employed scarf tension testing for repairs have used the test for carbon fiber composite materials rather than for glass fiber composites. A benefit of the scarf tension test for the evaluation of repair surfaces as opposed to more conventional tests like lap shear, DCB, and ENF is that in a scarf tension test, the glass fibers are exposed in a manner like what might exist in a field repair scenario. DIC has been used by Sun et al (2018), Stroili (2019), and Ibitoye (2018) to compare experimental surface strains to Abaqus results but has not been used to compare DIC surface strains to Abaqus results for co-bonded GFRP scarf joint specimens

tested in tension. The development of scarf tension test methods and comparing results between DIC and FEA for GFRP repair surface preparation methods could be beneficial for evaluating the effects of surface treatments.

In defining differences between structural and non-structural damage, Nijssen and Manrique (2020) described AEP loss in terms of leading edge erosion. However, AEP loss from other forms of damage, such as structural damage, is not well-understood. In addition, it is unclear how the degradation in strength and/or stiffness of the blade would be measured to understand whether the blade is at the affected or critical thresholds. In addition to evaluating more realistic repair surfaces, the scarf tension test may also be used to measure the tensile strength and stiffness losses in scarfed composite laminates.

Altogether, the research questions that were formulated are:

1. Does solvent wiping negatively affect the surface energy of a repair surface?
2. Can the bond line of a repair tolerate certain types of contaminants over others? Is contamination diffusion into a bond line time-dependent?
3. Can solvent cleaning, chemical treatment, or plasma treatment improve repairs?

The research questions that were posed are based on the literature that was reviewed and are in accordance with the need to develop well-informed and straightforward wind turbine blade repair procedures. The research questions were answered by completing the three objectives that are outlined in Chapter 3: Objectives.

3. OBJECTIVES

The following three objectives are subdivided into tasks and organized into test matrices that delineate the testing used to answer the research questions. The test matrices include the chapter locations, testing types, the technical issues addressed, and the outputs. Each of the method sections of Chapters 4-11 include test include more detailed test matrices that include the number of samples tested, the parameters examined, and the properties obtained in each test. The composites used for all the experimental testing methods described each objective were manufactured using VARTM.

3.1 Objective 1: Identify differences in contact angles, bond strengths, and failure modes of specimens that have been solvent wiped with common solvents used for solvent wipe surface preparation.

The methods, results, and conclusions for the tasks described in Table 3 are in Chapters 3-6. Profilometry, contact angle, lap shear, and DCB methods, results and conclusions for solvent wipe testing are included in this work, but can also be found in Lusty et al (2020) [107].

Table 3. The test matrix that was used to complete Objective 1.

Chapter	Type of Testing	Technical Issue(s)	Output(s)
4	Profilometry	Surface roughness of each side of sample, effects of grit size on surface roughness, and sanding consistency.	Surface roughness averages.
5	Contact angle	Solvent wipe effects on composite surfaces.	Water contact angles.
6	Lap shear	Solvent wipe effects on bond strength.	Maximum lap shear stress values, failure modes.
6	DCB	Solvent wipe effects on mode I fracture toughness and failure modes.	Mode I fracture toughness values and failure modes.
6	ENF	Solvent wipe effects on mode II fracture toughness.	Mode II fracture toughness and failure modes.
6	Solvent-wiped resin	Isolation of resin samples for surface observations	Visual observations of the resin surfaces.

3.2 Objective 2: Measure the changes in bond strengths due to contamination from composite dust and hydraulic oil with time

The methods, results, and conclusions for the task described in Table 4 are in chapter 7.

Table 4. The test matrix that will be used to complete Objective 2.

Chapter	Type of Testing	Technical Issue(s)	Output
7	Lap Shear	Effects of composite dust and hydraulic oil with time.	Maximum lap shear stress values, failure modes

3.3 Objective 3: Increase and equalize the surface energy of repair surfaces using plasma or sizing.

The methods, results, and conclusions for the tasks described in Table 5 are in chapters 8-10. Contact angle testing methods, results, and conclusions for plasma testing are included in this work, but can also be found in Lusty et al (2020) [107].

Table 5. The test matrix that will be used to complete Objective 3.

Chapter	Type of Testing	Technical Issue(s)	Output
8	Contact angle	Flame and blown ion treatment effects on composite surfaces for repair applications.	Water contact angle
9	Scarf tension with DIC	Effects of applying sizing to a tapered surface.	Force-displacement curves, strain contour plots, stress-strain curves, failure modes
9	FE SEM	Failure surface differences of specimens with and without sizing applied to surfaces.	Failure modes
9	EDS	Remains of sizing on the surface after testing.	Spectra and weight percents of elements
10	Scarf tension with FEA using CZM	Compare with experimental results.	Force-displacement curves, strain contour plots, stress-strain curves

4. PROFILOMETRY

4.1 Profilometry Methods

A Mitutoyo SJ-201 profilometer was used to examine differences in R_a values of epoxy and viny ester composites after manufacturing and after sanding. The sanding grits that were used were Federation of European Producers of Abrasives (FEPA) 320 and 1000. The 320 grit sandpaper was used in solvent wipe and contamination lap shear tests and the 1000 grit sandpaper was used in solvent wipe contact angle tests. Composite plates that are manufactured using VARTM result in a rough surface on one face and a smooth surface on the other. A rough surface results when a layup is in contact with peel ply, while a smooth surface is one that results when a layup is in contact with the caul plate. The type of peel ply used was polyester. The type of mold release used was Loctite Frekote 770-NC. The resulting rough and smooth surfaces from manufacturing are termed the rough and smooth sides in Tables 6 and 7. The smooth sides were sanded using a sanding table using either 320 or 1000 grit sandpaper, which removed mold release from samples. The test matrix used for profilometry testing is in Table 6 and results are in Table 7.

Table 6. Profilometry test matrix.

GFRP Composite Type	Surface Type	Number of Tests	Output
$[0]_4$ epoxy	unsanded smooth side	2	R_a
	unsanded rough side	2	R_a
	320 grit sanded smooth side	2	R_a
	1000 grit sanded smooth side	2	R_a
$[+/- 45]_6$ epoxy	unsanded smooth side	2	R_a
	unsanded rough side	2	R_a
	320 grit sanded smooth side	2	R_a
	1000 grit sanded smooth side	2	R_a
$[0]_4$ vinyl ester	unsanded smooth side	2	R_a
	unsanded rough side	2	R_a
	320 grit sanded smooth side	2	R_a
	1000 grit sanded smooth side	2	R_a
$[+/- 45]_6$ vinyl ester	unsanded smooth side	2	R_a
	unsanded rough side	2	R_a
	320 grit sanded smooth side	2	R_a
	1000 grit sanded smooth side	2	R_a

4.2 Profilometry Results

Table 7. Average surface roughness (μm) and standard deviations of specimens subjected to several surface treatments. Two measurements were made for each tabulated value.

GFRP Composite Type	Unsanded smooth side	Unsanded Rough Side	320 Grit Sanded Smooth Side	1000 Grit Sanded Smooth Side
$[0]_4$ Epoxy	0.460 ± 0.089	7.407 ± 0.483	0.818 ± 0.030	0.417 ± 0.168
$[+/- 45]_6$ Epoxy	0.353 ± 0.033	8.814 ± 1.173	0.815 ± 0.069	0.259 ± 0.069
$[0]_4$ Vinyl Ester	0.927 ± 0.292	9.058 ± 1.168	0.610 ± 0.229	0.335 ± 0.102
$[+/-45]_6$ Vinyl Ester	0.475 ± 0.003	8.735 ± 2.690	0.815 ± 0.107	0.191 ± 0.020

4.3 Profilometry Conclusions

Samples that were sanded with 320 grit sandpaper had higher R_a values than samples sanded with 1000 grit sandpaper. The rough side had the highest R_a values.

Standard deviations remained about the same between sanded and unsanded smooth-sided samples.

5. SOLVENT WIPE CONTACT ANGLE TESTING

5.1 Solvent Wipe Contact Angle Methods

For solvent wipe contact angle testing, glass and vinyl ester composite samples were first wet sanded using 1000 grit sandpaper, then wiped with a dry cloth to remove water. Wypall X60 cloths were used for solvent wiping. Wypall X60 cloths have low lint content and lack of adhesive binders, both features that will decrease the likelihood leaving of contamination and residues on a surface when used. After sanding, the water break test was used to ensure mold release was removed from composite surfaces. Next, the samples were wiped with another cloth that had been saturated with either distilled water, reagent-grade ISP, acetone, MIBK, or MEK. Then, samples were wiped with a dry cloth. Six contact angle tests were conducted for each sample in the locations illustrated in Figure 52. To ensure more surface regularity, the smooth sides of laminates were used for all contact angle and lap shear testing.

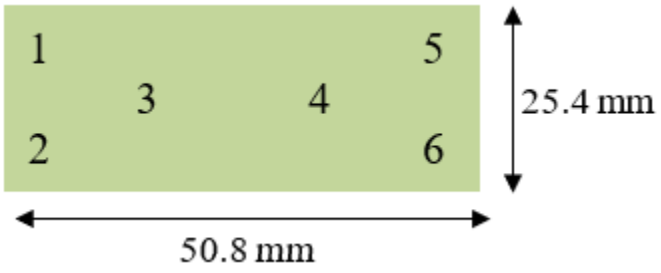

Figure 52. The six locations of contact angle test droplets on a 25.4 x 50.8 mm^2 composite surface.

Specimens were contact angle tested immediately after solvent wiping. The contact angle testing of a sample began by forming a 1 μL droplet of MilliQ 0.2 μm water at the tip of the needle. Then, the sample was slowly brought up to the droplet. Once the droplet contacted the surface, the substrate was lowered. The contact angle decreases linearly with time after a water droplet is placed on a surface. Conclusions from preliminary testing demonstrated that water droplets would stabilize, but not completely evaporate, after approximately 10 seconds. Thus, after the droplet was on a sample's surface for 10 seconds, an image was captured using VCA Optima software. Contact angles were also measured using VCA Optima. The test matrix used in solvent wipe contact angle testing is in Table 8.

Table 8. Solvent wipe contact angle test matrix.

Composite Type	Solvent Wipe Method Used	Number of Tests	Output
$[0]_4$ epoxy	unprepared	6	contact angle
	dry wipe	6	contact angle
	distilled water	6	contact angle
	ISP	6	contact angle
	acetone	6	contact angle
	MIBK	6	contact angle
	MEK	6	contact angle
$[+/- 45]_6$ epoxy	unprepared	6	contact angle
	dry wipe	6	contact angle
	distilled water	6	contact angle
	ISP	6	contact angle
	acetone	6	contact angle
	MIBK	6	contact angle
	MEK	6	contact angle
$[0]_4$ vinyl ester	unprepared	6	contact angle
	dry wipe	6	contact angle
	distilled water	6	contact angle
	ISP	6	contact angle
	acetone	6	contact angle
	MIBK	6	contact angle
	MEK	6	contact angle
$[+/- 45]_6$ vinyl ester	unprepared	6	contact angle
	dry wipe	6	contact angle
	distilled water	6	contact angle
	ISP	6	contact angle
	acetone	6	contact angle
	MIBK	6	contact angle
	MEK	6	contact angle

5.2 Solvent Wipe Contact Angle Results

Results for contact angle testing after wiping with solvents are summarized in Table 9. The *unprepared* samples were neither sanded nor solvent wiped, and still had

mold release on these surfaces. The *dry wipe* samples were wet sanded and wiped with dry cloths before contact angle testing.

Table 9. Average contact angle (degrees) for each surface treatment.

Treatment	$[0]_4$ Epoxy	$[+/- 45]_6$ Epoxy	$[0]_4$ Vinyl Ester	$[+/- 45]_6$ Vinyl Ester
Unprepared	87.7 ± 3.5	73.4 ± 5.0	87.8 ± 9.6	70.6 ± 12.8
Dry Wipe	64.3 ± 5.4	66.8 ± 9.7	67.1 ± 6.8	67.6 ± 6.3
Distilled Water	56.5 ± 5.9	79.0 ± 2.1	59.5 ± 9.9	82.1 ± 5.6
ISP	59.4 ± 5.4	70.2 ± 6.4	65.0 ± 9.1	72.0 ± 6.7
Acetone	54.5 ± 7.2	73.0 ± 2.6	67.3 ± 9.4	68.1 ± 3.7
MIBK	62.3 ± 6.1	58.7 ± 6.4	61.1 ± 5.2	71.8 ± 3.7
MEK	62.4 ± 7.3	65.5 ± 8.5	60.9 ± 8.9	68.3 ± 5.8

5.3 Solvent Wipe Contact Angle Conclusions

Student's t-tests were used to compare results from each solvent wipe method and the dry wipe treatment. The t-tests indicated statistically significantly lower contact angles for dry wipe specimens when compared with the unprepared specimens for each substrate type. The value $\alpha=0.05$ was used as the threshold for statistical significance and will be used for the remainder of the t-tests in this work. The drop in contact angles occurred because mold release was removed when specimens were sanded. T-tests between each solvent wipe method and dry wipe treatments indicated statistically significantly lower contact angles for distilled water-wiped $[0]_4$ epoxy and $[0]_4$ vinyl ester specimens, ISP- and Acetone- wiped $[0]_4$ epoxy, MIBK-wiped $[+/- 45]_6$ epoxy, and MIBK-wiped $[0]_4$ vinyl ester specimens. In addition, contact angles were significantly higher for distilled water-wiped $[+/- 45]_6$ epoxy and $[+/- 45]_6$ vinyl ester specimens. The

statistically significant drops among solvent-wipe methods could be attributed to the variations in fiber exposure rather than from increases in surface energy from the treatments. The high standard deviations in contact angle results may also be attributed to the variations in fiber exposure.

6. SOLVENT WIPE MECHANICAL TESTING

6.1 Solvent Wipe Mechanical Testing Methods

The solvent wipe mechanical test methods used were lap shear, DCB, and ENF. Although not a method found in the literature, resin samples were also tested by wiping the resins with solvents and performing observations using visual and optical microscopy methods. Composite coupons with dimensions 25 x 400 mm^2 were used for lap shear, DCB, and ENF tests. The *smooth* sides of substrates were hand sanded using 320 grit sandpaper. Then, the solvent wipe methods used in contact angle testing were used on both coupons prior to being secondary bonded with either Huntsman Araldite 2051 or Loctite EA 9396 Aero adhesives. Huntsman Araldite 2051 is a two component, toughened methyl methacrylate (MMA) general purpose adhesive that cures after 15 minutes at room temperature. No post-cure was used for the specimens adhered with the MMA adhesive. Loctite EA 9396 Aero is a two-component epoxy adhesive with low viscosity at room temperature. The specimens that were manufactured using the epoxy adhesive were post-cured at 66°C for one hour.

6.1.1 Solvent Wipe Lap Shear Testing Methods

Lap shear tests were used to compare the effects of solvent wipe techniques on the resulting maximum lap shear stress values and failure modes. For lap shear specimen fabrication, wires with 0.33 mm diameters were used as spacers and weights were used to reduce variation in adhesive thicknesses. The $[+/- 45]_6$ laminates were tested at 0.5 in/min

load rate to minimize creep, and $[0]_4$ laminates were tested at 0.05 in/min load rate [109]. No significant differences in maximum lap shear stress values were found between the two load rates. The specimen geometry used in lap shear testing is in Figure 53. The MMA adhesive was used to adhere tabs onto the lap shear specimens that were adhered with the MMA adhesive. The epoxy adhesive was used to adhere tabs onto the lap shear specimens that were adhered with the epoxy adhesive. The test matrix used for solvent wipe lap shear testing is in Table 10.

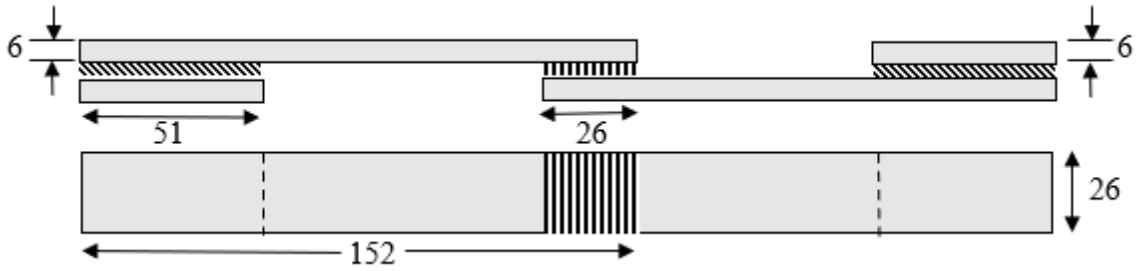

Figure 53. Lap shear specimen geometry.

Table 10. Solvent wipe lap shear test matrix.

Adhesive Type	Substrate Type	Treatment	Number of Tests	Outputs
MMA	$[0]_4$ epoxy	sanded	5	maximum lap shear stress, failure modes
		ISP	5	maximum lap shear stress, failure modes
		acetone	5	maximum lap shear stress, failure modes
		MIBK	5	maximum lap shear stress, failure modes
		MEK	5	maximum lap shear stress, failure modes
	$[+/- 45]_6$ epoxy	sanded	5	maximum lap shear stress, failure modes

		ISP	5	maximum lap shear stress, failure modes
		acetone	5	maximum lap shear stress, failure modes
		MIBK	5	maximum lap shear stress, failure modes
		MEK	5	maximum lap shear stress, failure modes
	$[0]_4$ vinyl ester	sanded	5	maximum lap shear stress, failure modes
		ISP	5	maximum lap shear stress, failure modes
		acetone	5	maximum lap shear stress, failure modes
		MIBK	5	maximum lap shear stress, failure modes
		MEK	5	maximum lap shear stress, failure modes
	$[+/- 45]_6$ vinyl ester	sanded	5	maximum lap shear stress, failure modes
		ISP	5	maximum lap shear stress, failure modes
		acetone	5	maximum lap shear stress, failure modes
		MIBK	5	maximum lap shear stress, failure modes
		MEK	5	maximum lap shear stress, failure modes
epoxy	$[0]_4$ epoxy	sanded	5	maximum lap shear stress, failure modes
		ISP	5	maximum lap shear stress, failure modes
		acetone	5	maximum lap shear stress, failure modes
		MIBK	5	maximum lap shear stress, failure modes
		MEK	5	maximum lap shear stress, failure modes
	$[+/- 45]_6$ epoxy	sanded	5	maximum lap shear stress, failure modes
		ISP	5	maximum lap shear stress, failure modes

		acetone	5	maximum lap shear stress, failure modes
		MIBK	5	maximum lap shear stress, failure modes
		MEK	5	maximum lap shear stress, failure modes
	$[0]_4$ vinyl ester	sanded	5	maximum lap shear stress, failure modes
		ISP	5	maximum lap shear stress, failure modes
		acetone	5	maximum lap shear stress, failure modes
		MIBK	5	maximum lap shear stress, failure modes
		MEK	5	maximum lap shear stress, failure modes
	$[+/- 45]_6$ vinyl ester	sanded	5	maximum lap shear stress, failure modes
		ISP	5	maximum lap shear stress, failure modes
		acetone	5	maximum lap shear stress, failure modes
		MIBK	5	maximum lap shear stress, failure modes
		MEK	5	maximum lap shear stress, failure modes

6.2.2 Solvent Wipe DCB Testing Methods

Teflon films were used as starter cracks and were placed at one end of each of the DCB specimens (Figure 54). Unlike for lap shear specimen preparation, wire spacers were not used for DCB specimen preparation. Instead, binder clips were used to secure coupons together while adhesives cured. After adhesives were cured, all edges of each specimen were trimmed and polished. Polishing is necessary for measuring the initial crack lengths. Aluminum tabs were adhered to specimens using Plexus MA310 methacrylate adhesive. Jigs were used to maintain the alignment of the tabs with the pins

that were used for testing. DCB specimens were tested in tension at a loading rate of 0.3 mm/sec. Load and displacement data was acquired using HP Logger software. Equation 11 was used to calculate G_{IC}, where E_{11} = 40270 MPa and E_{22} = 125 MPa. E_{11} and E_{22} values were measured using the tension testing methods described in [111]. P was found using the 5% rule. The test matrix used for DCB testing is in Table 11.

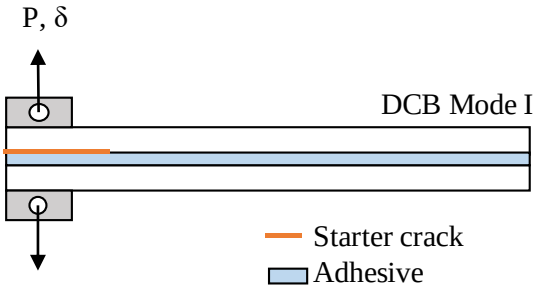

Figure 54. The DCB testing configuration.

Table 11. The test matrix used for DCB testing.

Adhesive Type	Substrate Type	Treatment	Number of Tests	Outputs
MMA	$[0]_6$ epoxy	sanded	5	G_{IC}, failure modes
		ISP	5	G_{IC}, failure modes
		acetone	5	G_{IC}, failure modes
		MIBK	5	G_{IC}, failure modes
		MEK	5	G_{IC}, failure modes
	$[0]_6$ vinyl ester	sanded	5	G_{IC}, failure modes
		ISP	5	G_{IC}, failure modes
		acetone	5	G_{IC}, failure modes
		MIBK	5	G_{IC}, failure modes
		MEK	5	G_{IC}, failure modes
epoxy	$[0]_6$ epoxy	sanded	5	G_{IC}, failure modes
		ISP	5	G_{IC}, failure modes
		acetone	5	G_{IC}, failure modes
		MIBK	5	G_{IC}, failure modes
		MEK	5	G_{IC}, failure modes
	$[0]_6$ vinyl ester	sanded	5	G_{IC}, failure modes
		ISP	5	G_{IC}, failure modes
		acetone	5	G_{IC}, failure modes
		MIBK	5	G_{IC}, failure modes
		MEK	5	G_{IC}, failure modes

6.1.3 Solvent Wipe ENF Testing Methods

Post-tested DCB specimens were used for the ENF tests. Each crack from the DCB specimen was manually propagated so that the crack tip ended between the loading nose and the left supporting roller (Figure 55). Having the crack tip between the two rollers mitigated local face sheet delamination from the loading nose. ENF specimens were tested in a three-point bending configuration at a loading rate of 0.3 mm/sec. Equation 12 was used to calculate G_{IIC}. A shear modulus of G_{13}=5050 MPa was used. The value of G_{13} was measured using Iosipescu notched-shear tests and DIC. For the strain calculations used to measure G_{13}, the surface component used was based on a facet

size of 25 and a point distance of 17 for the strain calculations in Aramis. A spatial average filter of 2 was used. After ENF testing, specimens were manually peeled apart and failure modes were visually characterized. The test matrix used for ENF testing is in Table 12.

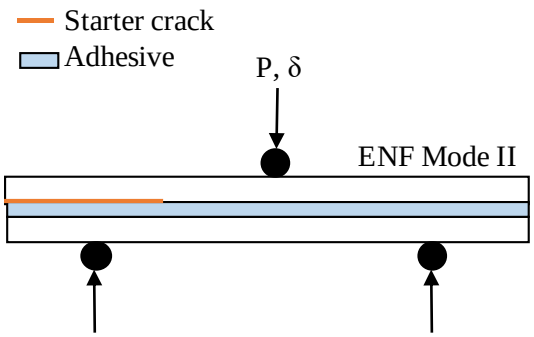

Figure 55. The ENF testing configuration.

Table 12. The test matrix used for ENF testing.

Adhesive Type	Substrate Type	Treatment	Number of Tests	Output
MMA	$[0]_6$ epoxy	sanded	5	G_{IIC}, failure modes
		ISP	5	G_{IIC}, failure modes
		acetone	5	G_{IIC}, failure modes
		MIBK	5	G_{IIC}, failure modes
		MEK	5	G_{IIC}, failure modes
	$[0]_6$ vinyl ester	sanded	5	G_{IIC}, failure modes
		ISP	5	G_{IIC}, failure modes
		acetone	5	G_{IIC}, failure modes
		MIBK	5	G_{IIC}, failure modes
		MEK	5	G_{IIC}, failure modes
epoxy	$[0]_6$ epoxy	sanded	5	G_{IIC}, failure modes
		ISP	5	G_{IIC}, failure modes
		acetone	5	G_{IIC}, failure modes
		MIBK	5	G_{IIC}, failure modes
		MEK	5	G_{IIC}, failure modes
	$[0]_6$ vinyl ester	sanded	5	G_{IIC}, failure modes
		ISP	5	G_{IIC}, failure modes
		acetone	5	G_{IIC}, failure modes
		MIBK	5	G_{IIC}, failure modes
		MEK	5	G_{IIC}, failure modes

6.1.4 Solvent-Wiped Resin Methods

For solvent-wiped resin experimentation, epoxy and vinyl ester resins were manufactured by pouring liquid resin onto mold release-treated aluminum pie pans, then cured at room temperature for 48 hours. Resins were post-cured for 12 hours at 80°C. Unlike the composite specimens used in solvent wipe lap shear tests, VARTM was not used to manufacture resin samples. Cured resins were cut into 26 mm x 26 mm samples. The side of each resin sample that was not in contact with the pie pan was separately wiped with distilled water, ISP, Acetone, MIBK, and MEK and wiped again with a dry cloth. Visual observations and optical microscopy were used to observe the solvent-wiped resin samples. The test matrix used for solvent-wiped resin tests is in Table 13.

Table 13. The test matrix used for solvent-wiped resin tests.

Resin Type	Treatment	Number of Tests	Outputs
epoxy	none	1	visual observations
	ISP	1	visual observations
	acetone	1	visual observations
	MIBK	1	visual observations
	MEK	1	visual observations
vinyl ester	none	1	visual observations
	ISP	1	visual observations
	acetone	1	visual observations
	MIBK	1	visual observations
	MEK	1	visual observations

6.2 Results

6.2.1 Solvent Wipe Lap Shear Testing Results

Solvent wipe lap shear testing yielded maximum lap shear stress values and failure modes. The moduli of the $[0]_4$ and $[+/- 45]_6$ adherends were 39.4 and 13.3 GPa, respectively. Lap shear test results for the MMA adhesive are in Table 14, Table 15, Figure 56, and Figure 57. Lap shear test results for the epoxy adhesive are in Table 16, Table 17, and Figure 58.

Table 14. The average maximum lap shear stress (MPa) values for a 658 ± 19 sq. mm average bond area of the MMA adhesive.

Surface Treatment	$[0]_4$ Epoxy	$[+/- 45]_6$ Epoxy	$[0]_4$ Vinyl Ester	$[+/- 45]_6$ Vinyl Ester
Sanded	14.89 ± 0.77	6.89 ± 0.29	22.61 ± 1.56	7.69 ± 0.63
ISP	14.52 ± 0.55	7.31 ± 0.58	22.17 ± 1.45	6.57 ± 0.93
Acetone	13.67 ± 2.33	6.88 ± 0.78	22.80 ± 0.46	8.48 ± 0.48
MIBK	14.13 ± 1.38	6.99 ± 0.94	22.75 ± 1.65	7.96 ± 0.13
MEK	13.49 ± 2.14	6.83 ± 1.21	23.63 ± 0.86	8.07 ± 0.38

For the MMA adhesive, the $[0]_4$ vinyl ester specimens had higher maximum lap shear stress values than the $[0]_4$ epoxy specimens. The epoxy and vinyl ester $[+/- 45]_6$ specimens all had around the same maximum lap shear stress values. There were no significant differences in maximum lap shear stress values from different solvents.

Table 15. Average adhesive and adherend thicknesses and lap shear failure modes for lap shear specimens tested using the MMA adhesive.

Substrate	Adhesive thickness (mm)	Adherend thickness (mm)	Primary Failure Mode
$[0]_4$ Epoxy	0.49 ± 0.14	3.21 ± 0.07	Interfacial failure
$[+/- 45]_6$ Epoxy	0.46 ± 0.18	2.09 ± 0.06	Fiber-tear failure
$[0]_4$ Vinyl Ester	0.33 ± 0.15	3.12 ± 0.07	Interfacial failure
$[+/- 45]_6$ Vinyl Ester	0.57 ± 0.20	2.24 ± 0.06	Fiber-tear failure

The adhesive thickness was generally higher than the diameter of the spacing wire used, likely from the high viscosity of the adhesive. The unidirectional specimens were about 1 mm thicker and had significantly higher moduli than the $[+/- 45]_6$ specimens. The $[0]_4$ specimens resulted in mostly interfacial failure, and the $[+/- 45]_6$ specimens had mostly fiber-tear failure. Although most $[0]_4$ vinyl ester specimens exhibited interfacial failure modes, those wiped with MEK exhibited the most instances of cohesive failure modes but did not have significantly higher maximum lap shear stress values. Compared to Figure 56c, there is more cohesive failure on the failure surfaces in Figure 57. Besides specimens wiped with MEK, failure modes among solvent wipe techniques did not vary significantly (Figure 56).

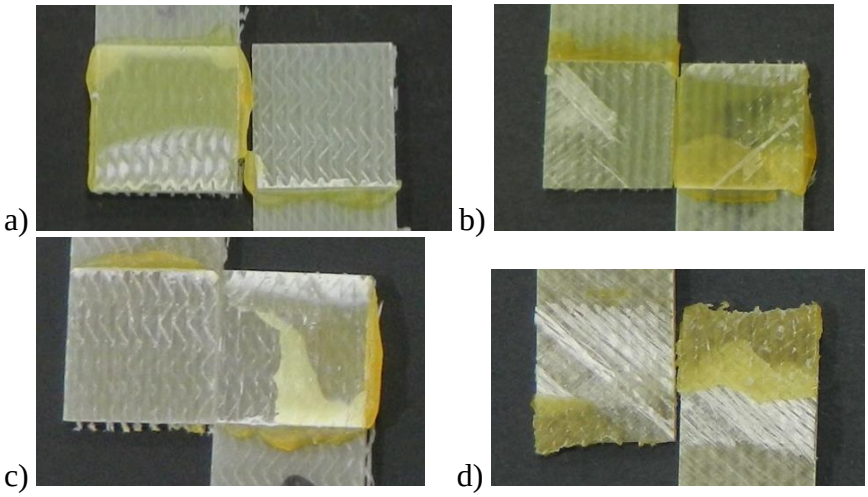

Figure 56. Photographs of the primary failure modes for substrates that had been adhered together with the MMA adhesive: a) $[0]_4$ epoxy fracture surface (ISP wipe) with interfacial failure; b) $[+/- 45]_6$ epoxy fracture surface (MIBK wipe) with fiber-tear failure; c) $[0]_4$ vinyl ester fracture surface (ISP wipe) with interfacial failure; d) $[+/- 45]_6$ vinyl ester fracture surface (MEK wipe) with fiber-tear failure.

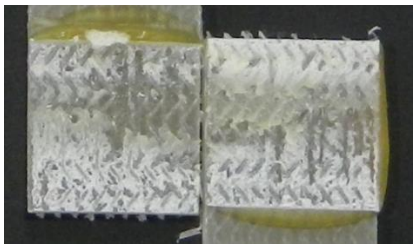

Figure 57. Failure mode for $[0]_4$ vinyl ester lap shear specimens wiped with MEK that had been adhered with the MMA adhesive.

Table 16. Average maximum shear stress values (MPa) for 658 ± 16 sq. mm average bond area of the epoxy adhesive.

Surface Treatment	$[0]_4$ Epoxy	$[+/- 45]_6$ Epoxy	$[0]_4$ Vinyl Ester	$[+/- 45]_6$ Vinyl Ester
Sanded	13.84 ± 0.82	8.12 ± 0.47	5.81 ± 0.26	4.62 ± 0.50
ISP	13.05 ± 0.91	8.23 ± 0.30	6.56 ± 0.48	5.67 ± 0.32
Acetone	12.54 ± 0.27	8.16 ± 0.19	5.40 ± 0.28	4.96 ± 0.62
MIBK	13.39 ± 0.72	8.21 ± 0.14	5.63 ± 0.61	4.94 ± 0.48
MEK	12.62 ± 0.60	8.24 ± 0.11	5.81 ± 0.47	4.77 ± 0.34

When the epoxy adhesive was used, the $[0]_4$ epoxy composite specimens had the highest maximum lap shear stress values while the vinyl ester specimens had the lowest maximum lap shear stress values.

Table 17. Average adhesive and adherend thicknesses and lap shear failure modes for epoxy specimens with the epoxy adhesive.

Substrate	Adhesive thickness (mm)	Adherend thickness (mm)	Primary Failure Mode
$[0]_4$ Epoxy	0.15 ± 0.12	3.14 ± 0.03	Cohesive failure
$[+/- 45]_6$ Epoxy	0.11 ± 0.08	2.29 ± 0.04	Fiber-tear failure
$[0]_4$ Vinyl Ester	0.13 ± 0.13	3.16 ± 0.06	Interfacial failure
$[+/- 45]_6$ Vinyl Ester	0.20 ± 0.18	2.39 ± 0.04	Fiber-tear failure

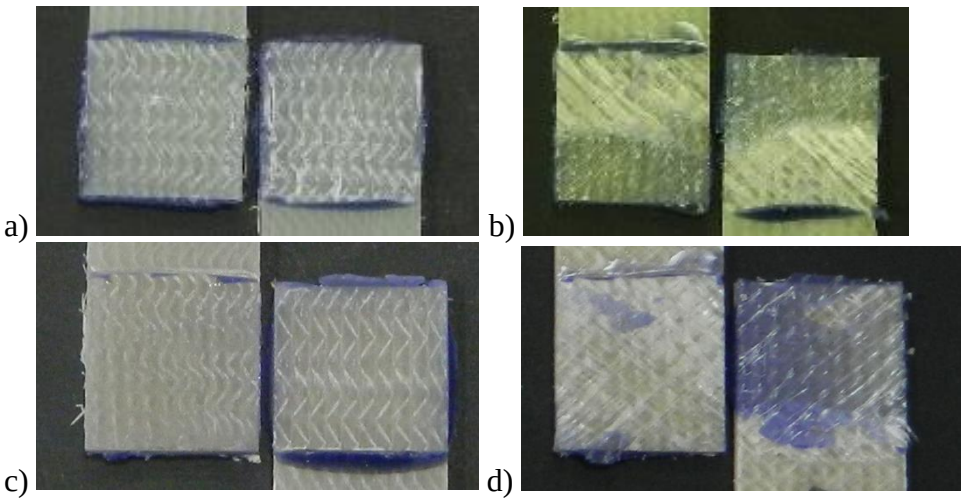

Figure 58. Photographs of the primary failure modes for each substrate adhered with the epoxy adhesive: a) $[0]_4$ epoxy (ISP wipe) with cohesive failure; b) $[+/- 45]_6$ epoxy (MEK wipe) with fiber-tear failure; c) $[0]_4$ vinyl ester (acetone wipe) with interfacial failure; d) $[+/- 45]_6$ vinyl ester (MIBK wipe) with fiber-tear failure.

The $[0]_4$ epoxy specimens resulted in mostly cohesive failure, while the $[0]_4$ vinyl ester specimens resulted in mostly interfacial failure.

6.2.2 Solvent Wipe DCB and ENF Testing Results

Solvent wipe DCB and ENF testing yielded G_{IC}, G_{IIC}, and failure modes. The results from the DCB and ENF tests for epoxy composites adhered with the MMA adhesive are in Tables 18 and 19. The results from the DCB and ENF tests for vinyl ester composites adhered with the MMA adhesive are in Tables 20 and 21. Typical failure modes for epoxy composites adhered with the MMA adhesive are in Figures 59 and 60. Typical failure modes for vinyl ester composites adhered with the MMA adhesive are in Figures 61 and 62.

Table 18. DCB results for $[0]_6$ epoxy composites adhered with the MMA adhesive.

Surface Treatment	G_{IC} (J/m^2)	% of specimens with interfacial failure	% of specimens with cohesive failure
Sanded	390 ± 222	20	80
ISP	605 ± 26	0	100
Acetone	551 ± 203	0	100
MIBK	583 ± 97	0	100
MEK	602 ± 104	0	100

Table 19. ENF results for $[0]_6$ epoxy composites adhered with the MMA adhesive.

Surface Treatment	G_{IIC} (J/m^2)	% of specimens with interfacial failure	% of specimens with cohesive failure
Sanded	8079 ± 2143	60	40
ISP	9170 ± 1297	0	100
Acetone	10235 ± 3664	0	100
MIBK	6601 ± 2630	0	100
MEK	7079 ± 1780	0	100

Table 20. DCB results for $[0]_6$ vinyl ester composites adhered with the MMA adhesive.

Surface Treatment	G_{IC} (J/m^2)	% of specimens with interfacial failure	% of specimens with cohesive failure
Sanded	553 ± 222	60	40
ISP	426 ± 417	40	60
Acetone	590 ± 168	0	100
MIBK	867 ± 408	40	60
MEK	702 ± 310	0	100

Table 21. ENF results for $[0]_6$ vinyl ester composites adhered with the MMA adhesive.

Surface Treatment	G_{IIC} (J/m^2)	% of specimens with interfacial failure	% of specimens with cohesive failure
Sanded	4468 ± 1821	100	0
ISP	5425 ± 3581	60	60
Acetone	2537 ± 1036	20	40
MIBK	4621 ± 3443	80	20
MEK	2209 ± 322	20	80

Failure modes for DCB testing tended to correspond with those for ENF for each specimen, so, often when a DCB specimen had interfacial failure, the ENF result was also interfacial. The epoxy composites with the MMA adhesive had the most consistent cohesive failure modes and those that were not wiped with solvents exhibited slightly more interfacial failure modes than those that were wiped with solvents. The vinyl ester composites adhered with the MMA adhesive had a mixture of interfacial and cohesive failure modes without a clear pattern besides that those that were wiped with MEK, which had consistent cohesive failure modes that were like those from lap shear testing (Figure 62). The failure surface in Figure 60 had cohesive failure where the MMA adhesive was in contact with the epoxy matrix, but interfacial failure where the MMA adhesive was in contact with glass fibers. The interfacial failure mode around the glass

fibers indicates that the adhesive adhesion was not as compatible between the glass fibers as the matrix. The fibers could either have been partially re-exposed while the surface was hand-sanded or the matrix layer that covered the fibers in the regions where there was interfacial failure was thin. In addition, for all DCB and ENF specimens adhered with the MMA, occurrences of interfacial failure modes decreased when the specimens were wiped with solvents rather than only sanded.

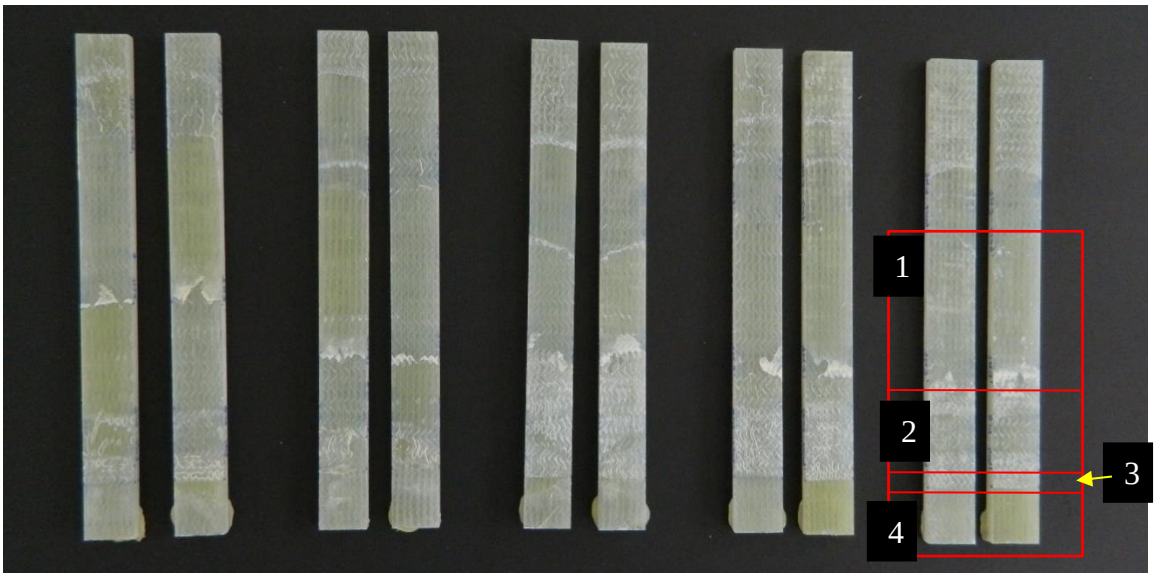

Figure 59. Failure surfaces for acetone-wiped $[0]_6$ epoxy adherends with the MMA adhesive with the red boxes indicating: 1) the ENF failure region, 2) the manual crack propagation region, 3) the DCB failure region, and 4) the Teflon pre-crack region.

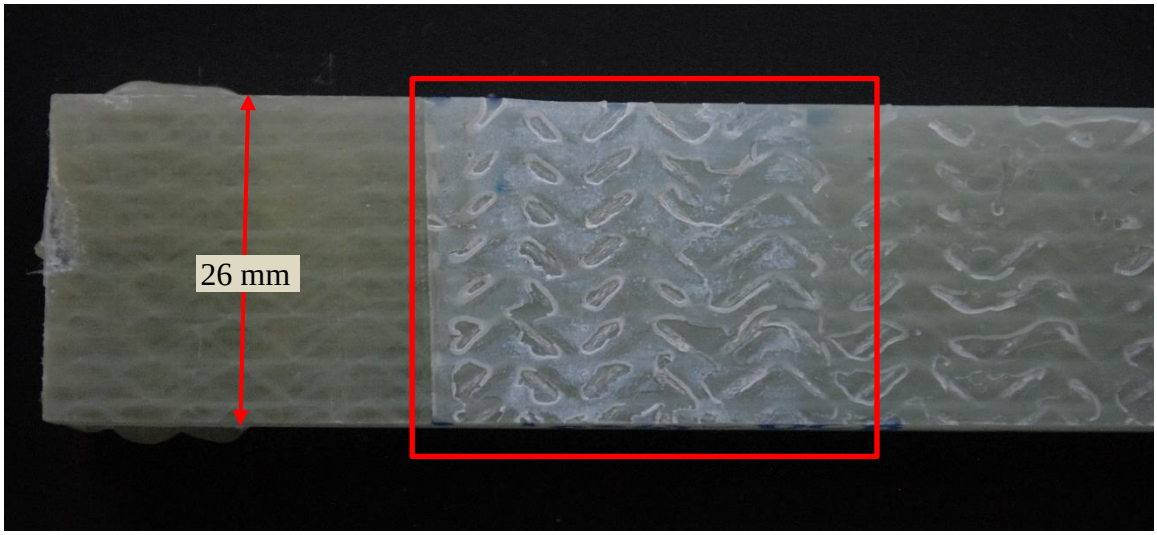

Figure 60. DCB failure mode for MEK-wiped $[0]_6$ glass fiber reinforced epoxy adherends with the MMA adhesive showing mostly cohesive failure.

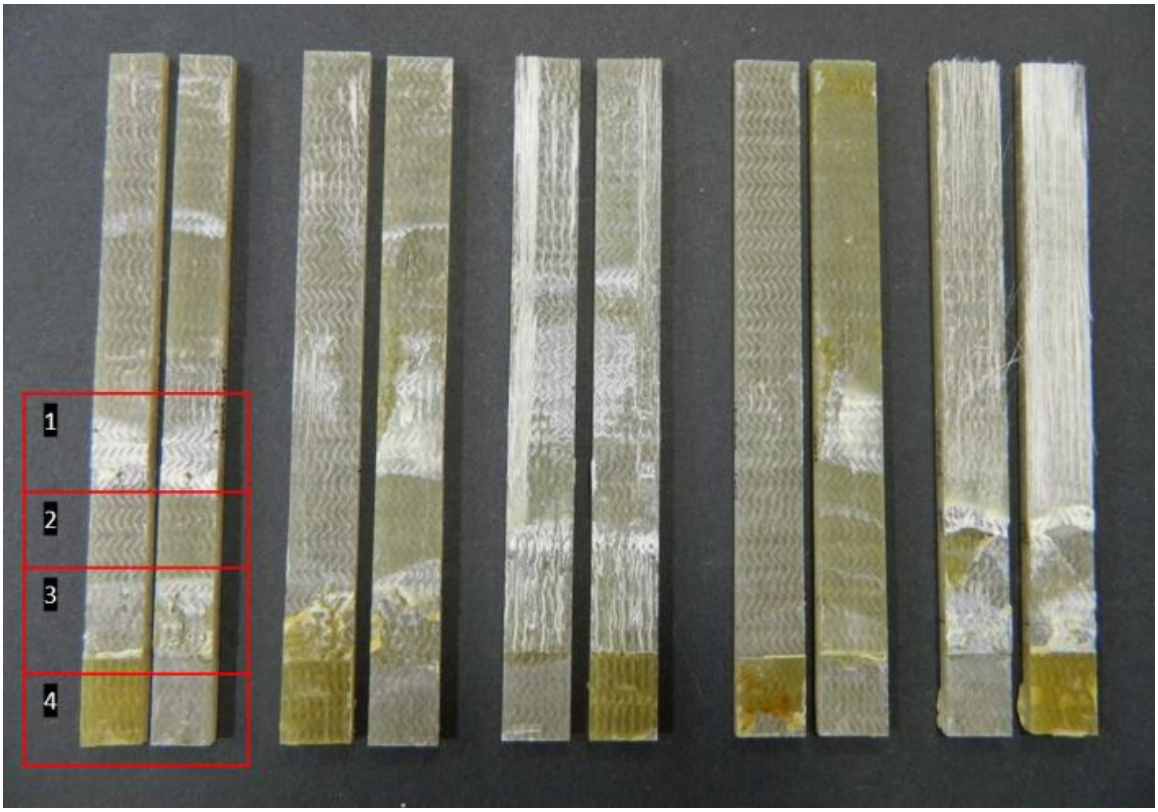

Figure 61. ISP wiped $[0]_6$ vinyl ester composites that were adhered with the MMA adhesive with the red boxes indicating: 1) the ENF failure region, 2) the manual crack propagation region, 3) the DCB failure region, and 4) the Teflon pre-crack region.

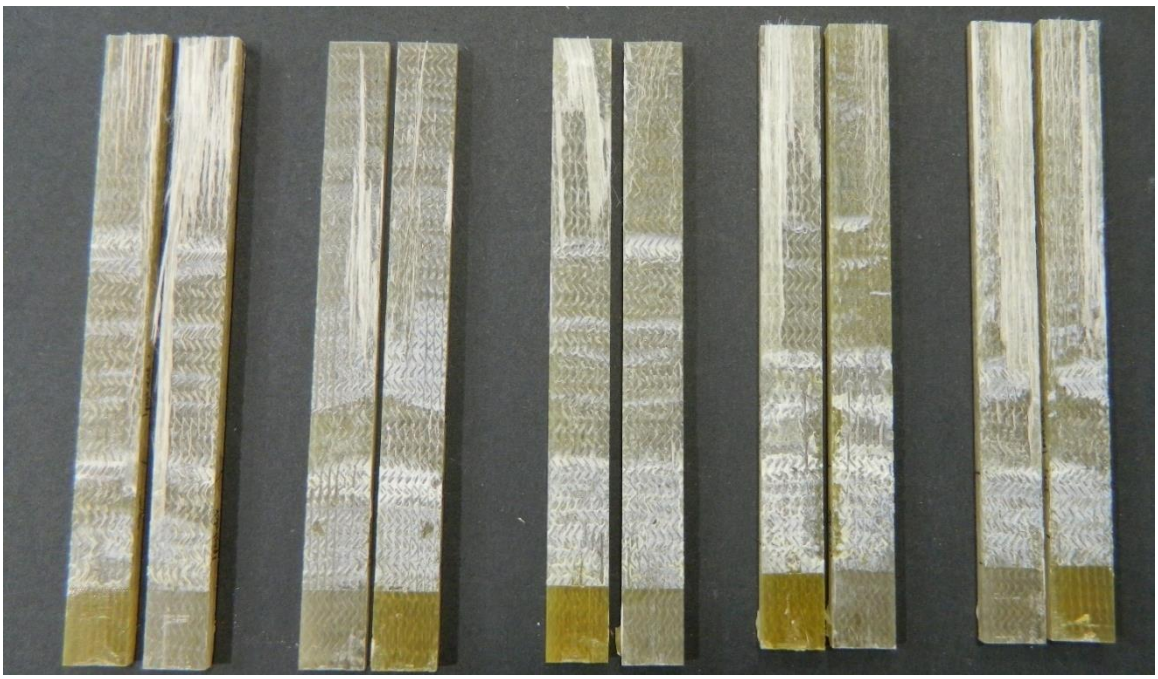

Figure 62. Failure surfaces for MEK-wiped $[0]_6$ vinyl ester adherends with the MMA adhesive.

The results from the DCB and ENF tests for epoxy composites adhered with the epoxy adhesive are in Tables 22 and 23. Typical failure modes for epoxy composites adhered with the epoxy adhesive are in Figure 63.

Table 22. DCB results for $[0]_6$ epoxy composites adhered with the epoxy adhesive.

Surface Treatment	G_{IC} (J/m^2)	% of specimens with interfacial failure	% of specimens with cohesive failure
Sanded	234 ± 72	0	100
ISP	166 ± 47	0	100
Acetone	149 ± 42	0	100
MIBK	157 ± 48	0	100
MEK	227 ± 83	0	100

Table 23. ENF results for $[0]_6$ epoxy composites adhered with the epoxy adhesive.

Surface Treatment	G_{IIC} (J/m^2)	% of specimens with interfacial failure	% of specimens with cohesive failure
Sanded	2772 ± 269	0	100
ISP	2418 ± 523	0	100
Acetone	2930 ± 661	0	100
MIBK	2173 ± 468	0	100
MEK	2943 ± 1115	0	100

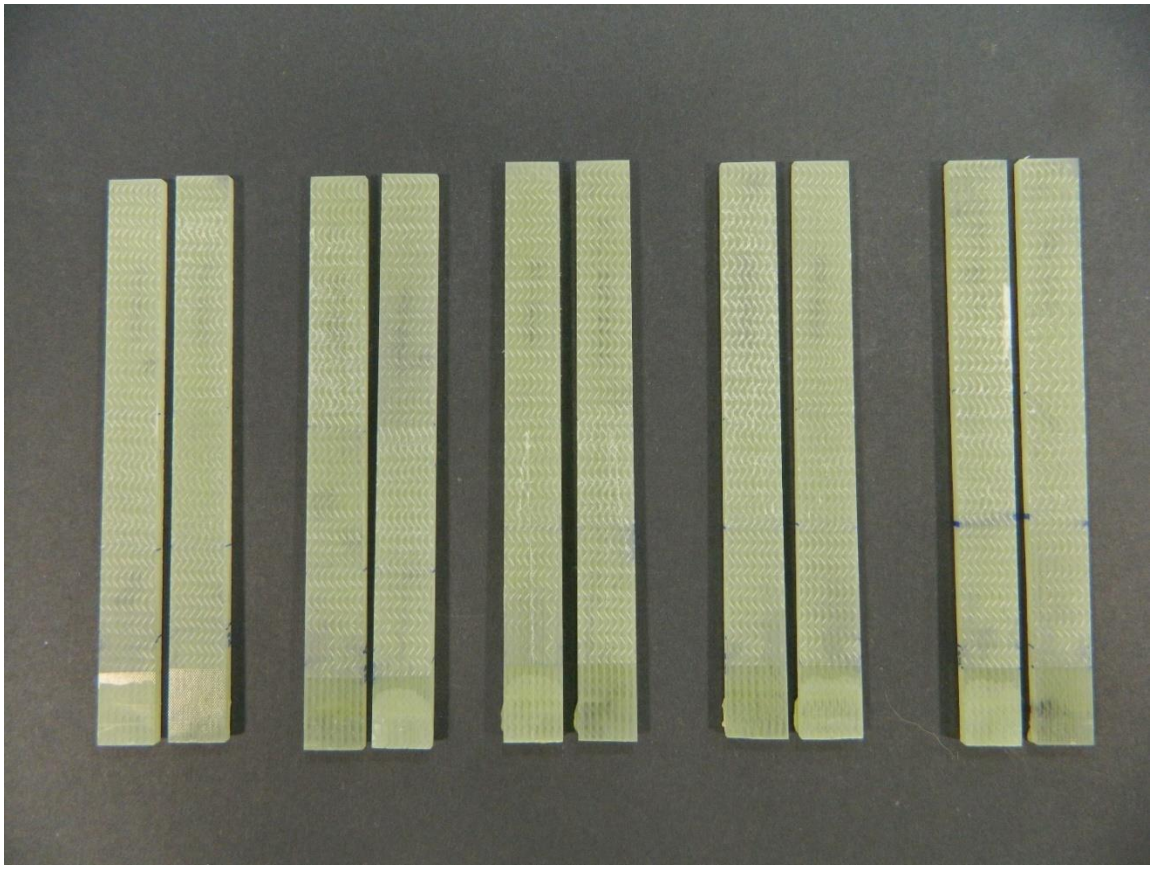

Figure 63. Failure modes for the DCB/ENF epoxy composite specimens adhered with the epoxy adhesive.

The vinyl ester specimens adhered with the epoxy adhesive could be pulled apart manually. Since the DCB specimens could be completely pulled apart manually and the DCB specimens were needed to perform ENF tests, the G_{IIC} values were not measured.

Both the epoxy and the vinyl ester specimens that were adhered with the epoxy adhesive resulted in cohesive failure modes regardless of the solvent wipe treatment used (Figure 64).

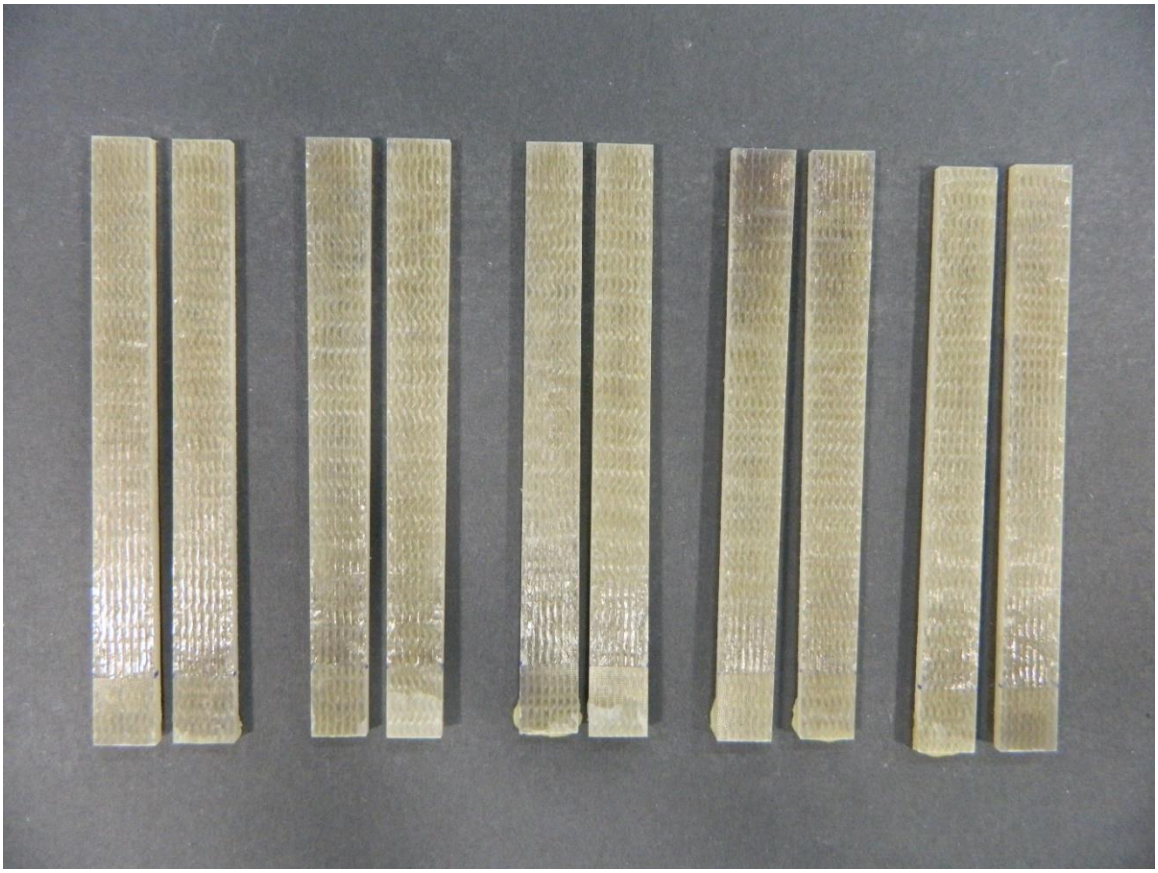

Figure 64. Failure modes for the DCB/ENF vinyl ester composite specimens adhered with the epoxy adhesive.

6.2.3 Solvent Wipe Unidirectional Adherend Results

Compared to adherend-adhesive combinations, wiping lap shear, DCB, and ENF adherends with solvents had minimal effects on resulting maximum lap shear stress, G_{IC}, and G_{IIC} values. The maximum lap shear stress, G_{IC}, and G_{IIC} values reported in Table 24

were averaged over all tests with unidirectional adherends regardless of the solvent wipe surface preparation methods used to summarize the overall effects of adherend-adhesive combinations. The $[+/- 45]_6$ adherends were not used for the maximum lap shear stress averages or failure modes in Table 24. The failure modes reported in Table 24 were the most common failure modes for each adherend-adhesive combination for each test type. Table 24 should not be used for solvent wipe surface preparation method comparisons.

Table 24. Generalized unidirectional adherend results for lap shear, DCB, and ENF tests with values averaged regardless of solvent wipe surface preparation method.

	epoxy adherend		vinyl ester adherend	
	MMA adhesive	epoxy adhesive	MMA adhesive	epoxy adhesive
maximum lap shear stress (MPa)	14.14 ± 1.43	13.09 ± 0.66	22.79 ± 1.20	5.84 ± 0.42
lap shear failure mode	interfacial	cohesive	interfacial	interfacial
G_{IC} (J/m^2)	546 ± 130	187 ± 58	628 ± 305	0
DCB failure mode	cohesive	cohesive	cohesive	cohesive
G_{IIC} (J/m^2)	8233 ± 2303	2647 ± 607	3852 ± 2041	N/A
ENF failure mode	cohesive	cohesive	interfacial	N/A

6.2.4 Solvent-Wiped Resin Testing Results

Streaks resulted on the surfaces of both epoxy and vinyl ester resin surfaces that were wiped with ISP, acetone, MIBK, and MEK. Streaks did not result when the resins were wiped with distilled water. Photos of typical solvent-wiped resin surfaces are shown in Figures 65, 66, and 67. Typical optical microscope image results are in Figure 68.

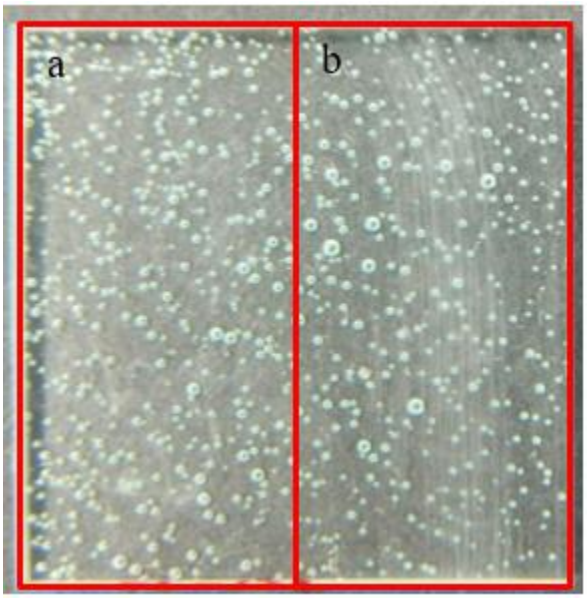

Figure 65. Epoxy resin (50 mm x 50 mm) with a) no wipe and b) ISP wipe with resulting streak.

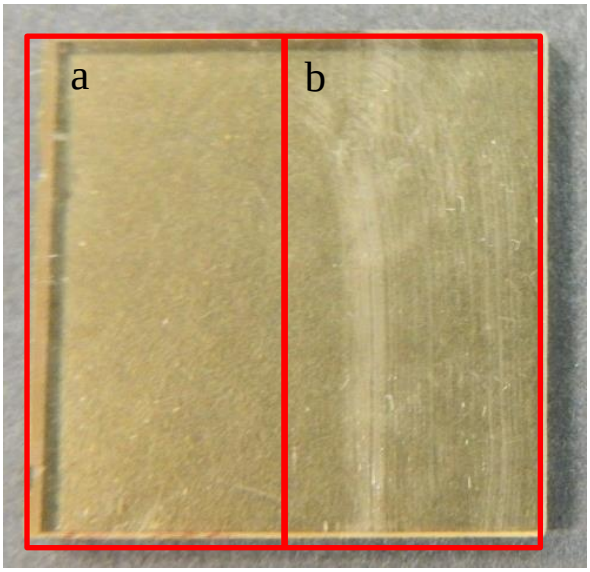

Figure 66. Vinyl ester resin (dimensions 50 mm x 50 mm) with a) no wipe and b) MEK wipe with resulting streak.

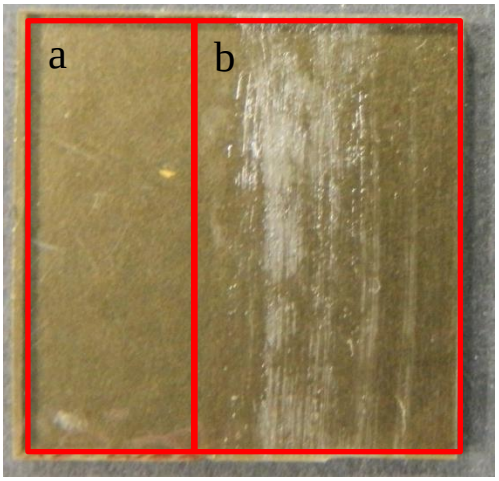

Figure 67. Vinyl ester resin (dimensions 50 mm x 50 mm) with a) no wipe and b) MIBK wipe with resulting streak.

a) 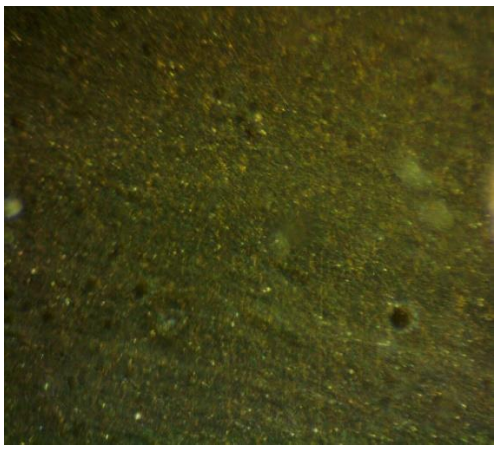 b) 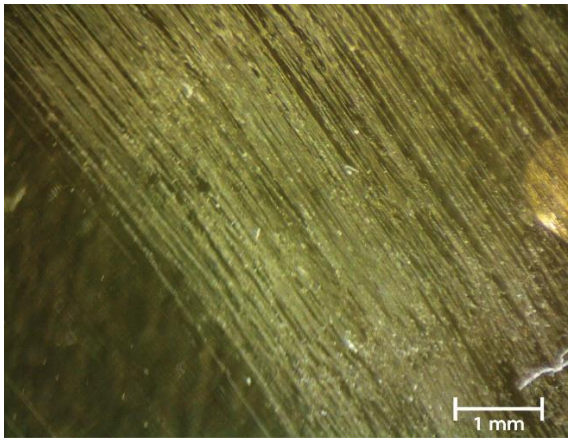

Figure 68. Optical microscope image of vinyl ester a) not wiped and b) wiped with ISP.

6.3 Conclusions

6.3.1 Solvent Wipe Lap Shear Testing Conclusions

T-tests comparing each solvent wipe method and the control specimens resulted in several statistically significant outcomes. For the MMA adhesive, wiping the $[+/- 45]_6$ vinyl ester specimens with acetone and MEK resulted in statistically significantly higher maximum lap shear stress values. Specimens adhered with the epoxy adhesive had both

significantly lower and higher outcomes. The statistically significantly lower maximum lap shear stress values occurred when the $[0]_4$ epoxy was wiped with either acetone or MEK and when the $[0]_4$ vinyl ester was wiped with acetone. The statistically significantly higher maximum lap shear stress values resulted when the $[0]_4$ vinyl ester was wiped with ISP and when the $[+/- 45]_6$ vinyl ester specimens were wiped with ISP. Although there were some significantly significant outcomes for some solvent-substrate-adhesive combinations, it is possible that hand-sanding and manually applying adhesives could have created the significant variations in the maximum lap shear stress results more than by wiping surfaces with different solvent types.

Differences observed when testing different lap shear substrates were mostly due to differences in adherend thicknesses and moduli, which was expected because the stiffness of adherends influences peel stress concentrations at the end of the joint in lap shear testing. Adhesive-matrix combination also had a significant effect on the maximum lap shear stress values. Unidirectional glass fiber vinyl ester lap shear specimens adhered with the MMA adhesive resulted in more cohesive failure when wiped with MEK than for those wiped with other solvents.

Typically, higher bond strengths result when adherends and adhesives have similar molecular structures. The epoxy specimens adhered with the epoxy adhesive likely had higher maximum lap shear stress values than the vinyl ester specimens when adhered with the epoxy adhesive because the epoxy substrates had similar molecular structures to the epoxy adhesive.

6.3.2 Solvent Wipe DCB and ENF Testing Conclusions

T-tests comparing each solvent wipe method and the control specimens did not result in any statistically significant outcomes for DCB tests but did result in two statistically significantly lower outcomes for ENF tests. The two lower outcomes were for the vinyl ester specimens adhered with the MMA adhesive and wiped with MEK and the epoxy specimens adhered with the epoxy adhesive and wiped with MIBK. Similar to the lap shear statistically significant outcomes, the variations due to hand sanding and manually applying adhesive could have caused the statistically significant results rather than the types of solvents used.

Across all DCB and ENF tests, G_{IIC} values were consistently higher than G_{IC} values, which is optimal for wind turbine field repairs, particularly scarf repairs, because patches are typically subjected to more shear stresses than peel stresses. Similarly to the solvent wipe lap shear results, adhesive-matrix combinations had significant effects on G_{IC} and G_{IIC} values and failure modes. The G_{IIC} values for specimens adhered using the MMA adhesive were twice as high for the epoxy specimens than the vinyl ester specimens. Both epoxy and vinyl ester specimens had similar G_{IC} values when adhered with the MMA adhesive. Most notably, vinyl ester composite substrates adhered extremely poorly to the epoxy adhesive, with no adhesive-matrix compatibility in mode I loading. Since the maximum lap shear stress values were nonzero, vinyl ester composite substrates adhered with the epoxy adhesive may have some shear strength, but since $G_{IC} = 0$ J/m^2, the epoxy adhesive should be considered unsuitable for repairs to vinyl ester composites.

The epoxy specimens adhered with the MMA adhesive that were not wiped with solvents exhibited slightly more interfacial failure modes than those that were wiped with solvents, which indicates that solvent wiping may have slightly improved the adhesion properties for those specimens.

6.3.3 Solvent-Wiped Resin Testing Conclusions

Overall, visual observations of the surfaces that were wiped with solvents were more effective once the resins used were isolated from the fibers. The epoxy resin in Figure 65 has a lot of porosity because VARTM was not used to manufacture the resin samples so air bubbles were trapped in the resin. The streaks shown in Figures 65, 67, and 68 indicate that solvent wiping affects thermoset polymer surfaces despite neither significantly affecting bond strengths nor failure modes in solvent-wipe lap shear results. The streak results occurred because of the interactions between the solvents and the thermoset polymer surfaces. The solvent diffused into the surface, creating a gel-like swollen layer. The swollen layer was amorphous and was smeared as the cloth passed over the surface. The differences between Figure 67a and Figure 67b also indicate that different solvents can affect the same resin differently. The MIBK gelled the vinyl ester surface more than MEK did.

Neither epoxy nor vinyl ester resins showed visible streaks when wiped with distilled water so a composite surface wiped with distilled water will not be altered as significantly as with ISP, acetone, MIBK, or MEK solvents. The streaks raise additional questions about the use of solvents in composite repair surface preparation methods. Will

a gelled polymer surface affect dissolving and removing contaminants from surfaces? Since composite dust consists of primarily glass and resin particles, could solvents gel the resin particles? Neither ISP, acetone, MIBK, nor MEK will dissolve glass particles, but the solvents could gel the surface and trap the glass and gelled resin particles. Since the glass particles in the composite dust will not dissolve and solvents besides distilled water will gel a polymer surface, is it beneficial to use solvents besides distilled water at all? Since solvents besides distilled water gel a polymer surface, could a gelled surface increase polymer chain entanglement between the adhesive and the substrate, resulting in higher bond strengths? MEK-wiped vinyl ester substrates adhered with the MMA adhesive for lap shear, DCB, and ENF testing did not result in changes in bond strengths, but failure modes were slightly altered. Furthermore, whichever combination of matrix resin, adhesive, and solvents that is considered for a repair application should be tested using DCB and ENF tests prior to being used in the field.

7. CONTAMINATION LAP SHEAR TESTING

7.1 Contamination Lap Shear Methods

Contamination lap shear testing was used to compare maximum lap shear stress values and failure modes between specimens contaminated with hydraulic oil or composite dust with specimens that did not have contamination applied. Composite dust was made by cutting composites using a clean radial arm saw. The composite dust particles were removed from the collection pan and set out to dry. Then, the particles were sifted through a 140 μm mesh. Before applying composite dust to the surfaces, glass fiber reinforced epoxy composite coupons with dimensions 25 mm x 400 mm were cut from composite plates. Then, the coupons were hand sanded on a flat granite plate using FEPA 320 grit sandpaper, rinsed with water, then wiped again with a dry cloth. Each coupon was weighed using a Cole-Parmer Symmetry PA220 scale. Contamination lap shear specimens were manufactured with either the MMA or the Scotch-Weld AF 163-2K film adhesives. Tabs were adhered with the adhesives being lap shear tested.

To apply the filtered composite dust to the composite surfaces, water was first added to the dust to create a paste. A stamp (Figure 69) was placed in the paste, then placed in the dry composite dust. The stamp was pressed onto the composite coupons, then lifted. The coupons were left out to dry for 3 hours, resulting a grid pattern of composite dust (Figure 70). The dust-contaminated specimens were weighed again to measure the amount of dust applied. The hydraulic oil was not applied to specimens using the stamp. A manual pipette filler was used to place 1 mL of hydraulic oil on each

coupon surface. After three hours, the hydraulic oil was wiped with a dry cloth. An oil residue remained on surfaces after wiping with the dry cloth.

The coupons that were adhered together using the MMA adhesive were not post-cured. The contaminated lap shear specimens were manufactured using MMA adhesive that had expired by 15 months. The expired adhesive was used to measure the combined effects of contamination and adhesive expiration. The combined effects of surface contamination and the use of expired adhesives can occur in the field, especially since detailed blade repair instructions are often unavailable. Maximum lap shear stress values and failure modes for control specimens were compared between the new and expired adhesive lap shear tests. The adhered coupons cured at room temperature for 24 hours then adhered to tabs and left to cure again for 24 hours. The specimen geometry used for contamination lap shear testing was the same as the geometry used in solvent wipe lap shear testing (Figure 53).

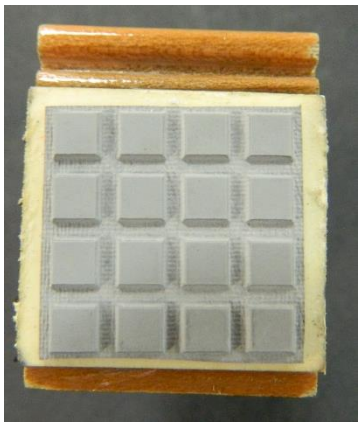

Figure 69. Custom rubber stamp used to apply composite dust. The 16 squares were each 3.8 mm^2 with 2 mm spacing.

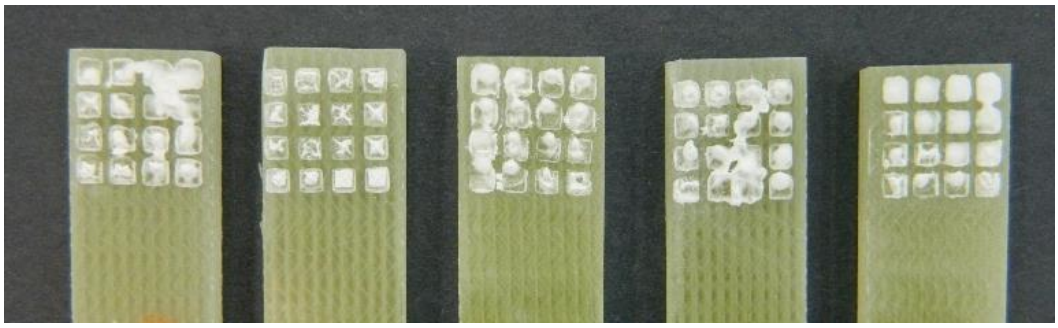

Figure 70. Lap shear surfaces after water had evaporated from the composite dust.

A set of 15 contamination lap shear specimens were also manufactured using the Scotch-Weld AF 163-2K film adhesive. The 15 specimens included three sets of five composite dust, hydraulic oil, and control specimens. Film adhesives are not typically used in wind turbine field repairs. Yet, the film adhesive was beneficial for comparing failure modes with the specimens adhered with the MMA adhesive. Since only failure mode comparisons between the two adhesives were of interest, contamination diffusion time effects were not studied for the film adhesive. Identical contamination application procedures as the MMA-adhered specimens were used for those using the film adhesive, however, the film adhesive specimens were post-cured for 12 hours at 80ºC. The film adhesive specimens were held together using binder clips during post-curing. ASTM D5868-01 was used as a guide for lap shear testing [109]. All lap shear specimens were tested at a load rate of 0.127 cm/min. The contamination lap shear test matrix is in Table 25.

Table 25. The test matrix used for contamination lap shear testing.

Adhesive Type	Number of Days after Manufacturing that the Specimens Were Tested	Contaminant Type	Number of Tests	Outputs
MMA	2	none	5	maximum lap shear stress, failure modes
		hydraulic oil	5	maximum lap shear stress, failure modes
		composite dust	5	maximum lap shear stress, failure modes
	9	none	5	maximum lap shear stress, failure modes
		hydraulic oil	5	maximum lap shear stress, failure modes
		composite dust	5	maximum lap shear stress, failure modes
	33	none	5	maximum lap shear stress, failure modes
		hydraulic oil	5	maximum lap shear stress, failure modes
		composite dust	5	maximum lap shear stress, failure modes
Film	9	none	5	maximum lap shear stress, failure modes
		hydraulic oil	5	maximum lap shear stress, failure modes
		composite dust	5	maximum lap shear stress, failure modes

7.2 Contamination Lap Shear Results

Results for $[0]_6$ glass fiber reinforced epoxy lap shear specimens subject to composite dust and hydraulic oil along bond lines are presented for those adhered with the MMA and the film adhesives.

7.2.1 MMA Adhesive Results

The MMA adhesive failure modes and maximum lap shear stress were compared between when the adhesive was not expired and when the adhesive was expired by 15 months. The failure modes for the not expired and expired adhesive were compared in Figures 71 and 72.

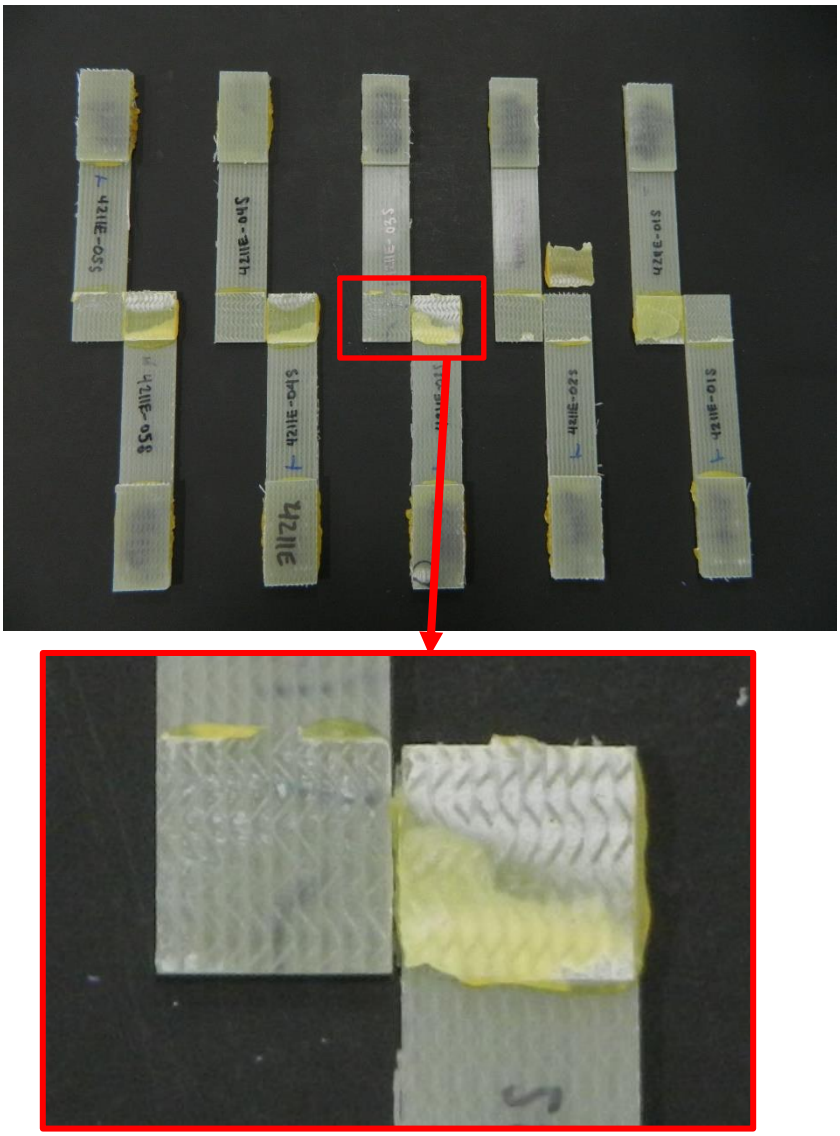

Figure 71. The MMA adhesive (not expired) with interfacial failure and the adhesive staying together with itself.

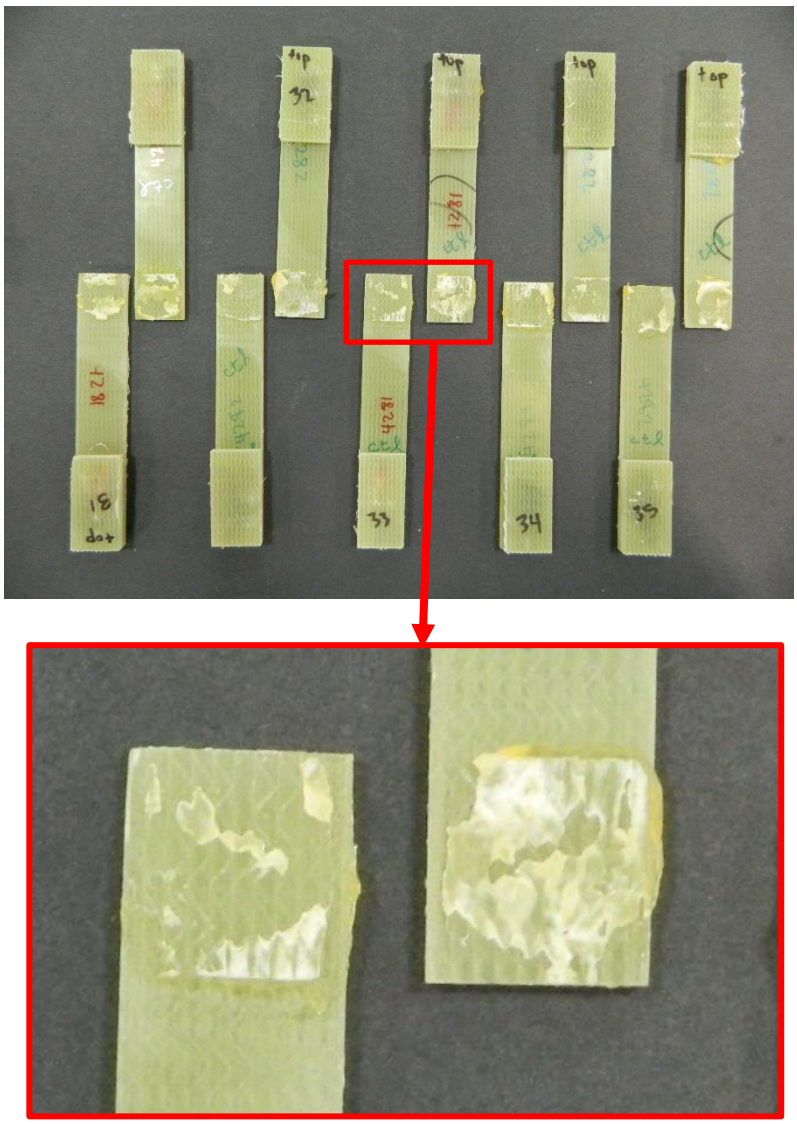

Figure 72. The MMA adhesive (expired by 15 months) in with interfacial failure and adhesive separation from itself.

When the adhesive was not expired and adhered to $[0]_4$ epoxy composites, lap shear testing resulted in an average maximum lap shear stress of 14.90 ± 0.77 MPa. The expired adhesive resulted in an average maximum lap shear stress of 13.93 ± 2.48 MPa. Thicker substrates typically result in higher maximum lap shear stress values, and the not expired lap shear specimens had two extra layers of glass fiber fabrics in the laminae. The

not expired set of lap shear adherends had an average thickness of 3.2 ± 0.1 mm, while the expired set of lap shear adherends had an average thickness of 4.5 ± 0.1 mm. If the adhesive properties had not changed, the maximum lap shear stress values would likely be higher for the specimens adhered with the expired adhesive because thicker composite substrates were used.

Besides a slightly lower maximum lap shear stress value, the maximum lap shear stress standard deviation was significantly higher when the adhesive used had expired. Although both sets of specimens exhibited interfacial failure modes, there were differences in how the adhesive itself failed. The adhesive stayed together with itself when the adhesive was not expired and separated from itself when the adhesive was expired. Despite differences in standard deviations and failure modes, the adhesive was still usable for comparing the effects of contamination on maximum lap shear stress values and lap shear failure modes. The maximum lap shear stress results with respect to testing time and contaminant used are listed in Table 26. The average adhesive bond thickness for contamination lap shear specimens adhered with the MMA adhesive was 0.34 ± 0.14 mm.

Table 26. MMA adhesive lap shear results. Lap shear specimens were tested 2, 9, and 33 days after initial manufacture and had contaminants including composite dust and hydraulic oil applied to surfaces.

Number of Days after Manufacturing that the Specimens Were Tested	Contaminant	Maximum Lap Shear Stress (MPa)
2	Control	13.93 ± 2.48
	Dust	8.07 ± 1.72
	Oil	12.34 ± 0.44
9	Control	14.39 ± 2.59
	Dust	7.76 ± 2.95
	Oil	13.58 ± 1.61
33	Control	15.85 ± 1.62
	Dust	8.30 ± 1.38
	Oil	15.43 ± 0.70

Compared to the corresponding control specimens, for lap shear specimens contaminated with dust, the maximum lap shear stress values were 42%, 46%, and 48% less after a 2, 9, and 33 days, respectively. For lap shear specimens contaminated with oil, the maximum lap shear stress values were 11%, 6%, and 3% less than control specimens after a 2, 9, and 33 days, respectively. Contamination lap shear failure modes for control, dust, and hydraulic oil specimens are in Figures 73, 74, and 75. The average composite dust amount that was applied was 0.037 ± 0.013 g. The standard deviation was high because of the variability of pressure and amount of water used during the manual application of the dust slurry with the stamp. The specimen with the most dust (0.0744 g) applied corresponded with a failure surface that had a larger region of dust on the failure surface and the lowest maximum lap shear stress value (3.23 MPa) (Figure 74b). All specimens adhered with the MMA adhesive exhibited interfacial failure modes. One specimen that was contaminated with hydraulic oil had pitting in the adhesive (Figure 75b), which did not occur in other failure modes.

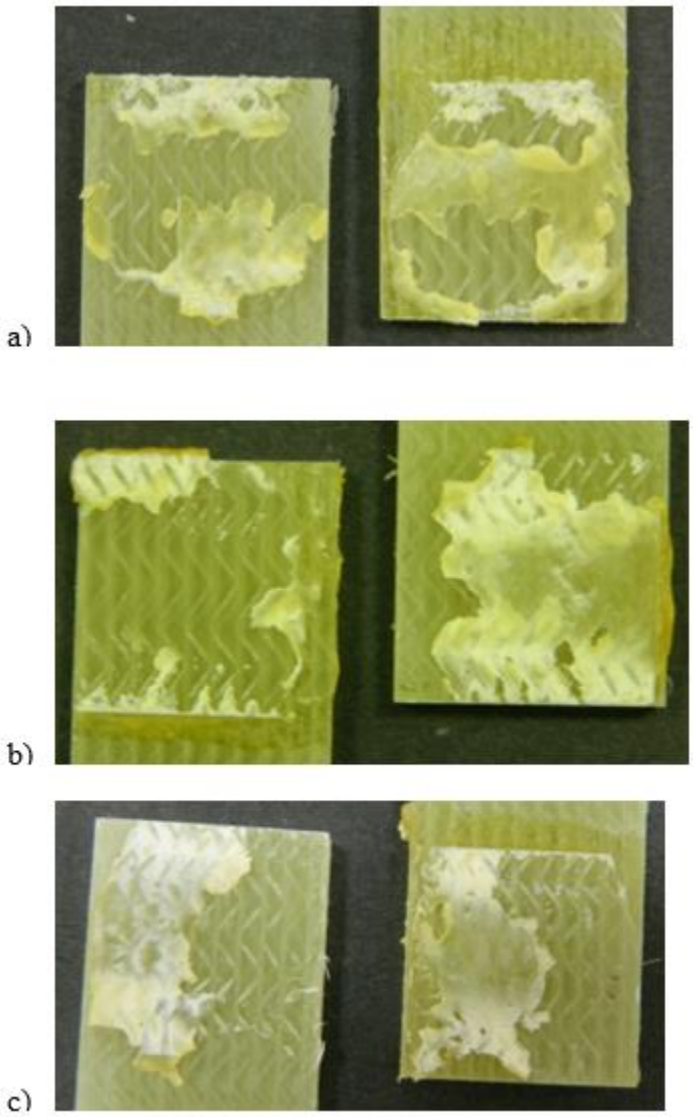

Figure 73. MMA adhesive fracture surfaces of control specimens tested a) 2, b) 9, and c) 33 days after manufacture.

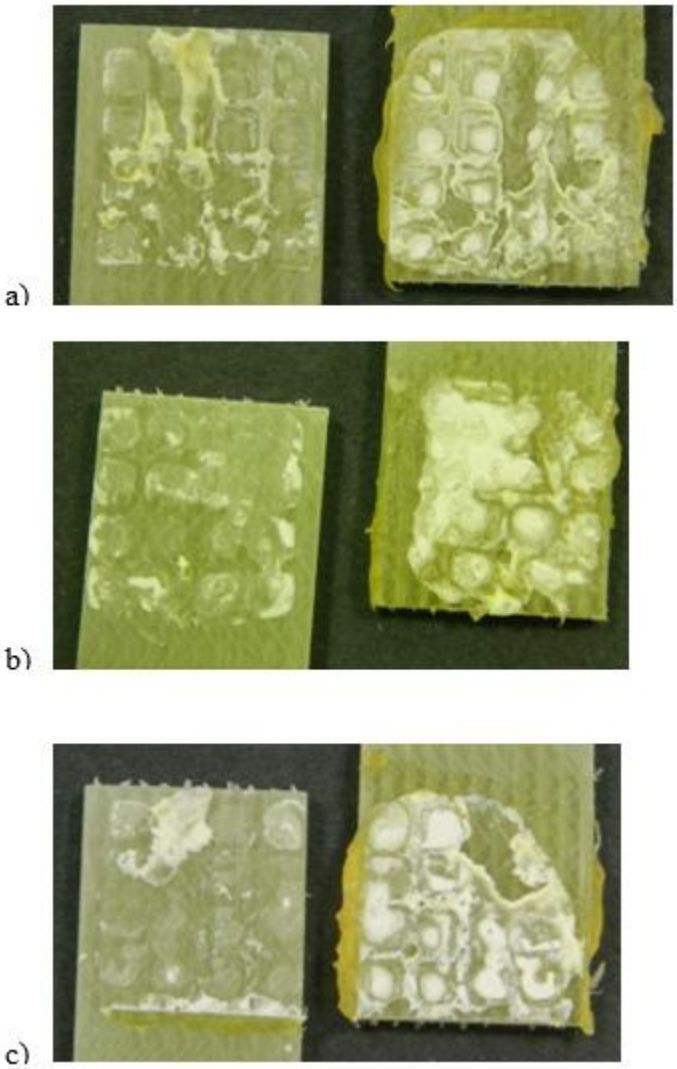

Figure 74. MMA adhesive fracture surfaces of specimens contaminated with composite dust tested a) 2, b) 9, and c) 33 days after manufacture.

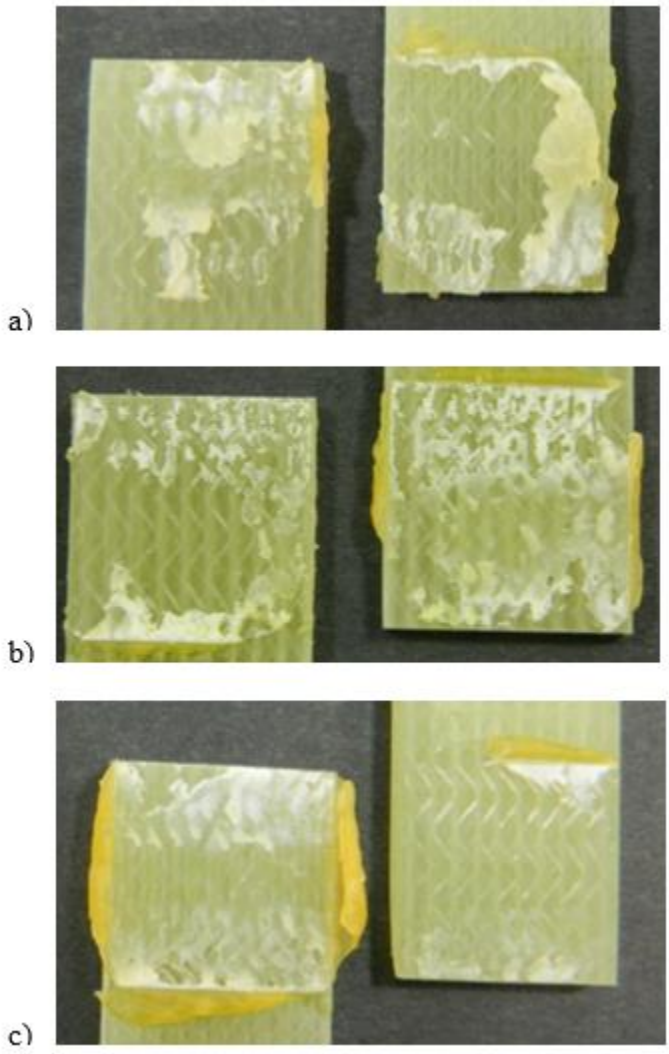

Figure 75. MMA adhesive fracture surfaces of specimens contaminated with hydraulic oil that were tested a) 2, b) 9, and c) 33 days after manufacture.

7.2.2 Film Adhesive Results

Maximum lap shear stress and failure mode results for the lap shear specimens adhered with the film adhesive tested after 9 days are in Table 27 and Figure 76. Maximum lap shear stress values dropped 12% when dust was applied and 19% when

hydraulic oil was applied. The average adhesive bond thickness for contaminated lap shear specimens adhered with the film adhesive was 0.13 ± 0.11 mm.

Table 27. Film adhesive results for contamination lap shear specimens tested after 9 days.

Contaminant	Maximum Lap Shear Stress (MPa)
Control	24.54 ± 1.88
Dust	21.70 ± 2.13
Oil	19.94 ± 1.30

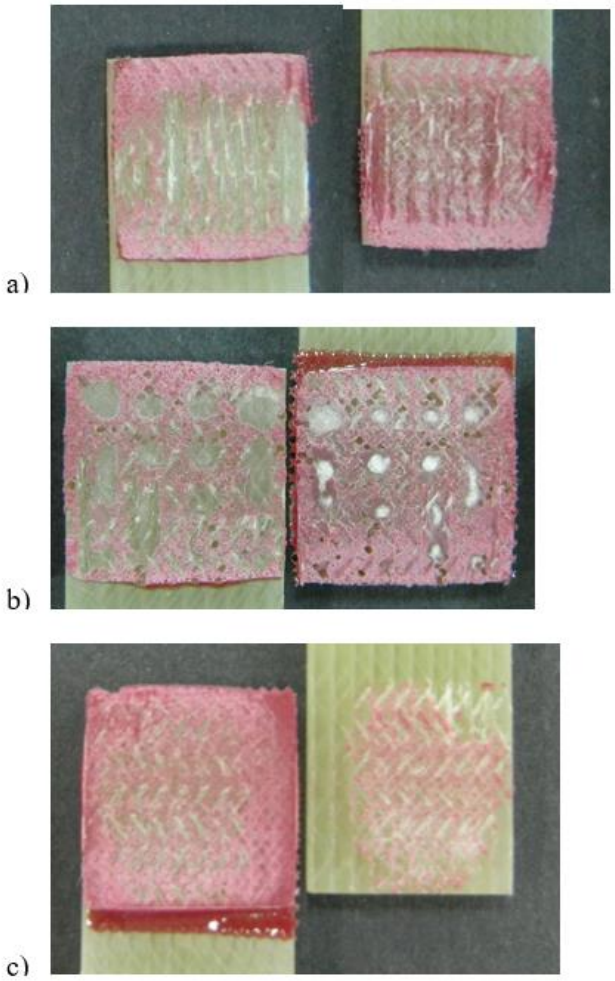

Figure 76. Typical film adhesive lap shear failure surfaces a) control, b) composite dust, and c) hydraulic oil specimens tested after 9 days.

Control specimens had cohesive failure on the edges where there was more peel stress and had interfacial failure and some fiber tear failure along the fiber direction in the center where there was more shear stress. Specimens contaminated with composite dust had cohesive failure in regions where the dust was not present and interfacial failure where dust was placed. Dust remained on the coupon that dust was applied on. Specimens contaminated with hydraulic oil had a mixture of interfacial and cohesive

failure. The interfacial failure occurred around the edges of the bond area, on the coupon where the hydraulic oil had been applied. The cohesive failure occurred in the center of the lap shear specimen.

Specimens contaminated with composite dust resulted in similar failure mode patterns to those from Musaramthota , Pribanic, and McDaniel (2014) ’s study where Freekote mold release was applied to surfaces using a stamp on DCB specimens (Figure 29) [76]. Evidently, using a grid stamp (Figure 69) creates locations where contamination is present where the stamp was in contact with the surface and locations where no contamination is applied. The adhesive can bond where the contaminant is not applied, but the overall strength of the bond is lowered because of the lower adhered surface area over the bond region. In lap shear testing, failure typically occurs at the ends of the overlap where peel stresses are high. Contamination along a bond line is a stress concentration that can also be the location for failure initiation depending on the loading scenario and joint design.

7.3 Contamination Lap Shear Conclusions

The higher standard deviations in the set of specimens adhered with the expired adhesive indicate that the MMA adhesive had less consistent bonding properties with age. The less consistent bonding properties and the adhesive separating from itself during failure occurred because as adhesives age, the solvents used in adhesives gradually evaporate. Even if the adhesive is in a container with an airtight seal, the seal will degrade over time and allow the solvents to evaporate. As solvents evaporate from adhesives, the viscosity of the adhesives increases. Increased adhesive viscosity hinders

an adhesive from flowing in the peaks and valleys of a surface. The adhesive coming apart from itself in the failure modes for the expired adhesive indicates that the adhesive was more brittle. Brittle adhesive joints will fail more suddenly than adhesive joints with more ductility. Furthermore, neither expired adhesives nor adhesives that result in brittle bond lines should be used in wind turbine blade field repairs or to adhere components together.

Maximum lap shear stress values for the MMA adhesive dropped an average of 45% for the lap shear specimens contaminated with dust and 7% for those contaminated with hydraulic oil. Although the composite dust resulted in more significant drops in maximum lap shear stress values than the hydraulic oil, the drops indicate that both contaminant types should be removed from bond surfaces.

Since after 9 days with dust applied, maximum lap shear stress values dropped 46% and 12% for specimens adhered with the MMA adhesive and film adhesives, respectively, the film adhesive was less sensitive to contamination than the MMA adhesive. The film adhesive was less sensitive to contamination likely due to the post-cure where the film adhesive decreased in viscosity when heated, which allowed the adhesive to flow around the stamped particles more effectively. The lower viscosity thus permitted a larger surface area to be adhered between the coupons.

Both the composite dust and hydraulic oil contaminated lap shear failure modes differed significantly from the control failure modes and from one another. Regardless of the adhesive used, contaminated lap shear specimens did not exhibit significant differences in neither maximum lap shear stress values nor failure modes from being

tested 2, 9, or 33 days after the specimens were manufactured, indicating that any diffusion effects that might have occurred along the bond line were negligible.

8. PLASMA CONTACT ANGLE TESTING

8.1 Plasma Contact Angle Methods

Specimens cut from the same composite plates as the solvent wipe contact angle tests were shipped to Enercon Industries Corporation for plasma treatments, followed immediately by contact angle testing. The same dimensions were used for plasma contact angle as solvent wipe contact angle testing (Figure 52). Specimens were sanded with FEPA 1000 grit sandpaper prior to shipment to remove mold release. Two areas on each sample were contact angle tested before and after being treated by either blown ion or flame treatments. Line speed was run at 30.5 cm per minute for both blown ion and flame treatments. The output used for the blown ion treatment was at 0.5 kW, and the output for the flame burner was 200 liters per minute. The distance between the blown ion treatment and the sample was 6.35 mm, and the distance between the flame treatment and the sample was 50.8 mm. The test matrix for plasma contact angle testing is in Table 28.

Table 28. The test matrix used for plasma contact angle testing.

Substrate Type	Treatment Type	Number of Tests	Output
$[0]_4$ epoxy	none (before flame treatment)	2	contact angle
	flame	2	contact angle
	none (before blown ion treatment)	2	contact angle
	blown ion	2	contact angle
$[+/- 45]_6$ epoxy	none (before flame treatment)	2	contact angle
	flame	2	contact angle
	none (before blown ion treatment)	2	contact angle
	blown ion	2	contact angle
$[0]_4$ vinyl ester	none (before flame treatment)	2	contact angle
	flame	2	contact angle
	none (before blown ion treatment)	2	contact angle
	blown ion	2	contact angle
$[+/- 45]_6$ vinyl ester	none (before flame treatment)	2	contact angle
	flame	2	contact angle
	none (before blown ion treatment)	2	contact angle
	blown ion	2	contact angle

8.2 Plasma Contact Angle Results

The contact angles of composites treated with blown ion and flame treatments are in Tables 29 and 30.

Table 29. Average contact angles of composite surfaces before and after blown ion treatment.

Treatment	$[0]_4$ Epoxy	$[+/- 45]_6$ Epoxy	$[0]_4$ Vinyl Ester	$[+/- 45]_6$ Vinyl Ester
Initial (before blown ion treatment)	73.5 ± 0.2	71.1 ± 0.7	75.0 ± 3.7	70.4 ± 3.7
After blown ion treatment	30.2 ± 2.2	30.6 ± 2.3	16.2 ± 0.0	22.9 ± 0.8

Across all the composite surface types in Table 29, there was a 66% drop between the average contact angles before and after blown ion treatment.

Table 30. Average contact angles and standard deviations of composite surfaces before and after flame treatment.

Treatment	$[0]_4$ Epoxy	$[+/- 45]_6$ Epoxy	$[0]_4$ Vinyl Ester	$[+/- 45]_6$ Vinyl Ester
Initial (before flame treatment)	70.2 ± 0.1	78.5 ± 2.5	63.5 ± 0.2	77.7 ± 1.3
After flame treatment	25.8 ± 0.4	28.9 ± 0.9	15.9 ± 0.4	18.8 ± 2.5

Across all the composite surface types in Table 30, there was a 69% drop between the average contact angles before and after flame treatment. Overall, contact angle dropped significantly between initial and plasma treated composite surfaces for both blown ion and flame treatments.

8.3 Plasma Contact Angle Conclusions

There was a 66% drop in contact angles on composite surfaces treated with blown ion plasma and a 69% drop in contact angles for composites treated with flame plasma. Since both blown ion and flame plasma treatments to composite surfaces decreased contact angle significantly, plasma treatments should continue to be considered in wind turbine blade field repair research. Plasma treatment is not likely to be feasible when technicians rappel from the nacelle to perform repairs but may be feasible when suspended platforms are used. Plasma treatment could also be used when the blade is accessible on the ground, such as for pre-installation repairs.

9. SCARF TENSION EXPERIMENTAL TESTING

9.1 Scarf Tension Experimental Methods

Scarf tension specimens were manufactured, then tested using DIC. Failure surfaces were photographed and imaged using FE SEM. EDS was used to obtain the weight percent (wt %) of elements C, O, Si, Ca, and Al on fibers and resin on the failure surfaces.

9.1.1 Scarf Tension Specimen Manufacturing

Scarf tension specimens were manufactured by co-bonding layers of glass fiber fabric onto a tapered composite plate. The tapered plate was manufactured by stacking 8 layers of unidirectional glass fiber fabric with stepped ends 1 cm apart. The stack was placed on a 38ºC caul plate, then impregnated with Hexion 135/1366 epoxy resin using VARTM (Figure 77). After curing under vacuum on the caul plate for 24 hours, the tapered composite plate was post-cured for 12 hours at 80ºC. After post-curing, the plate was cut, leaving 10 cm from the end of the tapered section to the top. The tapered section was wet sanded using a palm sander using P80 grit sandpaper, then hand sanded with P240 grit sandpaper. After hand sanding, the plate was rinsed with tap water to remove dust, then wiped using distilled water. The surface was wiped with a dry cloth to remove the distilled water. One half of the plate was covered in paper, then the paper was completely covered by painter's tape. The paper was used to ensure the adhesive from the painter’s tape did not leave a residue on the scarfed surface. The painter’s tape was used to block off one side of the plate so that sizing was not applied to the control surface.

Sizing was applied to the exposed half of the plate. To prepare the sizing, 6.6 grams of Michelman 181290IX sizing was dissolved in 300 mL of distilled water, resulting in a 1% solid content mixture. Sizing was sprayed in a sizing spray booth (Figure 78) onto the exposed, tapered surface for 5 seconds using a 0.01” diameter full-cone misting spray nozzle with a pressure of 30 psi and an 80-degree spray angle.

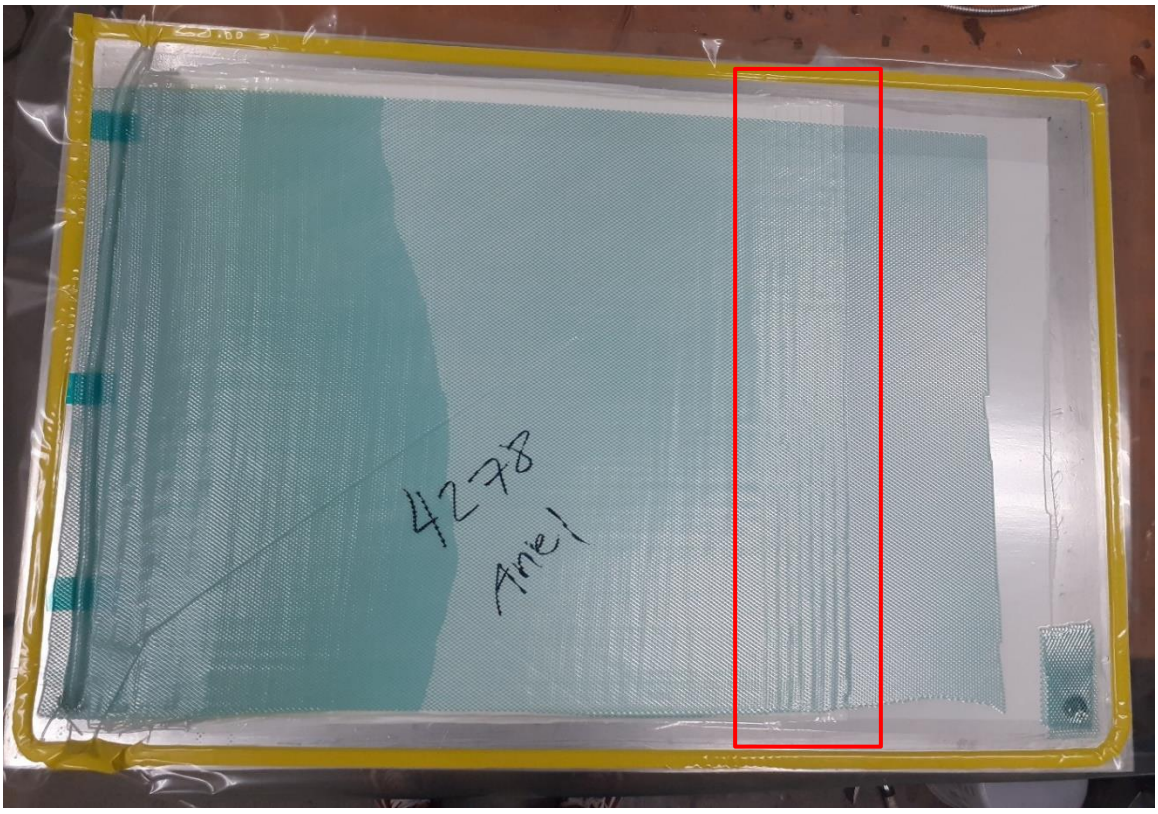

Figure 77. VARTM of the tapered plate used in scarf tension specimen manufacturing. The ply drops are in the red box. Each glass fiber ply used was the same dimension. The tapered area directly to the right of the spiral wrap was later removed and excess non-tapered material was used for the tension testing of non-scarfed specimens.

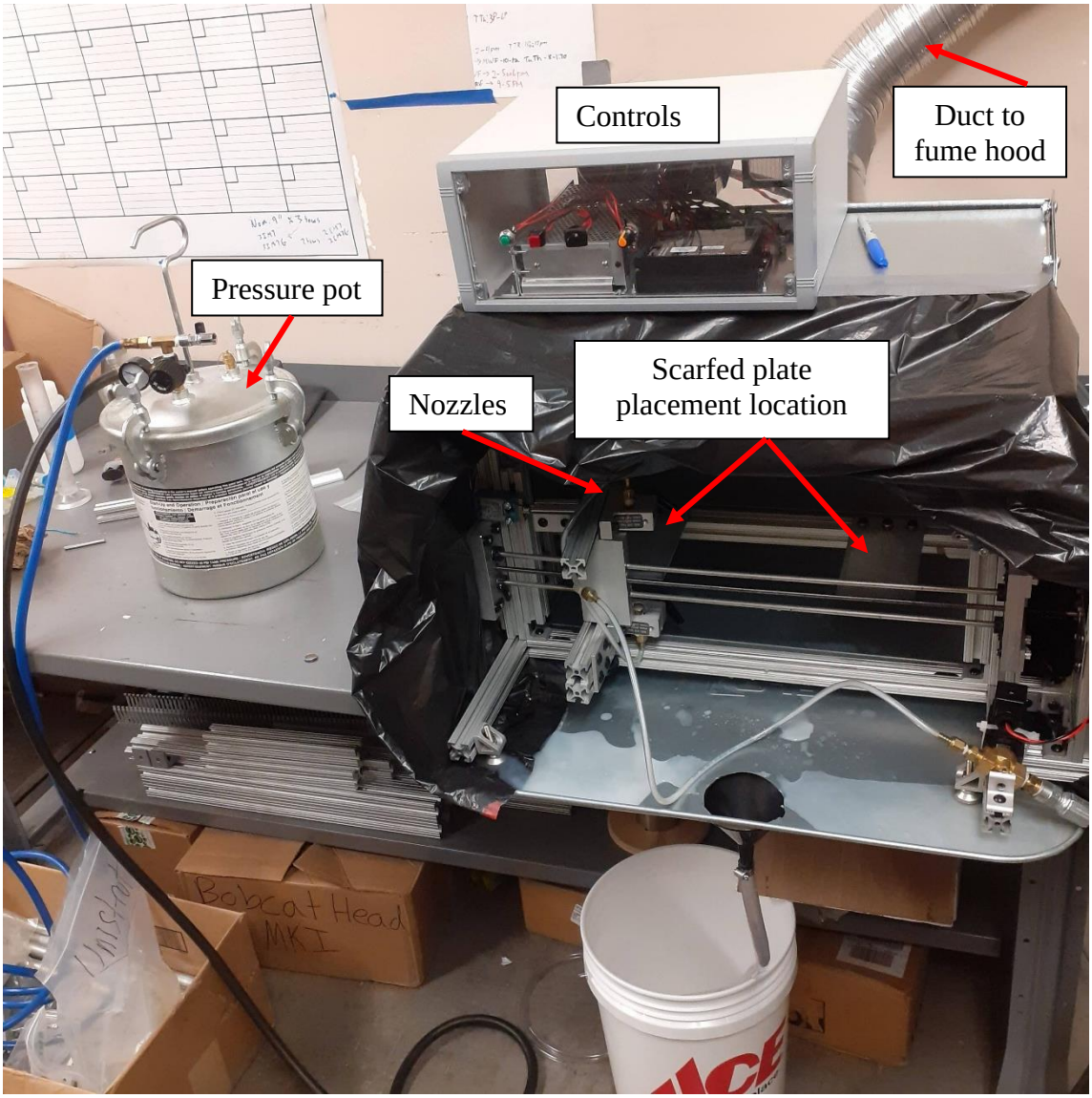

Figure 78. Sizing spray booth.

After sizing was applied to half of the tapered plate, the paper and painter's tape were removed. The tapered plate was placed back onto the caul plate for repair. To repair the tapered plate, 8 more layers of unidirectional glass fiber fabric were stacked with stepped ends 1 cm apart. Then, the stack was carefully flipped over and placed onto the tapered plate so that the stepped ends met the tapered side of the tapered plate (Figure

79). The new fibers were impregnated over the tapered plate with Hexion 135/1366 epoxy resin using VARTM (Figure 80). The repaired plate was post-cured for 12 hours at 80ºC. The plate was cut into 26 mm x 273 mm coupons with an average thickness of 6.13 mm (Figure 81). The average scarf angle was 5.2 ± 0.1°.

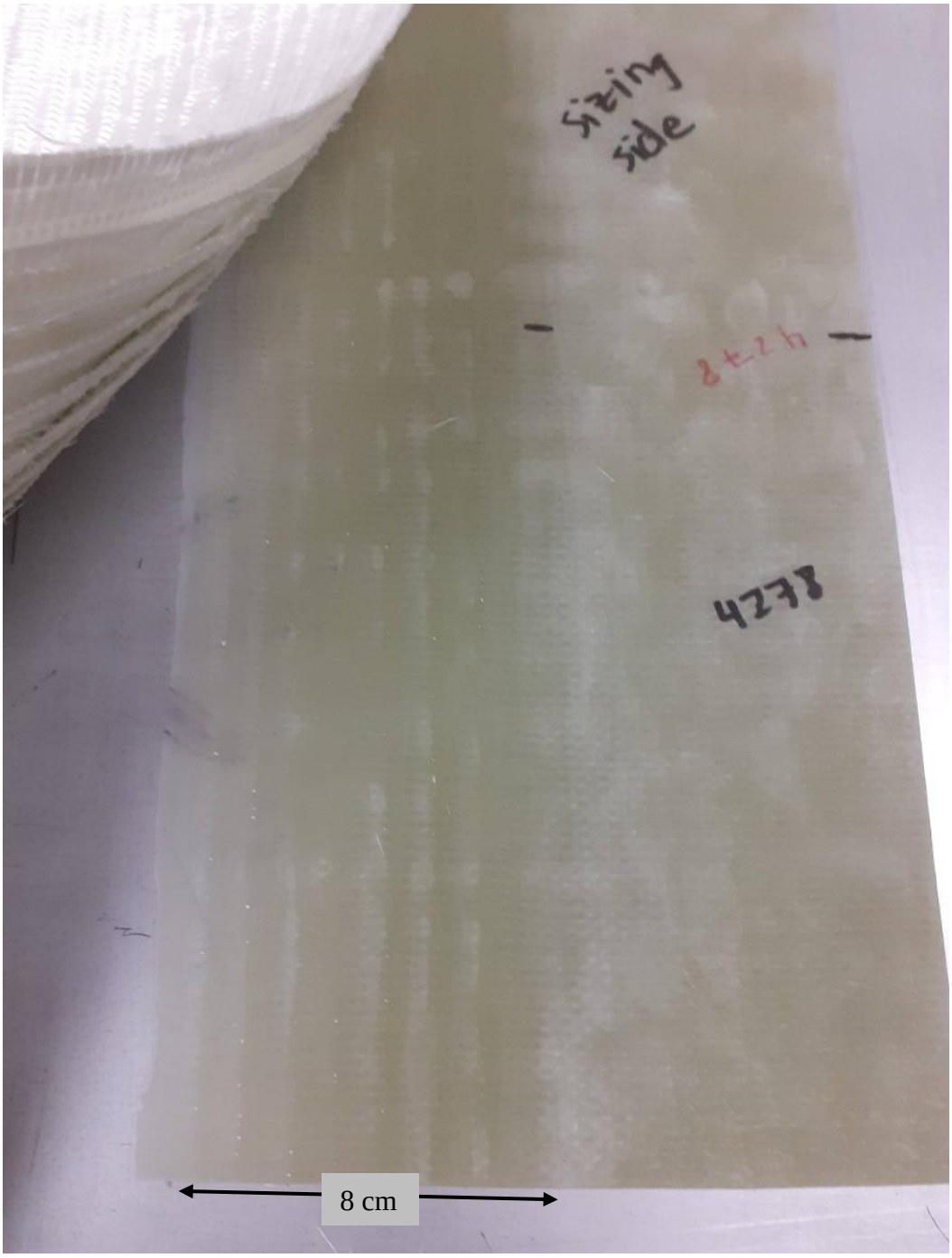

Figure 79. Scarfed GFRP composite plate with sizing on the top half and no sizing on the bottom half. Layers of glass fiber fabric are being placed on top of the cured plate (top left).

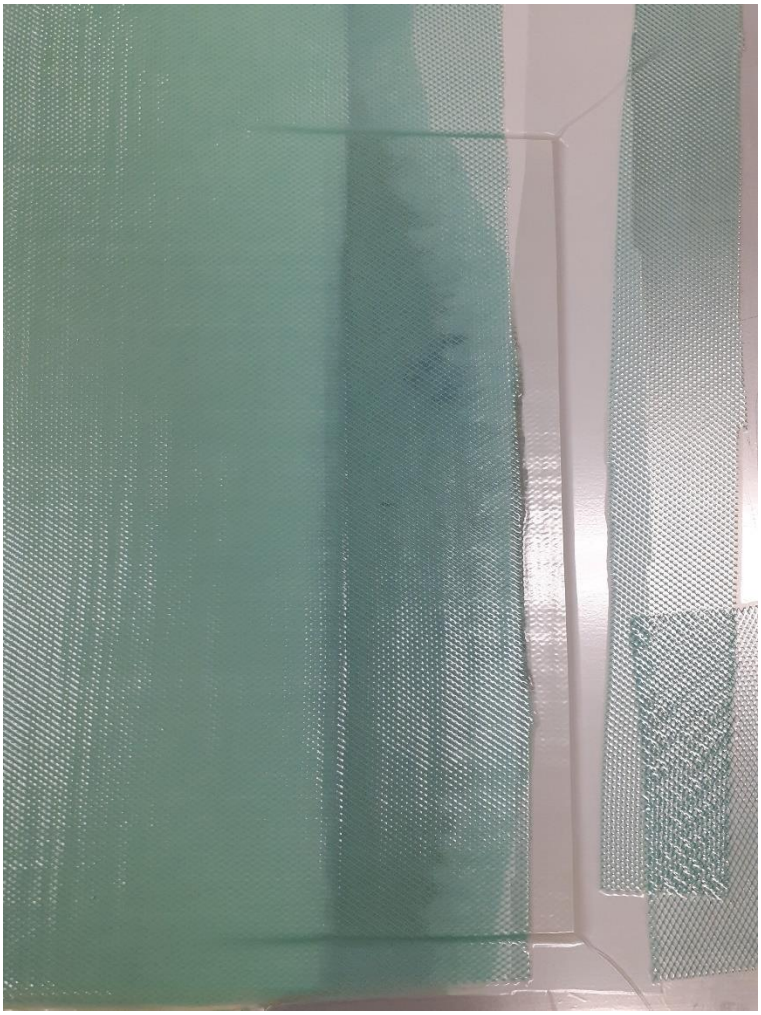

Figure 80. VARTM of glass fiber plies stacked onto the tapered plate.

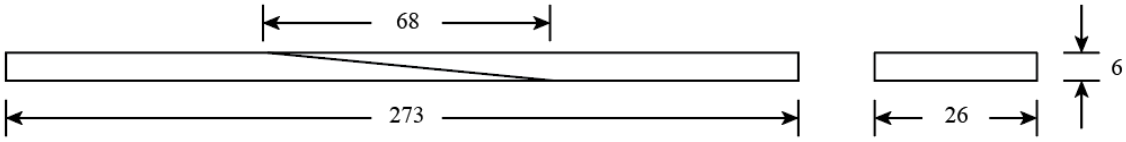

Figure 81. Side and cross-sectional views of composite scarf tension specimen dimensions (mm).

Although the tapered section was rinsed with tap water and wiped with distilled water, small pockets of contamination remained on the surface. In addition, fiber

exposure varied across the surface, as indicated by the lighter regions in the tapered section (Figure 79). To cut the glass fiber fabric from the roll, a rotary cutter was used, which created uneven edges as shown in the top left of Figure 79. A demonstration of how composite dust embeds into the discontinuity between ply drops is in Figure 82. There is a small layer of epoxy resin under the composite dust that remains unremoved by sanding, causing variation along the scarf tension bond line between exposed glass fibers and unremoved epoxy resin. The composite dust trapped in the discontinuities between ply drops is exclusive to the specimen manufacturing method studied and would not likely occur in field repairs. In field repairs, damage is removed from a more homogeneous material geometry instead of by sanding ply drops.

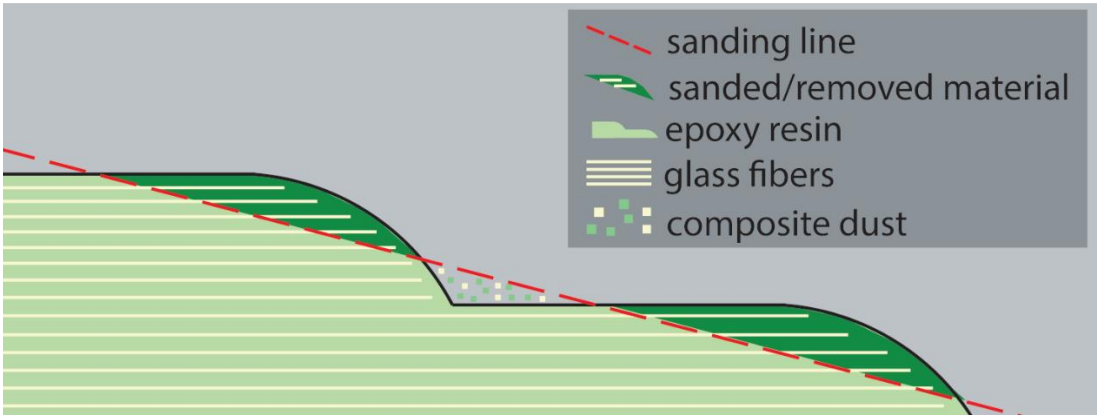

Figure 82. Side view schematic of two steps of tapered composite material with composite dust in the discontinuity.

The scarf tension specimens had a slight indentation where the repair plies met the top of the tapered section of the original plate, which is shown along the lower line of

blue dashes in Figure 83. Resin-rich regions are located at the slight indentations (Figure 84).

Figure 83. Laminate edge view of scarf tension specimens with scarfed region marked by blue dashes.

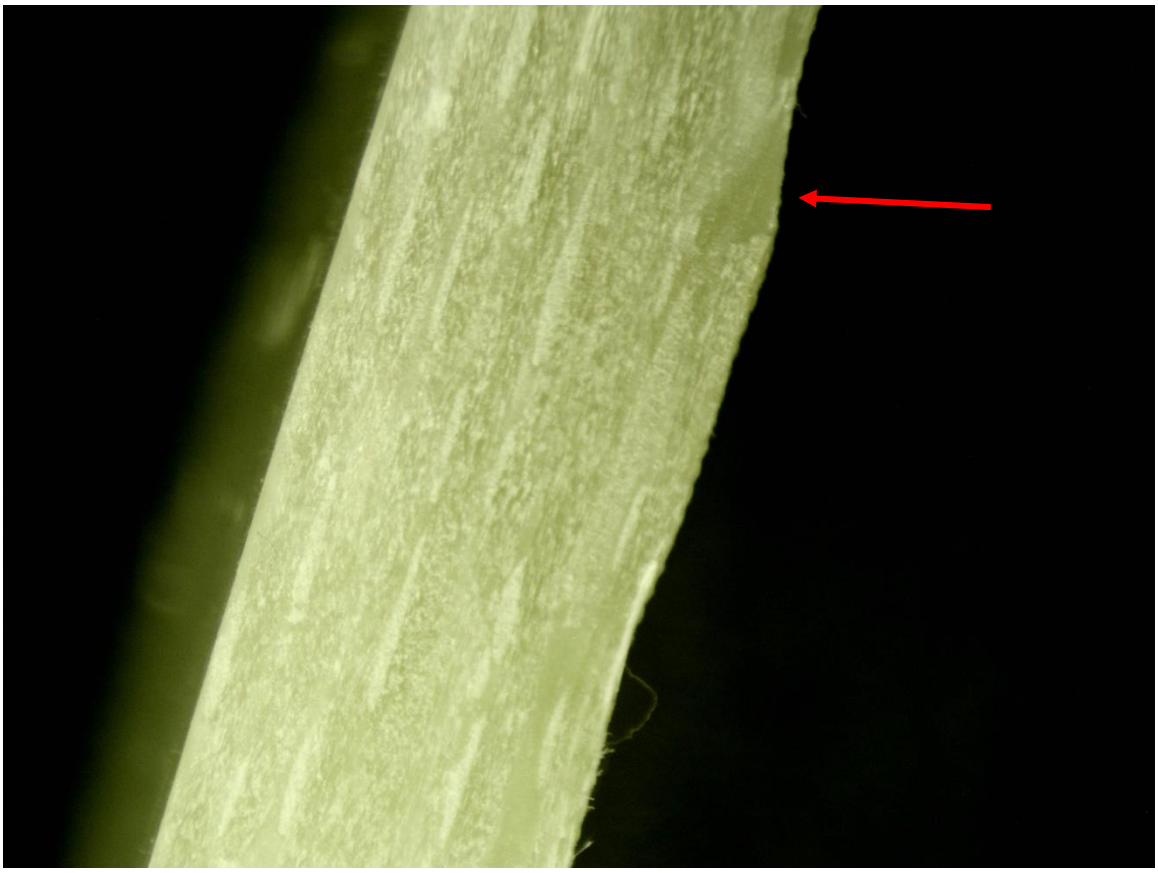

Figure 84. Side view of scarf tension specimen with red arrow pointing at the resin-rich region.

9.1.2 DIC Methods

After scarf tension specimens were manufactured, a stochastic pattern was applied to one side of each specimen for DIC testing using flat white spray paint followed by speckling black spray paint (Figure 85). Loads were tracked during scarf tension testing using Aramis Professional 2020 software. In addition, stages (frames) were acquired during testing. A 0.0254 cm/sec load rate was used. Scarf tension specimens were tested to failure, while non-scarfed tension specimens were tested to approximately 38,000 N. Non-scarfed tension specimens were too thick to test to failure, so stress-strain curves

were used to compare scarfed and non-scarfed tension specimens. After specimens were tested, stages were analyzed to calculate logarithmic strain in Aramis. Surface components were created after each test to select an area of interest for strain calculations. The number of pixels were 19 and 16 for the facet size and point distance, respectively. A 3-2-1 alignment was applied to assign a coordinate system to the surface component. A virtual extensometer was used to calculate strain and placed below the scarfed region to mitigate effects from the x-components of strain (Figure 86). A user-defined inspection was used on the surface component to calculate the natural log of the y-component of strain. A more detailed procedure for natural log calculations is in Appendix C.

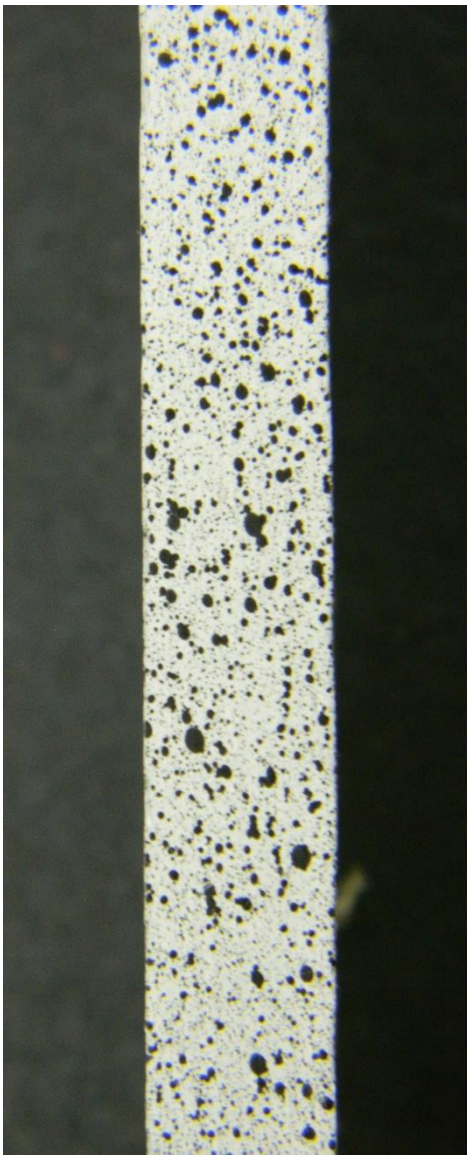

Figure 85. Side view of scarf tension specimen showing the stochastic pattern that had been applied using white, then black-speckled spray paint

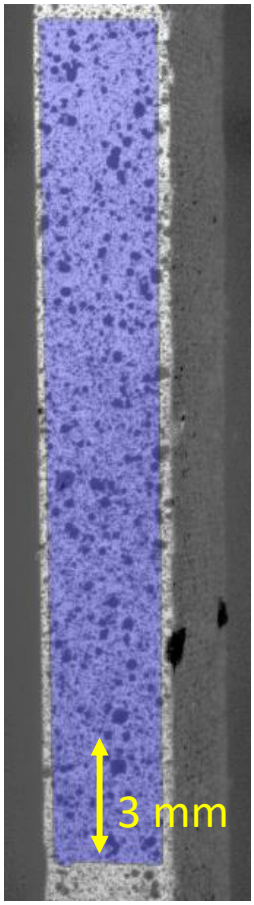

Figure 86. The location of the 3 mm virtual extensometer used in Aramis is indicated by the yellow double-headed arrow. The blue rectangle is the surface component at 0% strain.

9.1.3 SEM and EDS Methods

For the FE SEM studies, since GFRP composites are not conductive, scarf tension failure surfaces were sputter coated with Iridium for 60 seconds at 20 mA. The FE SEM was used to compare the scarf tension failure surfaces treated and not treated with sizing. EDS was used to map elemental spectra from scarf tension failure surfaces treated and not treated with sizing. Spectra were also collected from fiber and resin surfaces. The testing for scarf tension DIC, FE SEM, EDS, and FEA is summarized in Table 31.

Table 31. The test matrix that was used for scarf tension experimental testing.

Test Method	Treatment Type	Number of Tests	Outputs
DIC	sizing	5	force-displacement, stress-strain, strain contour prior to failure, visual failure modes
	none	5	force-displacement, stress-strain, strain contour prior to failure, visual failure modes
	not scarfed	5	stress-strain
FE SEM	sizing	2	failure modes in peel and shear regions
	none	2	failure modes in peel and shear regions
EDS	sizing	1	spectra for the fiber and matrix
	none	1	spectra for the fiber and matrix

9.2 Scarf Tension Results

9.2.1 Scarf Tension DIC Results

Scarf tension specimens were tested using DIC and simulated in Abaqus. The average maximum tensile stress values for experimentally tested specimens with sized surfaces and unsized surfaces were 257 ± 16 MPa and 248 ± 25 MPa, respectively. A t-test did not indicate any significant differences in the maximum tensile stress values. Non-scarfed tension specimens were tested and compared with scarf tension specimens. The stress-strain results are in Figure 87.

There were no significant differences in stress-strain results between scarf tension specimens treated and untreated with sizing. Non-scarfed tension specimens were not run to failure due to the high material thicknesses for Figure 87. In previous tension testing of the $[0]_8$ laminates, the average ultimate tensile strength was 980 ± 64 MPa.

There was a stiffness reduction in the scarfed specimens compared to the non-scarfed specimens at approximately 0.45% strain.

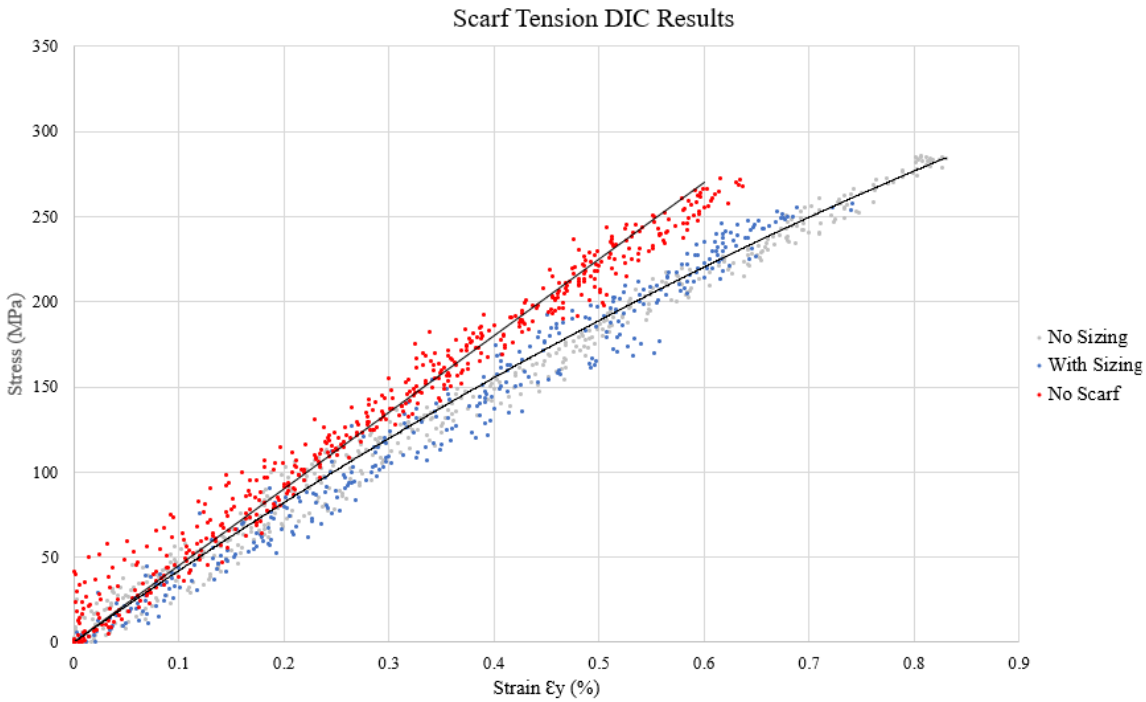

Figure 87. DIC stress-strain results between sized scarfed, not sized scarfed, and non-scarfed tension specimens.

In each image in Figure 88 the failure surfaces in the top rows had some delamination in the scarfed plies but the delamination was not as extensive as in the bottom rows of coupons. The bottom rows of coupons likely had more delamination because the ply surfaces had been sanded and thus were thinner than the top plies. All scarf tension specimens exhibited cohesive failure modes.

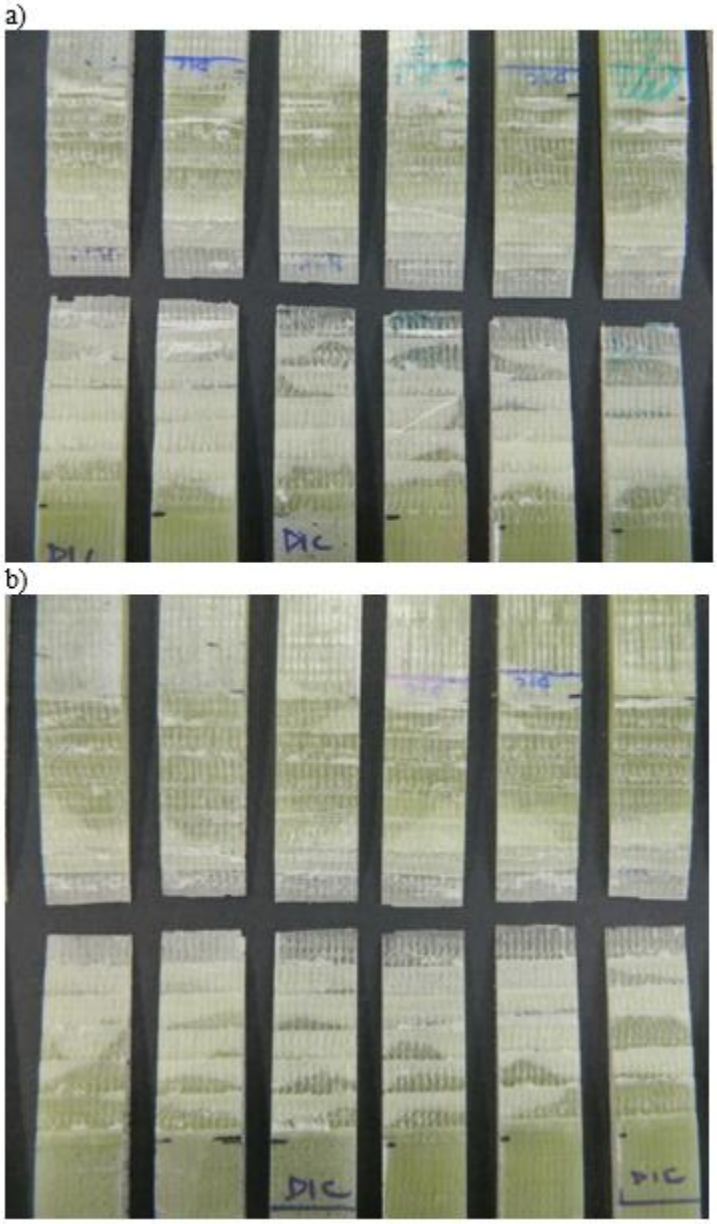

Figure 88. Scarf tension failure surfaces for specimens that a) had sizing applied to surfaces and b) did not have sizing applied to surfaces. The top rows of specimens in both a) and b) were the "repair" plies, while the bottom rows were the sanded plies.

Additional DIC results including force-displacement and stress-strain curves are reported in Section 10.2: Comparing Simulated and Experimental Scarf Tension Results.

9.2.1 FE SEM Results

FE SEM was used compare sized and not sized scarf tension failure surfaces (Figures 89, 90, and 91). EDS was used to map the elements on sized and not sized scarf tension failure surfaces (Figures 92, 93, and 94).

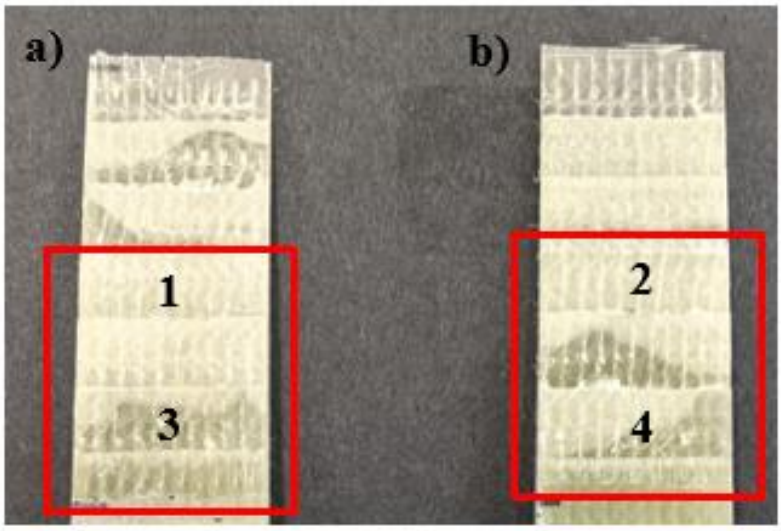

Figure 89. Scarf tension specimens selected for FE SEM failure surface analysis. Surface a) had sizing applied and surface b) did not have sizing applied. The regions in the red boxes were cut and analyzed. Points 1 and 2 exhibited more shear stresses during testing and were compared in Figure 90. Points 3 and 4 exhibited more peel stresses during testing and were compared in the FE SEM images in Figure 91. EDS mapping was also done on points 3 and 4 (Figure 91).

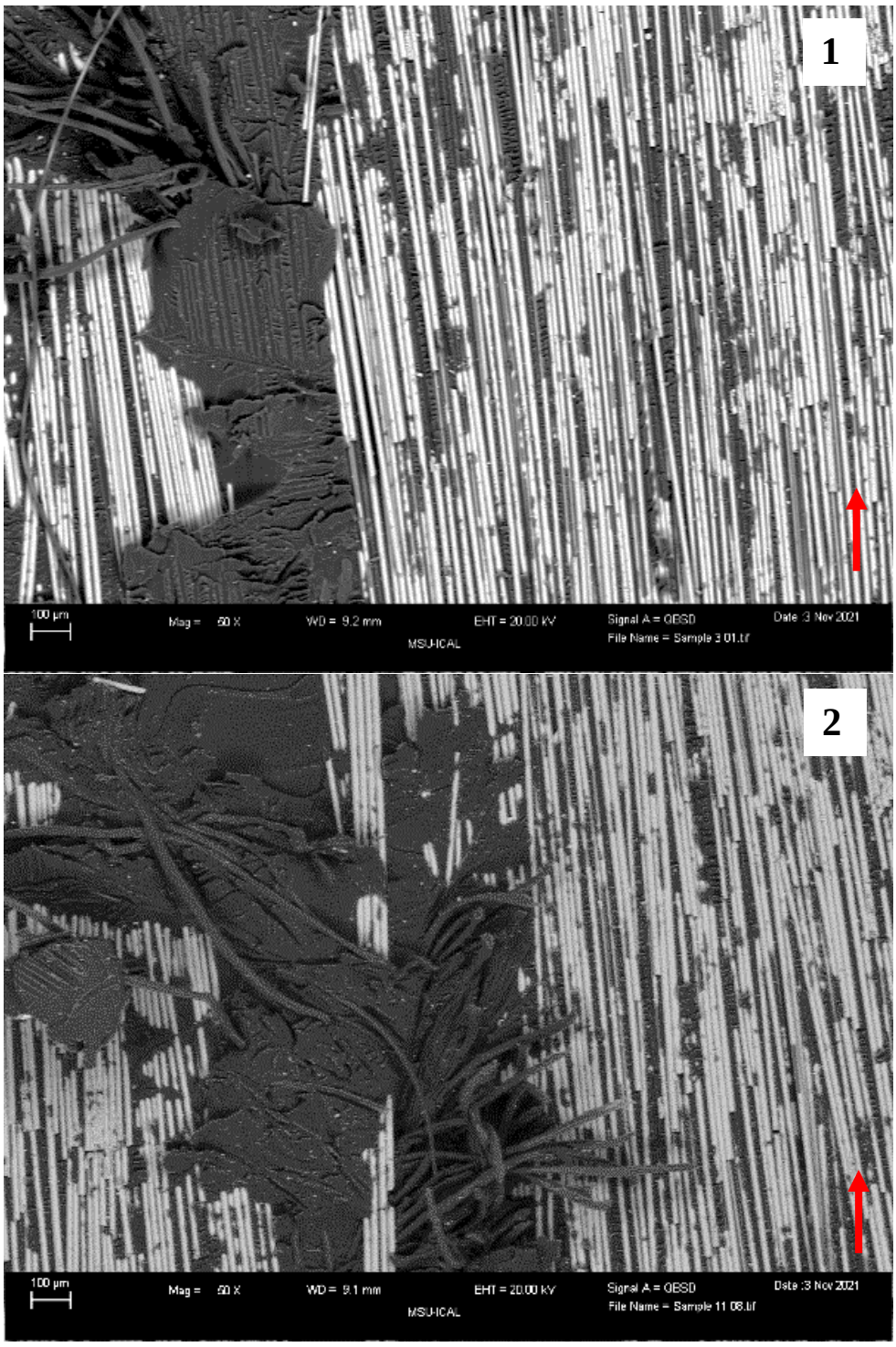

Figure 90. Scarf tension FE SEM images at shear stress locations (points 1 and 2 in Figure 89). Scarf tension shear stress FE SEM images. Image 1 had sizing applied to the surface prior to repair and scarf tensions testing, while image 2 had not. Both images were at 50x magnification. The fracture directions are indicated by the red arrows.

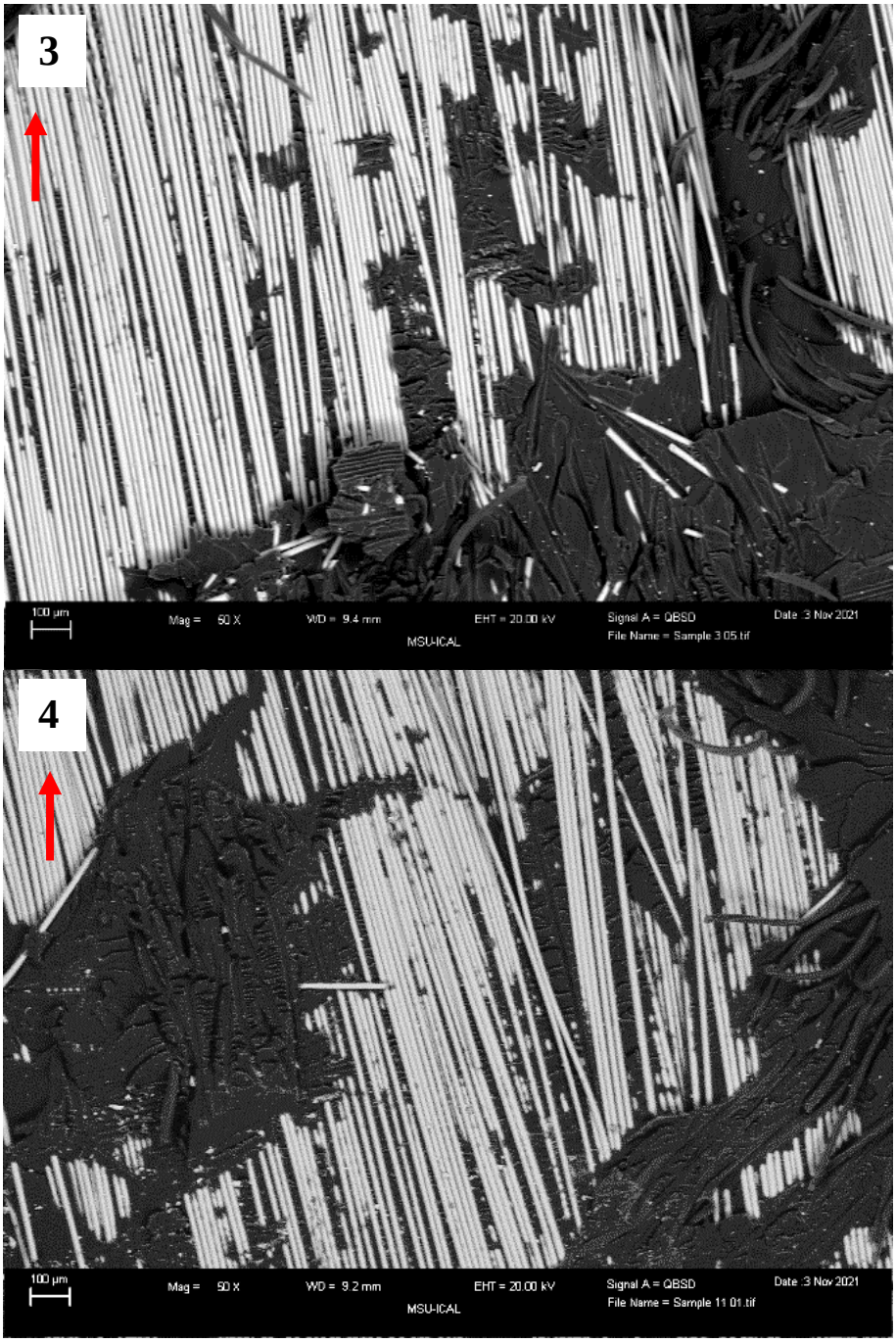

Figure 91. Scarf tension FE SEM images at peel stress locations (points 3 and 4 in Figure 89). Image 3 had sizing applied to the surface prior to repair and scarf tensions testing, while image 4 had not. Both images were at 50x magnification. The fracture directions are indicated by the red arrows.

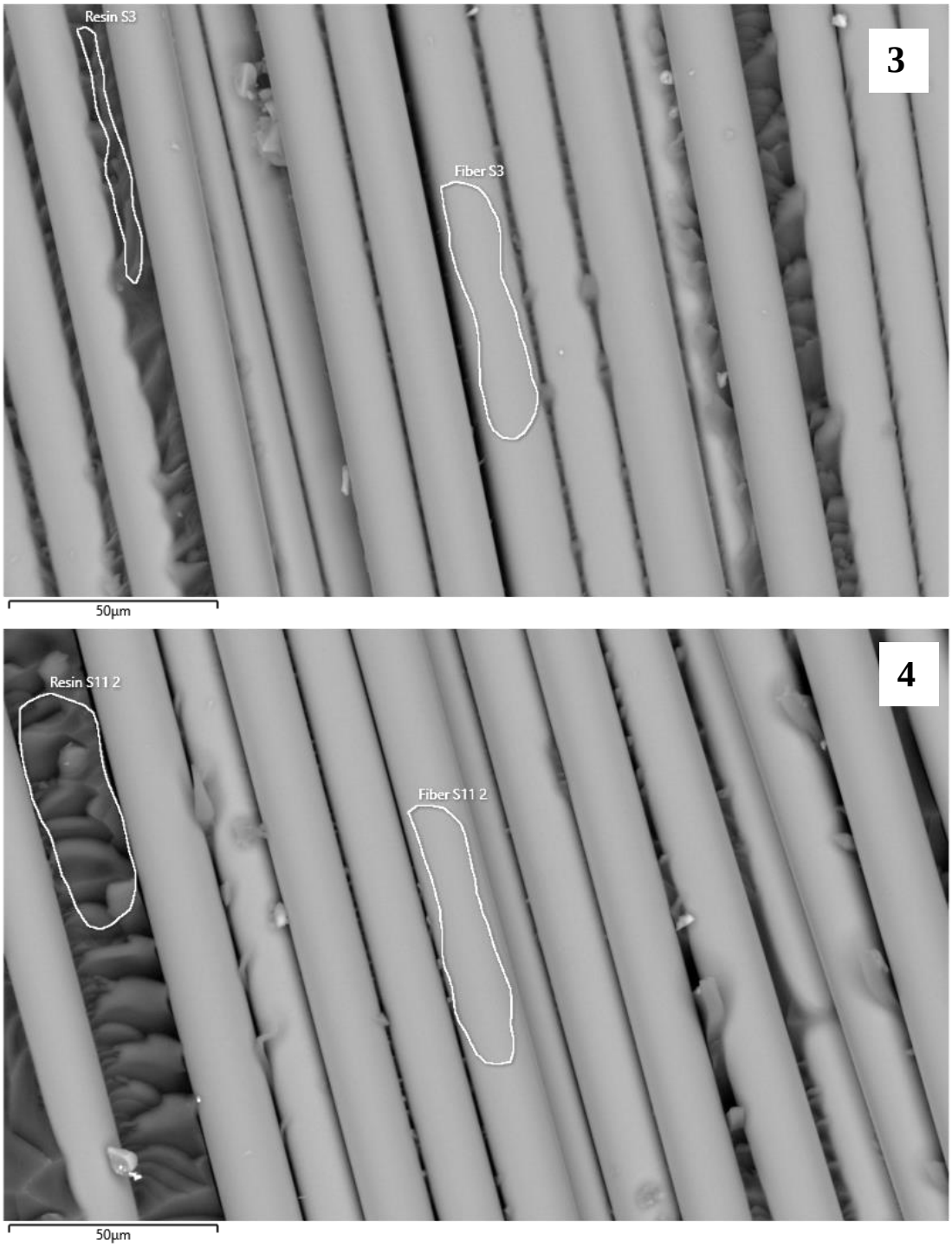

Figure 92. FE SEM images used for EDS at points 3 (sized) and 4 (not sized) from Figure 89. The circled regions were used for EDS analyses in Figures 93 and 94. The darker regions are the epoxy resin, and the lighter regions are the glass fibers.

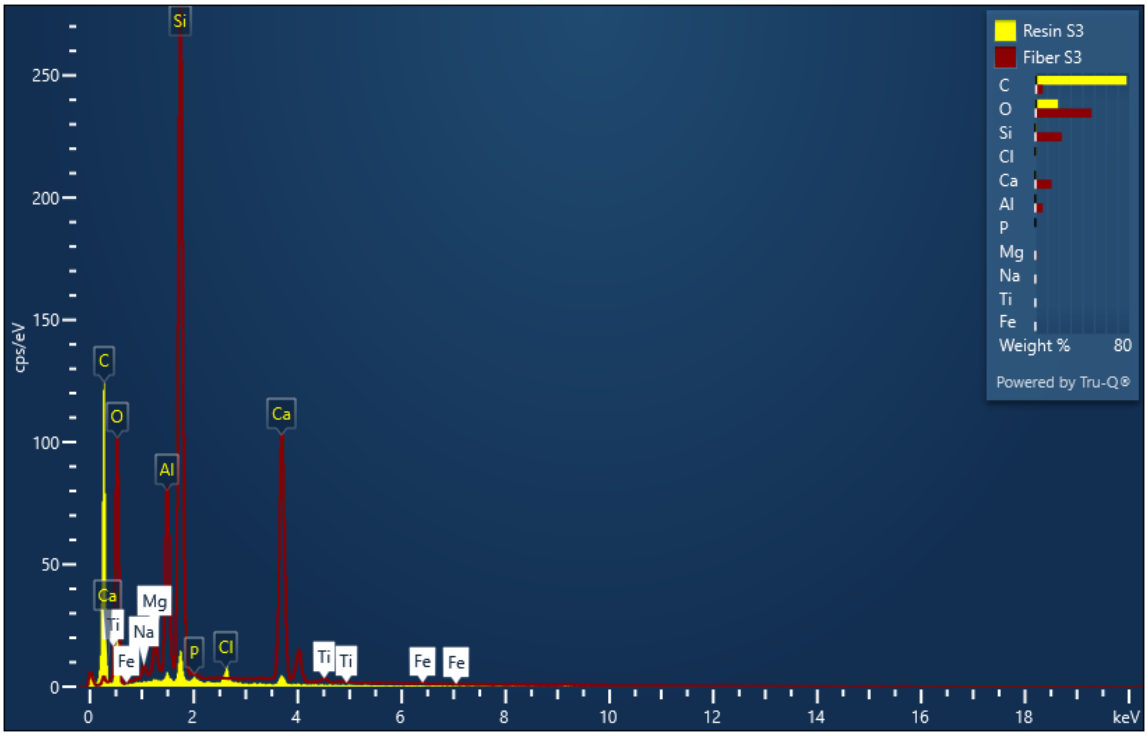

Figure 93. Elemental mapping of the epoxy resin (yellow) compared to the fibers (red) from point 3 (sized) in Figure 92.

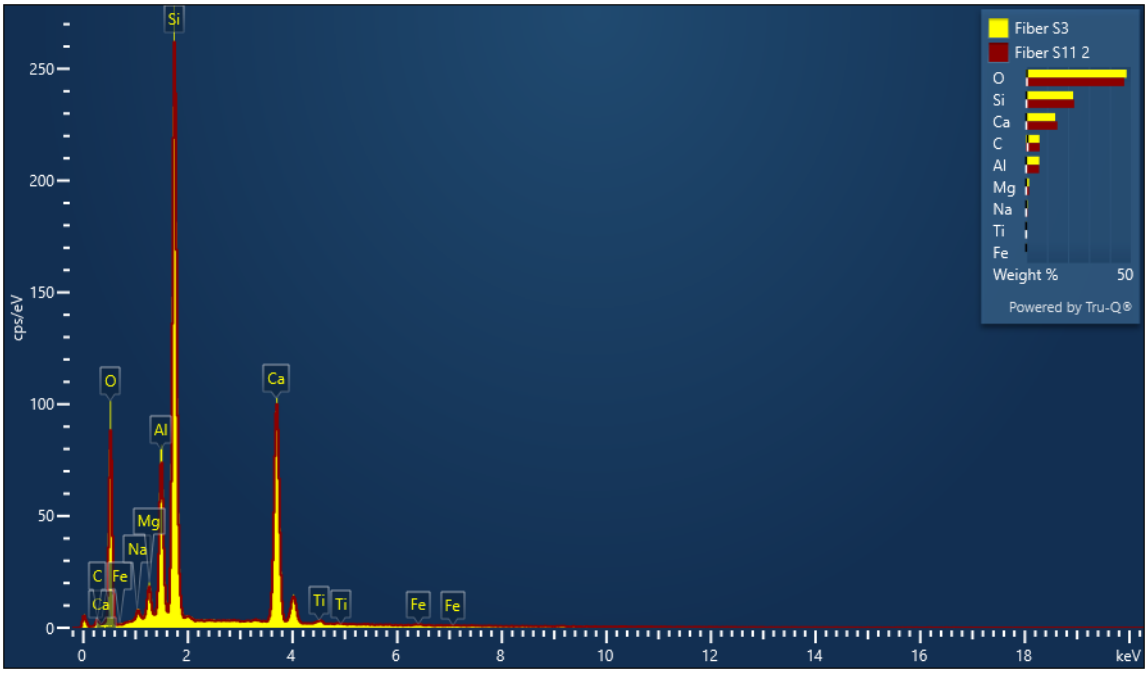

Figure 94. Elemental mapping of fibers with yellow showing the sized surface (point 3 from Figure 89), and red unsized (point 4 from Figure 89).

Table 32. Summary of EDS results at peel stress locations.

	sized		not sized	
wt %	resin	fiber	resin	fiber
C	75	5	80	5
O	20	45	15	45
Si	0	20	0	20
Ca	0	15	0	15
Al	0	5	0	5

The epoxy resin contained higher proportions of carbon, while the glass fibers showed more silicon, calcium, and aluminum. Fibers exhibited a higher proportion of oxygen peaks than the resin. There were no significant differences between the fibers on the surfaces that had been sized and not sized in Figure 94.

9.3 Scarf Tension Conclusions

Overall, applying sizing to tapered surfaces prior to scarf repairs did not affect scarf tension ultimate stress values, failure modes, or failure surface elemental composition. Factors that may have caused variation in maximum tensile stress values from the scarf tension tests were due to specimen manufacturing processes including sanding, slight shifting of glass fiber plies, and variations along the edges of glass fiber plies from cutting by hand. The variations from the scarf tension specimen manufacturing methods may have prevented smaller differences or effects from the sizing application on the surface from being detected. However, similar factors also play a role in wind turbine blade field repairs.

The stiffness reduction in the scarf specimens compared to the non-scarfed specimens at 0.45% strain is because the stiffness of the composite was not fully restored

using the scarf joint. A composite's stiffness is largely determined by the continuity in the fibers and methods are not currently available to restore fiber continuity. Therefore, wind turbine blades must be designed so that allowable stiffness reductions in areas along the blade are understood. Understanding allowable stiffness reductions will inform repair design decisions so that wind turbine blade design can shift from the safe-life approach more towards a damage tolerant approach.

FE SEM images of scarf tension failure modes did not have notable differences between the surfaces that had had sizing applied and those that did not. In addition, EDS results did not have significant differences between the fibers that had had sizing applied and those that did not. Furthermore, adding sizing to a repair surface will neither improve nor worsen repair surfaces. Additional conclusions for experimental testing will be discussed in Chapter 11 after the comparisons of experimental results with simulated results in Section 10.2.

10. SCARF TENSION SIMULATION

10.1 Scarf Tension Simulation Methods

One experimental scarf tension specimen's properties and dimensions were entered into and analyzed using Abaqus FEA. Identical methods were used to simulate results for hypothetical specimens with 3 and 7 degree scarf angles. Mixed-mode CZM was used. The parts, material parameters, section creation, assembly, step, boundary conditions, mesh, and history output requests used are described. Outputs were compared with DIC results. The testing used for the scarf tension simulation is summarized in Table 33.

Table 33. The test matrix for scarf tension simulation testing.

Test Method	Treatment Type	Number of Tests	Outputs
FEA	none	5	force-displacement, stress-strain, strain contour prior to failure

10.1.1 Parts

Parts were created using the measured dimensions of one of the scarf tension specimens that was tested using DIC. A rectangle with a 0.01 mm width was used for the adhesive. The length of the adhesive rectangle is equivalent to the length of the tapered portion of the part in Figure 95.

Figure 95. Left side of the scarf tension specimen with two partitions. The red arrow indicates the part thickness of 6.16 mm.

10.1.2 Materials

Two materials were used to model the scarf tension specimen: the $[0]_8$ GFRP composite and the Hexion 135/1366 epoxy resin. The Quads damage criterion was used to model the adhesive with the properties in Table 34. Traction type elastic material behavior was used. Damage evolution with energy type, linear softening, maximum degradation, B-K mixed mode behavior, energy mix mode ratio, and a power of 1.75 was used. A viscosity coefficient of 0.001 was used for cohesive damage stabilization. A density of 1.15×10^{-6} tonne/mm^3 was used.

Table 34. Hexion 135/136 constants used in Abaqus.

Cohesive constants	
Nominal Stress Normal-Only Mode (t_n^0)	26
Nominal Stress First Direction (t_s^0)	26
Nominal Stress Second Direction (t_t^0)	26
Normal Mode Fracture Energy	0.3185
Shear Mode Fracture Energy First Direction	2.094
Shear Mode Fracture Energy Second Direction	2.094
E/Enn	1000
G1/Ess	1000
G2/Ett	1000

10.1.3 Section

The out-of-plane width of 26.75 mm was entered in the "Section" part of the setup under plane stress/plane strain thickness for the solid, homogeneous material. The out-of-plane width of 26.75 mm was also used for the cohesive section. A traction-separation response was selected for the cohesive section.

10.1.4 Assembly

Dependent part instances were used for the assembly. Frictionless tangential behavior and "Hard" contact properties for normal behavior were used for the interaction properties. A surface-to-surface interaction with a finite sliding formulation was used between the left and right composite parts. Tie constraints were used to eliminate relative motion between the cohesive part surfaces and the corresponding composite part surfaces.

10.1.5 Step

A time period of 1 was used with nonlinear geometry turned on. An automatic stabilization damping factor of 5×10^{-5} was used. The maximum number of increments used was 10000, with an initial increment size of 0.0001, a minimum increment size of 1×10^{-12}, and a maximum increment size of 0.001.

10.1.6 Boundary conditions

A ramp amplitude with a uniform distribution in the y-direction and set to zero in the x-direction for the displacement boundary conditions on the bottom edge nodes. An encastre boundary condition was applied to the top edge of the assembly. The maximum y-displacement amplitude from Aramis was used for the displacement boundary condition.

10.1.7 Mesh

Totals of 1388 plane strain (CPE4R) and 230 linear triangular elements were used for each composite part and 132 cohesive (COH2D4) elements were used for the adhesive part. CPE4R elements have four nodes, reduced integration, and hourglass control. COH2D4 elements have four nodes and two integration points (Figure 96). Quad-dominated free element shapes were used for the composite part (Figure 97) with triangular plane strain elements (CPE3) placed near the tip of the tapered region (Figure 98). CPE3 is a 3-node linear plane strain triangular element. Quad structured elements were used for the cohesive part.

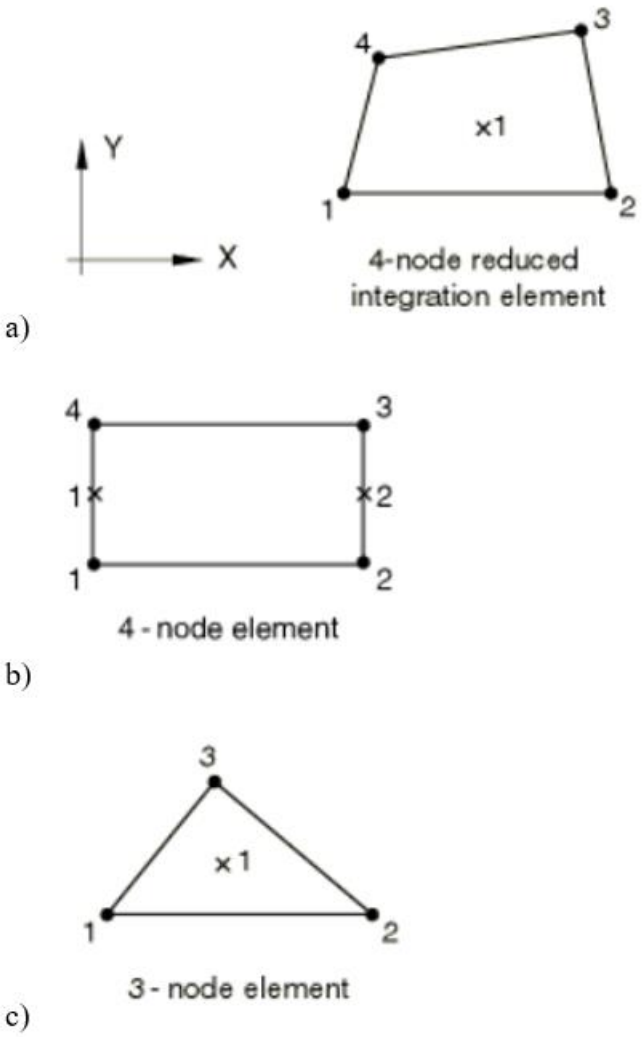

Figure 96. The element types used in the FEA models: a) CPE4R plane strain element. b) Cohesive COH2D4 element with four nodes and the two integration points indicated by the two x's. c) CPE3 triangular plane strain element.

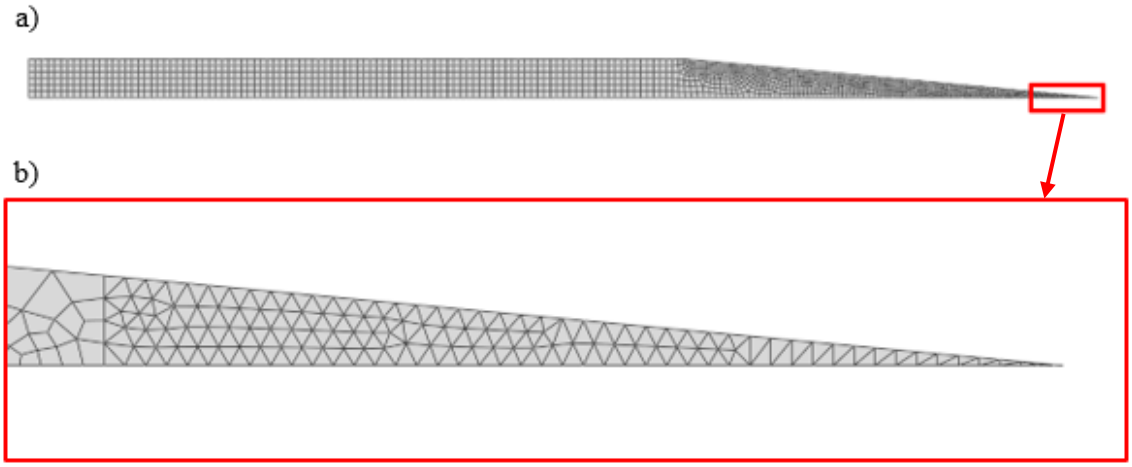

Figure 97. a) One side of scarf tension specimen showing mostly quad-dominated elements, with the location of the triangular elements in the red box. b) Zoomed in triangular elements.

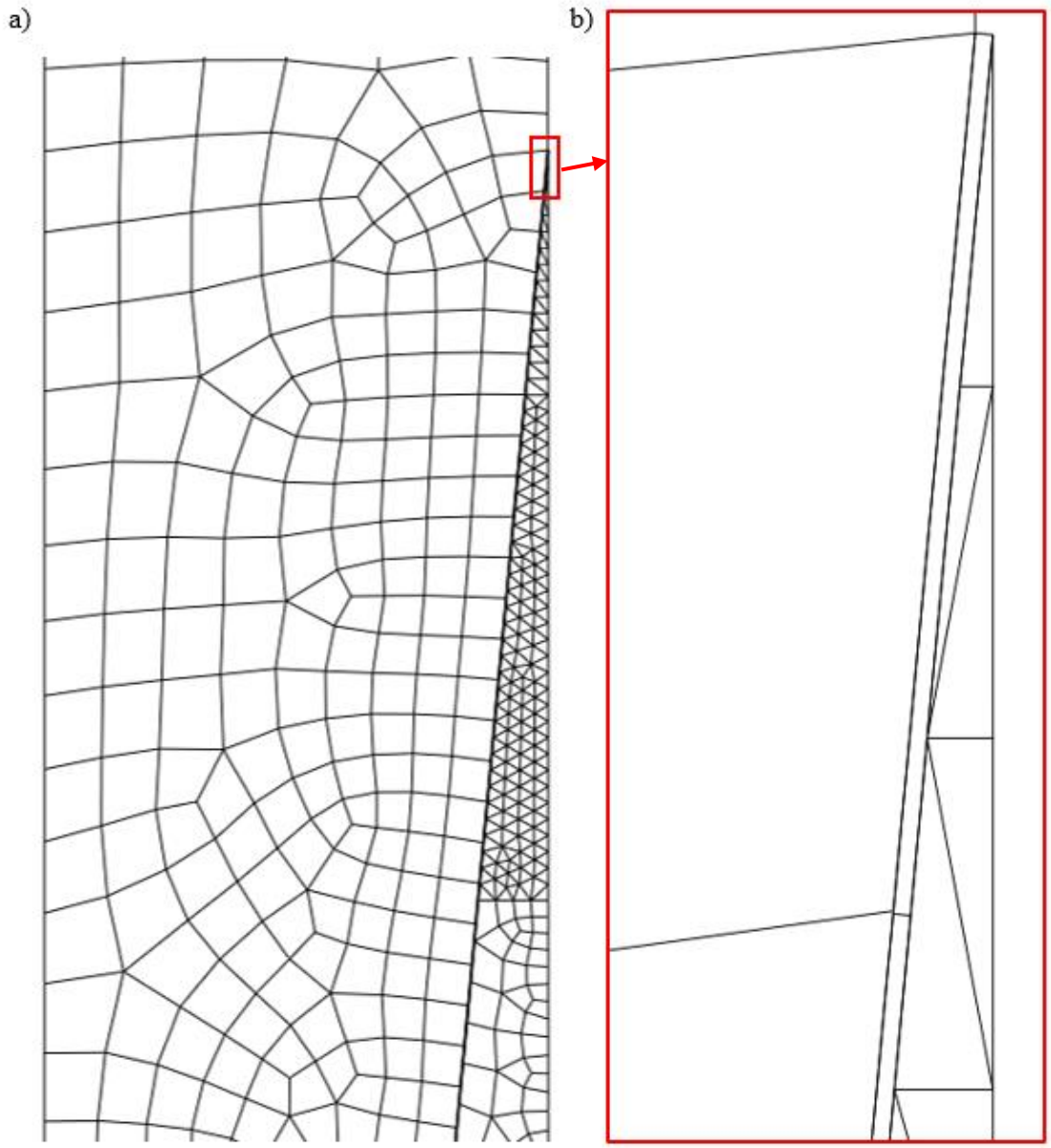

Figure 98. a) Assembled scarf tension mesh with the location of the tip of the right composite section tied to the cohesive zone section in the red box. b) Zoomed in tip showing thin cohesive section between composite bulk sections.

10.1.8 Output requests

Field and history output requests were selected in Abaqus at the locations shown in Figure 99. The field output requests included the logarithmic strain (LE) over the

whole model and the stress (S) in element set A. The history output requests are listed in Table 35.

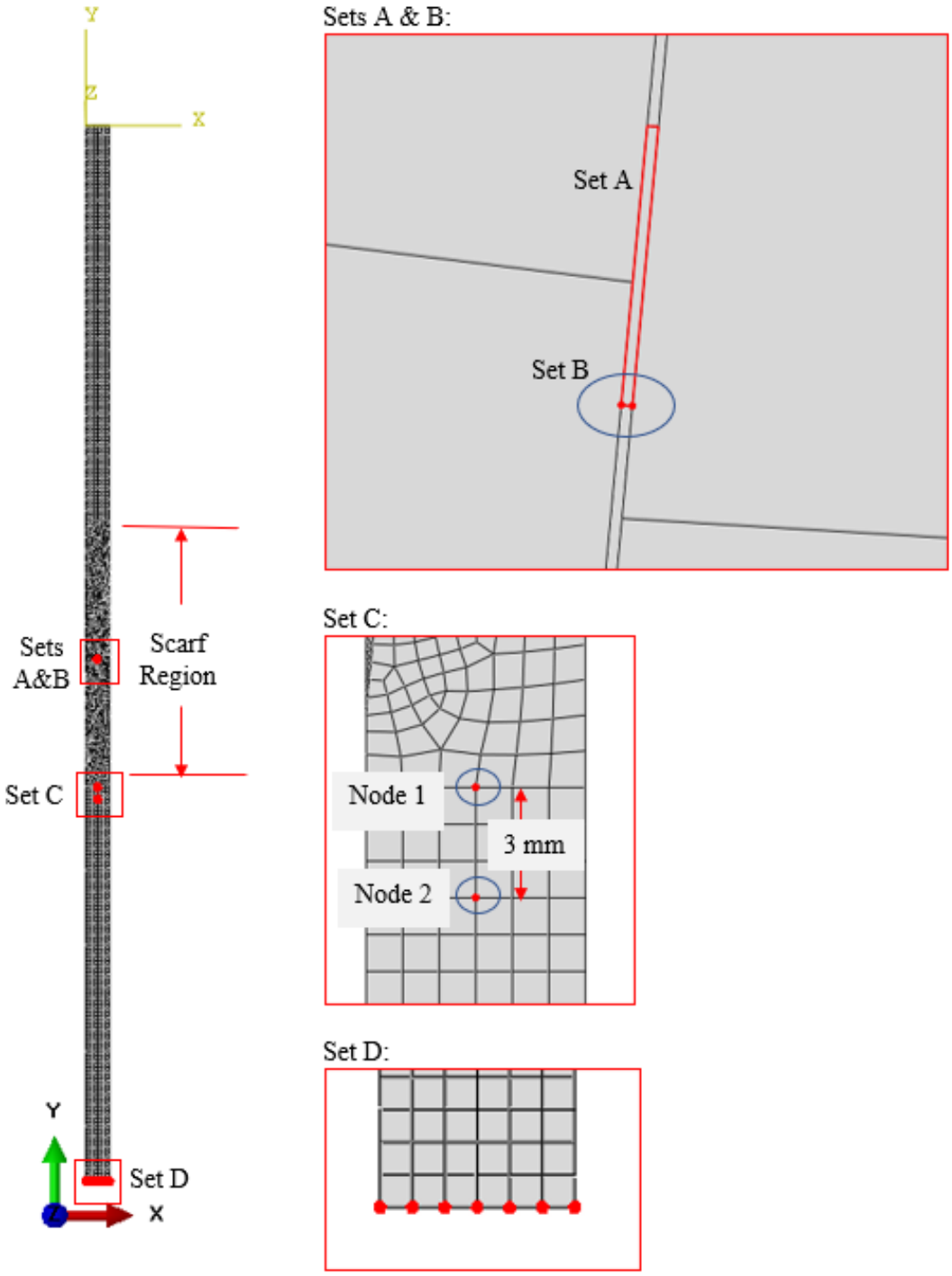

Figure 99. The node and element sets used for output requests.

Table 35. History output requests, where the set locations in the model are indicated in Figure 99.

Output	Set
Coordinates (COOR1, COOR2)	B
Y-Displacement (U2)	C
Reaction Force (RF), Y-Displacement (U2)	D

10.2 Comparing Simulated and Experimental Scarf Tension Results

` The logarithmic strain contour maps in the y-direction at a displacement of 1.44 mm were compared between Abaqus (Figure 100) and Aramis (Figure 101). The displacement of 1.44 mm was used because the displacement at the frame before failure in Aramis was 1.44 mm. In the Aramis results, the red, higher strain regions in Figure 101 corresponded with the location of the scarfed bond line. The red regions are not uniform along the joint because there was higher strain at the discontinuities caused by individual ply drops. Besides the lower uniformity along the bond line, the overall strain distribution in the adherends was more uniform like the strain distributions in the adherends in the Abaqus results (Figure 101). In addition, there were higher strains at the pointy tips of the adherends in both strain contour maps. The higher strains at the pointy tips of the adherends were due to the higher peel stresses. The ends of the delaminated plies in Figure 102 correspond with the high strain regions in Figure 101.

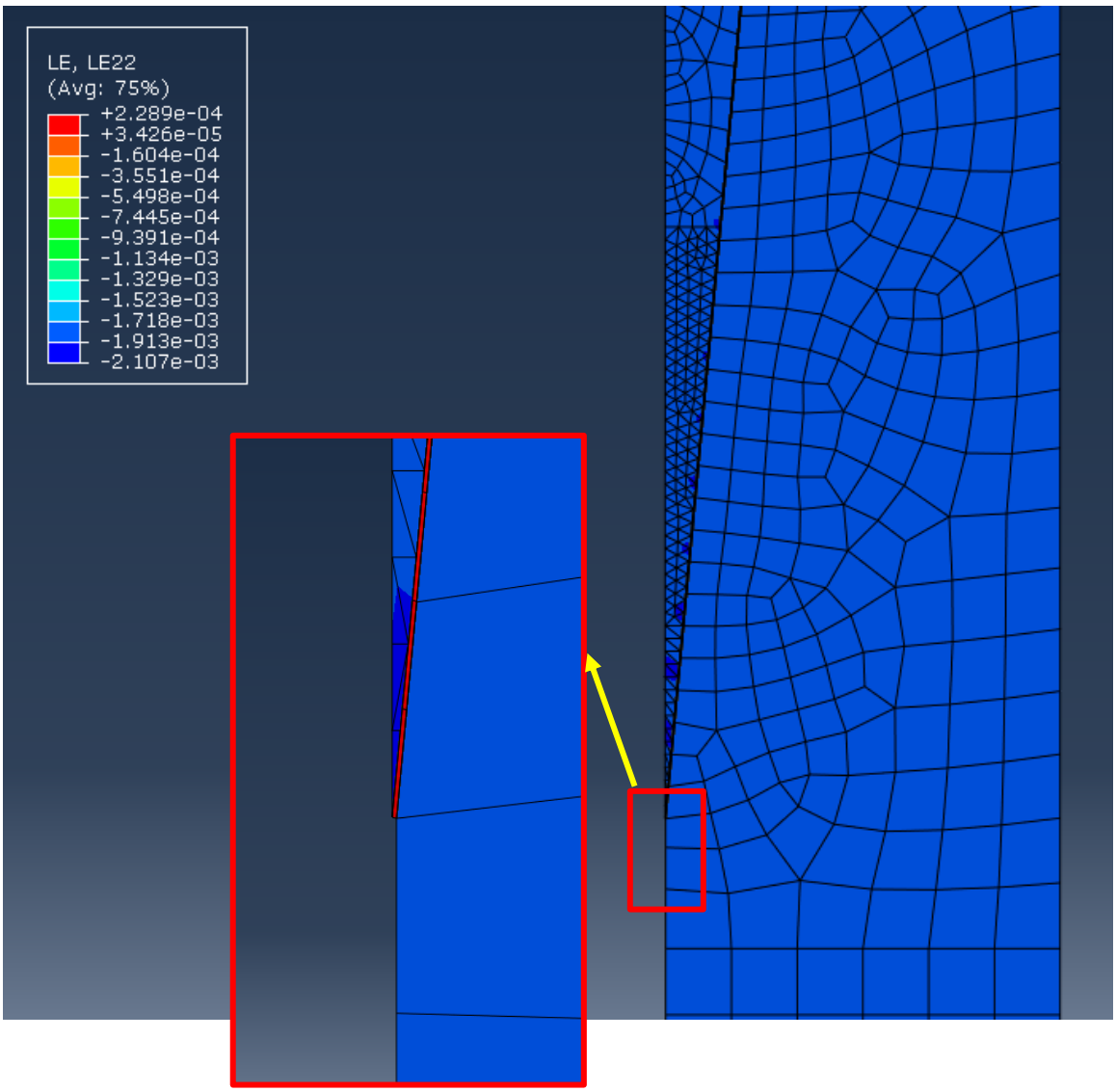

Figure 100. Logarithmic strain (LE) in y-direction at a -1.44 mm displacement.

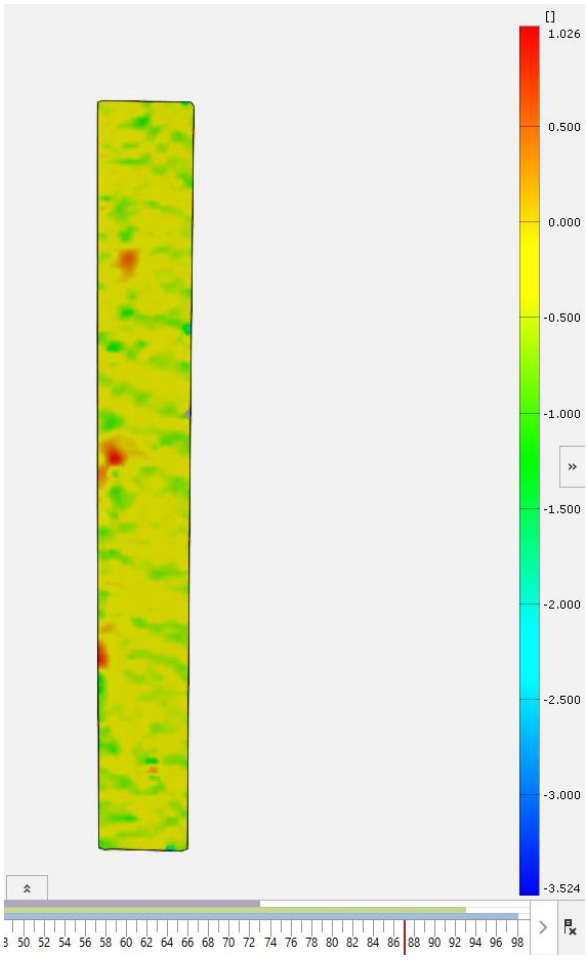

Figure 101. Natural log of the y-component of strain (%) at a displacement of -1.44 mm in Aramis at the frame prior to failure.

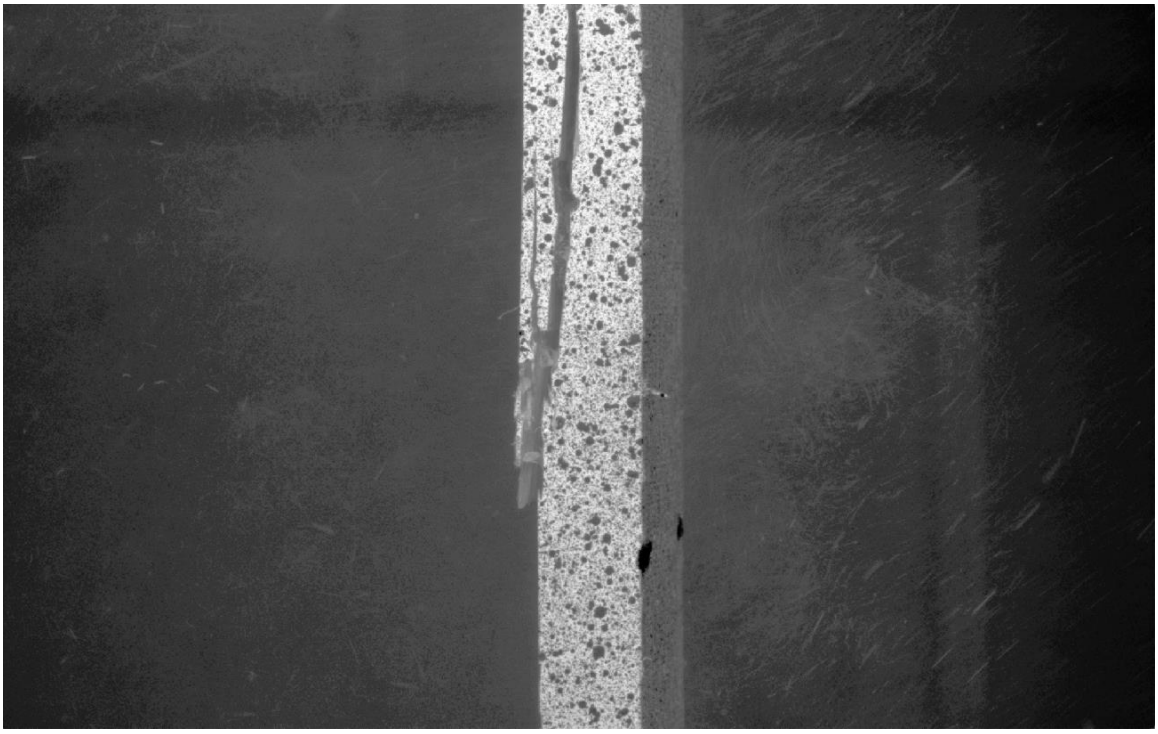

Figure 102. Scarf tension specimen at failure with delaminated plies on the left side of the failed coupon and bond line failure up to the top of the image.

Logarithmic strain was used to visualize results over the surfaces, but virtual extensometers were used to measure the strains for the stress-strain curves in Figure 103. The stress in Aramis was calculated using the load divided by the initial cross-sectional area, and the stress in Abaqus was calculated by summing the x and y reaction forces on the nodes in set D (Figure 99) and dividing by the initial cross-sectional area. The stress-strain curves were all linear, with catastrophic failure occurring experimentally. The stress-strain curve for the unscarfed experimental specimen was plotted using the known ultimate stress and strain values, but intermittent points were not plotted (Figure 103). Progressive failure in the cohesive zone at critical stress is demonstrated in the traction-separation curves in Figure 106. The traction was the stress output in the element in set A

(Figure 99) and the separation was the distance calculated from the coordinates for the nodes in set B (Figure 99). Force-displacement curves were also compared between Abaqus and Aramis (Figure 104). Node 2 in Figure 99 was used to track displacement for the force-displacement curve in Figure 103. The experimental force-displacement curve was nonlinear beginning at a displacement of 0.5 mm up to failure, while the simulated force-displacement curve was linear up until failure. There was a sharp drop in the experimental force-displacement curve at failure because failure was catastrophic, while the gradual drop at failure in the simulated force-displacement curve at failure was due to the progressive failure of the cohesive elements. Far field stress-strain curves are in Figure 105, with stress calculated in the same manner as in Figure 103 and strain calculated using the average of the y-displacement output for set D in Figure 99 and $\in = \Delta l/l$. Overall, there was good agreement between the Abaqus and Aramis stress-strain and force-displacement results.

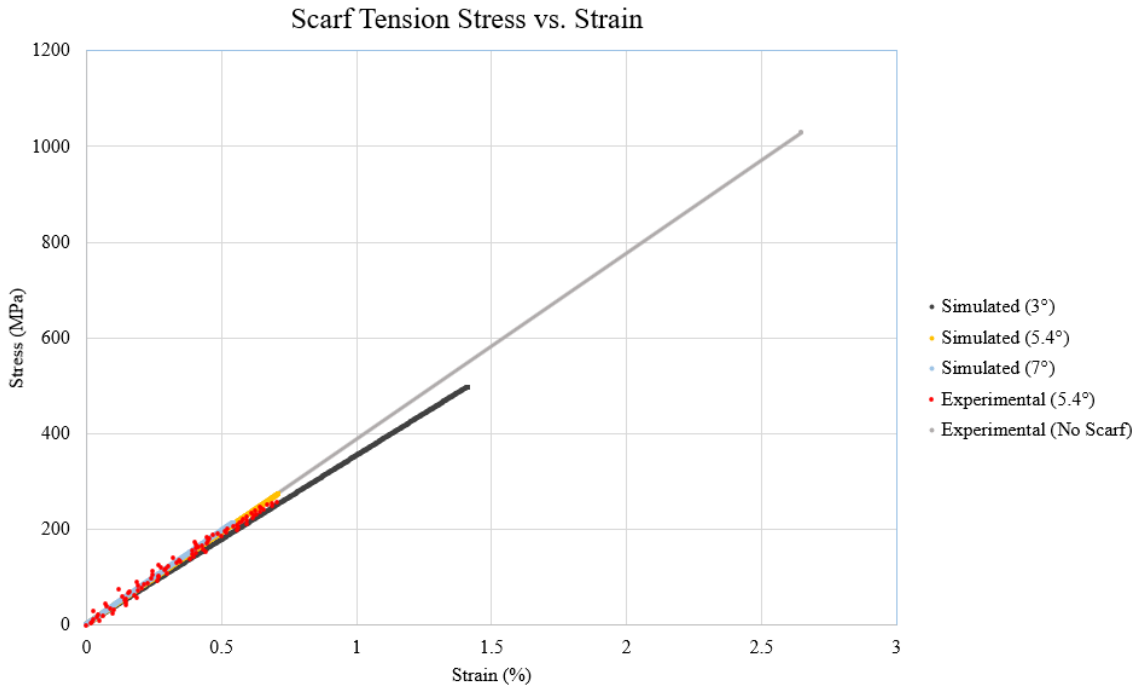

Figure 103. Experimental and simulated scarf tension stress-strain curves with strains calculated from virtual extensometers.

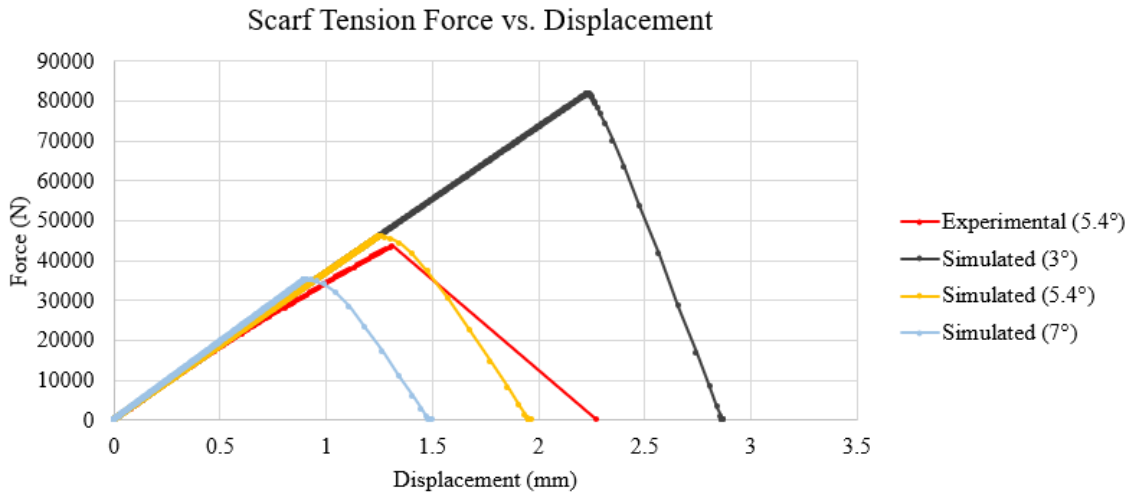

Figure 104. Scarf tension force-displacement curves comparing experimental and simulated results.

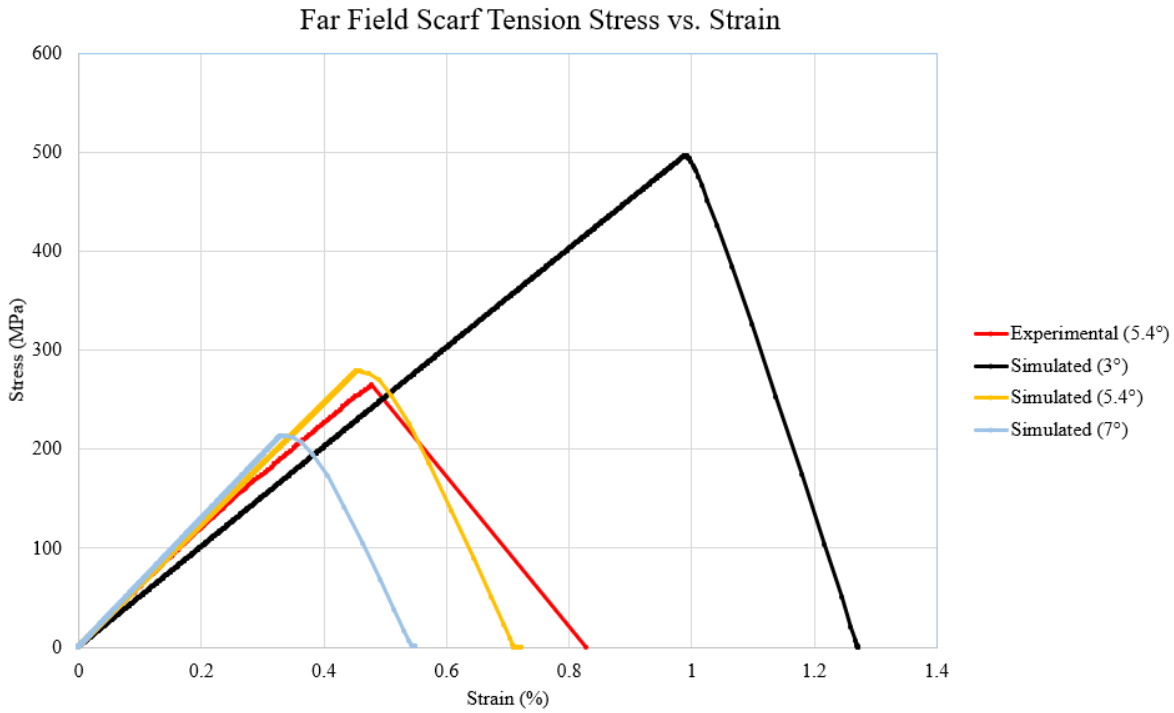

Figure 105. Scarf tension far field stress-strain curves comparing experimental and simulated results.

a)

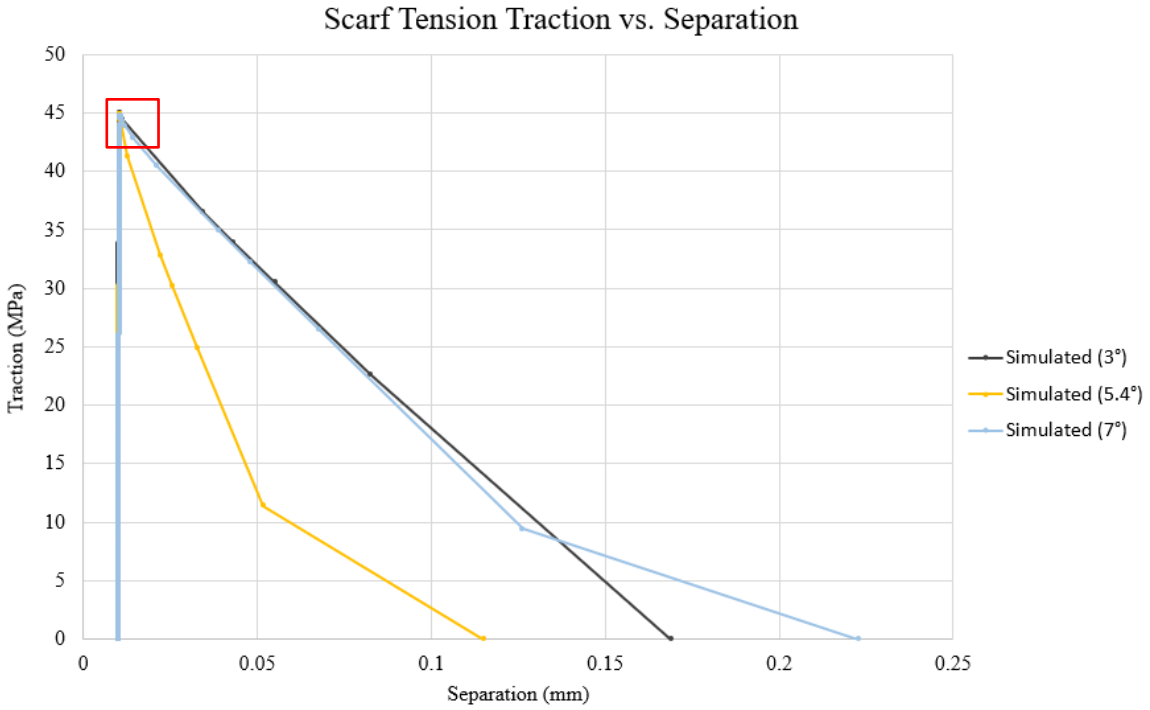
Scarf Tension Traction vs. Separation
Traction (MPa)
Separation (mm)
0
5
10
15
20
25
30
35
40
45
50
0
0.05
0.1
0.15
0.2
0.25
Simulated (3°)
Simulated (5.4°)
Simulated (7°)

b)

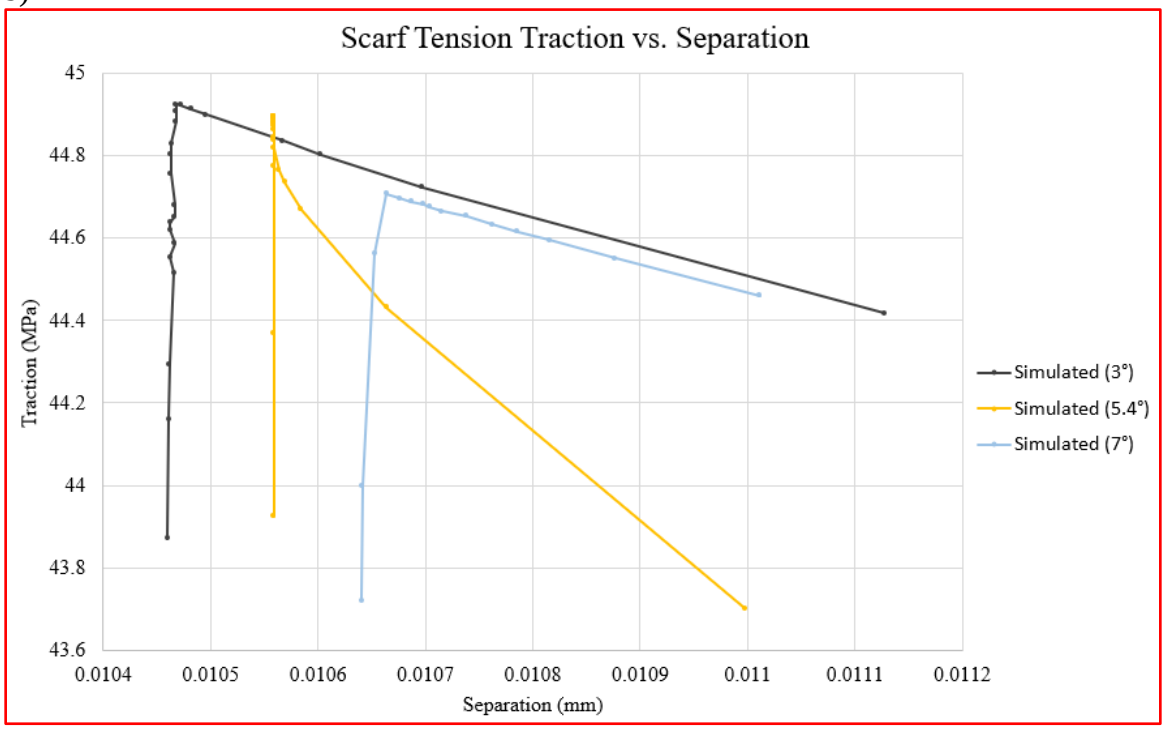
Scarf Tension Traction vs. Separation
Traction (MPa)
Separation (mm)
43.6
43.8
44
44.2
44.4
44.6
44.8
45
0.0104
0.0105
0.0106
0.0107
0.0108
0.0109
0.011
0.0111
0.0112
Simulated (3°)
Simulated (5.4°)
Simulated (7°)

Figure 106. a) Simulated scarf tension traction-separation results at the cohesive zone with red box around the area described in part b. b) Simulated scarf tension traction-separation results zoomed in at the critical stress.

The results for scarf angles at 3 and 7 degrees indicate that lowering the scarf angle increases the force, displacement, stress, and strain required to fracture the scarf joint. At 3 degrees, failure is predicted to occur at around twice the stress as the 5.4 degree specimen and half the stress as the unscarfed specimen. Simulating scarf angles at 1 and 2 degrees did not result in failure of the cohesive elements, indicating that scarf joints approach the undamaged properties as scarf angles decrease. Full tensile strength restoration is expected between 0 and 2 degree scarf angles. Since the scarf tension specimens were co-bonded, there were brittle bond lines along the scarf joint, which were where the cracks initiated. Since composite longitudinal tensile strength is determined by the continuity of the longitudinal fibers, reducing the scarf angle will approach, but not reach, the adherend properties. Once broken, the continuity of glass fibers cannot be restored in a reasonable manner for field repairs. The shifts along the curves in Figure 106b as the cohesive elements approach critical stress, particularly for the 3 degree scarf angle, might also be indicating increased numerical instability with decreased scarf angle. Force-displacement and stress-strain curves may be used to make estimates for the scarf angles needed for a wind turbine blade design. The forces, displacements, stresses, strains at a particular location along a wind turbine blade can be identified using blade modeling software such as the Numerical Manufacturing and Design Tool (NuMAD) and

compared with scarf joint simulations in Abaqus to make predictions for effective repair designs.

11. CONCLUSIONS

Three main motivations from the literature review were used to formulate three sets of research questions. The first motivation was that there were discrepancies between Horton (1990), Petrie (2007), Sperling (2006), and Dorworth, Gardiner, and Mellema (2009) around the use of solvent wipe surface preparation methods [8, 63, 70, 77]. In addition, no data was found that supported the surface preparation methods that had been recommended. Blinov and Tager (1987) said that crosslinked polymer can reach the gel layer state when interacting with solvents and Sperling (2006) said that the orientation of a polymer at surface is almost always different from the interior [60]. Therefore, it was possible that using solvents for contamination removal could gel a composite surface and affect bond strength results. The discrepancies around the use of solvent wipe surface preparation methods combined with the potential for composite surface gelation from solvents motivated the first research question: Does solvent wiping negatively affect the surface energy of a repair surface?

The second motivation concerned understanding the effects of contamination on bond strengths. Shang (2013) and Musaramthota, Pribanic, and McDaniel (2014) had demonstrated that hydraulic oil, mold release, and silicone spray along a bond line would diminish bond strength [72, 73]. Additionally, Amaro et al (2014)’s oil immersion tests demonstrated that hydraulic oil can diffuse into and affect the strengths of GFRP laminates [74]. Yet, the effects of composite dust on bond strengths and the time-dependence of hydraulic oil contamination diffusion along bond lines had not been studied. The two potential contamination effects motivated the second set of research

questions: Can the bond line of a repair tolerate certain types of contaminants over others? Is contamination diffusion into a bond line time-dependent?

The first research question addresses the effectiveness of current surface preparation methods, but other methods of improving composite repair adhesion like chemical and plasma treatments had not been formally considered. Sizing is used to coat glass fibers during manufacturing, and glass fibers are re-exposed during damaged composite material damage removal, but the possibility of sizing improving the adhesion properties after being applied to a tapered surface had not been considered. Findings by Webster and Wightman (1990) and Liston, Martinu, and Wertheimer (1993) had indicated that plasma treatment would improve epoxy surface adhesion properties, but plasma treatment had not been considered for wind turbine field repair applications [91, 96]. The unknowns in thermoset surface gelation combined with the lack of consideration of chemical and plasma treatments for improving composite repair adhesion properties motivated the third research question: Can solvent cleaning, chemical treatment, or plasma treatment improve repairs?

Three objectives were used to answer the three research questions. The three objectives were:

1. Identified differences in contact angles, bond strengths, and failure modes of specimens that have been solvent wiped with common solvents used for solvent wipe surface preparation.
2. Measured the changes in bond strengths due to contamination from sanding particles and hydraulic oil with time.

3. Increase and equalize the surface energy of repair surfaces using plasma or sizing.

To complete the first objective, contact angle, lap shear, DCB, ENF, and resin-wipe tests were executed. Solvent wiping did not significantly affect contact angles, maximum lap shear stress, or fracture toughness values for contact angle, lap shear, DCB, or ENF tests. Differences in maximum lap shear stress values were due to different substrate thicknesses and moduli and adhesive-substrate combinations. However, failure surfaces of MEK-wiped vinyl ester composites adhered with a MMA adhesive exhibited slightly more cohesive failure. The slightly different failure surfaces for MEK-wiped vinyl ester composites motivated the solvent-wiped resin tests, which showed that despite null results from the contact angle and the mechanical tests, resin surfaces were affected by solvent wiping. Besides distilled water, which did not affect resin surfaces, solvent wiping with ISP, acetone, MEK and MIBK resulted in streaks on resin surfaces. The streaks were caused by the solvents diffusing into the surface and creating a gel-like swollen layer, which was smeared as the cloth passed over the surface. The resulting streaks raise concerns that a gelled polymer surface might affect dissolving and removing contaminants since contaminants could become trapped by the gelled surface.

The resin-wipe tests also demonstrated that different solvents affect the surfaces of the same resin slightly differently, so the slightly different failure surfaces for the MEK-wiped vinyl ester composites could have occurred either because the solvent had dissolved slightly further into the vinyl ester specimens than other solvents or altered the surface in a way that made the adhesive adhere to the vinyl ester differently.

Since composite dust contains glass particles that cannot be dissolved by common solvents and resin surfaces can be gelled by common solvents, it is possible that using solvents on composite surfaces will cause composite dust particles to adhere along a bond line and become crack initiation origins. Besides the streaks that resulted from resin wipe tests, the DCB results for vinyl ester specimens adhered with an epoxy adhesive resulting in fracture toughness values of zero motivates the repair recommendation to test the sand grit, solvent wipe, composite surface, and adhesive combinations that will be used in the field using DCB and ENF testing. The adhesive-substrate combinations that were used in this research are commonly used materials used in wind turbine blade repairs, however, are not representative of every repair scenario that will be encountered.

To complete the second objective, contamination lap shear tests were conducted where composite dust and hydraulic oil were applied to lap shear substrate surfaces prior to bonding with either an MMA adhesive or a film adhesive and tested after 2, 9 and 33 days. Time effects were examined for the MMA adhesive, but not for the film adhesive. Lap shear results indicated that contamination was not significantly time-dependent for the composite dust or the hydraulic oil. For lap shear specimens adhered with the MMA adhesive, compared to the corresponding control specimens, lap shear specimens contaminated with dust had maximum lap shear stress values 42%, 46%, and 48% less after a 2, 9, and 33 days, respectively. For lap shear specimens adhered with the MMA adhesive, compared to the corresponding control specimens, lap shear specimens contaminated with oil had maximum lap shear stress values 11%, 6%, and 3% less than control specimens after a 2, 9, and 33 days, respectively.

For the lap shear specimens adhered with the film adhesive and tested after 9 days, maximum lap shear stress values dropped 12% when dust was applied and 19% when hydraulic oil was applied. The film adhesive was less sensitive to contamination than the MMA adhesive when testing composite dust because the heating during post-cure decreased the adhesive viscosity and allowed the adhesive to flow around the stamped particles more effectively. The lower viscosity of the heated film adhesive thus permitted a larger surface area to be adhered between the coupons. Using a lower-viscosity adhesive in applications where contamination is more of a concern may be more effective in increasing blade repair durability. However, using an adhesive with too low of a viscosity for vertical wind turbine blade field repairs could be detrimental to the patch integrity because the adhesive could flow from the repair area down the blade during repairs.

In addition to the changes in maximum lap shear stress values, the failure modes were different for specimens that had had contamination applied. For lap shear specimens where the MMA had been used, the composite dust and the hydraulic oil affected the failure surfaces differently. The composite dust remained in the stamped grid pattern and had not been significantly altered besides being surrounded by the adhesive while there were not significant changes between the control and the hydraulic oil- contaminated failure surfaces. For lap shear specimens where the film adhesive had been used, the composite dust had also remained in the stamped grid pattern, but the hydraulic oil-contaminated substrates caused more interfacial failure around the bond area. Moreover, since all specimens contaminated with composite dust and hydraulic oil resulted in lower

maximum lap shear stress values and altered most failure modes, composite dust and hydraulic oil should be removed prior to bonding to improve repair durability. Besides examining contamination effects on lap shear failure modes, the lap shear failure modes of specimens tested using the expired MMA adhesive were used to demonstrate that using the expired adhesive results in more brittle bond lines. Brittle bond lines can lead to more sudden failures, so expired MMA adhesives should not be used for repairs.

To complete the third objective, contact angle testing was used to measure plasma treatment effects on composite surfaces and scarf tension testing experiments and simulations were employed to measure sizing effects on composite repair surfaces. Solvent wiping effects were addressed in completing the first objective, and without the addition of contamination, did not improve adhesion properties significantly. Therefore, if the gelation effects from solvent wiping do not promote contamination particle embedding, solvent wiping would primarily improve resulting composite joint bond strengths through removing contamination.

Composite surfaces were contact angle tested after blown ion and flame plasma treatments. There were 66% and 69% drops in contact angle for blown ion and flame treatments, respectively. The significant drop in contact angles indicate that plasma treatment could be effective in preparing composite surfaces for repairs. Due to the larger machine size, however, plasma treatments may only be feasible for repairs to wind turbine blades with suspended platforms. The effect of chemical treatments for improving composite repairs was addressed in scarf tension testing by applying sizing along the scarf tension specimen bond lines during coupon manufacturing. Based on the lack of

significant differences between the maximum tensile stress values for scarf tension specimens that had sizing applied to the surfaces and those that did not, applying sizing to a repair surface does not affect the resulting bond strength of a repair. In addition, the failure modes did not differ significantly. FE SEM was also used to demonstrate that there were no resulting chemical changes on the tapered surfaces after failure between the sized and not sized specimens.

Along with comparing sized and unsized scarf tension specimens, the stress-strain curves were compared between scarfed and non-scarfed tension specimens. The non-scarfed tension specimens were not tested to failure, but there was a stiffness reduction in the scarfed specimens beginning at approximately 0.45% strain, indicating that the scarf tension repair did not fully restore the composite plate's original properties. It is highly unlikely for any repair to fully restore a composite's properties because a composite's strength lies primarily in the continuity of its fibers. Fiber continuity is not restored in a composite repair. In addition to comparing scarfed and non-scarfed stress-strain results, experimental results were contrasted with simulated results using virtual extensometers in Aramis and Abaqus. Progressive failure analysis was used to model the composite adherends, while CZM was used to model the bond line. Stress-strain and force-displacement curves were used to compare simulated and experimental scarf tension results, and a traction-separation curve from the Abaqus results was used to demonstrate progressive failure. The stress-strain curves were both linear, with catastrophic failure occurring experimentally. Progressive failure in the cohesive zone at critical stress was demonstrated in the traction-separation curve. The experimental force-displacement

curve was nonlinear beginning at a displacement of 0.5 mm up to failure, while the simulated force-displacement curve was linear up until failure. There was a sharp drop in the experimental force-displacement curve at failure because failure was catastrophic, while the gradual drop at failure in the simulated force-displacement curve at failure was due to the progressive failure of the cohesive elements. Overall, there was good agreement between the Abaqus and Aramis stress-strain and force-displacement results.

Prior to the completion of the three objectives in this research, wind turbine blade repair surface preparation wind turbine blade surface preparation procedure recommendations deviated significantly and were informed by experience rather than by published data. By answering the research questions posed, future repair procedures will be more straightforward and have less variability. Adhesion testing techniques existed, but composite repair surface preparation testing was minimal. Some contamination tests had been used to examine effects of hydraulic oil and mold release, but the contamination lap shear tests were the first that studied the effect of composite dust on bond line strengths. The scarf tension tests were also novel for testing surface preparation methods for glass fiber reinforced epoxy composites. The scarf tension test will be critical for understanding other surface preparation and adhesion effects on composites cut at angles through the thickness, such as those in wind turbine blade field repairs. The procedures were also refined for DIC testing of composites and comparing results with Abaqus using virtual extensometers. The composite repair surface preparation testing methods that were developed refine surface preparation procedure recommendations and motivate additional research. Refined surface preparation procedure methods will reduce cost

uncertainty for wind turbine O&M estimates by facilitating inefficiency identification. Cost inefficiency identification will decrease lifetime costs and increase energy production for wind turbines. Increased energy production for wind turbines will ultimately reduce reliance on fossil fuels for societal energy needs.

12. REPAIR PROCEDURE RECOMMENDATIONS

The repair procedure recommendations developed in this dissertation elaborate on Dorworth, Gardiner, and Mellema (2009)'s general steps in performing a composite scarfed repair, which are in Section 2.7 of this dissertation. The general steps may be used for wind turbine blade field repairs, but there was further development on steps 3 and 5, where step 3 was, "remove all damaged and contaminated material," and step 5 was, "taper sand/scarf the repair area according to repair design instructions to create a smooth, flat surface with high surface energy [58]." All of Dorworth, Gardiner, and Mellema (2009)'s steps continue to be recommended, but details regarding contamination removal and creating surfaces with high surface energy were investigating using testing and simulation methods due to the discrepancies described in Section 2.9: Surface Preparation of Composite Scarf Repairs with regards to the use of solvents in contamination removal methods.

Solvent wipe methods did not result in significant changes in lap shear, DCB, or ENF results, but did result in streaks on resin surfaces that indicate that composite surfaces do gel due to solvent application. Therefore, the discrepancies over solvent wiping are eliminated and are replaced with recommendation to: "Test whichever surface preparation methods, potential contamination types and amounts encountered, and adhesive-substrate combinations that are used and encountered for a repair using lap shear, DCB, ENF, and scarf tension testing. Results from lap shear, DCB, ENF, and scarf tension tests should be used to inform the surface preparation procedures used in the field. The methods described in this work may be used to guide testing methods.

The scarf angle selected for a wind turbine blade repair is dependent on the loads that the location of the repair will endure in service. Locations along the blade that experience higher loads should generally be repaired using lower scarf angles.

13. FUTURE WORK

Future work regarding wind turbine blade repairs should involve further investigation of the wind industry's current cost structures and repair methods while continuing to conduct research on surface preparation techniques and testing methods. A more detailed investigation of the wind industry's current cost structures should include a model of repair costs. The cost of manufacturing a wind turbine blade has been modeled by Bortolotti et al (2019) and costs of repairing wind turbine blades were discussed by Mishnaevsky and Thomson (2020), but repair costs have not been modeled [132, 5]. Having informed estimates of repair costs using a repair cost model will allow inefficiencies to be identified and remediated. Inefficiency identification can then be used to prioritize research topics. Informed repair cost estimates combined with a better understanding of repair durability can be used to make decisions on whether a wind turbine blade should be repaired or replaced.

In addition to repair cost uncertainties, the repair methods used in the field are largely undocumented. Several inspection techniques were reviewed in Section 2.5 of this work but few to no procedures or recommendations were found that included details on inspection frequency, inspection type selection, or inspection procedures for each type. The damage inspection and repair procedures used prior and immediately following blade installation also merit further investigation. Additional research on scarf angle selection with regards to location along a blade could limit the amount of undamaged material that must be removed in a repair. That is, in noncritical regions a repair which does not reduce

to original values might be acceptable if the margins are still high with the repaired strength.

Besides needing more detailed cost models and inspection procedures, damage thresholds must be clearly defined. Nijssen and Manrique (2020) developed definitions for affected and critical thresholds for structural and non-structural repairs [27], but an indicator that is based on prior analysis of stiffness and strength degradations in particular damaged sites and the repercussions of the degradation would have much higher fidelity and be more usable (Nijssen, personal communication, March 11, 2022).

Continued research on surface preparation techniques should include further evaluations of current challenges, currently used methods, examinations of contamination effects on bond line integrity, and considerations of alternative techniques for improving repair surface energy. One current surface preparation challenge is that wind turbine blade field repairs involve patching aged composites with new material. A wind turbine blade that necessitates repair could have additional cracks from fatigue or have environmental degradation from factors such as UV rays, precipitation, and humidity. Degraded material properties and adhesion strengths with the new patch materials have yet to be quantified. Repair durability also needs to be quantified, which will require data from wind farms and blade repair companies.

Solvent wiping is a currently used surface preparation method that continues to merit further investigation. Contact angle testing was used to measure changes in contact angles among solvent-wiped composite surfaces. Contact angle results had high standard deviations, likely due to the variations in fiber exposure on surfaces. To mitigate the

effects of fiber exposure variations, future contact angle testing could omit fibers from specimens and measure the effects on contact angles from resin samples alone. Variations in fiber exposure should continue to be considered in composite surface preparation recommendations but contact angle tests of resin samples could be more effective in resin-adhesive compatibility estimates. Besides omitting fibers for contact angle tests, other analysis techniques could be employed to further understand the effects of solvents on composite surfaces. Laurila et al (2012), for example, used X-ray photoelectron spectroscopy (XPS), surface specific infrared spectroscopy (IR), and surface free energy evaluations to analyze changes on polymer surfaces from plasma and chemical methods to improve epoxy adhesion [65]. Contact angle testing using a nonpolar liquid such as diidomethane can be used in surface free energy evaluations.

Solvent-wiped resin testing demonstrated that solvents gel resin surfaces. Gelled resin surfaces could trap contaminants such as composite dust along a bond line. Further mechanical testing and microscopy techniques could be used to measure the combined effects of solvent wiping and contamination along a bond line. More testing and spectroscopy could also be used to measure the effectiveness of solvents in removing contaminants from surfaces.

Future contamination studies should include varied factors such as hydraulic oil types and diffusion times, composite dust application methods, and adhesives used. Wind turbine blade repairs must often endure for up to 20 or more years, so lap shear, DCB, and ENF studies could be performed after longer time periods than 33 days to observe potential time-dependence of hydraulic oil diffusion into a bond line. Besides lengthening

time periods for hydraulic oil diffusion tests, composite dust application methods merit further investigation because the grid stamp created regions where there were large amounts of composite dust that were not representative of how composite dust will likely lay on a composite surface after damage removal in a repair. The stamp was effective for creating a pattern that could be traced back to during failure mode observations, but composite dust would likely thinly cover a repair surface rather than in concentrated large amounts with gaps between them for adhesive flow between. The MMA adhesive used in the contamination lap shear tests was expired by 15 months, so additional contamination studies that use an unexpired adhesive could lead to less variability in maximum lap shear stress values and failure modes. More studies on adhesive expiration effects could also be beneficial, such as those that examine how bond strengths degrade after adhesives have expired for different time periods. It is unlikely that expired adhesives will be candidates for critical, structural composite repairs, but slightly expired adhesives might be effective for repairing superficial damage if studies show that the expired adhesives perform to the superficial damage repair design criteria.

Considerations of alternative repair surface preparation techniques should include plasma and chemical treatments. Decreased contact angles after composite surfaces were found for plasma treated surfaces and motivates further studies on plasma treatment feasibility in repairs and mechanical methods on plasma treated composite joints. As with surface preparation problems from hand sanding, handheld plasma devices can cause variability across a surface. Using robot arms can reduce variability but are unlikely to be used in near-future wind turbine blade repairs. Furthermore, plasma treatments could be

applied to surfaces and tested using lap shear, DCB, ENF, or scarf tension methods to examine the effects on bond strengths and failure modes of virgin and repair surfaces. Mechanical tests on plasma treated surfaces would supplement the contact angle results. Continued discussions with wind turbine blade repair industry leaders should inform the feasibility of using plasma treatment in field repairs. Plasma treatment may only be feasible for repairs performed using suspended platforms.

Despite neither affecting scarf tension tensile strengths nor failure modes, chemical treatments could still be considered for repair surface preparation. Additional research on chemical treatments could include using other sizing types, changing spray parameters, or changing the type of chemical used.

Continued research on testing methods should include improvements to glass fiber reinforced epoxy scarf tension manufacturing and analysis methods. Preparing scarf tension specimens using tapered ply drops created variation in fiber exposure and discontinuities that trapped composite dust particles. Machining a tapered section from the bulk material could reduce variation and create a surface that has even fiber exposure. With a more even surface, solvent effects on repair rather than as-manufactured surfaces could be examined more effectively. On top of changing the tapered region of the scarf repair surface, creating thinner specimens would permit scarf tension specimen failure stresses to be compared to those that were not scarfed. Besides creating more even composite repair surfaces for scarf tension testing, more effective machining methods such as CNC-machining could be used to create more consistent and complex repair geometries. CNC-machining may not be feasible in the field but could be helpful in

mitigating surface variabilities in experimentation methods. Mitigating surface variabilities could be beneficial in measuring the effects of surface preparation methods.

In addition to improving machining methods, future scarf tension or scarf repair studies could compare soft-patch to hard patch methods. Factors that could be considered in testing hard-patch methods include scarf angle, adhesive type, humidity effects, and surface preparation methods. Scarf tension method in this work used a single scarf joint but testing joints manufactured in the configuration in Figure 26 would be more representative of real-life repair scenarios. Either soft- or hard- patch methods could incorporate overplies. Overplies can be used to reduce peel stresses at the pointy tips of adherends but may also increase the stiffness of the joint. Depending on the location where the patch is used and the size of a patch, higher stiffness in the joint of a repair could affect the overall flexural properties in a wind turbine blade. Adding an overply could also lower the size of the resin-rich region between the patch and the substrate. Since wind turbine blades are susceptible to a variety of loading conditions, mechanical testing in other loading scenarios such as compression could be employed.

Future scarf tension analysis methods could include a refined mesh along the cohesive zone to match the triangular element sizes in the scarf tension adherends to improve simulation convergence. In addition, scarf tension analyses should include measurements of peel and shear stress distributions in addition to the cohesive zone progressive damage modeling along the bond line in future work. Analyses of peel and shear stresses can be used for designing repairs with minimized peel stresses and shear dominant stress states. Very localized high stresses might be mitigated with bond

geometry to improve adhesive joint repairs. If sufficient resolution can be achieved, DIC frames should include the entire bond line of scarf joint. Analysis of peel and stress distributions using Abaqus involves creating a path along the bond line and plotting the peel and shear stress changes along the path's distance.

All in all, future wind turbine blade repair research can include more investigations into the wind industry's current cost structures and repair methods while continuing to research surface preparation techniques and testing methods. This research was in part sparked by inquiries from industry leaders. Future work on wind turbine blade repair surface preparation recommendations should continue to be driven and prioritized with collaboration between industry and academia.

14. REFERENCES CITED

[1] “July 2021 Monthly Energy Review,” 2021.

[2] “October 2021 Monthly Energy Review,” Washington, D.C., 2021.

[3] E. (Erich) Hau, *Wind turbines : fundamentals, technologies, application, economics*, 2nd ed.. Berlin : Berlin , 2006.

[4] W. R. Stahel, “Circular economy,” *Nature*, vol. 531, no. 7595, pp. 435–438, Mar. 2016, doi: http://dx.doi.org/10.1038/531435a.

[5] J. P. Jensen and K. Skelton, “Wind turbine blade recycling: Experiences, challenges and possibilities in a circular economy,” *Renew. Sustain. Energy Rev.*, vol. 97, pp. 165–176, 2018, doi: https://doi.org/10.1016/j.rser.2018.08.041.

[6] J. W. Pearce-Higgins, L. Stephen, A. Douse, and R. H. W. Langston, “Greater impacts of wind farms on bird populations during construction than subsequent operation: results of a multi-site and multi-species analysis,” *J. Appl. Ecol.*, vol. 49, no. 2, pp. 386–394, Feb. 2012, [Online]. Available: http://www.jstor.org.proxybz.lib.montana.edu/stable/41433362.

[7] M. G. Molina, “Technical and Regulatory Exigencies for Grid Connection of Wind Generation,” J. G. A. E.-G. O. Suvire, Ed. Rijeka: IntechOpen, 2011, p. Ch. 1.

[8] M. Bilgili, A. Yasar, and E. Simsek, “Offshore wind power development in Europe and its comparison with onshore counterpart,” *Renew. Sustain. Energy Rev.*, vol. 15, no. 2, pp. 905–915, 2011, doi: https://doi.org/10.1016/j.rser.2010.11.006.

[9] L. Mishnaevsky and K. Thomsen, “Costs of Repair of Wind Turbine Blades: Influence of Technology Aspects,” *Wind Energy*, vol. 23, no. 12, pp. 2247–2255, 2020, doi: https://doi.org/10.1002/we.2552.

[10] A. Shrivastava, *Introduction to Plastics Engineering*. Saint Louis: Saint Louis: Elsevier Science & Technology Books, 2018.

[11] E. J. Barbero, “Introduction to composite materials design. Third edition.” London, England : CRC Press, 2018.

[12] K. Ha and J.-H. Jeong, “Stress states investigation of adhesive bonded joint between spar cap and shear webs of a large wind turbine rotor blade,” *J. Mech. Sci. Technol.*, vol. 35, no. 5, pp. 2107–2114, 2021, doi: 10.1007/s12206-021-0426-2.

[13] L. Mishnaevsky, K. Branner, H. N. Petersen, J. Beauson, M. McGugan, and B. F. Sørensen, “Materials for wind turbine blades: An overview,” *Materials*. 2017, doi: 10.3390/ma10111285.

[14] K. B. Katnam, A. J. Comer, D. Roy, L. F. M. da Silva, and T. M. Young, “Composite Repair in Wind Turbine Blades: An Overview,” *J. Adhes.*, vol. 91, no. 1–2, pp. 113–139, 2015, doi: 10.1080/00218464.2014.900449.

[15] A. C. M. Association, *Basic Composites Manual*. Arlington, VA: American Composites Manufacturers Association, 2017.

[16] A. Lusty and D. Cairns, “Alternative Damage Tolerant Materials for Wind Turbine Blades: An Overview,” Albuquerque, NM, 2021.

[17] P. Murdy, “Combining acoustic emission and guided ultrasonic waves for global property prediction and structural health monitoring of glass fiber composites.” Montana State University - Bozeman, College of Engineering, 2019.

[18] B. F. Sørensen, J. W. Holmes, P. Brøndsted, and K. Branner, “Blade materials, testing methods and structural design,” *WIT Trans. State-of-the-art Sci. Eng.*, vol. 44, pp. 417–466, 2010.

[19] G. Díaz, J. Gómez-Aleixandre, and J. Coto, “Dynamic evaluation of the levelized cost of wind power generation,” *Energy Convers. Manag.*, vol. 101, pp. 721–729, 2015, doi: https://doi.org/10.1016/j.enconman.2015.06.023.

[20] C. Moné, M. Hand, M. Bolinger, J. Rand, D. Heimiller, and J. Ho, “2015 Cost of Wind Energy Review,” Golden, CO, 2017.

[21] L. Fingersh, M. Hand, and A. Laxson, “Wind Turbine Design Cost and Scaling Model,” Golden, CO, 2006.

[22] T. Stehly, P. Beiter, and P. Duffy, “2019 Cost of Wind Energy Reivew,” Golden, CO, 2020.

[23] E. Byon, L. Ntaimo, C. Singh, and Y. Ding, “Wind Energy Facility Reliability and Maintenance,” Berlin, Heidelberg: Berlin, Heidelberg: Springer Berlin Heidelberg, 2014, pp. 639–672.

[24] N. Johnson *et al.*, “Big Adaptive Rotor Phase I Final Report,” no. December, 2021, [Online]. Available: www.nrel.gov/publications.

[25] M. Martin-Tretton, M. Reha, M. Drunsic, M. Keim, P. Schwabe, and S. Tegan, “Data Collection for Current U.S. Wind Energy Projects: Component Costs, Financing, Operations, and Maintenance,” Seattle, WA, 2011.

[26] L. Mishnaevsky, “Repair of wind turbine blades: Review of methods and related computational mechanics problems,” *Renew. Energy*, vol. 140, pp. 828–839, 2019, doi: https://doi.org/10.1016/j.renene.2019.03.113.

[27] R. Nijssen and E. Manrique, “Literature Review of Structural and Non-Structural Wind Turbine Blade Damage,” Petten, Netherlands, 2020.

[28] D. Katsaprakakis, N. Papadakis, and I. Ntintakis, “A Comprehensive Analysis of Wind Turbine Blade Damage,” *Energies*, vol. 14, no. 18, p. 5974, 2021, doi: http://dx.doi.org/10.3390/en14185974.

[29] M. Jureczko, M. Pawlak, and A. Mężyk, “Optimisation of wind turbine blades,” *J. Mater. Process. Technol.*, vol. 167, no. 2, pp. 463–471, 2005, doi: https://doi.org/10.1016/j.jmatprotec.2005.06.055.

[30] B. Hayman, “Approaches to Damage Assessment and Damage Tolerance for FRP Sandwich Structures,” *J. Sandw. Struct. Mater.*, vol. 9, no. 6, pp. 571–596, Nov. 2007, doi: 10.1177/1099636207070853.

[31] F. Zhang, J. Dai, D. Liu, L. Li, and X. Long, “Investigation of the Pitch Load of Large-Scale Wind Turbines Using Field SCADA Data,” *Energies (Basel)*, vol. 12, no. 3, p. 509, 2019, doi: 10.3390/en12030509.

[32] P. Veers *et al.*, “Trends in the Design, Manufacture and Evaluation of Wind Turbine Blades,” *Wind Energy*, vol. 6, pp. 245–259, Jul. 2003, doi: 10.1002/we.90.

[33] J. Tang and X. Chen, “Experimental investigation on ultimate strength and failure response of composite box beams used in wind turbine blades,” *Compos. Struct.*, vol. 198, pp. 19–34, 2018, doi: https://doi.org/10.1016/j.compstruct.2018.05.042.

[34] J. W. Nelson, “A comparison of continuum and discrete modeling techniques of the effects of manufacturing defects common to composite structures.” Montana State University - Bozeman, College of Engineering, 2014.

[35] R. Talreja, “Studies on the failure analysis of composite materials with manufacturing defects,” *Mech. Compos. Mater.*, vol. 49, p. 35+, Jun. 2013, [Online]. Available:

https://link.gale.com/apps/doc/A373680940/AONE?u=mtlib_1_1123&sid=AONE&xid=a9d7f7a6.

[36] A. S. Verma, N. P. Vedvik, P. U. Haselbach, Z. Gao, and Z. Jiang, "Comparison of numerical modelling techniques for impact investigation on a wind turbine blade," *Compos. Struct.*, vol. 209, pp. 856–878, 2019, doi: https://doi.org/10.1016/j.compstruct.2018.11.001.

[37] J. C. Marín, A. Barroso, F. París, and J. Cañas, "Study of fatigue damage in wind turbine blades," *Eng. Fail. Anal.*, vol. 16, no. 2, pp. 656–668, 2009, doi: https://doi.org/10.1016/j.engfailanal.2008.02.005.

[38] R. Seltzer, C. González, R. Muñoz, J. LLorca, and T. Blanco-Varela, "X-ray microtomography analysis of the damage micromechanisms in 3D woven composites under low-velocity impact," *Compos. Part A Appl. Sci. Manuf.*, vol. 45, pp. 49–60, 2013, doi: https://doi.org/10.1016/j.compositesa.2012.09.017.

[39] J. Tomblin, T. Lacy, B. Smith, S. Hooper, a Vizzini, and S. Lee, "Review of Damage Tolerance for Composite Sandwich Airframe Structures," *~Bericht*, 1999, doi: DOT/FAA/AR-99/49.

[40] X. Fan, Q. Sun, and M. Kikuchi, "Review of Damage Tolerant Analysis of Laminated Composites," *J. Solid Mech.*, vol. 2, Jan. 2010.

[41] Y. Wang, "Multiphysics analysis of lightning strike damage in laminated carbon/glass fiber reinforced polymer matrix composite materials: A review of problem formulation and computational modeling," *Compos. Part A Appl. Sci. Manuf.*, vol. 101, pp. 543–553, 2017, doi: https://doi.org/10.1016/j.compositesa.2017.07.010.

[42] R. Kithil, "Case Study of Lightning Damage to Wind Turbine Blade," 2008.

[43] J. Nash, M. Stack, and I. Zekos, "Mapping of Meteorological Observations over the Island of Ireland to Enhance the Understanding and Prediction of Rain Erosion in Wind Turbine Blades," *Energies*, vol. 14, p. 4555, Jul. 2021, doi: 10.3390/en14154555.

[44] T. Lu, E. Solis-Ramos, Y. Yi, and M. Kumosa, "UV degradation model for polymers and polymer matrix composites," *Polym. Degrad. Stab.*, vol. 154, pp. 203–210, 2018, doi: https://doi.org/10.1016/j.polymdegradstab.2018.06.004.

[45] H. K. Reddick, “SAFE-LIFE AND DAMAGE-TOLERANT DESIGN APPROACHES FOR HELICOPTER STRUCTURES.,” 1983.

[46] D. Broek and J. R. Rice, “Elementary Engineering Fracture Mechanics,” *J. Appl. Mech.*, 1975, doi: 10.1115/1.3423697.

[47] J. S. Nielsen and J. D. Sørensen, “Bayesian Estimation of Remaining Useful Life for Wind Turbine Blades,” *Energies*, vol. 10, no. 5, p. 664, 2017, doi: http://dx.doi.org/10.3390/en10050664.

[48] C. Meola, *Infrared thermography recent advances and future trends*. Oak Park, Ill.: Oak Park, Ill. : Bentham Science, 2012.

[49] “Offshore Wind Energy Inspection Procedure Assessment,” Houston, TX, 2015.

[50] J. Gryzagoridis and D. Findeis, “Tap testing of composites benchmarked with digital shearography,” *Insight (Northampton)*, vol. 56, no. 1, pp. 35–38, 2014, doi: 10.1784/insi.2014.56.1.35.

[51] C. U. Grosse, A. Jüngert, and P. Jatzlau, “Local Acoustic Resonance Spectroscopy,” in *Handbook of Advanced Nondestructive Evaluation*, N. Ida and N. Meyendorf, Eds. Cham: Springer International Publishing, 2019, pp. 271–294.

[52] Y. Duan *et al.*, “Reliability assessment of pulsed thermography and ultrasonic testing for impact damage of CFRP panels,” *NDT E Int.*, vol. 102, pp. 77–83, 2019, doi: https://doi.org/10.1016/j.ndteint.2018.11.010.

[53] M. Owner-Petersen, “Digital speckle pattern shearing interferometry: limitations and prospects,” *Appl. Opt.*, vol. 30, no. 19, pp. 2730–2738, Jul. 1991, doi: 10.1364/AO.30.002730.

[54] W. Steinchen, L. X. Yang, G. Kupfer, P. Maeckel, and F. Voessing, “Application of laser diodes in digital speckle pattern shearing interferometry,” vol. 3415. Bellingham WA: SPIE, Bellingham WA, pp. 87–94, 1998, doi: 10.1117/12.326622.

[55] K. B. Katnam, L. F. M. Da Silva, and T. M. Young, “Bonded repair of composite aircraft structures: A review of scientific challenges and opportunities,” *Prog. Aerosp. Sci.*, vol. 61, pp. 26–42, 2013, doi: https://doi.org/10.1016/j.paerosci.2013.03.003.

[56] L. J. Hart-Smith, “Adhesive-Bonded Scarf and Stepped-Lap Joints,” Hampton, VA, 1973.

[57] O. A. Ibitoye, “Experimentation and Finite Element Analysis of Repairs on Composite Laminates and Sandwich Beam Structures,” Montana State University, Bozeman, Montana, 2018.

[58] L. C. Dorworth, G. L. Gardiner, and G. M. Mellema, *Essentials of Advanced Composite Fabrication and Repair*. Aviation Supplies & Academics, Inc., 2009.

[59] P. Hiemenz, “Principles of Colloid and Surface Chemistry, Revised and Expanded, 3rd Edition.” 2016.

[60] L. H. Sperling, *Introduction to Physical Polymer Science*, Fourth. John Wiley & Sons, Inc., 2006.

[61] W. D. Callister, *Fundamentals of materials science and engineering : an integrated approach,* 4th editio. Hoboken, NJ : Wiley, 2015.

[62] J. G. Speight, *Environmental organic chemistry for engineers* , 1st editio. Amsterdam, [Netherlands: Elsevier, 2017.

[63] X. Huang, D. Kim, M. Im, J. Lee, J. -B. Yoon, and Y. Choi, “‘Lock-and-Key’ Geometry Effect of Patterned Surfaces: Wettability and Switching of Adhesive Force,” *Small*, vol. 5, no. 1, pp. 90–94, 2009, doi: 10.1002/smll.200800649.

[64] K. L. Mittal, *Contact angle, wettability and adhesion. Volume 3* , First edit. Boca Raton, FL: CRC Press, an imprint of Taylor and Francis, 2003.

[65] T. Laurila, V. Vuorinen, M. Paulasto-Kröckel, M. Turunen, T. T. Mattila, and J. Kivilahti, *Interfacial Compatibility in Microelectronics Moving Away from the Trial and Error Approach* , 1st ed. 20. London: Springer London, 2012.

[66] H. Y. Erbil, *Surface Chemistry of Solid and Liquid Interfaces*. Oxford, UK: Blackwell Publishing Ltd, 2006.

[67] R. G. Dillingham and B. R. Oakley, “Surface Energy and Adhesion in Composite–Composite Adhesive Bonds,” *J. Adhes.*, vol. 82, no. 4, pp. 407–426, 2006, doi: 10.1080/00218460600683944.

[68] D. Y. Kwok and A. W. Neumann, “Contact Angle Measurement and Contact

Angle Interpretation," *Adv. Colloid Interface Sci.*, 1999, doi: 10.1016/S0001-8686(98)00087-6.

[69] J. D. Bardis and K. Kedward, "Surface Preparation Effects on Mode I Testing of Adhesively Bonded Composite Joints," *Compos. Technol. Res.*, vol. 24, no. 1, pp. 30–37, 2002, doi: 10.1520/CTR10895J.

[70] L. Moretti, P. Olivier, B. Castanié, and G. Bernhart, "Experimental study and in-situ FBG monitoring of process-induced strains during autoclave co-curing, co-bonding and secondary bonding of composite laminates," *Compos. Part A Appl. Sci. Manuf.*, vol. 142, p. 106224, 2021, doi: https://doi.org/10.1016/j.compositesa.2020.106224.

[71] R. G. Dillingham, "25 - Composite bond inspection," in *Structural Integrity and Durability of Advanced Composites*, Elsevier Ltd, 2015, pp. 695–706.

[72] R. E. Horton, "Bonded Structure Repair," in *Engineered Materials Handbook: Adhesives and Sealants*, ASM International, 1990.

[73] J. Liniger, M. Soltani, H. C. Pedersen, J. Carroll, and N. Sepehri, "Reliability based design of fluid power pitch systems for wind turbines," *Wind energy (Chichester, England)*, vol. 20, no. 6, pp. 1097–1110, 2017, doi: 10.1002/we.2082.

[74] A. M. Amaro, P. N. B. Reis, M. A. Neto, and C. Louro, "Effect of different commercial oils on mechanical properties of composite materials," *Compos. Struct.*, vol. 118, pp. 1–8, 2014, doi: https://doi.org/10.1016/j.compstruct.2014.07.017.

[75] X. Shang, "Role of contamination on the bondline integrity of composite structures," Iowa State University, 2013.

[76] V. Musaramthota *et al.*, "Effect of Surface Contamination on Composite Bond Integrity and Durability," *FAA JAMS 2014 Technical Review Meeting*. Baltimore, Maryland, 2014, [Online]. Available: https://depts.washington.edu/amtas/events/jams_14/papers/p6.Probanic.pdf.

[77] DNV-GL, "DNVGL-ST-0376," *Rotor Blades for Wind Turbines*. 2015.

[78] M. R. Gude, S. G. Prolongo, T. Gómez-del Río, and A. Ureña, "Mode-I adhesive fracture energy of carbon fibre composite joints with nanoreinforced epoxy adhesives," *Int. J. Adhes. Adhes.*, vol. 31, no. 7, pp. 695–703, 2011, doi:

https://doi.org/10.1016/j.ijadhadh.2011.06.016.

[79] “Quick Guide to Surface Roughness Measurement Bulletin No. 2229,” 2016. [Online]. Available: www.mitutoyo.com.

[80] Edwarrd M. Petrie, *Handbook of Adhesives and Sealants*, Second. New York: The McGraw-Hill Companies, Inc., 2007.

[81] F. C. Campbell, “Manufacturing Processes for Advanced Composites.” New York : Elsevier, New York, 2004.

[82] F. Awaja, M. Gilbert, G. Kelly, B. Fox, and P. J. Pigram, “Adhesion of polymers,” *Prog. Polym. Sci.*, vol. 34, no. 9, pp. 948–968, 2009, doi: https://doi.org/10.1016/j.progpolymsci.2009.04.007.

[83] H. Zeng, “Polymer adhesion, friction, and lubrication.” Hoboken, N.J. : Wiley, Hoboken, N.J., 2013.

[84] P. Fabbri and M. Messori, “Surface Modification of Polymers,” *Modification of polymer properties /*. Boston, MA :, pp. 109–130, 2017, doi: 10.1016/B978-0-323-44353-1.00005-1.

[85] J. L. Thomason and D. W. Dwight, “Use of XPS for characterization of glass fibre coatings,” *Compos. Part A Appl. Sci. Manuf.*, 1999, doi: 10.1016/S1359-835X(99)00042-1.

[86] E. P. Plueddemann, “Surface Chemistry of Silanes at the Interface,” in *Silane Coupling Agents*, Boston, MA: Springer US, 1991, pp. 79–114.

[87] M. Tanoglu, S. H. McKnight, G. R. Palmese, and J. W. Gillespie Jr, “The effects of glass-fiber sizings on the strength and energy absorption of the fiber/matrix interphase under high loading rates,” *Compos. Sci. Technol.*, vol. 61, no. 2, pp. 205–220, 2001, doi: 10.1016/S0266-3538(00)00195-0.

[88] E. Le Bourhis, “Glass : mechanics and technology.” Weinheim, Germany : Wiley-VCH, 2014.

[89] J. L. Thomason, “Glass fibre sizing: A review,” *Compos. Part A Appl. Sci. Manuf.*, vol. 127, p. 105619, 2019, doi: https://doi.org/10.1016/j.compositesa.2019.105619.

[90] T. E. of Encyclopaedia, “silane,” *Encyclopedia Britannica Britannica*. 2012,

[Online]. Available: https://www.britannica.com/science/silane.

[91] G. L. Patrick, “Organic chemistry.” New York, New York , 2012.

[92] D. Zhu, N. Hu, and D. W. Schaefer, “Chapter 1 - Water-based sol–gel coatings for military coating applications,” P. Zarras, M. D. Soucek, and A. B. T.-H. of W. C. Tiwari, Eds. Elsevier, 2020, pp. 1–27.

[93] J. Speight, “9.1 Introduction,” *Handbook of Industrial Hydrocarbon Processes*. Elsevier, 2011, [Online]. Available: https://app.knovel.com/hotlink/khtml/id:kt0090TKBQ/handbook-industrial-hydrocarbon/chemical-p-introduction.

[94] J. G. Speight, “Chapter Two - Inorganic Chemistry,” in *Environmental Inorganic Chemistry for Engineers*, J. G. Speight, Ed. Butterworth-Heinemann, 2017, pp. 51–110.

[95] H. F. Webster and J. P. Wightman, “Effects of oxygen and ammonia plasma treatment on polyphenylene sulfide thin films and their interaction with epoxy adhesive,” *J. Adhes. Sci. Technol.*, vol. 5, no. 1, pp. 93–106, 1991, doi: 10.1163/156856191X00846.

[96] S. Farris, S. Pozzoli, P. Biagioni, L. Duó, S. Mancinelli, and L. Piergiovanni, “The fundamentals of flame treatment for the surface activation of polyolefin polymers – A review,” *Polym.*, vol. 51, no. 16, pp. 3591–3605, 2010, doi: 10.1016/j.polymer.2010.05.036.

[97] S. Ebnesajjad, “Surface treatment of materials for adhesive bonding.” Amsterdam : Elsevier/William Andrew, 2014.

[98] W. Choi, S. Koh, and H. Jung, “ Surface chemical reaction between polycarbonate and kilo-electron-volt energy Ar + ion in oxygen environment ,” *J. Vac. Sci. Technol. A Vacuum, Surfaces, Film.*, 1996, doi: 10.1116/1.580024.

[99] H. Gnaser, “Low-Energy Ion Irradiation of Solid Surfaces.” Berlin, Heidelberg : Springer Berlin Heidelberg : Imprint: Springer, 1999.

[100] E. M. Liston, L. Martinu, and M. R. Wertheimer, “Plasma surface modification of polymers for improved adhesion: a critical review,” *J. Adhes. Sci. Technol.*, vol. 7, no. 10, pp. 1091–1127, 1993, doi: 10.1163/156856193X00600.

[101] L. E. Nielsen, “Cross-Linking–Effect on Physical Properties of Polymers,” *J. Macromol. Sci. Part C*, vol. 3, no. 1, pp. 69–103, 1969, doi: 10.1080/15583726908545897.

[102] H. Dodiuk and S. H. Goodman, *Handbook of Thermoset Plastics*. Burlington: Elsevier Science & Technology Books, 2021.

[103] B. A. Miller-Chou and J. L. Koenig, “A review of polymer dissolution,” *Prog. Polym. Sci.*, vol. 28, no. 8, pp. 1223–1270, 2003, doi: https://doi.org/10.1016/S0079-6700(03)00045-5.

[104] A. A. Tager and V. S. Blinov, “Thermodynamic Compatibility of Polymers,” vol. 56, no. 6, pp. 579–590, Jun. 1987, doi: 10.1070/rc1987v056n06abeh003291.

[105] B. Duncan and L. Crocker, “Review of Tests for Adhesion Strength,” National Physics Laboratory Materials Centre, Teddington, Middlesex, UK, 2001.

[106] E. E. Gdoutos, *Fracture Mechanics: An Introduction*, 3rd ed. 20., vol. 263. Cham: Cham: Springer International Publishing.

[107] A. Lusty, D. Cairns, D. Miller, and D. Samborsky, “A comparison of surface preparation techniques for wind turbine field repairs (updated results),” *IOP Conf. Ser. Mater. Sci. Eng.*, vol. 942, no. 1, 2020, doi: 10.1088/1757-899X/942/1/012012.

[108] T. N. Ritchey, “Development of Failure Criteria and Experimental Testing for Composite Adhesively Bonded Scarf Repairs Utilizing Structural Paste Adhesives,” Montana State University, Bozeman, MT, 2014.

[109] “ASTM D5868-01: Standard Test Method for Lap Shear Adhesion for Fiber Reinforced Plastic (FRP) Bonding.” ASTM International, West Conshohocken, PA, 2014, doi: 10.1520/D5868-01R14.

[110] J. R. Reeder and J. H. Crews, “Mixed-mode bending method for delamination testing,” *AIAA J.*, vol. 28, no. 7, pp. 1270–1276, Jul. 1990, doi: 10.2514/3.25204.

[111] “ASTM D3039/D3039M-17 Standard Test Method for Tensile Properties of Polymer Matrix Composite Materials.” ASTM International, West Conshohocken, PA, doi: https://doi.org/10.1520/D3039_D3039M-17.

[112] P. Agastra, “Mixed Mode Delamination of Glass Fiber/Polymer Matrix

Composites," Montana State University, 2003.

[113] "D7079/D7078M-20 Standard Test Method for Shear Properties of Composite Materials by V-Notched Rail Shear Method." ASTM International, West Conshohocken, PA, 2020, doi: https://doi-org.proxybz.lib.montana.edu/10.1520/D7078_D7078M-20.

[114] S. B. Kumar, I. Sridhar, S. Sivashanker, S. O. Osiyemi, and A. Bag, "Tensile Failure of Adhesively Bonded CFRP Composite Scarf Joints," *Mater. Sci. Eng. B*, no. 132, pp. 113–120, 2006, doi: https://doi.org/10.1016/j.mseb.2006.02.046.

[115] W. P.M., K. Katnam, M. H.F., and T. Young, *Composite Scarf Repairs Using Vacuum Infusion And Bondline Veils*. Limerick, Ireland, 2014.

[116] G. Sun, X. Liu, G. Zheng, Z. Gong, and Q. Li, "On fracture characteristics of adhesive joints with dissimilar materials – An experimental study using digital image correlation (DIC) technique," *Compos. Struct.*, vol. 201, pp. 1056–1075, 2018, doi: https://doi.org/10.1016/j.compstruct.2018.06.018.

[117] C. Stroili, "Validation of high strain rate, multiaxial loads using an in-plane loader, digital image correlation, and FEA." Montana State University - Bozeman, College of Engineering, 2019.

[118] D. Systèmes, "Abaqus 2016 Online Documentation," 2015. http://130.149.89.49:2080/v2016/index.html.

[119] V. Buljak and G. Ranzi, "Chapter 2 - Calibration of constitutive models," V. Buljak and G. B. T.-C. M. of E. M. Ranzi, Eds. Academic Press, 2021, pp. 43–53.

[120] B. Duncan, "14 - Developments in testing adhesive joints," in *Woodhead Publishing in Materials*, D. A. B. T.-A. in S. A. B. Dillard, Ed. Woodhead Publishing, 2010, pp. 389–436.

[121] E. J. Barbero, *Finite Element Analysis of Composite Materials Using Abaqus*. Boca Raton, FL: CRC Press: Taylor & Francis Group, 2013.

[122] R. D. (Robert D. Cook and R. D. Cook, *Concepts and applications of finite element analysis*, 4th ed.. New York, NY: New York, NY : Wiley, 2001.

[123] Y. Wang, M. Tong, and S. Zhu, *Three Dimensional Continuum Damage Mechanics Model of Progressive Failure Analysis in Fibre-Reinforced Composite*

Laminates. 2009.

[124] F. A. Leone, C. G. (Carlos G. Dávila, and D. Girolamo, *Progressive damage analysis of bonded composite joints* . Hampton, Virginia: National Aeronautics and Space Administration, Langley Research Center, 2012.

[125] V. Ranatunga and S. B. Clay, "Cohesive modeling of damage growth in z-pinned laminates under mode-I loading," *J. Compos. Mater.*, vol. 47, no. 26, pp. 3269–3283, 2013, doi: 10.1177/0021998312464078.

[126] W. M. Peterson, "Effect of fiber diameter on stress transfer and interfacial damage in fiber reinforced composites." Montana State University - Bozeman, College of Engineering, 2013.

[127] D. F. O. Silva, R. D. S. G. Campilho, F. J. G. Silva, and U. T. F. Carvalho, "Application a direct/cohesive zone method for the evaluation of scarf adhesive joints," *Appl. Adhes. Sci.*, vol. 6, no. 1, pp. 1–20, 2018, doi: 10.1186/s40563-018-0115-2.

[128] M. Kenane, Z. Azari, S. Benmedakhene, and M. L. Benzeggagh, "Experimental development of fatigue delamination threshold criterion," *Compos. Part B Eng.*, vol. 42, no. 3, pp. 367–375, 2011, doi: https://doi.org/10.1016/j.compositesb.2010.12.019.

[129] N. Egorov and E. Sheshin, "Basic Principles BT - Field Emission Electronics," N. Egorov and E. Sheshin, Eds. Cham: Springer International Publishing, 2017, pp. 1–42.

[130] L. Juhsaz *et al.*, "False Morphology of Aerogels Caused by Gold Coating for SEM Imaging," *Polymers (Basel).*, vol. 13, no. 4, p. 588, 2021, doi: http://dx.doi.org/10.3390/polym13040588.

[131] J. Bergström, "2.6.2 Energy Dispersive Spectroscopy," *Mechanics of Solid Polymers - Theory and Computational Modeling*. Elsevier, 2015, [Online]. Available: https://app.knovel.com/hotlink/khtml/id:kt00UD0FR3/mechanics-solid-polymers/energy-dispersive-spectroscopy.

[132] G. Swadener, K. Liechti, and Y.-M. Liang, "Shear induced toughening in bonded joints: Experiments and analysis," *Int. J. Fract.*, vol. 114, pp. 113–132, Mar. 2002, doi: 10.1023/A:1015013618976.

[133] L. Liao, C. Huang, and T. Sawa, “Effect of adhesive thickness, adhesive type and scarf angle on the mechanical properties of scarf adhesive joints,” *Int. J. Solids Struct.*, vol. 50, no. 25–26, pp. 4333–4340, 2013, doi: 10.1016/j.ijsolstr.2013.09.005.

[134] M. Ridha, V. B. C. Tan, and T. E. Tay, “Traction–separation laws for progressive failure of bonded scarf repair of composite panel,” *Compos. Struct.*, vol. 93, no. 4, pp. 1239–1245, 2011, doi: 10.1016/j.compstruct.2010.10.015.

[135] R. D. S. G. Campilho, M. F. S. F. de Moura, A. M. G. Pinto, J. J. L. Morais, and J. J. M. S. Domingues, “Modelling the tensile fracture behaviour of CFRP scarf repairs,” *Compos. Part B Eng.*, vol. 40, no. 2, pp. 149–157, 2009, doi: https://doi.org/10.1016/j.compositesb.2008.10.008.

[136] G. T. Klise, “Sandia Wind Energy Program FY21 Accomplishments,” Albuquerque, NM, 2021. [Online]. Available: https://www.osti.gov/biblio/1854446.

[137] A. Mentes and O. Turan, “A new resilient risk management model for Offshore Wind Turbine maintenance,” *Saf. Sci.*, vol. 119, pp. 360–374, 2019.

[138] P. Bortolotti *et al.*, “A Detailed Wind Turbine Blade Cost Model.” 2019.

15. APPENDICES

15.1 APPENDIX A

A HOW-TO GUIDE FOR DIC DATA COLLECTION

The following steps should be followed to begin a project and calibrate the system for quasi-static tests using a 5MP camera system:

1. Choose appropriate camera lens (if options available).
2. On the computer, click on the icon for Aramis Professional 2018 (Figure 107).

Figure 107. Icon for Aramis Professional 2018.

3. Start a new project from the main menu on screen.
    a. If asked: Do you want to initialize the detected sensors? Select YES.
4. Ensure the lights with the camera are on.
    a. If not, click on the top bar ACQUISITION prompt → sensors → light on.
5. Select the second icon on the top bar, setup
6. Adjust your cameras for calibration and testing.
    a. With your testing sample in place, move cameras so that the entire sample is in view of both cameras. The computer will have one window for each camera. Cameras should be pointing to the same spot on the sample.
    b. Once you see the entire sample, swap out the sample for a calibration block (be careful not to touch the front dotted surface of the calibration block).

i. Choose a calibration block that most closely matches the desired field of view for the test.

c. With the calibration block in view of both cameras, measure the distance between the block and the center of the camera bar.

d. To achieve an optimum 25 degree angle between the cameras, set the distance between the cameras to 0.4x the distance between the block and the camera bar OR input the measuring distance into the bottom right hand prompt and it will adjust the slider distance (distance between cameras) appropriately.

7. Adjust the camera focus for calibration.

a. Once you can see the calibration block with both cameras, open the aperture on each camera by adjusting the aperture knob on the lens.

b. Decrease the shutter speed until you can see the calibration dots on the computer screen by using the middle mouse wheel on the bottom of each camera window.

c. Adjust the focus ring on each camera until the calibration dots are completely clear.

i. Lock the focus rings in place – the camera focus must not be changed after calibration.

d. Adjust the shutter speed to your desired test rate (test dependent).

i. Avoid shutter speeds greater than 30 ms.

e. Close the camera aperture until over-exposure is not present (i.e. the calibration dots are not too bright).

8. Select the third icon to start calibration.

    a. In the calibration pop up window, select the correct calibration block ID. Select OK.

9. Follow the prompts on the right side of the screen for calibration block adjustments. For each adjustment, make sure the center cross-hairs are within the center box of calibration dots. The cross-hairs do not need to be exactly centered or aligned with specific dots, just within the center box.

10. The sequence for calibration is as follows.

NOTE: After each adjustment, select >snap on the bottom right corner of the screen. Check the orange gridded images that appear, the grid should cover close to the entire calibration block. If there are more than a few discontinuities, select <back and readjust the block before snapping another image.

    a. Center – calibration block in center of measurement volume.

    b. Closer to cameras – move block closer to cameras, must still be in focus.

    c. Farther from cameras – move block away from cameras, must still be in focus.

d. Center tilt – move the block back to the center of the measurement volume and tilt it slightly forward or backwards.

e. Center tilt 180 degree rotation – maintaining the same (or close) tilt angle, rotate the block 180 degrees.

f. Center left camera – from the center of the measurement volume, point the block towards the left camera. The right camera should still have its cross hairs within the center box of dots.

g. Center left rotate 90 degrees *repeat 4 times* - rotate the block 90 degrees, still facing the left camera.

h. Center right camera – center the block on the measurement volume and point towards the right camera.

i. Center right rotate 90 degrees *repeat 4 times* - rotate the block 90 degrees, still facing the right camera

11. Once all the calibration images are captured, the software will compute the calibration. A popup will appear in the left corner of the screen. If two green circle checks are present, the calibration was successful. If one or more red x's are present, make sure the cameras are properly focused and repeat the calibration images.

12. You can now move on to data acquisition.

16.1.2 Data Acquisition with a quasi-static system

1. From the main menu, select New Project. Assign a descriptive name for the project.
2. From the far left of the top menu bar, select the second option from the dropdown DATA ACQUISITION.
3. Select the third icon on the top bar and choose the first option “start measuring sequence”
    a. Assign the sequence a name.
    b. Set desired measuring mode, such as a fixed frame rate.
    c. Set the finish condition. Example: if you choose “finish at abort” then the test data acquisition will stop when you press the Esc key.
4. Start the acquisition by clicking the OK button.
5. Watch the bottom bar until you see “capturing images.”
6. Start your test.
7. Select the left drop down icon to “inspection.”
    a. Select “surface component.”
    b. Assign the component a name.
    c. If the software is selecting points off of your test sample, you can select sample boundaries with the polygon button along the bottom display bar.
    d. After your surface component has loaded, toggle the image on/off with the bottom display bar.

i. Looking at the surface without the image lets you make sure a complete surface has been created. Check to make sure there are no holes in your area of interest. If there are, create a polygon boundary for the sample.

8. Save your project with Save as… from the file menu.

15.2 APPENDIX B

A HOW-TO GUIDE FOR DIC DATA ANALYSIS

This analysis guide uses the Aramis Professional 2018 software. Note: once data has been collected, data can be analyzed in the free GOM Correlate software. Be sure to make a note of all chosen parameters for inclusion in your data write-up. Follow instructions under the appropriate section for your desired test type. If you want to practice analysis, sample data sets are available online from the GOM Correlate website.

B.1 Creating a project and uploading data

1. From the main menu select “New Project.”

    a. Choose a menu using the top toolbar “Workspace selection” (Figure 108).

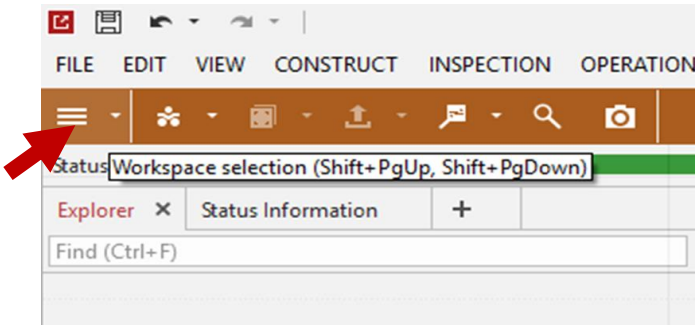

Figure 108. Workspace selection screenshot.

2. Drag and drop collected stage files into the grid side of the screen.

    a. The stage files should be the images and any associated load data collected during your experiment.

B.2 Analysis with strain fields

1. On the top tool bar, select the second icon from the left and choose “surface component…”

a. In the popup window choose your pixel and facet size.

b. Facets are recommended to be at least 10 pixels (Usually 25x25 pixels). The exact size depends on the size of your DIC speckle pattern; you should have each dot should be 3-7 pixels and there should be about 3-7 dots per facet.

2. Using the bottom 3D toolbar click the “select/deselect on surface” icon to select only a section of your sample to analyze.

    a. Use the left mouse button to select points to create the edges of your polygon (Figure 109). Right click to finish.

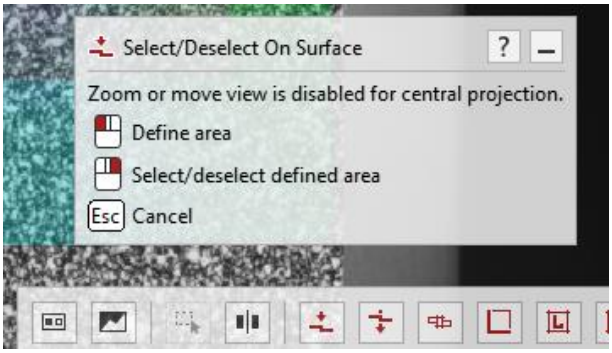

Figure 109. Polygon selection screenshot.

3. Define a local coordinate system for your surface component by selecting “321 alignment” from the top right “+” icon. By creating a coordinate system relative to your surface you define the planes for strain analysis.

    a. Select the ZZZ-YY-X Rule. Use “Ctrl+left click” to select points.

b. Select 3 points to establish the Z plane, then 2 points to establish the Y axis, and one final point establish the X axis (Figures 110 and 111).

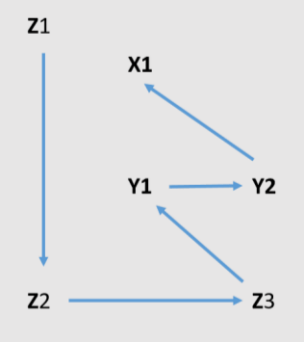

Figure 110. Recommended point locations.

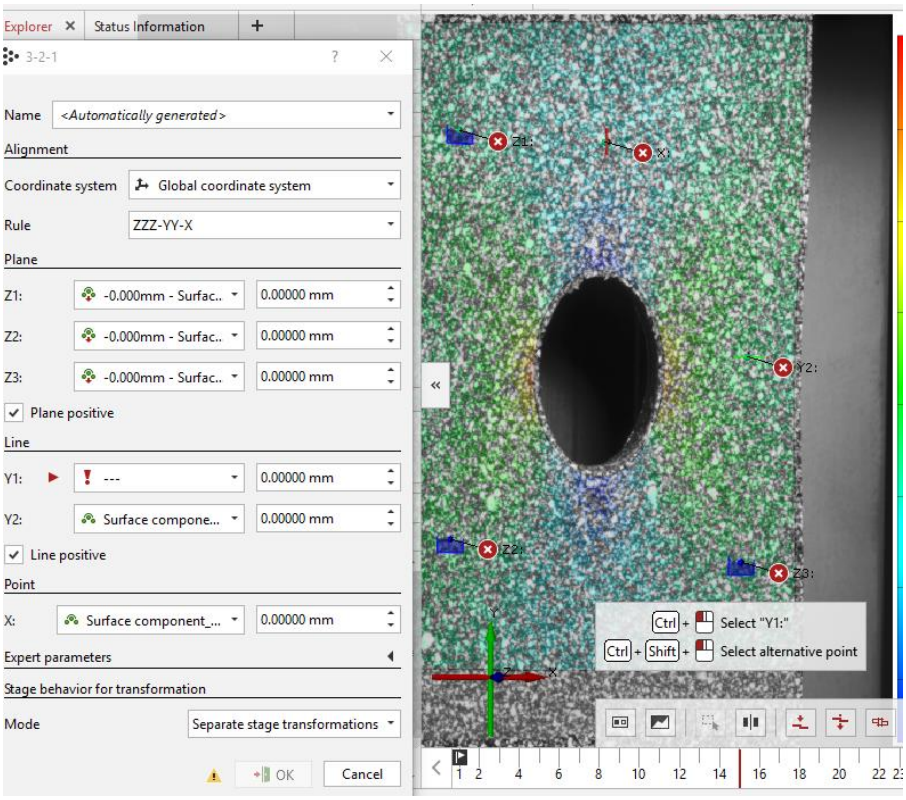

Figure 111. Alignment selection screen.

4. To check the strain values click on the surface.
    a. On the top menu select “INSPECTION” → “Check dimensions” → “Strains” → Epsilon XY. Click OK.
        i. There are multiple strain options in this menu, so make sure you select what field you are interested in.
        ii. You can add filters in the popup window when you pick a strain type. There are spatial and temporal filters. The most common are the averages which average strain values over a larger space or between stages. The average filters generally reduce noise in the data.
        iii. CAUTION: if you choose to use filters, you must be able to justify why you used them. It is always good to check your strain field without filtering first.
    b. You can scroll through the stages by dragging the bottom timeline to see the strain map and color scale throughout the experiment.
5. To clean up the color map scaling right click the color map bar on the right of the screen.
    a. Select “Scaling” → all visible stages.
    b. This creates the same color scale for every stage, emphasizing the strain locations.

6. To change what part of the surface you want to analyze. This allows you to select specific facets to create a strain vs time plot.
    a. Left click on the surface to select a component.
    b. On the top toolbar click on the magnifying glass icon (6th from the left).
    c. Choose the “check” icon.
    d. Select “Deviation Label Arithmetic Mean.”
        i. Right click the surface (or select on the bottom 3D toolbar) and choose “Select/deselect through surface.”
        ii. Select the edges of your area of interest with the left mouse button.
        iii. Right click to exit the selection too.
        iv. Click the “OK” check box in the popup window.
7. To view a strain vs time plot and export your analysis as a csv file.
    a. Select the “+ Open tab” icon in the center window.
    b. Select “Diagram” from the dropdown menu.
    c. Click the save icon on the top left of the diagram.
    d. Choose a folder and filename and select “OK.”
8. Export Force and XY strains using instructions in the manual.

9. To create a report page with images and diagrams:

    a. Select the camera “create report page” icon on the top toolbar.

    b. Add a title and edit the style in the popup window.

    c. To view as a pdf select “FILE” from the top main menu, scroll down to “EXPORT” and select “Report.”

15.3 APPENDIX D

CALCULATING LOG STRAIN IN ARAMIS

To calculate the natural log of the y-component of strain in Aramis, a user-defined inspection is used on the surface component. To do the user-defined inspection, the surface component is selected from the Explorer Tab, then in the following drop-down order: Inspection, Surface Comparisons, Surface Component Analyses. Then, Inspection is selected from the ribbon, then in the following drop-down order: Check Dimensions, Other, and User-Defined. In the User-Defined pop-up, the drop-down arrow for the "Additional input elements/values" section is selected. Under the column, "Element/Value," the inspection is selected. The natural log formula is entered into the "Actual expression" box. Fx is selected, followed by the natural log function. When typing the equation, after the "." is put after the variable (i.e. A), a menu will pop up that will list all relevant keywords for that element. The "value" keyword will be third in the list and will be "[indexed]." Being indexed means that the value will be calculated for each point instead of obtaining one number for the whole component. The formula will look like "ln(A.value)." Figure 112 includes a screenshot of the final dialog box.

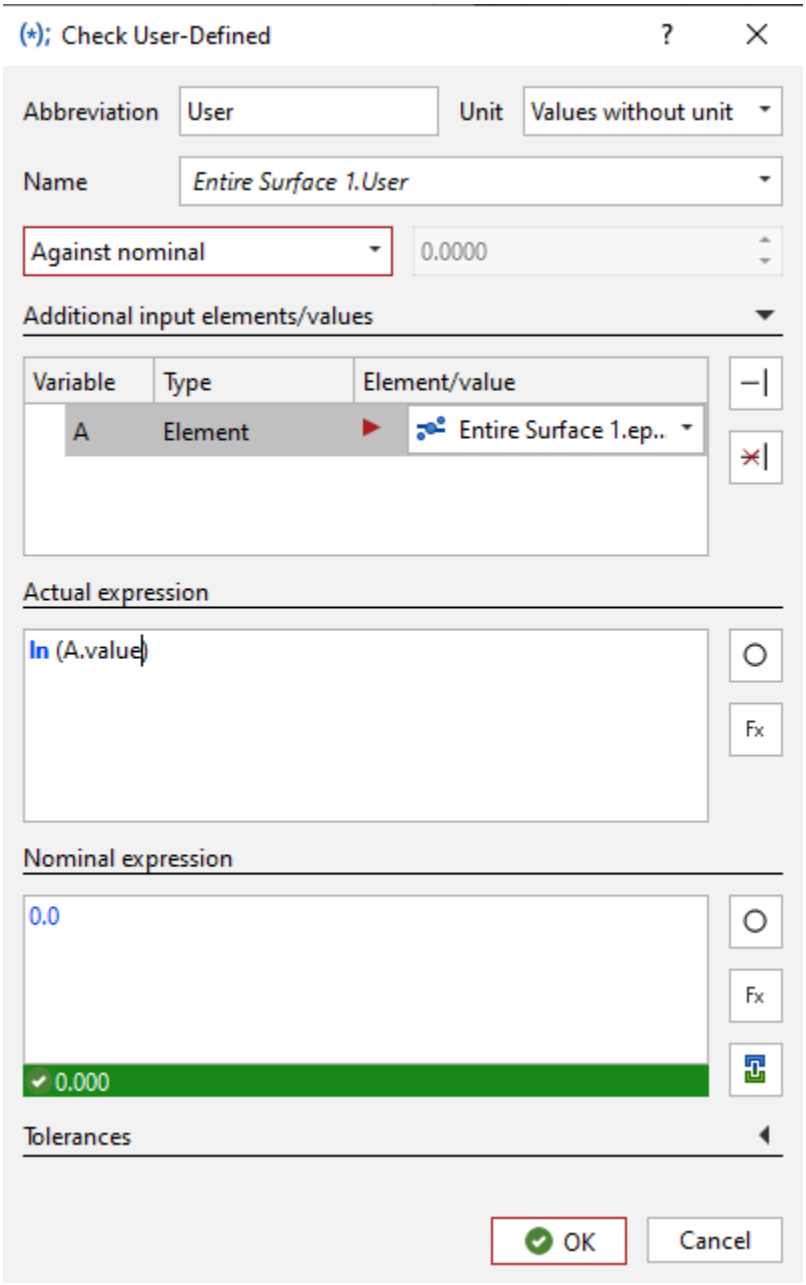

Figure 112. Screenshot of the final dialog box for logarithmic strain calculations in Aramis.

15.4 APPENDIX D

NOTE ON DIC AND FEA COMPARISONS

DIC results can be directly compared to Abaqus results in Aramis, but S8R shell elements must be used in Abaqus. S8R shell elements were not used in this work because S8R shell elements are incompatible with cohesive elements.

15.5 APPENDIX E

RUNNING A UMAT SUBROUTINE

It is recommended to contact SIMULIA support to set up the FORTRAN 77 compiler to run UMAT subroutines. The latest version of Abaqus should be installed. Once the compiler is set up and there is a .cae file to run the subroutine from, Abaqus CAE should be run from the "Abaqus Command" window rather than with the "Abaqus CAE" shortcut. To run Abaqus from the Abaqus Command window, first navigate to the working directory where the .cae file is, then type 'abaqus cae' without quotes and hit enter.

There are two ways to code in FORTRAN, in free format or in fixed format. Free format can be used for compilers that compile FORTRAN 90 and FORTRAN 95 code, while compilers that compile FORTRAN 77 code require fixed format code. For fixed format code, spaces must be used instead of tabs when indenting lines. Additionally, statement numbers go in columns 1-5, continuation characters in column 6, and executable statements in columns 7-72. FORTRAN 77 fixed format code is saved with a .for file extension. Typically, subroutine compilers that are set up with Abaqus only compile FORTRAN 77 code. To debug UMAT subroutines, .log files can be used and are found in the working directory in which the job was run.

15.6 APPENDIX F

ADDITIONAL ACKNOWLEDGEMENTS

- This work was performed in part at the Montana Nanotechnology Facility, a member of the National Nanotechnology Coordinated Infrastructure (NNCI), which is supported by the National Science Foundation (Grant# ECCS-1542210).
- The how-to guides for DIC (Appendices A and B) were primarily developed by Charlotte Berg.
- Special thanks to Enercon Industries Corporation for plasma-treating and contact angle testing composite specimens.
- Ryan Clarke's assistance with finite element modeling was appreciated.